



# ESRF HIGHLIGHTS

## 2011



# Highlights 2011

EUROPEAN SYNCHROTRON RADIATION FACILITY

Pages

3	<b>Introduction</b>
5	<b>Status of the Upgrade Programme</b>
9	<b>Scientific Highlights</b>
9	<i>Dynamics and Extreme Conditions</i>
26	<i>Structure of Materials</i>
44	<i>Soft Condensed Matter</i>
58	<i>Electronic Structure and Magnetism</i>
77	<i>Structural Biology</i>
102	<i>X-ray Imaging</i>
118	<b>Enabling Technologies</b>
128	<b>Accelerator and X-ray Source</b>
136	<b>Facts and Figures</b>

**Cover**

A design by Stanislav Markaryan, inspired by the article *Cold melting and solid structures of dense lithium* by C.L. Guillaume *et al.*, page 11.

Photo on back cover, credit: P. Ginter/ESRF.



## Dear Reader

2011 has once again been a year of excellent results for the ESRF with outstanding scientific output as measured in the number of publications, exceptional performance of the accelerator complex and major advances in the Upgrade Programme 2009-2018.

The number of proposals, as well as publications in peer-reviewed journals, was very high and comparable to the record figures of previous years. The same can be said for the number of experimental sessions and User visits, taking into account the start of the Upgrade Programme's "long shutdown" on 5 December 2011. Although the final figures for the number of publications are not yet available at the time that we go to press, it is already known that 2011 was outstanding in terms of publications in the most prestigious scientific journals. This emphasises the increasing role synchrotron science plays in twenty-first century frontline research.

The Upgrade Programme is now well in swing and truly into the beginning of its delivery phase. The beamline portfolio saw the inauguration of the first of eight Upgrade Beamline projects (UPBLs) on ID24 and BM23. Rapid progress is also being made in the construction of UPBL10, the future structural biology beamline complex on ID30, along with UPBL6, the future inelastic scattering beamline on ID20, and the imaging beamline UPBL4 on ID16. The other UPBLs have either entered into the construction planning phase or will see their Technical Design Reports presented to the Science Advisory Committee (SAC) in 2012. In parallel, important refurbishments have started for existing beamlines, notably on ID10 and ID19.

The Source Upgrade continues with a focus on the RF system. Most notably, test operation of the new solid state amplifiers and of the new higher-order mode damping cavities are very promising and so far reaching the design specifications. The shutdown periods have been used to install more 6m-long straight sections, and to prepare the 7m section implementation on ID23 in 2012.

The instrumentation development programme saw the start of CRISP (Cluster of Research Infrastructures for Synergies in Physics), a 12 M€ ESRF-led project funded by the European Commission. CRISP is strongly focussed on accelerator component R&D, detector and data acquisition technologies, as well as on IT and data management, thereby complementing the efforts undertaken within the Upgrade Programme.



Credit: ESRF / Molyneux Associates.

In May 2011, the new data centre in the Central Building was inaugurated, ensuring that we meet the ever-increasing computing needs, in particular for imaging experiments.

In September 2011, the Experimental Hall extension project (EX2) entered into the construction phase. A five-month "long shutdown" will set the foundation of this crucial element of the whole Upgrade Programme, and the delivery of the new buildings will start to take place in 2013. The progress of this highly complex project is proceeding as planned. The heavy construction work on the site so far has had a close-to-nil impact on the User operation. Beamtime delivery was reduced by just two weeks, in December 2011. In 2012, however, two long shutdowns from January to May and in August to September will lead to an overall reduction of beamtime delivery of about four months, with a return to normal User operation in 2013.

In the 2011-2013 period the ESRF has to absorb a 6% budget reduction. This is related to the general economic situation in Europe and the ensuing difficulties for certain Member Countries. A strategy has been developed which does not compromise the quality of the ESRF User service. The greatest consequence was that two beamlines, ID20 and ID32, both highly productive, had to be temporarily closed. The choice of these two specific beamlines has also been linked to a new logistic of relocating those UPBL beamlines which were initially planned to be in the Vercors experimental hall extension. This extension had to be cancelled in the wake of the reduced budget.

The ESRF Management and Council have worked hand in hand to face the financial difficulties, including efforts to attract new Members and Associates. On 22 June 2011 Russia, which has a strong synchrotron science programme, signed a Memorandum of Understanding in view of becoming a full ESRF Member. Other countries in Europe and in emerging market economies throughout the world also have strong scientific communities using synchrotrons; some have expressed interest in an association with the





ESRF. New Members and Associates should provide, possibly as of 2012 or 2013, an opportunity to return to budget scenarios commensurate with the original Upgrade Programme plans.

The future of the ESRF, with an extended circle of Members and Scientific Associates, is based on its solid and long-term scientific vision. In 2011, the ESRF started to discuss possible scenarios for Phase II of the Upgrade Programme, covering the period 2015-2020. During 2012 and 2013, a full scientific and technical conceptual design will be developed with the help of the new ESRF SAC and the Users' community at large. In parallel, the ESRF Council established a working group which will conduct consultations and interviews with the objective to present, by the end of 2012, a long-term strategic vision for the ESRF well beyond 2020, both on a European and worldwide level.

Local partnerships also continue to thrive. On 16 February 2011, the ESRF, the ILL, the CEA and the CNRS launched the Technology Platform Grenoble (TP-G). This initiative is dedicated to the characterisation of materials and processes and will provide coordinated access for applied and industrial R&D to large-scale instruments in Grenoble. The TP-G and two other partnerships will be housed in the future Science Building between the ESRF and the ILL, directly accessible from both facilities. The construction of this building, funded by French regional and local authorities, will start early in 2012 and will be completed in 2014.

On 19 March 2011, the international synchrotron community, and the ESRF staff in particular, learned with much grief of the loss of Pascal Elleaume, Director of the Accelerator and Source Division, who died in an accident. Pascal was very well known and appreciated by the whole community for his major contributions in the development of third-generation synchrotron sources. Despite the terrible loss of Pascal, the Accelerator and Source Division has been able to continue to ensure the operation of the storage ring. Record-breaking values have been obtained in the various 2011 Machine statistics. I wish to thank, on behalf of the whole of the ESRF User community, the staff of the division for their work and motivation. These excellent results could not have been obtained, however, without the wise and careful guidance of Laurent Farvacque, who will ensure the interim directorship of the Accelerator and Source Division until February 2012.

Serge Pérez, Director of Research for chemistry and life sciences, decided to leave the ESRF at the end of 2011 for personal reasons. I would like to thank him for his numerous contributions, notably in the development of new partnerships and relations with our host country. In February 2012, Pantaleo Raimondi will join the ESRF as the new Director of the Accelerator and Source Division. We all welcome Pantaleo.

I would like to thank our Member and Associate Countries and their delegates to Council, AFC and SAC, for their continued support and trust. Special thanks go to the ESRF SAC members and to the SAC Chairman, Prof. R. Abela, for the advice and guidance during the last three years (2009-2011), and for their crucial role during the launching of the Upgrade Programme. I welcome the new SAC (2012-2014), recently appointed by the Council, and its Chairman, Prof. Keijo Hämäläinen. I wish also to express my gratitude to all members of the Beamtime Allocation Panels and of the Beamline Review Committees for their dedication and hard work. My thanks also go to the French authorities, in particular to the *Ville de Grenoble*, the *Grenoble-Alpes Métropole*, the *Conseil Général de l'Isère* and the *Région Rhône-Alpes* for their attention and for granting funding for site infrastructure projects. Similarly, I acknowledge the actions of the European Commission which continues to provide crucial support to the ESRF in a highly visible way.

Finally, I wish to acknowledge the efforts and motivation of the ESRF staff who are on the frontline of both facility operations as well as Upgrade Programme implementation.

Last, but certainly not least, I wish to thank the thousands of Users who make it all worth it with the outstanding science that they carry out at the ESRF. A few highlights are presented on the following pages.

Francesco Sette,  
ESRF Director General



## Status of the Upgrade Programme

With the start of the long shutdown we have now reached the peak activity in the Upgrade Programme. All divisions of the ESRF are involved in heavy works bringing about the most profound changes since the inauguration of the ESRF. The Technical Infrastructure Division is realising the EX2 project while gearing up for the site infrastructure works for the CPER programme running in parallel. The Accelerator and Source Division takes full advantage of the long shutdown to install major components for the upgrade of the accelerator and source complex. Finally, the Experiments Division and the Instrumentation Services and Development Division together are taking the opportunity to deeply upgrade, refurbish, and modify a large number of beamlines to realise improved performance for our users.

### New Buildings

The project for the extension of the experimental hall has progressed according to schedule. Following the approval of the work contracts by an exceptional Administrative and Finance Committee and Council meeting at the end of July 2011, works were started in September with many preparatory actions to clear and prepare the areas in front of the current experimental hall on both sides of the Central Building. This phase included the installation of the construction headquarters, the displacement of underground networks, the move of the Central Building heat exchangers and one of the big liquid nitrogen tanks, the move of several bicycle sheds, and last but not least the preparatory works for the demolition of three sector buildings.

The extended winter shutdown started as planned on 5 December 2011 and allowed the demolition of the sector buildings (**Figure 1**) and the heavy earth works to start. By the end of January 2012, some 20 000 m<sup>3</sup> will have to be moved to the temporary storage area in front of the Central Building. During the extended shutdown, most of the disruptive works will be done while minimising the impact and maintaining the best possible working conditions in the Experimental Hall, because this period of time is also of crucial importance for many other activities linked to the construction of the upgrade beamlines. Notably the work on the fluids and electricity networks will unavoidably result in cut-offs which will be carefully planned and communicated to the staff.

The current planning foresees the delivery of the ID16 building in September 2012, the Chartreuse experimental hall and the Lab. and Office Building in March 2013, and the Belledonne experimental hall in May 2013. By then 12 000 m<sup>2</sup> of new buildings, and in particular more than 4 000 m<sup>2</sup> of high quality slab for the Upgrade beamlines, will become available.

The State/Region funded project (CPER – Contrat Plan Etat Region) has also made significant progress. The construction of the Science Building (under the authority of the ILL) will start in March/April 2012 with an expected delivery of the building in September 2013. The Science Building will host laboratories and services common to the ILL and ESRF: the Theory Group, library, PSCM, chemistry lab., material science lab., and the characterisation & technology platform.

The project funded by the CPER to create a new site entrance on the Avenue des Martyrs and to upgrade the Common Building restaurant has entered into the technical specification phase to prepare the documents for the tender exercise. The building contracts will be placed this summer and delivery of the new premises is expected to take place at the end of 2013.



**Fig. 1:** Demolition of sector buildings.



## Upgrade of the source

In 2011 the upgrade of the Accelerator System went on mostly during the planned shutdowns without interfering with the User programme.

During the winter 2010-2011 shutdown, the installation of a new set of skew quadrupole correctors, together with improved algorithms, allowed the vertical emittance to be further reduced and stabilised at around 4 pm. Work on the new beam position feedback continued with the installation of the processors and fast network. The first tests were performed during fall and confirmed an excellent performance. The new system will replace the old one in the first run of 2012.

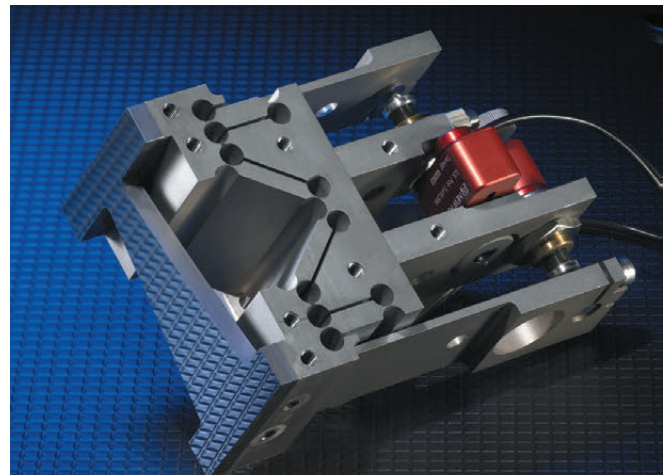
At the end of 2011, 4 straight sections were lengthened to 6 m, with ID24 being the 1<sup>st</sup> section to accommodate 4 undulator carriages. Preparatory work for the first 7 m long straight section on ID23 also started with the delivery and magnetic measurement of the new quadrupole magnets.

The upgrade of the RF system reached a major milestone with the delivery of the solid state amplifiers that will replace the klystron on the Booster. The tests on load were successfully completed in December and the connection to the Booster RF cavities will be done at the beginning of 2012. Simultaneously, two prototypes of new HOM-free RF cavities were delivered, and the first cavity was installed in the storage ring. It behaved perfectly in passive mode during User runs and was successfully tested in accelerating mode during machine dedicated time.

## Renewal of beamlines

2011 saw the first reduction in the number of beamlines operated by the ESRF owing to a 6% budget cut and the construction of new beamlines. The magnetic scattering programme on beamline ID20 made way for UPBL6, a beamline employing high resolution spectroscopy for the study of electronic excitations, and the spectroscopy beamline ID32 was closed at the end of the year to prepare the ground for the moving of beamline ID08 to its new location within the UPBL7 project.

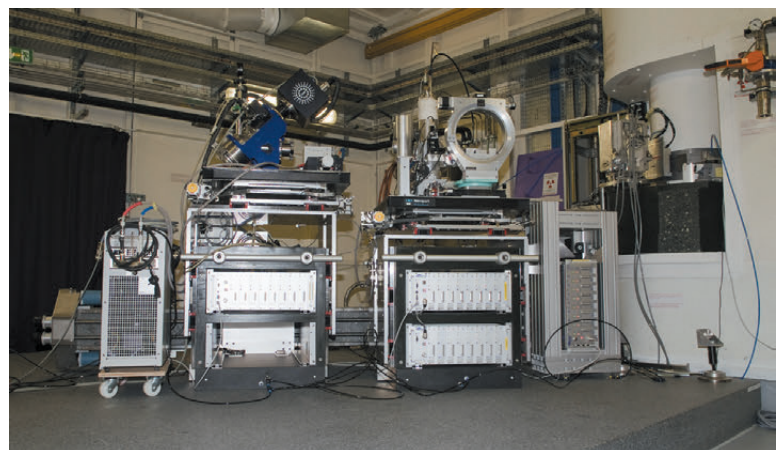
Many improvements have been achieved not only on beamlines already under construction in the frame of the Upgrade Programme (**Figure 2**). Equal importance is placed on optical components, sample manipulation and environment systems, as well as on detectors with vastly improved performance. The first upgraded beamlines have been commissioned and inaugurated. Continuous investments are also being made on many other beamlines. The upgrade and refurbishment projects on beamlines are being realised in close collaboration between the Instrumentation Services and Development Division and the Experiments Division. The following lists the main projects tackled in 2011.



Credit: Artechnique

**Fig. 2:** Compact multilayer KB mirror for beamline ID22NI.

- UPBL4: Procurement of most of the optical components.
- UPBL6: Installation of the beamline infrastructure; design of the two spectrometers (high resolution IXS spectrometers and large solid angle IXS spectrometer); procurement of the optical components.
- UPBL7: Preparation for move of ID08 to ID32; design studies for optical components and the RIXS spectrometer.
- UPBL9A: Completion of the TDR; design works for beamline components.
- UPBL10: Completion of ID30A infrastructure; Design and procurement of optical and endstation components; Commissioning of a new sample robot; Launch of an R&D project for the next generation of sample robotics; complete installation of BM29 optics.
- UPBL11: Installation of beamline components on ID24-S and ID24-L branch lines; commissioning of ID24-S branch (**Figure 3**); start of user operation on BM23 (March 2011).
- ID10 refurbishment: design of beamline components for merged ID10A/B/C beamline complex; start of in-depth refurbishment during long shutdown.
- ID19 refurbishment: design of beamline components; start of in-depth refurbishment during long shutdown.
- BM14 refurbishment: Installation of commissioning of new optical elements (channel-cut monochromator; flat mirror; toroidal mirror).



Credit: C. Argoud / ESRF

**Fig. 3:** New beamline branch ID24-S.





The range of new detectors spreads from high performance pixel detectors (Pilatus, Maxipix) to large area flat panel detectors (Perkin Elmer) and ultrafast CMOS cameras (PCO Dimox) for the imaging beamlines, to name only a few. The Instrumentation Services and Development Division is deeply involved not only in in-house detector programmes (Maxipix, FReLoN), but also in new detector developments coordinated between facilities on the European level. Generic ESRF developments such as IcePAP for motion control, LIMA as an interface for 2D detector integration, and TANGO devices for both the accelerator complex and beamline instruments have been further developed and installed. To handle the enormous amount of user data produced by this equipment, a new data centre (**Figure 4**) has been installed hosting new data storage systems, high performance computers for online data analysis, and long-term data archival on tapes.

*R. Dimper, L. Farvacque,  
H. Reichert and J. Susini*



**Fig. 4:** New data centre in the central building.







# Dynamics and Extreme Conditions

The selected articles for the 2011 edition of the Highlights provide a representative slice of the research performed on the Dynamics and Extreme Conditions Group's beamlines, but can only give a flavour of the many excellent results obtained in the course of the year. The Highlights include the comparative study of the vibrational properties of a glass and its crystalline counterpart, which marks the end point of a decade-long search for the nature of the so-called boson peak. Elemental solids ranging from free-electron-like alkali metals to correlated solids such as cerium and uranium still provide fertile ground for investigations and remarkable new findings are unearthed when pressure is applied, and temperature is exploited as additional variable. Examples demonstrating the importance of an advanced and versatile sample environment are the characterisation of novel compounds synthesised under extreme conditions and an innovative sample design to study the chemical state and function of Pt-dopants in gas sensors. The development of new techniques and advances in theory are key to the creation of new opportunities and for a deeper understanding. This is illustrated by a new tomographic technique, sapphire crystals for monochromatising high-energy X-rays to sub-meV energy resolution, and the development of a simplified formalism for resonant inelastic X-ray scattering.

As in previous years, besides supporting a cutting edge scientific programme, substantial efforts went into new developments. Funds by the German ministry (BMBF, Verbundforschung) allowed a group from the Universität Bayreuth to develop a new double-sided laser heating system for nuclear resonance experiments. The first high-pressure high-temperature nuclear inelastic and nuclear forward scattering data were recorded at ID18 and, with the same system, the first laser-heated single crystal studies were performed at ID09A. A new two-dimensional fast detector (timepix) was commissioned on ID16. The first ultra-fast XAS-XES pump and probe experiments using a MHz laser were conducted on ID26, in collaboration with scientists from the European XFEL. ID27 successfully developed an *in situ* X-ray micro-fluorescence setup interfaced to the double-sided laser heating system, and commissioned a rotating large volume press

system (ROTOPEC project) for *in situ* X-ray diffraction tomography at high pressure and high temperature in collaboration with a team from the University of Paris. ID28 upgraded its focusing optics and achieved a spot size of  $14 \times 7 \mu\text{m}^2$  (horizontal x vertical, FWHM).

Following the arrival and installation of the new tooling for the large volume press in February 2011, commissioning of the press was started. Several key features and techniques have been successfully tested, and it is hoped that the large volume press can be opened for user operation in the second half of 2012, provided that the required funds can be mobilised.

ID16 closed its doors after sixteen years of very successful operation. The programme on the high-frequency dynamics of liquids and glasses will continue on ID28, while the study of electronic and magnetic structure and dynamics will be at the focus of UPBL6 – Inelastic X-ray Scattering - located on ID20. Hutch construction has been completed, and following radiation tests and commissioning in 2012, UPBL6 will start user operation in March 2013.

ID22N, operational since 1998, and offering the user community - besides ID18 - a second station to conduct a wide range of nuclear resonance studies, was closed in March 2011. Efforts are currently focusing to investigate a possible exploitation of the 7/8 filling mode of the storage ring for nuclear resonance applications.

Finally, the high pressure beamlines ID09A and ID27 were reviewed in Spring 2011 and received very positive feedback. Both beamlines are considered world leading in their field. The panel further appreciated the increasing interest in the field of solid state chemistry and the synthesis of new materials.

M. Krisch



**Principal publication and authors**

A.I. Chumakov (a), G. Monaco (a), A. Monaco (a), W.A. Crichton (a), A. Bosak (a), R. Ruffer (a), A. Meyer (b), F. Kargl (b), L. Comez (c), D. Fioretto (c,d), H. Giefers (e), S. Roitsch (e), G. Wortmann (e), M.H. Manghnani (f), A. Hushur (f), Q. Williams (g), J. Balogh (e), K. Parliński (h), P. Jochym (h) and P. Piekarczyk (h), *Physical Review Letters* **106**, 225501 (2011).

- (a) ESRF
- (b) Technical University of Munich (Germany)
- (c) University of Perugia (Italy)
- (d) University of Rome (Italy)
- (e) University of Paderborn (Germany)
- (f) University of Hawaii (USA)
- (g) University of California at Santa Cruz (USA)
- (h) Institute of Nuclear Physics, Krakow (Poland)

**Glass physics**

**Equivalence of the boson peak in glasses to the transverse acoustic van Hove singularity in crystals**

Glasses are remarkably different from crystals at low temperature. They accumulate more heat and conduct less. This anomaly is related to a particular ensemble of atomic motions called the “boson peak”, whose nature has remained unknown for more than 50 years.

Before the 1960s, a glass was thought to be an ideal elastic medium, where atomic motions are determined by sound waves according to the Debye model. According to C. Kittel’s textbook, “the point was so obvious that it did not encourage experimental investigation”. Measurements of specific heat and thermal conductivity, however, revealed strong deviations from the Debye behaviour. A little later these deviations were attributed to the boson peak – a universal feature in the density of vibrational states (DOS) for all glasses. Since then, the vibrations of atoms in glasses have remained a point of controversy. Dozens of theoretical models

thermodynamically so different from ordered crystals. Driven by the distinction from crystalline properties, the majority of theoretical models explained the boson peak by embracing features beyond sound waves. However, recent studies conducted on beamlines **ID18**, **ID27**, and **ID28** shows that this is not the case.

In this work, the atomic motions in a glass and a crystal were compared using nuclear inelastic scattering, a technique that determines the exact number of vibrational states. The results show that around the boson peak, the number of states in a glass is exactly the same as the number of sound wave states in the crystal around the transverse acoustic (TA) van Hove singularity (**Figure 5**). Thus, the glass has no additional modes in excess of the sound waves in the crystal.

The equivalence of the boson peak and the TA singularity in the absolute number of states suggests that the vibrational states of the boson peak belong to acoustic branches. Indeed, an alternative attribution of the boson peak to additional modes would face a problem to explain the ~35% deficit of acoustic states in the glass.

Application of pressure causes the transformation of the reduced DOS of the glass towards the reduced DOS of the crystal: the boson peak decreases in height and shifts to higher energy, moving towards the TA singularity (**Figure 6a**). Measurements of density and sound velocity suggest that the transformation is caused by a gradual stiffening of the elastic medium. Once corrected for the difference

and hundreds of experimental results did not provide a unified picture of how disorder in atomic positions makes glasses

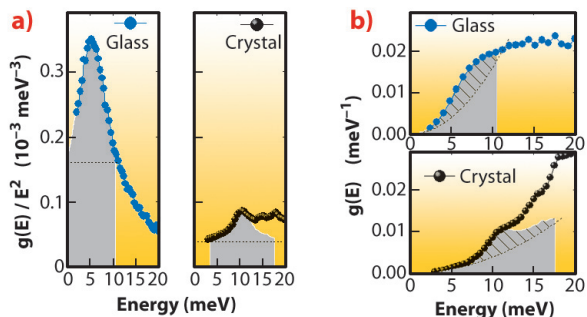
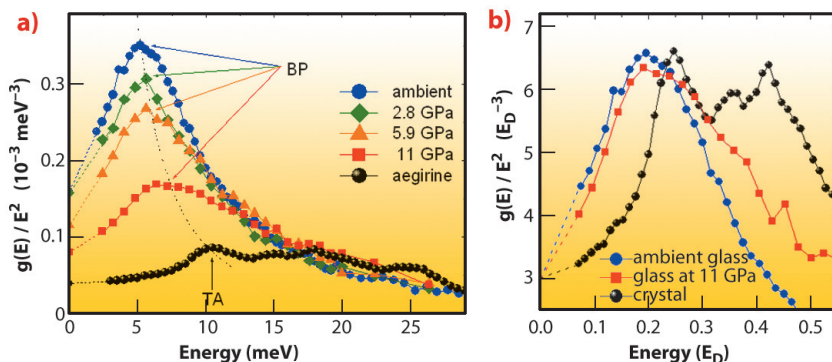


**Fig. 5:** Comparison of atomic vibrations in the sodium silicate glass and in the corresponding crystal. There is an apparent excess of states in the glass relative to the crystal in the reduced DOS  $g(E)/E^2$  (panel a), but the number of states is the same (panel b). The filled areas of the DOS in (b) correspond to the filled areas of the reduced DOS in (a) within the FWHM of the boson peak (in the glass) and of the TA singularity peak (in the crystal), respectively. The dashed lines show the Debye levels. The hatched parts of the filled areas mark the excess of states over the Debye level.

**Fig. 6:** a) With increasing pressure the boson peak (BP) moves towards the transverse acoustic (TA) singularity of the crystal. b) Once corrected for the difference in the elastic medium, the boson peak matches the TA singularity in height and energy.





in the elastic medium (re-plotted in the Debye energy ( $E_D$ ) units), the boson peak matches the transverse acoustic singularity in height and energy (Figure 6b).

These observations unambiguously identify the boson peak with sound waves. They lead to the conclusion that the anomaly in the heat capacity of glasses arises not from

additional modes, but from sound waves, which have, however, lower frequencies in glasses due to structural disorder. Unexpectedly, but in accordance with the general theory of knowledge, the sound-wave nature of glass anomalies revealed here is a return to the earliest ideas, but with a new level of understanding.

## ■ New light on elemental solids

### Cold melting and solid structures of dense lithium

The alkali metals, due to their simplicity, have attracted the attention of physicists and chemists alike for more than hundred years. They have been used by scientists to create the Bose-Einstein condensates and to develop the theory of the solid state. Undoubtedly, there are still more surprises to be discovered with the alkali metals.

Our investigation focuses on how light alkali (Na and Li) melt when their density is greatly increased. We have discovered an unprecedented pressure-induced drop in the sodium melting temperature from 1,000 K at 30 GPa (30,000 Atm) down to room temperature at 120 GPa (1.20 MAtm) [1] (see also Figure 7) – a highly unusual and contra-intuitive result. This study was inspired by the prediction that at very high pressures, currently un-attainable in laboratory, hydrogen will be metallic and liquid even at  $T=0$  K, a novel quantum state of matter never observed before.

Since the sodium atom is too heavy to be a quantum system, we have turned our attention to its lighter counterpart – lithium. At low pressure and very low temperatures, lithium forms rhombohedral crystals that, at higher pressures and temperatures, transform to face-centred cubic and then body-centred cubic crystals – all three among the simplest known crystal structures. However, what happens at very high pressures? In the past few years, intriguing deviations from simple metallic behaviour were observed, for example a metal to semiconductor-transition and even superconductivity at 17 K. In our study, we found even more surprises: above 60 GPa, lithium adopts three novel, complex crystal structures with 40, 88 and 24 atoms per unit cell

that were not previously observed in any element (see Figure 7). The most complex structures with 40 and 88 atoms had never even been predicted theoretically. Interestingly, the samples in these phases were becoming progressively darker with pressure, indicating profound changes in their electronic structure. This prompted us to conduct a joint theoretical and experimental study in which we have shown that lithium is a semiconductor with a band-gap of 1 eV [2].

The melting of lithium under pressure also revealed some unexpected results. While the melting point of a material usually rises with pressure (besides Na), and even the lightest gaseous elements, hydrogen and helium, melt at 1000 K and 50 GPa, lithium remains liquid at this pressure down to temperatures as low as

#### Principal publication and authors

C.L. Guillaume (a),  
E. Gregoryanz (a),  
O. Degtyareva (a),  
M.I. McMahon (a),  
M. Hanfland (b), S. Evans (b),  
M. Guthrie (c), S.V. Sinogeikin (d)  
and H-K. Mao (c,d), *Nature Physics*  
7, 211-214 (2011).

(a) SUPA, School of Physics  
and Astronomy, and Centre for  
Science at Extreme Conditions, The  
University of Edinburgh (UK)

(b) ESRF

(c) Geophysical Laboratory,  
Carnegie Institution of Washington,  
Washington D.C. (USA)

(d) HPCAT, Carnegie Institution of  
Washington, Argonne (USA)

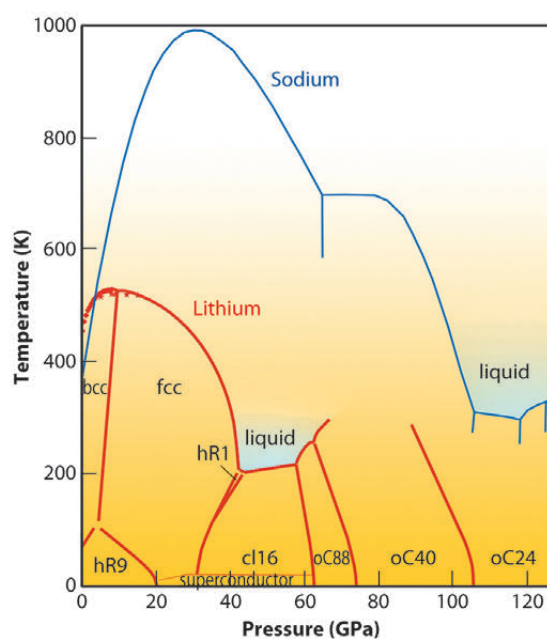


**Fig. 7:** Phase diagram of lithium (red) and sodium (blue). The lithium phase diagram indicates the various solid states and also the liquid state at 50 GPa (0.5 Mbar) and temperatures below 200 K.





### References

- [1] Gregoryanz *et al.*, *Phys. Rev. Lett.* **106**, 185502 (2005).  
 [2] Marques *et al.*, *Phys. Rev. Lett.* **106**, 095502 (2011).

190 K. This is by far the lowest melting temperature observed for any material at this pressure.

One of the possible explanations of the overall appearance of the lithium phase diagram, and particularly of the anomalously low melting temperatures, is that quantum effects are starting to play the dominant role at high compressions.

However, further investigations, particularly theoretical calculations, are needed to clarify this. We also speculate that a ground metallic liquid state, which has been predicted but never observed for hydrogen and which should exhibit highly unusual properties, might be constructed on the basis of the lithium-rich compounds e.g. the combination of lithium with light gases such as hydrogen or helium.

### Principal publication and authors

I. Loa (a,b), K. Syassen (a), G. Monaco (c), G. Vankó (c,d), M. Krisch (c) and M. Hanfland (c), *Phys. Rev. Lett.* **107**, 086402 (2011).  
 (a) Max-Planck-Institut für Festkörperforschung, Stuttgart (Germany)  
 (b) Present address: The University of Edinburgh (UK)  
 (c) ESRF  
 (d) Present address: KFKI Research Institute for Particle and Nuclear Physics, Budapest (Hungary)

## Plasmons in sodium under pressure

“Simple” or nearly free-electron (NFE) metals are characterised by a weak interaction between the conduction electrons and the atomic cores (the electron-ion interaction), and they crystallise in high-symmetry densely-packed crystal structures such as body-centred-cubic (bcc). At ambient conditions, sodium is one of nature’s best manifestations of a simple metal, but its properties change fundamentally at high compression. In the megabar pressure range, a series of phase transitions into lower-symmetry crystal structures has been observed, accompanied by marked changes in its optical properties and culminating in the formation of a nonmetallic, visually transparent phase at ~200 GPa.

A central question is how the transformation from a simple metal to a semiconductor progresses, *i.e.*, does the non-NFE behaviour of sodium start only with the transitions into the lower-symmetry phases above 105 GPa, or are there significant precursors in the bcc and face-centred cubic (fcc) phases at lower pressure? To provide an answer, we have used inelastic X-ray scattering

(IXS) on beamline **ID16** to measure plasmon energies and dispersion relations of sodium at high pressure, up to 43 GPa. Plasmons are collective electronic excitations – longitudinal charge density waves with finite wave vectors – and they determine the optical response of a metal. As the plasmon energies of an electron gas scale with its density, high-pressure experiments are an excellent tool to tune and study plasmon properties. Electron energy-loss spectroscopy (EELS) has long been used to measure plasmons, but this technique is not suitable for samples enclosed in high-pressure cells, and we have therefore used IXS.

**Figure 8a** shows typical IXS spectra of sodium that was compressed in diamond anvil high-pressure cells. For a given momentum transfer  $q$ , the single plasmon peak of sodium shifts towards higher energies as the pressure is increased.

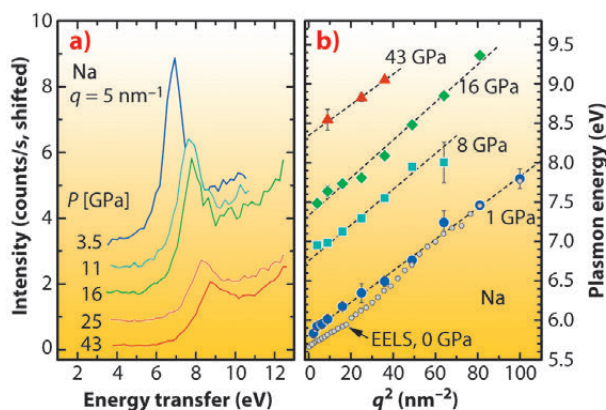
**Figure 8b** shows a summary of the experimental plasmon dispersion relations.

The theoretical description of plasmons in simple metals is well established. The most commonly used approach starts from the free-electron (FE) gas and uses the random phase approximation (RPA). It yields a simple quadratic relation for the plasmon energy dispersion,

$$E(q) = \hbar\omega_p + \frac{\hbar^2}{m} \alpha q^2,$$

where  $\omega_p$  is the plasma frequency,  $\alpha$  the dispersion coefficient and  $m$  the electron mass. Both the plasma frequency and the dispersion coefficient scale with the electron density  $n$  ( $\omega_p \propto n^{1/2}$ ,  $\alpha \propto n^{1/6}$ ), and in sodium we increased the electron density up to 2.6-fold relative to normal density. Refined versions of this simple FE/RPA model include the polarisability

**Fig. 8:** a) IXS spectra of polycrystalline sodium at pressures up to 43 GPa and a fixed momentum transfer of  $q = 5 \text{ nm}^{-1}$ . b) Plasmon energies of sodium as a function of momentum and pressure.





of the atomic cores (FE/RPA+core polarisation model) and use a better description of the electronic band structure ("PG model" after Paasch and Grigoryan).

The results shown in **Figure 8b** are in *qualitative* agreement with the predictions for a free-electron gas: the dispersions show the expected  $q^2$  dependence, and the plasmon energies increase with increasing density. Quantitatively, however, there are striking discrepancies as illustrated in **Figure 9** for the  $q = 5 \text{ nm}^{-1}$  plasmon. If the core polarisation is taken into account, the FE/RPA model yields a good description at low pressure, but at high pressure, both FE/RPA models significantly overestimate the plasma frequency as well as the plasmon dispersion coefficient, and consequently the plasmon energies. While the PG model is on equal footing with the FE/RPA+core polarisation model, it uses a more accurate description of the shape of the conduction band, which we determined in *ab initio* electronic structure calculations. The PG model, which does not have any adjustable parameters, yields plasmon energies in excellent agreement with the IXS results.

The observed deviation from NFE behaviour can in part be attributed to the polarisability of the ionic cores, but to a larger extent it is caused by pressure-induced changes in the electronic band structure. These, in turn, originate from the electron-ion interaction in sodium becoming stronger with increasing

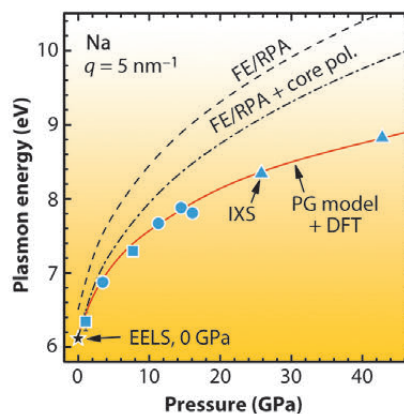


**Fig. 9:** Pressure dependence of the  $q = 5 \text{ nm}^{-1}$  plasmon of sodium as measured by IXS (symbols), and comparison with three different models (lines).

pressure. In other words, the behaviour of sodium departs increasingly from that of a NFE gas, and this can be seen as a precursor of the fundamental changes at megabar pressures.

Deviations from NFE behaviour have been observed before for other metals (at zero pressure), but, with few exceptions, they were attributed to electron exchange and correlations effects, and a number of extensions of the RPA were proposed in this spirit. As exchange and correlation effects decrease with increasing density, they can be excluded as the origin of the deviations we observed for sodium. In a constant-pressure experiment, this balance between band structure and exchange-correlation effects is more difficult to assess, and our present results indicate that band structure effects may be more important for the plasmon properties of metals than previously thought.

## Cerium's unusual behaviour

When a solid is subjected to high pressure, its atomic arrangement may simply contract continuously or it might change abruptly at some point. For most elements, the transition is accompanied by an abrupt decrease in volume, which usually would imply that a single crystal crushes into a poly-crystal or a powder. However, recent high-pressure and high-temperature X-ray diffraction experiments on pure cerium –the most abundant rare-earth element, with applications ranging from catalysts to fluorescent lamps– reveal that this element does not conform to this picture.

Diffraction data refinements do not provide any evidence in favour of a possible structure distortion of cerium along the  $\gamma \leftrightarrow \alpha$  transformation, irrespective of the poly- or single-crystalline nature of the samples. In a unique manner among all the elements of the periodic table, the phase transition in cerium can be described as an isomorphic first-order transition with a volume collapse of about 15% at 300 K. Moreover, the non-equilibrium phase diagram of cerium confirms the entropic term  $T\Delta S$  to be the predominant driving force of the transition, in agreement with the notion that the  $\gamma \leftrightarrow \alpha$  transition is controlled by the behaviour

### Principal publications and authors

F. Decremps (a), L. Belhadi (a), D. L. Farber (b), K. T. Moore (b), F. Occelli (c), M. Gauthier (a), A. Polian (a), D. Antonangeli (a), C. M. Aracne-Ruddle (b), and B. Amadon (c), *Phys. Rev. Lett.* **106**, 65701 (2011)

(a) IMPMC, Université Pierre et Marie Curie, Paris (France)

(b) LLNL, Livermore, California (USA)

(c) CEA, DAM, DIF, Arpajon (France)



**Fig. 10:** Clapeyron diagram of cerium along isotherms. The coexistence (dashed-dotted red) line delimits the region where the system is in a biphasic configuration, whereas the spinodal line (dashed-dotted black line) represents the boundary between metastable and unstable conditions.

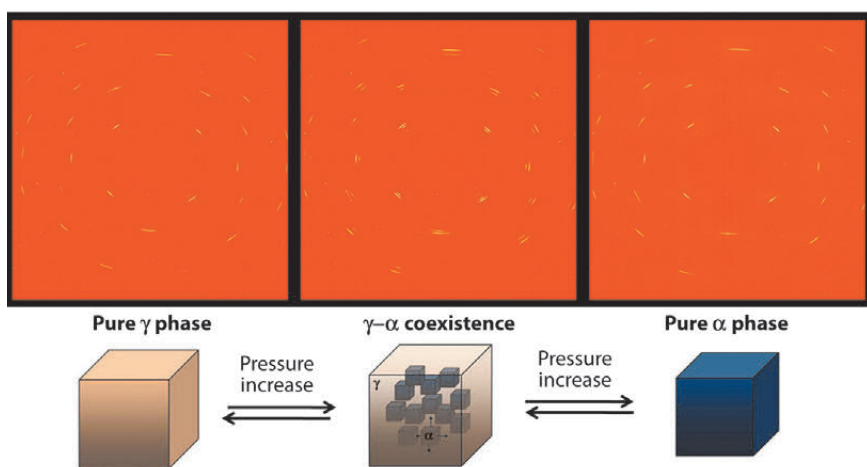
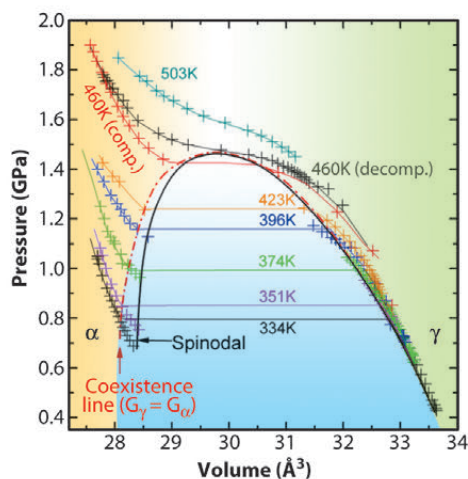


**Fig. 11:** X-ray diffraction patterns acquired along the [001] direction of single crystalline cerium metal at 318 K. Three different pressures are shown on the left: (a) 0.32 GPa ( $\gamma$ -Ce), 0.61 GPa ( $\alpha$ - and  $\gamma$ -Ce) and 1.19 GPa ( $\alpha$ -Ce). At 0.61 GPa,  $\gamma$  and  $\alpha$  phases coexist, with the same crystallographic structure and the same orientation, but a 14% difference in volume. Below : suggested transformation mechanism: as the  $\gamma$ -sample is compressed, numerous small blocks of  $\alpha$ -phase nucleate and grow uniformly across the sample. As the particles grow and impinge upon one another, their interfaces are in registry, allowing the  $\alpha$  crystallites to form one large crystal.

corresponding to a gas-like regime. Conversely, the  $\alpha$ -phase can be pictured as a “liquid” where the probability of double occupancy is calculated to be significant.

The angular dispersive X-ray diffraction patterns collected in runs using single-crystalline samples allowed us also to address the transformation mechanisms of the  $\gamma \rightarrow \alpha$  transition in detail. Here again, cerium behaves in very counter-intuitive ways when subjected to high pressures: at temperatures around ambient conditions, both the single crystalline nature and the orientation of the crystals are preserved in spite of the 15% volume collapse across the phase transition. Even more intriguing, the occurrence of two single-crystals in coexistence with the same structure and orientation (**Figure 11**) is recorded in the metastable region. All these features clearly call for a fascinating scenario of a diffusionless phase transformation induced by the strain energy. This picture is consistent with the very large softening of the longitudinal elastic modulus and the absence of effects on the shear modulus [1], but contrasts to what is usually observed in a purely martensitic transformation. Though such phenomenological description has never been previously proposed for any kind of element, we emphasise that a dislocation-based mechanism could sustain this conjecture. Since the  $\alpha$  and  $\gamma$  crystals remain in crystallographic registry, there must be a large number of edge dislocations, possibly forming the periodic array of misfit necessary to accommodate the large volume difference [2].

of the single 4f electron, archetypical paradigm of the localisation-delocalisation phenomenon encountered in f-electron systems.

Surprisingly, this X-ray diffraction study has confirmed that the  $\gamma \rightarrow \alpha$  transition line ends at a solid-solid critical point (460 K and 1.44 GPa) where the pressure dependence of the lattice parameter shows a vertical tangent. The analogy between the experimental  $p(V)$  curves given in **Figure 10** and the liquid-gas transition is obviously tempting. The  $\gamma \rightarrow \alpha$  transformation in cerium can indeed be pictured in the framework of a generic description where the most probable atomic configuration of the f electron in  $\gamma$ -cerium is a single occupied state,

In conclusion, these sets of experiments, carried out at beamline **ID09**, clearly show that the surprising phase transition and transformation mechanism in cerium can be understood on the basis of crystallographic and thermodynamic arguments. These observations represent an important step forward in achieving a reliable and unambiguous picture of the mechanism of phase transformation in cerium, an element archetypical of the localisation-delocalisation phenomenon encountered in f-electron systems, including plutonium and other actinides.

#### References

- [1] F. Decremps, D. Antonangeli, B. Amadon and G. Schmerber, *Phys. Rev. B* **80**, 132103- (2009).
- [2] K.T. Moore, L. Belhadi, F. Decremps, D.L. Farber, J.A. Bradley, F. Occelli, M. Gauthier, A. Polian and C.M. Aracne-Ruddle, *Acta Materialia* **59**, 6007-6016 (2011).





## Lattice dynamics of cerium metal across the $\gamma \rightarrow \alpha$ transition

Many physical and chemical properties of the light rare-earths and actinide elements are governed by an active role of f electrons, at the border between localisation and itinerancy. This is reflected in very rich phase diagrams and anomalous pressure and temperature dependence of many physical quantities. However, despite intensive efforts, the detailed mechanisms of phase stability and phase transitions remain poorly understood.

Undoubtedly the most famous example is the isostructural  $\gamma - \alpha$  transition in cerium which was discovered more than seven decades ago and remains the only known solid-solid transition in an element that has a phase boundary ending at a critical point. At ambient temperature, the first order transition occurs at 7.5 kbar, and leads to a volume decrease of the fcc lattice by ~15% [1].

New insights into this intriguing phase transition were recently gained through an inelastic X-ray scattering experiment conducted at beamline ID28 on a single crystal of cerium metal compressed up to  $P = 25$  kbar at  $T = 297$  K, in conjunction with *ab initio* lattice dynamics calculations.

The experimental phonon dispersions just below ( $P = 6$  kbar) and above ( $P=8$  kbar) the transition are reported in **Figure 12**, together with a Born-von Kàrmàn force constant model fit and the results of the *ab initio* calculations. We note that several of the phonon branches show significant changes; the most striking one occurs for the longitudinal acoustic (LA) branch along the [110] direction. A quantitative representation of the phonon energy changes,  $E$ , across the transition is provided by the mode Grüneisen parameters,

$$\gamma_q = -\frac{\partial(\ln E(q))}{\partial(\ln V)},$$

displayed in **Figure 13**. While positive values of  $\gamma_q$  (increase of phonon energy with increasing pressure/decreasing volume,  $V$ ) are common behaviour, negative values can occur as precursor of phase transitions or as a signature of electron-phonon interactions. Besides the low- $q$  portion of the L[001] branch and a small portion of the T[111] branch around  $q = 0.3$ , the most pronounced regions of negative  $\gamma_q$ 's occur around the X point. It is interesting to note that the suggested ordering of electrical quadrupoles

### Principal publication and authors

M. Krisch (a), D.L. Farber (b), R. Xu (c), D. Antonangeli (b,d), C.M. Aracne (b), A. Beraud (a), T.-C. Chiang (c), J. Zarestky (e), D. Y. Kim (f), E. Isaev (f), R. Ahuja (f) and B. Johansson (f,g), *PNAS* **108**, 9342-9345 (2011).

(a) ESRF

(b) Lawrence Livermore National Laboratory, Livermore, California (USA)

(c) Department of Physics, University of Illinois at Urbana-Champaign (USA) and Frederick Seitz Materials Research Laboratory, Urbana, Illinois (USA)

(d) Institut de Minéralogie et Physique des Milieux Condensés, UMR CNRS 7590, Institut de Physique du Globe de Paris, Université Pierre et Marie Curie, Université Paris Diderot (France)

(e) Ames Laboratory and Department of Physics and Astronomy, Iowa State University, Ames, Iowa (USA)

(f) Condensed Matter Theory Group, Physics Department, Uppsala University (Sweden)

(g) Department of Materials and Engineering, Applied Materials Physics, Royal Institute of Technology, Stockholm (Sweden)

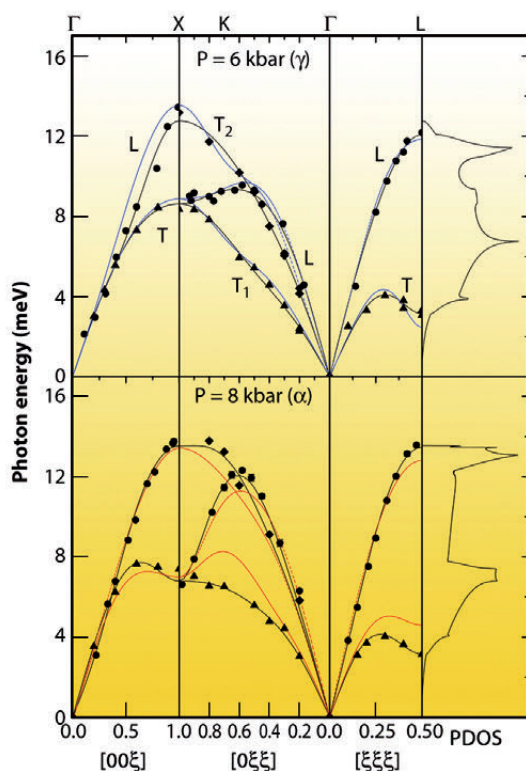


**Fig. 12:** Phonon dispersion of cerium metal at 6 kbar ( $\gamma$ -phase) and 8 kbar ( $\alpha$ -phase). L branches (circles),  $T_{1<110>}$  branch (diamonds), and  $T_{2<001>}$  branches (triangles). The black solid lines are the results of a Born-von-Kàrmàn fit. The corresponding phonon density of states (PDOS) is reported in the right panels. The blue and red lines represent *ab initio* calculations (within GGA, and using the PBE parameterisation) with the trivalent potential and tetravalent potential, respectively, both scaled by 0.9.

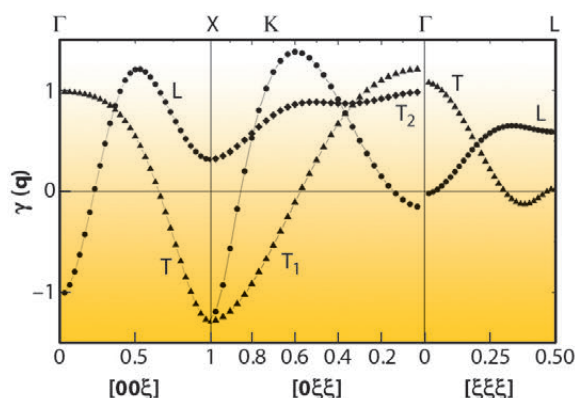


**Fig. 13:** Evolution of the mode Grüneisen parameters across the  $\gamma \rightarrow \alpha$  transition in cerium as derived from the Born-von-Kàrmàn fit to the experimental dispersion.





### References

- [1] P.W. Bridgman, *Proc. Am. Acad. Arts Sci.* **62**, 207 (1927).  
 [2] A.V. Nikolaev and K.H. Michel, *Eur. Phys. J.* **B 9**, 619 (1999); **17**, 363 (2000).  
 [3] F.F. Voronov, L.F. Vereshchagin and V.A. Goncharova, *Soviet Physics-Doklady* **135**, 1280 (1960).

in the  $\alpha$ -phase, though never directly observed, leads to strong coupling to the phonons at the X point [2].

The vibrational entropy change per atom across the transition can be derived directly from the corresponding phonon density-of-states (PDOS) using well established integral equations, and we obtain  $\Delta S_{vib}^{\gamma-\alpha}$  of  $0.33 \pm 0.03 k_B$ , in remarkable agreement with ultrasound measurements performed 50 years ago [3], thus underlining that the lattice contribution to the phase transition cannot be neglected.

*Ab initio* calculations of the  $\gamma$ -phase, treating the 4f electron as localised (trivalent potential), yield the best agreement with experiment, while in the  $\alpha$ -phase best agreement is achieved when the 4f electron is treated as part of the valence band (tetravalent potential). Our experimental results provide a unique benchmark to test theoretical models and will stimulate further experimental efforts to improve our understanding of this unique isostructural phase transformation.

### Principal publication and authors

S. Raymond (a), J. Bouchet (b), G.H. Lander (c), M. Le Tacon (d,e), G. Garbarino (d), M. Hoesch (d), J.-P. Rueff (f,g), M. Krisch (d), J.C. Lashley (h), R.K. Schulze (h) and R.C. Albers (h), *Physical Review Letters* **107**, 136401 (2011).  
 (a) CEA, DSM, INAC, Grenoble (France)  
 (b) CEA, DAM, DIF, Arpajon, (France)  
 (c) Institute for Transuranium Elements, Karlsruhe (Germany)  
 (d) ESRF  
 (e) Max-Planck-Institut für Festkörperforschung, Stuttgart (Germany)  
 (f) Synchrotron SOLEIL, Gif-sur-Yvette (France)  
 (g) Laboratoire de Chimie Physique, Paris (France)  
 (h) Los Alamos National Laboratory, New Mexico (USA)

## The role of electron-phonon coupling in understanding the phase diagram of uranium

Competition between different ground states is a central issue in condensed-matter physics. Much discussed examples are those between superconductivity and magnetism in cuprates, iron pnictides, and heavy fermions. Equally important is that between a charge density wave (CDW) and superconductivity. We have employed inelastic X-ray scattering (IXS) and *ab initio* calculations to investigate the mechanisms that govern such an interplay in uranium.

Uranium crystallises at room temperature in an unusual orthorhombic structure ( $\alpha$ -U phase) unique for an element at ambient pressure. A phase transition to a CDW state occurs below 43 K [1] and this behaviour has been ascribed to nesting of certain features of the Fermi surface [2]. The CDW state (called  $\alpha_1$ -U), to a first approximation, may be considered as a doubling of the a-axis of the unit cell. Under pressure the CDW disappears at

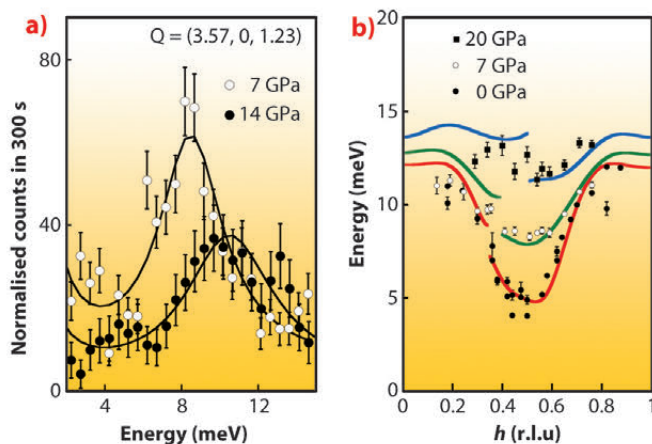
around 1.5 GPa while superconductivity exhibits a maximum transition temperature ( $T_c$ ) of about 2 K.

The key aspect, which stabilises the low-symmetry  $\alpha$ -U structure is the narrow band containing about three 5f electrons at the Fermi level. Treating accordingly the 5f electrons, the unusual phonon spectrum of  $\alpha$ -U was reproduced only in 2008 by *ab initio* calculations [3], almost 30 years after its experimental determination [4]. A prediction of this calculation is that, under pressure, the energy of the soft phonon mode  $\Sigma_4$  in the [100] direction increases, until the anomaly disappears near 20 GPa.

To validate this theoretical prediction we performed an IXS experiment at beamline ID28 on a single-crystal sample placed in a diamond anvil cell. Figure 14a shows IXS spectra taken around the key position in reciprocal space for two pressures. This establishes the hardening of the  $\Sigma_4$  mode as pressure is increased. Figure 14b shows the experimental (points) and theoretical (lines) dispersion along the [100] direction for three pressures.

The excellent agreement between theory and experiment led us to further investigate the phase diagram. Our theoretical studies reveal that the Fermi surface, and consequently the nesting conditions,

**Fig. 14:** a) IXS phonon spectra of  $\alpha$ -U for  $Q = (3.57, 0, 1.23)$  at 7 and 14 GPa, and  $T = 297$  K  
 b) Measured (symbols) and calculated (lines) phonon dispersion of the  $\Sigma_4$  mode in  $\alpha$ -U at the three indicated pressures.





evolves only very little with pressure. In contrast, we found that the electron-phonon coupling is very sensitive to the wave-vector, reaching a maximum where the soft mode occurs. This maximum is, however, rapidly suppressed when pressure increases. Thus, electron-phonon coupling is the crucial ingredient for the formation and the disappearance of the  $\alpha_1$ -U state. Fermi-surface nesting is indeed present, but although necessary, it is not the unique ingredient.

For phonon-mediated superconductivity, the knowledge of the electron-phonon coupling allows, furthermore, the determination of  $T_c$ . Our calculation shows that electron-phonon coupling increases in the CDW phase until the structure is unstable just above 1 GPa (see inset of **Figure 15**). In contrast, at higher pressures the electron-phonon coupling decreases in the  $\alpha$  phase, as discussed above. Thus the dome shape of the superconducting region is explained by the pressure dependence of electron-phonon coupling in concomitance with the respective stability of the  $\alpha_1$ -U and  $\alpha$ -U phases. **Figure 15** shows the good agreement between the measured and calculated superconducting

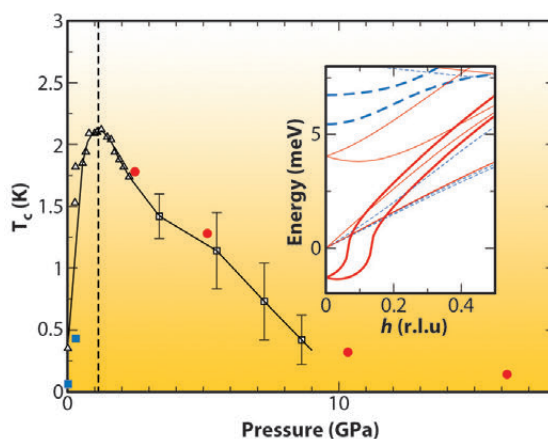


**Fig. 15:** T-P phase diagram of uranium in the superconducting region. The vertical line indicates the calculated transition between  $\alpha_1$ -U and  $\alpha$ -U phases. The experimental data (open triangles and squares) for  $T_c$  are taken from Ref. [1]. The blue squares and red circles correspond to the calculated  $T_c$  in the  $\alpha_1$ -U and  $\alpha$ -U phases, respectively. The inset shows the phonon dispersion in the  $\alpha_1$ -U phase at 0 (blue) and 5 (red) GPa.

transition temperatures as a function of pressure.

Our phonon measurement in uranium confirms the theoretically predicted disappearance of the soft mode under pressure. Further investigation of the mechanism at play emphasises that the momentum and pressure dependence of the electron-phonon coupling plays the central role in determining the complex phase diagram of uranium including the CDW and the superconductivity, whereas the Fermi-surface nesting is independent of pressure.

#### References

- [1] G.H. Lander *et al.*, *Advances in Physics* **43**, 1 (1994) and references therein.
- [2] L. Fast *et al.*, *Phys. Rev. Lett.* **81**, 2978 (1998).
- [3] J. Bouchet, *Phys. Rev. B* **77**, 024113 (2008).
- [4] W.P. Crummett *et al.*, *Phys. Rev. B* **19**, 6028 (1979).

## Chemistry and Earth sciences

### Role of platinum in tin oxide based gas sensors: a study under working conditions

Chemical gas sensors based on semiconducting metal-oxides are currently one of the most abundant and best studied types of sensor device for the detection of toxic gases and pollutants. The state of the art design of these sensors comprises the deposition of the polycrystalline porous metal-oxide film onto a ceramic substrate (see **Figure 16**). To monitor the electrical changes as a function of the surrounding atmosphere, these substrates are equipped with electrical contacts and a heater. In most cases, minute quantities of noble metals (Pt, Pd and Au) are added in the first synthesis steps to the metal-oxide in order to tune their selectivity, lower the operation temperature and improve the response time.

Although this “doping” technique has been known since the early days of

metal-oxide based gas sensors, there is still a strong discussion about how these additives contribute to the improved performance. The chemical state of the additives, their distribution in the material and whether they change structurally during the sensing procedure is still a matter of debate [1]. This had not been studied under real sensing conditions because experimental requirements are very challenging: the platinum from the electrodes and the heater of the device would dominate the information from the platinum additive in the sensing layer. In the present study, carried out at beamline **ID26**, this obstacle has been overcome by a new design of the substrate. Gold was employed instead of platinum to produce the ohmic contacts, and an alloy of Pd and Ag was used instead of Pt for the heater. To eliminate the disturbing fluorescence lines

#### Principal publication and authors

M. Hübner (a), D. Koziej (b), M. Bauer (c), N. Barsan (a), K. Kvashnina (d), M.D. Russell (b), U. Weimar (a) and J.-D. Grunwaldt (c), *Angew. Chem. Int. Ed.* **50**, 2841–2844 (2011).  
(a) Faculty of Science, Institute of Physical Chemistry, Tuebingen University (Germany)  
(b) Department of Materials, ETH Zürich (Switzerland)  
(c) Institute for Chemical Technology and Polymer Chemistry, Karlsruhe Institute of Technology (Germany)  
(d) ESRF

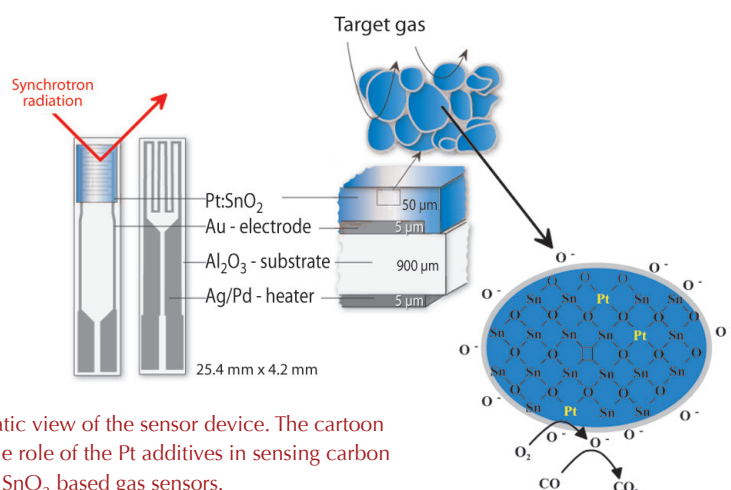
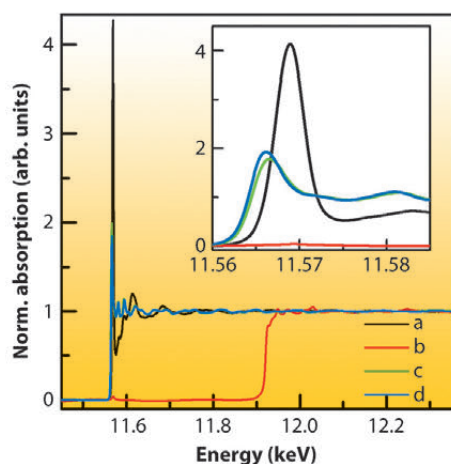


**Fig. 16:** Schematic view of the sensor device. The cartoon demonstrates the role of the Pt additives in sensing carbon monoxide with SnO<sub>2</sub> based gas sensors.

**Fig. 17:** Pt L<sub>3</sub> edge EXAFS spectra of a 0.2 wt % Pt:SnO<sub>2</sub> sensor with Au electrodes measured in (a) high energy resolved fluorescence detection (HERFD) and (b) traditional detection mode where the spectrum is dominated by the Au edge at 11.9 keV; as reference HERFD-XANES spectra of a sensor with Pt electrodes (c) and Pt foil (d) are shown.



of gold and to detect the small amount of 0.2 wt.% Pt in the 50 μm thick SnO<sub>2</sub> sensing layer, the generally-used solid-state detector was replaced by an X-ray emission spectrometer [2]. This allowed the effect of the lifetime broadening at the Pt L<sub>3</sub>-edge to be minimised and thus high energy-resolution fluorescence-detected X-ray absorption spectra on the modified sensor devices were successfully recorded. The state of Pt and its role in sensing could consequently be investigated under real sensor operation conditions (exposure to reducing gases at a temperature of 300°C).

**Figure 17** presents the Pt L<sub>3</sub>-XAS spectra. Comparing the spectra of the Pt doped SnO<sub>2</sub> with those of the metallic Pt and PtO<sub>2</sub> references, one can clearly conclude, that Pt in the sensing layer is in an oxidised state (almost identical to the spectra of the PtO<sub>2</sub>). The stronger white line intensity when compared to the spectra of PtO<sub>2</sub> illustrates that Pt is even in a more ionic state than in the reference. Furthermore, the evaluation of the range-extended (beyond the Au edge) EXAFS data indicates that Pt is at an atomic level incorporated in the matrix of the metal-oxide. It seems that some of the Sn sites are substituted by Pt during the synthesis.

The role and state of the Pt additives was further investigated by recording XAS spectra simultaneously with resistance changes during target gas exposure (H<sub>2</sub> and CO) at different operation temperatures (200-400°C). Only minor changes in the electronic structure could be observed, while large resistance changes were detected upon CO and H<sub>2</sub> exposure in air.

The improved sensing properties of Pt doped SnO<sub>2</sub> sensors were previously attributed to either metallic Pt particles or clusters on the surface of the metal-oxide. This assumption can now be excluded because we were able to demonstrate that Pt is in its oxidised state even under harsh reducing conditions. The studies further indicate that Pt substitutes some of the Sn sites in the SnO<sub>2</sub> matrix. The overall improved selectivity and sensitivity of the Pt doped SnO<sub>2</sub> can therefore be explained by a combination of a surface effect, namely the creation of new adsorption sites for oxygen (see **Figure 16**), and by an additional bulk effect. The role of Pt in metal oxide base gas sensors is therefore more complex than initially anticipated.

#### References

- [1] D. Koziej, M. Hübner, N. Barsan, U. Weimar, M. Sikora and J.D. Grunwaldt, *Phys. Chem. Chem. Phys.* 11-38, 8620-8625 (2009).
- [2] P. Glatzel, F.M.F. de Groot and U. Bergmann, *SRN* 22, 12-14 (2009).

## Silicon carbonate formed from carbon dioxide and silicon dioxide

CO<sub>2</sub> and SiO<sub>2</sub> are two archetypal group IV oxides of paramount importance for chemistry and planetary sciences. The chemical relationship between these substances, in particular their reactivity, is of great interest. Although both systems are group IV oxides, they are remarkably different under ambient conditions: CO<sub>2</sub>

is molecular and is held together by C=O double bonds, while SiO<sub>2</sub> forms network structures involving Si-O single bonds. These bonding patterns radically change under pressure. CO<sub>2</sub> has been found to form non-molecular solid phases above 30 GPa similar to SiO<sub>2</sub> [1]. A possible approach to favour the chemical reaction





between  $\text{CO}_2$  and  $\text{SiO}_2$  is to select a micro-porous silica polymorph, such as silicalite. At ambient conditions, silicalite is characterised by a framework of four-, five-, six- and ten-membered rings of  $\text{SiO}_4$  tetrahedra with 5.5 Å pores that can be completely filled by  $\text{CO}_2$  under pressure [2] (Figure 18, inset). The choice of silicalite was motivated by the large effective surface exposed to the  $\text{CO}_2$  in the pores, which is a crucial factor for enhancing the chemical reaction.

We examined chemical reactions between silicalite  $\text{SiO}_2$  and  $\text{CO}_2$ , by compressing mixed samples at 18-26 GPa and subsequent heating at 600-740 K. In the infra-red (IR) spectrum of the temperature-quenched material (Figure 18a) the peaks of silicalite are remarkably reduced and the peaks of micro-confined  $\text{CO}_2$  almost completely vanished. At the same time, two new peaks appeared, labelled A and B, that belong neither to molecular  $\text{CO}_2$  nor to silicalite. Therefore, the most fundamental aspect of a binary chemical reaction is demonstrated: two substances, silicalite and  $\text{CO}_2$ , react with each other, and a product is formed, identified by peaks A and B. Upon lowering pressure the new peaks gradually disappear below 15 GPa, and a new, non-molecular peak, C, emerges. In parallel, we observe the formation of micro-confined  $\text{CO}_2$  and the intensification of the silicalite peaks again (Figure 18b). Finally, at room pressure, peak C disappears after a few days along with the peak of residual confined  $\text{CO}_2$ , thereby showing the overall reversibility of the transformation. The new IR peaks were assigned to C-O stretching modes of unidentate, bidentate and bridged silicon carbonate species.

As an additional proof of the chemical reaction and of the nature of the compound, we measured the X-ray diffraction patterns (Figure 19) on a sample compressed to 21.4 GPa and then heated to 723 K at beamline ID27. The Bragg peaks of orthorhombic silicalite progressively broaden upon increasing temperature. This is a clear indication

of the chemical reaction, as diffraction peaks should instead sharpen because of the usual temperature enhancement of the crystal quality and relaxation of any deviatoric stress. This also shows that the chemical reaction takes place progressively, ending up in a product that is a highly-strained crystal still exhibiting the structure of the original silicalite. This is not unexpected, since the carbonates form at the micro-pore surface, which in turn does not alter the pore arrangement within the unit cell, but affects the long range periodicity of the structure. The carbonate groups form in a random manner without any long-range order. They can also be expected to induce local geometrical distortions to the framework.

The data presented here consistently shows that  $\text{SiO}_2$  and  $\text{CO}_2$  undergo high P-T chemical reactions of the type:  $x\text{SiO}_2 + y\text{CO}_2 \leftrightarrow \text{Si}_x\text{C}_y\text{O}_{(2x+2y)}$ , that result

#### Principal publication and authors

M. Santoro (a,b), F.A. Gorelli (a,b), J. Haines (c), O. Cambon (c), C. Levelut (d) and G. Garbarino (e), *Proc. Natl. Acad. Sci. U.S.A.* **108**, 7689-7692 (2011).

(a) European Laboratory For Non Linear Spectroscopy (LENS), Firenze (Italy)

(b) IPCF-CNR, Roma (Italy)

(c) Institut Charles Gerhardt Montpellier, Equipe Chimie et Cristalochimie des Matériaux, UMR 5253, CNRS, UM2, Montpellier (France)

(d) Laboratoire Charles Coulomb, UMR 5221, CNRS, UM2, Montpellier (France)

(e) ESRF

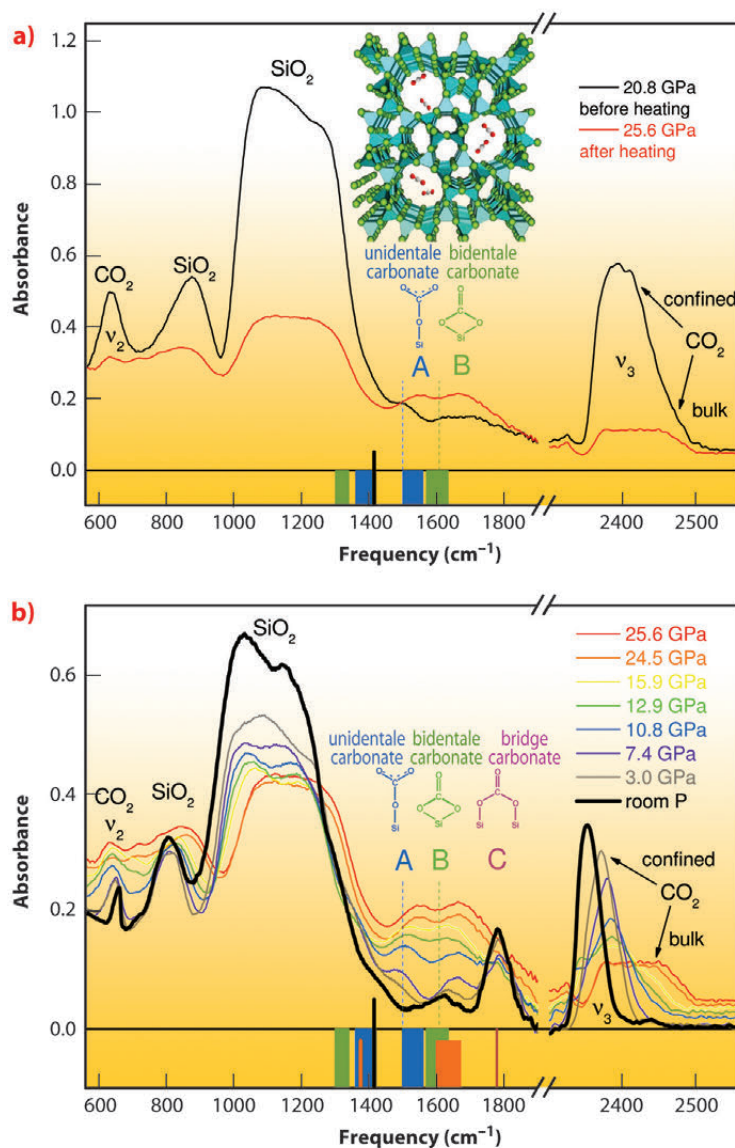
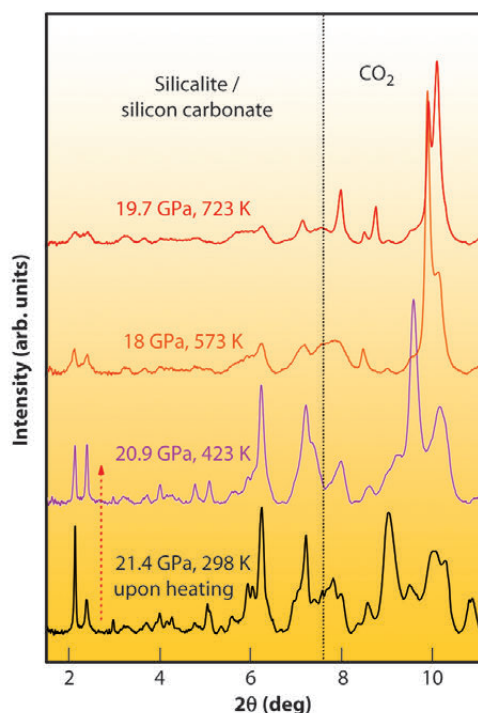


**Fig. 18:** IR spectra of mixed silicalite and  $\text{CO}_2$  showing the formation of silicon carbonate. The new compound is identified by the peaks A, B and C, assigned to unidentate, bidentate and bridged silicon carbonate species. Inset: silicalite structure.  $\text{CO}_2$  fills the micro-pores of the zeolite under pressure, and reacts with the silica framework upon heating.





**Fig. 19:** High pressure X-ray diffraction patterns of the silicalite- $\text{CO}_2$  mixture, showing the formation of a highly-strained, disordered crystal upon heating. At angles higher than the dashed vertical line the pattern is dominated by peaks of different molecular phases of bulk  $\text{CO}_2$ .



in the formation of one or more silicon carbonate compounds. Although the reaction occurs at the surface of the silicalite micropores, the final product has the nature of a real bulk compound due to the particular structure of zeolitic silicalite. In fact, all of the tetrahedra in silicalite are on the surface of the micro-pores, thus a surface reaction can involve, in principle, all the  $\text{SiO}_2$  as would be the case in a bulk reaction. However, the silicalite framework is retained, although highly strained, and the product is thus a non-stoichiometric silicon carbonate.

#### References

- [1] M. Santoro and F.A. Gorelli, *Chem. Soc. Rev.* **35**, 918-931 (2006).  
 [2] J. Haines et al., *J. Am. Chem. Soc.* **132**, 8860-8861 (2010).

#### Principal publication and authors

E. Boulard (a,b), A. Gloter (c), A. Corgne (a,d), D. Antonangeli (a), AL. Auzende (a), J.P. Perrillat (e,f), F. Guyot (a) and G. Fiquet (a), *Proceed. Nat. Acad. Sciences*, **108**, 5184-5187 (2011).

(a) IMPMC, IPGP, Université Pierre et Marie Curie, CNRS, Université Paris Diderot (France)

(b) Extreme Environments Laboratory, Stanford University (USA)

(c) Laboratoire de Physique des Solides, Université Paris Sud 11, CNRS (France)

(d) Institut de Recherche en Astrophysique et Planétologie, Université de Toulouse, CNRS (France)

(e) ESRF

(f) Géologie de Lyon, Université Claude Bernard, ENS Lyon, CNRS (France)

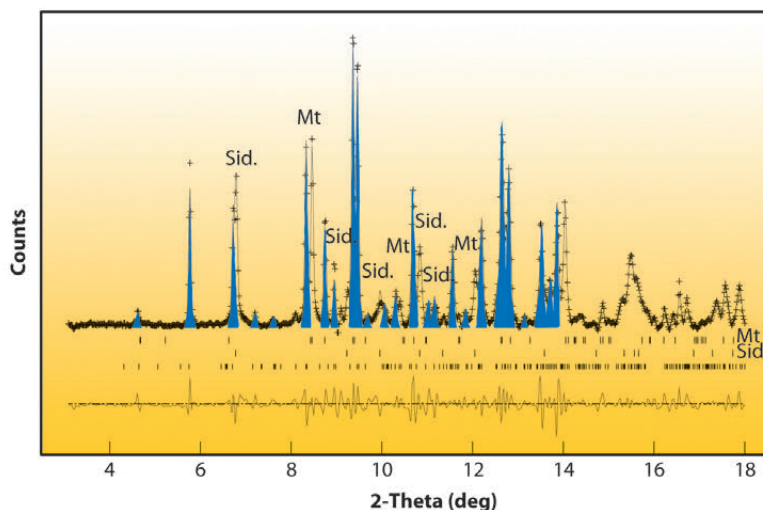
## New host for carbon in the deep Earth

Carbon exchange occurs between the Earth's interior and the surface. This deep carbon cycle, taking place over geological timescales of millions of years, has controlled climates of the planet since its formation. However, the extent of recycling and the nature of carbon reservoirs at depths are still poorly known. Carbon is recycled in subduction zones as solid carbonate minerals, their major constituents being magnesite  $\text{MgCO}_3$  and siderite  $\text{FeCO}_3$ , whereas surficial carbonates are dominated by calcite  $\text{CaCO}_3$ . The pressure-temperature stability of these phases thus plays a key role in the global carbon cycle. Previous studies,

focusing on the stability of calcium and magnesium rich carbonates, demonstrated the possibility of carbon recycling into the mantle, e.g. [1]. Thanks to synchrotron radiation studies we have been able to follow the fate of  $\text{MgCO}_3$  and  $\text{FeCO}_3$  in the deep Earth.

We performed high pressure – high temperature experiments using a laser-heated diamond anvil cell. Two types of experiments were conducted, with starting materials being either natural carbonate samples ( $\text{MgCO}_3$  and  $(\text{Fe,Mg})\text{CO}_3$ ) or a mixture of oxides ( $\text{MgO} + \text{CO}_2$  and  $(\text{Fe,Mg})\text{O} + \text{CO}_2$ ). The reacted mixtures

**Fig. 20:** X-ray diffraction pattern of  $(\text{Fe,Mg})\text{CO}_3$  collected at 80 GPa and  $\sim 2050$  K. Blue peaks highlight diffraction peaks of the new high-pressure phase. Sid. refers to the siderite-rich starting material  $(\text{Fe,Mg})\text{CO}_3$ , Mt to magnetite ( $\text{Fe}_3\text{O}_4$ ).





and their phase contents were analysed *in situ* at high-pressure and high-temperature by X-ray diffraction at the high-pressure beamline ID27. *Ex situ* analyses by scanning transmission electron microscopy - electron energy loss spectroscopy (STEM-EELS) were performed on the samples recovered at ambient conditions.

New X-ray diffraction peaks (in blue in **Figure 20**) were observed for all compositions, indicating the existence of a new high-pressure phase of  $\text{MgCO}_3$  and  $(\text{Fe,Mg})\text{CO}_3$  at pressures exceeding 80 GPa and temperatures above 1850 K. These conditions correspond to depths larger than 1,800 km in the Earth's mantle. A new silicate-like crystal structure has been discovered (see **Figure 21**). It is based on  $(\text{CO}_4)^{4-}$  groups instead of  $(\text{CO}_3)^{2-}$  molecules characteristic of low pressure carbonates. This phase is close to that predicted by first principle calculations [2]. *Ex situ* STEM-EELS analyses coupled to Density Functional Theory (DFT) calculations confirmed that the peculiar spectroscopic signature at the carbon K-edge is explained by the presence of  $(\text{CO}_4)^{4-}$  groups. The implications of this new phase are far reaching because its solubility in silicates and its melting behaviour are likely to be different from those of low-pressure carbonates. These properties remain yet to be determined.

Furthermore, iron revealed an interesting behaviour in these experiments: the normal state of iron in carbonates, ferrous iron (labeled  $\text{Fe}^{2+}$  or  $\text{Fe}^{\text{II}}$ ), was found to be unstable in the presence of carbonate ions.  $\text{Fe}^{\text{II}}$  was oxidised into ferric iron ( $\text{Fe}^{3+}$  or  $\text{Fe}^{\text{III}}$ ), coupled to reduction of carbon from  $\text{CO}_2$  or carbonate ions into carbon monoxide (CO) and nano-diamonds, as shown by EELS performed

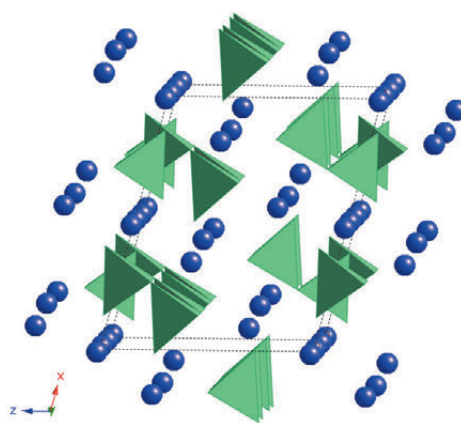


**Fig. 21:** Structure of the new high-pressure phase.  $(\text{CO}_4)^{4-}$  tetrahedra appear in green and magnesium or ferric iron atoms are shown as violet spheres.

at the C-K edge on samples recovered at ambient conditions. Those oxidation-reduction reactions explain the presence of magnetite  $\text{Fe}_3\text{O}_4$  (Mt in **Figure 20**) in the high-pressure X-ray diffraction patterns. Moreover, *ex situ* STEM-EELS analyses showed that iron in the new high-pressure phase (**Figure 21**) was indeed  $\text{Fe}^{\text{III}}$ . These reactions provide a possible new mechanism for driving carbon-bearing minerals down to the core-mantle boundary of the Earth and for generating ultra-deep diamonds within an oxidised subducted carbonate starting material.

A new picture of the evolution of carbon in the deep Earth is thus emerging. If subducted iron and magnesium carbonates are sufficiently isolated from the surrounding mantle, for instance, in a relatively cold subducted slab, they might be transported beyond 1,800-km depth. There, they will transform into the newly observed phase and diamonds will be produced as well. The validity of the proposed mechanism needs to be further studied in actual silicate-bearing mantle assemblages and within minute inclusions found in ultra-deep diamonds coming from the lower mantle.

#### References

- [1] S. Poli, E. Franzolin, P. Fumagalli and A. Crottini, *Earth Planet. Sci. Lett.*, **278**, 350-360 (2009).
- [2] A.R. Oganov, S. Ono, Y.M. Ma, C.W. Glass and A. Garcia, *Earth Planet. Sci. Lett.*, **273**, 38-47 (2008).

## Novel X-ray imaging technique with molecular-bond sensitivity

X-ray spectroscopic imaging techniques can study the distribution of elements and chemical compounds inside a material. For this purpose X-ray images can, for example, be taken by varying the energy of monochromatic X-rays in the vicinity of the elements' characteristic absorption edges. This is feasible for elements belonging to at least the third row of the periodic table since only then the required X-ray energy is high enough

to probe matter on macroscopic length scales. But what if one would like to study lighter elements, such as carbon and oxygen? The corresponding X-rays are rather soft and probe matter only at a depth of a few micrometres. Even though such chemical imaging can be done [1], there are severe constraints for samples to be studied in three dimensions. Hard X-rays (from 10 keV up) are capable of probing materials in three dimensions over

#### Principal publication and authors

S. Huotari (a,b), T. Pylkkänen (a,b), R. Verbeni (a), G. Monaco (a) and K. Hämäläinen (b), *Nature Mater.* **10**, 489-493 (2011).  
(a) ESRF  
(b) University of Helsinki (Finland)



**Fig. 22:** Schematics of the setup. A phantom sample is represented by an ensemble of a sphere and a cube. The analyser reflects scattered photons, producing a mirror image of a two-dimensional section of the sample on the pixel detector.

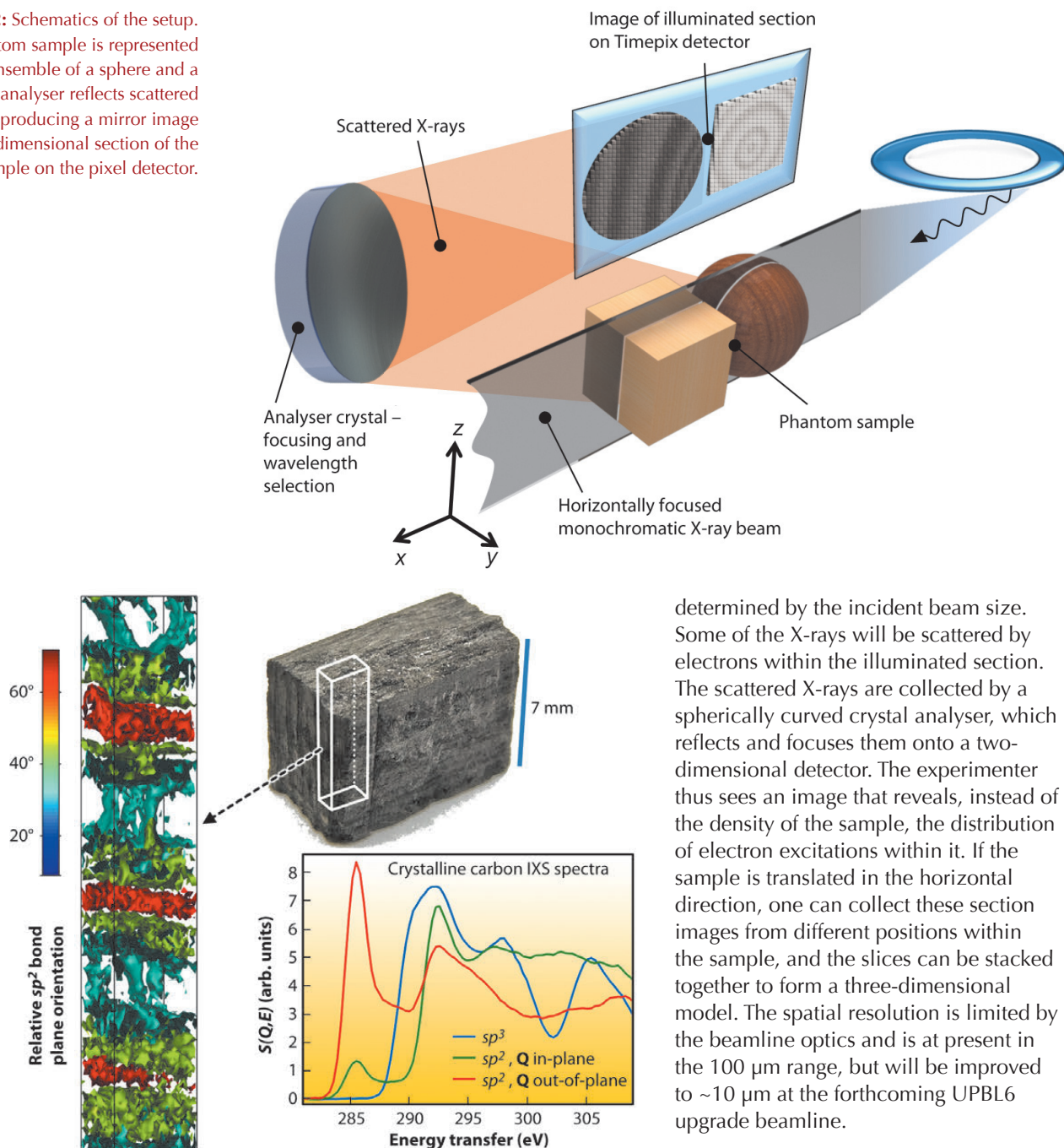


**Fig. 23:** Application of the technique to a carbon composite sample.

macroscopic length scales, so would it be possible to use them to study the chemistry of light elements? A new technique has now been developed at ID16 to do exactly that. The principle is based on inelastic X-ray scattering (IXS) [2].

IXS probes electron excitations by measuring the energy-loss spectra of hard X-rays scattered by electrons. In the experiment, the sample is placed in a monochromatic X-ray beam focused in one dimension (Figure 22). The X-rays pass through the sample illuminating a slice-shaped region, the thickness of which is

determined by the incident beam size. Some of the X-rays will be scattered by electrons within the illuminated section. The scattered X-rays are collected by a spherically curved crystal analyser, which reflects and focuses them onto a two-dimensional detector. The experimenter thus sees an image that reveals, instead of the density of the sample, the distribution of electron excitations within it. If the sample is translated in the horizontal direction, one can collect these section images from different positions within the sample, and the slices can be stacked together to form a three-dimensional model. The spatial resolution is limited by the beamline optics and is at present in the 100 μm range, but will be improved to ~10 μm at the forthcoming UPBL6 upgrade beamline.

The analyser is the heart of the experiment. It is actually a focusing monochromator, and reflects only those scattered photons that fall into a certain energy bandwidth (about 0.5 eV at 10 keV). While analyser crystals have been used in the IXS experiments for decades, their imaging capabilities have not been fully exploited before. To achieve this, the ID16 team has developed new technologies to optimise analysers for imaging. The IXS spectra are measured by changing the incident X-ray beam energy, and spectra are recorded for each pixel of the illuminated section.

One can use the technique to determine for instance local molecular bond variations in carbon composite materials.





**Figure 23** shows the application of the method to a carbon fibre reinforced silicon carbide sample as an example of a materials science characterisation. A typical example of an IXS excitation is that of a deeply-bound core electron, in which case IXS spectra are comparable to those of X-ray absorption spectroscopy. Therefore, from the IXS spectra of carbon 1s core electrons, different carbon bonds are easily discernible. Each measured voxel contains an IXS spectrum that reveals the average carbon bond type within it. From the sample shown in **Figure 23**, we determined the carbon bond distribution, and found crystalline  $sp^2$  dominating. Since the  $sp^2$  bond is

anisotropic, the spectra are also sensitive to its orientation, revealing a periodically alternating bond orientation.

In conclusion, it is now possible to study the three-dimensional distribution and chemistry of light elements in bulk samples and in confined environments. This is achieved by using novel contrast mechanisms for three-dimensional imaging such as IXS. Examples of potential research objectives are batteries, fuel cells, and rare geological samples. This should open up new perspectives in materials science, chemistry, physics and geology, once the IXS Upgrade beamline UPBL6 becomes operational.

#### References

- [1] G.A. Johansson, T. Tyliczszak, G.E. Mitchell, M.H. Keefe and A.P. Hitchcock, *J. Synchrotron Rad.* **14**, 395-402 (2007).
- [2] *Electron Dynamics by Inelastic X-Ray Scattering*, W. Schülke, Oxford University Press, Oxford (2007).

## Sapphire monochromator for hard X-rays (> 30 keV) with sub-meV bandwidth

High efficiency nuclear inelastic scattering measurements above 30 keV with sub-meV resolution are now possible through the use of a sapphire backscattering monochromator in combination with improved upstream X-ray optics at the nuclear resonance beamline **ID18**. This development permits detailed lattice dynamics characterisation of novel functional materials based on elements such as tellurium and antimony.

Sub-meV monochromatisation of X-rays with high efficiency is a keystone for inelastic scattering techniques such as inelastic X-ray scattering or nuclear inelastic scattering. Typically, meV monochromatisation is achieved by single crystal diffraction in backscattering geometry or by using a multiple crystal arrangement. Silicon is the material of choice, as large ingots of extremely good quality are available. However, both approaches encounter difficulties above 30 keV if monochromatisation at a specific energy is required. Backscattering from a crystal with lower symmetry than silicon, *i.e.* with a large spectral density of back reflections, may overcome these difficulties [1]. Sapphire is the best crystal material for achieving efficient monochromatisation for any X-ray photon energy above 20 keV by proper choice of Bragg reflection and temperature variation of the lattice spacing [1]. The only limiting factor is the availability of high quality defect free sapphire crystals.

Here, an approach is presented which demonstrates that an almost ideal performance can be achieved even with imperfect sapphire crystals. At beamline ID18, the synchrotron radiation beam was focused to  $0.2 \times 0.2 \text{ mm}^2$  at the crystal position and a sapphire with a thickness of 1-2 mm was utilised. The part of the crystal with the best quality was selected and used as a monochromator. A test of the monochromator was performed at 35.49 and 37.13 keV, the nuclear resonance energies of  $^{125}\text{Te}$  and  $^{121}\text{Sb}$ , respectively. The (9 1 10 68) and (8 16 24 40) reflections were chosen to match the resonance energies of  $^{125}\text{Te}$  and  $^{121}\text{Sb}$  at 220 and 237 K, respectively. The sapphire crystal was installed in a cryostat developed in-house [2]. The instrumental function was measured by recording the time integrated nuclear forward scattering, see **Figure 24**. An energy resolution of

#### Principal publication and authors

I. Sergueev (a), H.-C. Wille (b), R.P. Hermann (c,d), D. Bessas (c,d), Y.V. Shvyd'ko (e), M. Zając (a,f) and R. Ruffer (a), *J. Synchrotron Rad.* **18**, 802–810 (2011).

(a) ESRF

(b) DESY, Hamburg (Germany)

(c) Jülich Center for Neutron Science JCNS and Peter Grünberg Institut PGI, JARA-FIT, Forschungszentrum Jülich GmbH, Jülich (Germany)

(d) Faculté des Sciences, Université de Liège (Belgium)

(e) APS, Argonne (USA)

(a,f) Faculty of Physics and Applied Computer Science, AGH University of Science and Technology, Kraków (Poland)

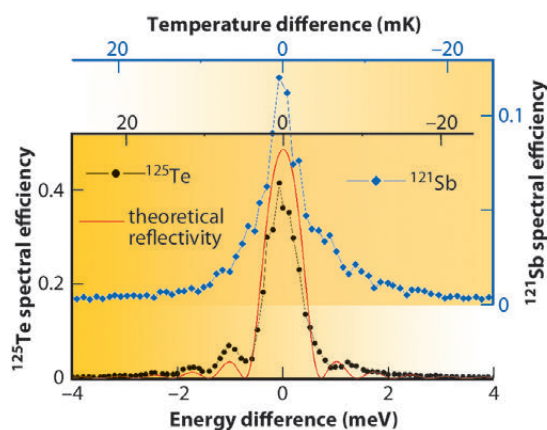
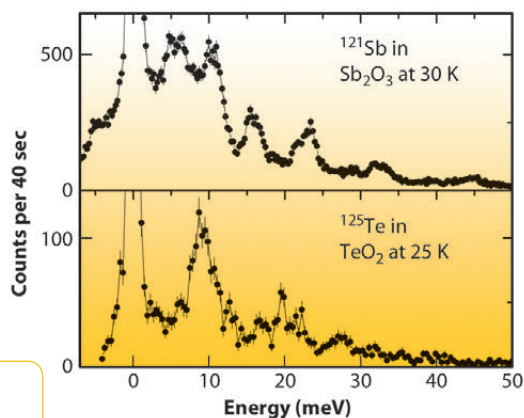


**Fig. 24:** The instrumental functions of the sapphire backscattering monochromator as measured by nuclear forward scattering from  $^{125}\text{Te}$  (black points) and  $^{121}\text{Sb}$  (blue squares) via variation of the sapphire temperature. The theoretical reflectivity for the (9 1 10 68) reflection and crystal of 1 mm thickness is shown as red line.





**Fig. 25:** Nuclear inelastic scattering spectra of  $\text{Sb}_2\text{O}_3$  and  $\text{TeO}_2$  with natural abundance of  $^{121}\text{Sb}$  and  $^{125}\text{Te}$ . The total measurement time was  $\sim 2$  hours for each spectrum.



With a 100 mA electron current a flux of  $10^8$  photons/sec was obtained with this monochromator. Thus, time efficient measurements of nuclear inelastic scattering can be carried out for compounds containing Te and Sb. This is demonstrated in **Figure 25**, where measured spectra of  $\text{TeO}_2$  and  $\text{Sb}_2\text{O}_3$  with natural abundance of  $^{125}\text{Te}$  and  $^{121}\text{Sb}$  are shown. The data give direct access to the Sb and Te partial density of phonon states as well as dynamical and thermodynamical properties, e.g. Lamb-Mössbauer factor, mean sound velocity, Debye temperature.

This new monochromator development has opened the field of nuclear inelastic scattering for many functional materials bearing Te and Sb, such as phase-change materials [3], thermoelectric materials [4], photovoltaic semiconductors, and iron-chalcogenide superconductors.

#### References

- [1] For a review see Y. Shvyd'ko, X-Ray Optics. High-Energy-Resolution Applications, Springer Berlin, 98 (2004).
- [2] P. van der Linden, H.-C. Wille and Y.V. Shvyd'ko, *AIP Conf. Proc.* **879**, 915 (2007).
- [3] T. Matsunaga *et al.*, *Adv. Funct. Mater.* **21**, 2232 (2011).
- [4] A. Möchel *et al.*, *Phys. Rev. B* **84**, 064302 (2011).

$\sim 0.7$  meV (FWHM) was obtained for both energies. This resolution is close to the theoretically expected one for the (9 1 10 68) reflection and 1 mm crystal thickness. The good quality is also confirmed by the visible Pendellösung fringes due to the interference between the radiation reflected from the front and the back crystal surface.

#### Principle publication and authors

J.J. Kas (a), J.J. Rehr (a), J.A. Soininen (b) and P. Glatzel (c), *Phys. Rev. B* **83**, 235114 (2011).  
 (a) Department of Physics, University of Washington, Seattle (USA)  
 (b) Department of Physics, University of Helsinki (Finland)  
 (c) ESRF

## Real-space multiple-scattering approach to resonant inelastic X-ray scattering

Resonant inelastic X-ray scattering (RIXS) is a powerful spectroscopic tool for examining both ground state and excited state electronic structure of complex materials. In the RIXS process a high-energy incoming photon excites a deep core electron, creating a photoelectron, and an outgoing photon is radiated when the empty core state is filled. We have recently developed a theoretical description of the direct RIXS process based on a real-space Green's function approach within a real-space multiple scattering (RSMS) framework. Due to the importance of many-body effects on RIXS spectra, *ab initio* calculations can be quite

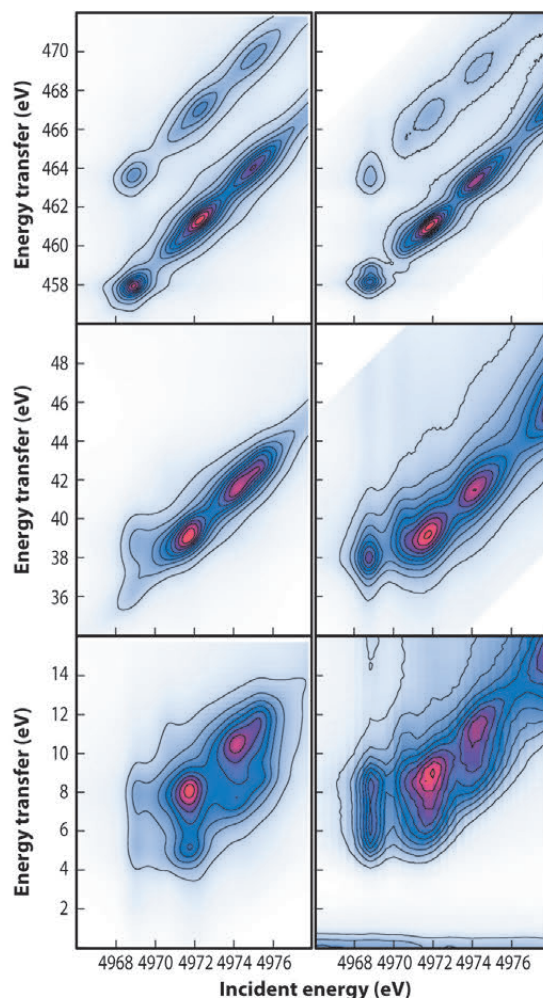


**Fig. 26:** Calculated (left) and experimental (right) RIXS spectra of  $\text{TiO}_2$  as a function of incident and transferred energies. The Ti K- $\alpha$ , - $\beta$ , and -valence spectra are shown from top to bottom.



demanding. With several simplifying assumptions, however, we find that RIXS can be approximated as a convolution of the X-ray absorption (XAS) and X-ray emission spectra (XES). Additional many-body effects can be taken into account via a convolution with a spectral function. In particular, we find that the Kramers-Heisenberg equation,

$$\frac{d^2\sigma}{d\Omega d\omega} = \frac{\omega}{\Omega} \sum_i \langle F | \Delta_2^* | M \chi M | \Delta_1 | I \rangle \delta(\Omega - \omega + E_i - E_f),$$

can be approximated by

$$\frac{d^2\sigma}{d\Omega d\omega} = \frac{\omega}{\Omega} \int d\omega_1 \frac{\mu_{\text{XES}}(\omega_1) \bar{\mu}_{\text{XAS}}(\Omega, \Omega - \omega - \omega_1 + E_b)}{|\omega - \omega_1 + i\Gamma_b|},$$

where  $\Omega$  is the frequency of the incoming photon,  $\omega$  is the frequency of the outgoing photon,  $E_b$  is the deep core-level energy, and  $\Gamma_b$  is the inverse core-hole lifetime, and unless otherwise noted, we have used atomic units,  $e = \hbar = m = 1$ . As in the RSMS treatment of XAS [2], the effective X-ray absorption signal  $\bar{\mu}_{\text{XAS}}$  can also be

$$\bar{\mu}_{\text{XAS}}(\omega_1, \omega_2) = \frac{1}{\pi} \text{Im}[\langle b | T^*(\omega_1) g^c(\omega_2 + E_c) T(\omega_1) | b \rangle],$$

expressed in terms of Green's functions, where  $T(\omega)$  is a non-local, energy dependent operator that replaces the usual dipole operator in XAS, and  $g^c(\omega + E_c)$  is the single particle Green's function calculated in the presence of a core hole in level  $|c\rangle$  and shifted by the core energy  $E_c$ . With this expression, we obtain a theoretical description of RIXS that includes core hole effects in both the intermediate and final states of the system. If we neglect core-hole effects  $\bar{\mu}_{\text{XAS}}$  is equivalent to the usual XAS, yielding the simpler result

$$\frac{d^2\sigma}{d\Omega d\omega} \propto \frac{\omega}{\Omega} \int d\omega_1 \frac{\mu_{\text{XES}}(\omega_1) \mu_{\text{XAS}}(\Omega, \Omega - \omega - \omega_1 + E_b)}{|\omega - \omega_1 + i\Gamma_b|}.$$

This formula is similar to one involving a convolution of occupied and unoccupied densities of states [1], except that it now builds in transition-matrix elements. Additional many-body effects can be included *a posteriori* via convolution of this expression with a many-body spectral function  $A(\omega, \omega')$ . This approach has been implemented as an extension to the FEFF9 RSMS code, which has been used extensively for various spectroscopies [2,3]. The RSMS formalism in FEFF is advantageous since it does not rely on any particular symmetry, making it possible to

treat periodic and aperiodic systems alike, including molecules and amorphous systems, over a broad spectral range. As an illustration, our implementation has been used to investigate core-hole effects on the RIXS of anatase  $\text{TiO}_2$ . **Figure 26** shows the calculated Ti K- $\alpha$ , - $\beta$ , and -valence spectra of  $\text{TiO}_2$  as a function of incident photon-energy  $\Omega$ , and energy transfer  $\Omega - \omega$  compared to experiment. Overall, the experimental results (left) are reproduced fairly well by the calculations (right). In addition, the calculations reproduce the qualitative behaviour as a function of the core-hole depth. The core hole potential is strongest in the 1s intermediate state of the X-ray absorption process and gives rise to a K absorption pre-edge feature that extends over 8 eV [4]. The core hole potential is weaker in the final state with a vacancy in the 2p (K- $\alpha$ ), 3p (K- $\beta$ ) or valence shell. This can be directly observed in the RIXS planes: The first peak progresses to higher energy transfer as the final state core-hole becomes shallower, going from a final state with a 2p core hole (top) to a final state with a 3p core hole (middle), then to a final state with a valence hole (bottom). We thus observe that states localised around the absorbing atom in  $\text{TiO}_2$  anatase - which are strongly affected by the core hole - migrate toward higher energy transfer as a function of the strength of the core hole. We conclude that the key interactions in hard X-ray RIXS can now be satisfactorily modelled in terms of XAS and XES using an RSMS formalism, thus opening the way toward a more quantitative interpretation.

#### Acknowledgement

This research was supported by DOE BES Grant DE-FG03-97ER45623, the DOE CMCSN (JJR, JJK), the Eemil Aaltonen and Magnus Ehrnrooth Foundations (JAS) and by the ESRF (PG).

#### References

- [1] P. Glatzel *et al.*, *J. Am. Chem. Soc.* **132**, 2555 (2010).
- [2] J.J. Rehr *et al.*, *Comptes Rendus Physique* **10**, 548 (2009).
- [3] J.J. Rehr and R.C. Albers, *Rev. Mod. Phys.* **72**, 621 (2000).
- [4] D. Cabaret *et al.*, *J. Synchrotron Radiat.* **6**, 258-260 (1999).



## Structure of Materials

This chapter gives a number of examples where the structure, reactivity and interactions in materials have been investigated through the use of synchrotron radiation at ESRF. The study of materials covers a wide range of fundamental and applied science and is one of the primary areas of research at the ESRF. The measurements can lead to a real understanding of why systems behave the way they do, and can result in the longer term to the design and production of new materials with enhanced properties and to the optimisation of the behaviour and longevity of existing systems. The ESRF's powerful X-ray beams can be tailored to probe structures on different scales, revealing the ordering of atoms in crystalline substances or the microstructural arrangement of crystallites in bulk materials, as well as providing detailed structural information at surfaces and interfaces that control so many properties like catalytic activity, corrosion resistance, and are exploited in the design and production of advanced microstructures and electronic components. The great intensity of the X-ray beams coupled with detectors that can operate at high speed allow studies of systems as they undergo change, thus permitting experiments that follow *in situ* the evolution of samples under conditions that may resemble those approaching realistic operating conditions.

One such *in situ* study developed a novel method for observing the formation of clathrate hydrates, which are crystalline solids in which small molecules (particularly gas molecules) are trapped inside cages composed of hydrogen-bonded water molecules. Clathrates can form spontaneously and block oil and gas pipelines. Large quantities of methane clathrates reside in the cold high-pressure environments on ocean floors, and there are ideas that clathrates might be exploited as a fuel source, or even used to sequester carbon dioxide from the atmosphere. In the study, droplets were suspended free of contact in an acoustic levitator and high-speed photography and X-ray scattering were used to follow the process of crystallisation, allowing insight into the mechanism of clathrate formation. In another *in situ* study, electrochemical etching of gold was followed in a special cell on the millisecond time scale by grazing-incidence X-ray scattering at rates comparable to those in

microchip metallisation processes. For etching, the measurements gave clear evidence for a layer-by-layer dissolution mechanism. The opposite process, that of electrochemical deposition which is also of great technological importance, can also be followed by the same approach.

On the instrumental front in the structure of materials group of beamlines, plans for UPBL1 (upgrade of ID01) and UPBL2 (upgrade of ID15 to be built at ID31), and the transfer and refurbishment of ID31 continue to develop. Both ID01 and ID11 installed new high precision diffractometers during the year and ID03 will install a new diffractometer next year. On the downside, it has been decided to close ID32, devoted to hard X-ray photoelectron spectroscopy (HAXPES), X-ray standing waves (XSW), electrochemistry and general surface science, to make way for UPBL7. This is a consequence of the reduction in ESRF's operating budget, and the need to relocate UPBL7 in a different sector of the ring, and represents a significant loss to the ESRF's scientific capacity. No further experiments have been accepted for the beamline, which will complete its outstanding user programme. A workshop attached to the 2012 users meeting will explore the future needs and the conceptual design for a future renewed HAXPES/XSW beamline at ESRF.

A. Fitch





## Discovery of a novel zeolite-like framework in an oxonitridophosphate

Zeolites are microporous compounds built up from three-dimensionally interconnected  $\text{TX}_4$  tetrahedra (typically  $\text{T} = \text{Si}, \text{Al}, \text{P}$ ;  $\text{X} = \text{O}$ ) with ions or small molecules within their cavities and channels. Some of these inorganic open-framework structures are used as absorbents, e.g. in detergents, and are essential in industrial processes, e.g. ZSM-5 as a catalyst for hydrocarbon isomerisation reactions. Prompted by such achievements and the potential for future application as sensors or optical systems, aluminosilicates and aluminophosphates have been intensively developed since the 1980s with the goal of generating new materials with different pore shapes and sizes. By October 2011, 197 zeolite framework types had been identified [1]. As the variety is already high, it becomes increasingly difficult to find new topologies in the field of classical zeolite chemistry.

To discover novel frameworks, we shifted from purely oxidic systems to nitridic ones where nitrogen atoms bridge the tetrahedra. After the first nitridic zeolite  $\text{Li}_x\text{H}_{12-x-y+z}[\text{P}_{12}\text{O}_y\text{N}_{24-y}]\text{X}_z$  ( $\text{X} = \text{Cl}, \text{Br}$ ) [2] (three letter code *NPO*), the higher structural flexibility of nitrogen recently lead once more to an unprecedented zeolite-like framework in the oxonitridophosphate

$\text{Ba}_{19}\text{P}_{36}\text{O}_{6+x}\text{N}_{66-x}\text{Cl}_{8+x}$  ( $x \approx 4.54$ ) whose structure was elucidated using the high-resolution powder-diffraction beamline ID31.

$\text{Ba}_{19}\text{P}_{36}\text{O}_{6+x}\text{N}_{66-x}\text{Cl}_{8+x}$  was obtained by heating phosphoryl triamide  $\text{OP}(\text{NH}_2)_3$ , thiophosphoryl triamide  $\text{SP}(\text{NH}_2)_3$ ,  $\text{BaS}$ , and  $\text{NH}_4\text{Cl}$  in an evacuated and sealed silica glass ampoule at  $750^\circ\text{C}$ . The identification was challenging as the complex synthesis yielded only microcrystalline products with minor unknown side phases. Hence, we made use of a complementary approach including high-resolution powder X-ray diffraction (HR-PXRD), transmission electron microscopy, and solid-state nuclear magnetic resonance (NMR). After evaluation of several HR-PXRD data sets from different samples measured at ID31 (with  $\lambda = 0.4 \text{ \AA}$ ), a primitive cubic unit

cell with  $a = 1342.95 \text{ pm}$  or its twofold superstructure (cubic face centred) with doubling of  $a$  came into consideration. However, through independent symmetry information gained by electron diffraction and scanning transmission electron microscopy images, the correct lattice parameter as well as the correct space group symmetry could be unequivocally derived. The crystal structure of  $\text{Ba}_{19}\text{P}_{36}\text{O}_{6+x}\text{N}_{66-x}\text{Cl}_{8+x}$  (Figure 27) was solved with the charge-flipping algorithm and refined with the Rietveld method in space group  $Fm\bar{3}c$  on the basis of the HR-PXRD data. The structural model was corroborated by  $^{31}\text{P}$  double-quantum (DQ) /single-quantum (SQ) and triple-quantum

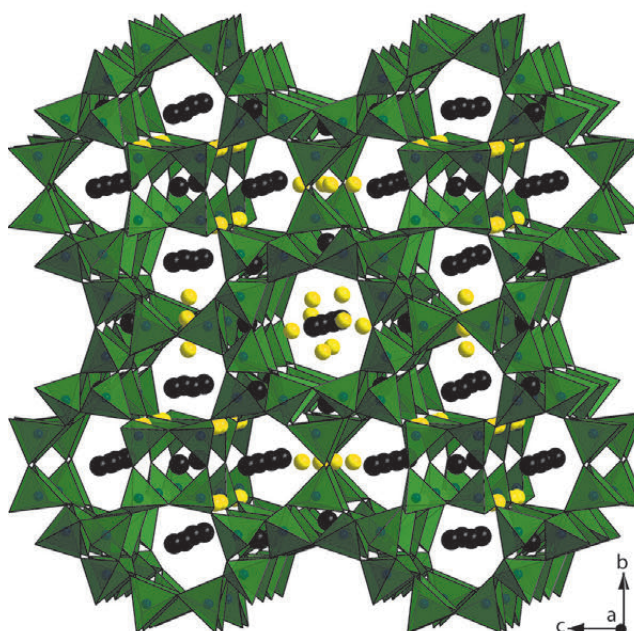


**Fig. 27:** Crystal structure of  $\text{Ba}_{19}\text{P}_{36}\text{O}_{6+x}\text{N}_{66-x}\text{Cl}_{8+x}$  ( $\text{Ba}^{2+}$  black,  $\text{Cl}^-$  yellow,  $\text{P}(\text{O},\text{N})_4$  tetrahedra green). Reprinted with permission from *J. Am. Chem. Soc.* **133**, 12069–12078 (2011). Copyright 2011 American Chemical Society.

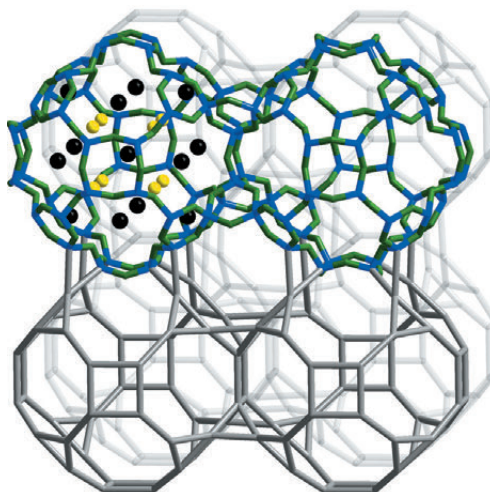


**Fig. 28:** Interconnected  $3^84^68^{12}$  cages in  $\text{Ba}_{19}\text{P}_{36}\text{O}_{6+x}\text{N}_{66-x}\text{Cl}_{8+x}$ ; top: drawing with P–N bonding and cage content (left); bottom: representation with only P–P linking. Reprinted with permission from *J. Am. Chem. Soc.* **133**, 12069–12078 (2011). Copyright 2011 American Chemical Society.





### References

- [1] C. Baerlocher, L.B. McCusker, *Database of Zeolite Structures*: <http://www.iza-structure.org/databases/>, accessed January 2012.
- [2] S. Correll, N. Stock, O. Oeckler and W. Schnick, *Angew. Chem., Int. Ed.* **42**, 3549–3552 (2003).
- [3] M.D. Foster and M.M.J. Treacy, *A Database of Hypothetical Zeolite Structures*: <http://www.hypotheticalzeolites.net>, accessed June 2010.

(TQ) /single-quantum (SQ) 2D correlation MAS NMR spectroscopy.  $^{31}\text{P}\{^1\text{H}\}$  C-REDOR NMR measurements ruled out that stoichiometric amounts of hydrogen are present.

$\text{Ba}_{19}\text{P}_{36}\text{O}_{6+x}\text{N}_{66-x}\text{Cl}_{8+x}$  comprises a framework of all-side vertex sharing  $\text{P}(\text{O},\text{N})_4$  tetrahedra representing a topology that has been previously predicted as a hypothetical zeolite structure based on  $\text{SiO}_2$  [3]. The tetrahedra build up slightly distorted cages with 3, 4, and 8 rings (Figure 28). Interconnected through their four rings, these  $3^84^68^{12}$  cages (superscript numbers mean frequency) generate a network with a low framework density of  $14.9 \text{ T}/1000 \text{ \AA}^3$  (typical range for zeolites:  $12.5\text{--}20.2 \text{ T}/1000 \text{ \AA}^3$ ) and a 3D 8-ring

channel system with a free diameter of 292 pm. The extra-framework ions  $\text{Ba}^{2+}$  and  $\text{Cl}^-$  are incorporated in the cages as well as in the channels. Activation of these ions for ion exchange is the subject of continuing investigations. We now focus on the development of  $\text{Ba}_{19}\text{P}_{36}\text{O}_{6+x}\text{N}_{66-x}\text{Cl}_{8+x}$  as a material for applications as it has a high thermal stability (up to  $1100^\circ\text{C}$ ). To conclude, this novel zeolite-like framework, as the second nitridic zeotype after *NPO* which is mainly built up from 3-rings, is an important step towards establishing the nitride approach in zeolite chemistry. Since the 15th of October, the network of  $\text{Ba}_{19}\text{P}_{36}\text{O}_{6+x}\text{N}_{66-x}\text{Cl}_{8+x}$  has been registered in the database of the International Zeolite Association as NPT, nitridophosphate two [1].

### Principal publication and authors

Y.-Y. Kim (a), K. Ganesan (a), P. Yang (b), A.N. Kulak (a), S. Borukhin (c), S. Pechook (c), L. Ribeiro (d), R. Kröger (e), S.J. Eichhorn (d), S.P. Armes (b), B. Pokroy (c) and F.C. Meldrum (a), *Nature Mater.* **10**, 890-896 (2011).  
 (a) School of Chemistry, University of Leeds (UK)  
 (b) Department of Chemistry, University of Sheffield (UK)  
 (c) Faculty of Materials Engineering and the Russell Berrie Nanotechnology Institute, Technion, Israel Institute of Technology, Haifa (Israel)  
 (d) School of Materials and the Northwest Composites Centre, Paper Science Building, Sackville Street, University of Manchester (UK)  
 (e) Department of Physics, University of York, Heslington (UK)

## ■ Occlusion of copolymer micelles in calcite single crystals generates an artificial biomineral

The composite structure of biominerals endows them with mechanical properties far superior to their synthetic counterparts. This derives from the association of organic molecules with the mineral host, where the organics can be located not only between crystalline units, as occurs in a structure such as nacre, but also within single crystals, as occurs for example in sea urchin spines. Indeed, single crystal biominerals can occlude organic macromolecules of levels of a few wt%, which is surprising given that crystallisation is a traditional method for purifying solids.

We have attempted the formation of an “artificial biomineral” by the encapsulation of organic additives within single crystals. Calcite crystals were precipitated in the presence of 20–30 nm anionic diblock copolymer micelles which exhibit a coronal layer of anionic carboxylated chains at pH values above  $\approx 7$ . The crystals were principally 30–50  $\mu\text{m}$  rhombohedral calcite (Figure 29a) and examination of cross-sections through fractured crystals revealed highly efficient occlusion of the polymer micelles at levels of a 20–30 vol.% (Figure 29b). IR spectroscopy revealed that the crystals possess a level of atomic disorder comparable with biogenic calcite.

The influence of the particle inclusions on the calcite lattice was also investigated using synchrotron high-resolution powder diffraction (XRD) at beamline ID31 (Figure 30). In contrast to pure synthetic/geological calcite, which gives isotropically-shaped diffraction peaks, the peaks from the nanocomposite crystals were highly anisotropic and showed larger broadening towards higher  $2\theta$  (smaller  $d$ ) values. This demonstrates the presence of a high compressive strain gradient in the calcite lattice, decreasing from a maximum at the calcite-micelle interface.

Concomitant heat treatment and XRD analyses of the samples were performed for temperatures between  $100^\circ\text{C}$  and  $600^\circ\text{C}$ . Two phenomena occurred on heating, namely a reduction in the peak anisotropy up to  $300^\circ\text{C}$ , followed by a general broadening of the peaks with further heat treatment. The decrease in peak anisotropy can be attributed to softening and then decomposition of the particles on heating, which reduces their effect on the crystal lattice. Peak broadening on annealing, in contrast, is unusual and “conventional” materials typically exhibit the opposite effect due to a reduction in the number of defects and an increase in grain sizes on



heating. Interestingly, biogenic calcite and aragonite – which also occlude organic macromolecules – exhibit the same broadening effect. The observed broadening in our “artificial biomineral” can therefore be ascribed to an increase in the micro-strain fluctuations/free surface of calcite after the organics are burned away.

TEM studies were also performed to investigate how the single crystal lattice accommodates the micellar impurities. Imaging of thin sections through the nanocomposite crystals not only revealed the presence of the occluded particles, but also showed that they were anisotropic, with oval cross-sections (Figure 29c). Furthermore, the intra-crystalline particles were all co-aligned and were situated on {104} planes. The soft micellar particles therefore appear to undergo a change in morphology on binding to {104} faces during crystallisation, and subsequently become overgrown and occluded within the crystal.

Finally, the mechanical properties of the nanocomposite crystals were measured using nano-indentation methods. Comparison with pure synthetic calcite showed that the nanocomposite crystals were approximately 16% harder than their synthetic counterparts, and that cracks and steps appear at the indent impression in pure calcite which were not observed around the indent in the nanocomposite crystal.

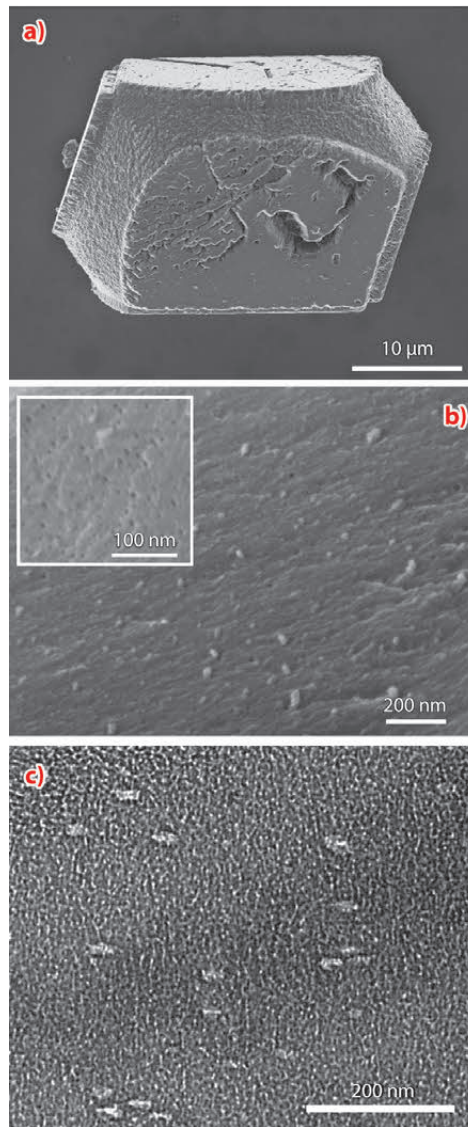


**Fig. 29:** a) SEM image of a calcite single crystal occluding 20-30 vol% of copolymer micelles, b) SEM image of a cross-section through a fractured crystal revealing occluded copolymer micelles, c) TEM image of a thin section cut through a nanocomposite crystal showing the occluded particles.

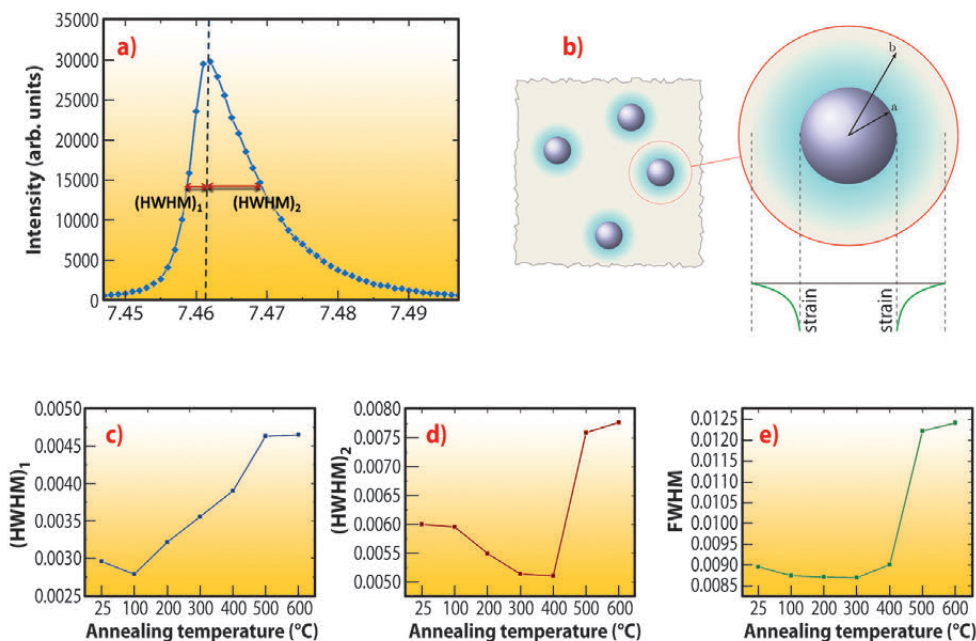


**Fig. 30:** XRD data of calcite crystals occluding polymer micelles. (a) Diffraction peak from the (006) reflection of calcite showing the two FWHMs (full-width half maximum) used when fitting the data. The peak is anisotropically distorted in the direction of lower d-spacing. (b) Schematic diagram of the model used to evaluate the effect of the particles on the crystal lattice, where a particle of radius  $a$  causes a strain gradient in the lattice to a distance  $b$  from its centre (strain affected zone). Beneath the particle and its strain-affected zone, one can see the distribution of compressive strain (in green). (c-e) The HWHM (half-width half maximum) and FWHM as a function of temperature for the (104) diffraction peak, where (c) is HWHM<sub>1</sub>, (d) shows HWHM<sub>2</sub> and (e) shows the FWHM.



### Principle publication and authors

A. Sarfraz (a), M.C. Schlegel (a), J. Wright (b) and F. Emmerling (a), *Chem. Comm.* **47**, 9369-9371 (2011).

(a) BAM Federal Institute for Materials Research and Testing, Berlin (Germany)

(b) ESRF

## Warming up for clathrates research

Scientists have developed a love-hate relationship with clathrates, which have been known for over a century. In oil pipelines, clathrates are seen as a nuisance owing to their ability to block these pipelines. Moreover, ocean floors contain ample quantities of methane clathrates which are thought as a potential future energy source. These materials are also regarded as an alternative route for hydrogen storage for fuel cells. Clathrates were recently in the media when in the Gulf of Mexico oil spill, the recovery efforts were hindered by buildup of methane clathrates. It is clear that these

are materials which pose a threat to the energy industry, but also seem promising as a future alternative fuel source. Clathrate hydrates consist of molecular cages in which guest molecules (noble gases and hydrocarbons) can be trapped. Clathrates are usually formed at low temperatures and high pressures.

In our experiment, it was possible to form and stabilise clathrate hydrates at ambient conditions for the first time. A small droplet of seed solution ( $\sim 4 \mu\text{l}$ ) was suspended in air by using an acoustic levitator and the formation of clathrate hydrates could subsequently be observed. Due to the efficient evaporation of the seed solution, subzero temperatures were rapidly achieved at the droplet's surface. A fast camera was used to capture the formation of the clathrate hydrates *in situ* (see **Figure 31**). The images show the transition from a transparent droplet to an icy crystalline material and then eventually to a droplet with significantly less volume. It can be seen that the droplet begins to solidify 20-30 seconds after being injected. This process is driven by condensation and subsequent freezing of water on the droplet's surface. This fast process could be characterised by means of time-resolved X-ray diffraction at beamline **ID11**. With a time resolution of 500 ms, we obtained diffraction patterns which elucidated the formation process of clathrate hydrate, including the transition from amorphous starting solution to crystalline material.

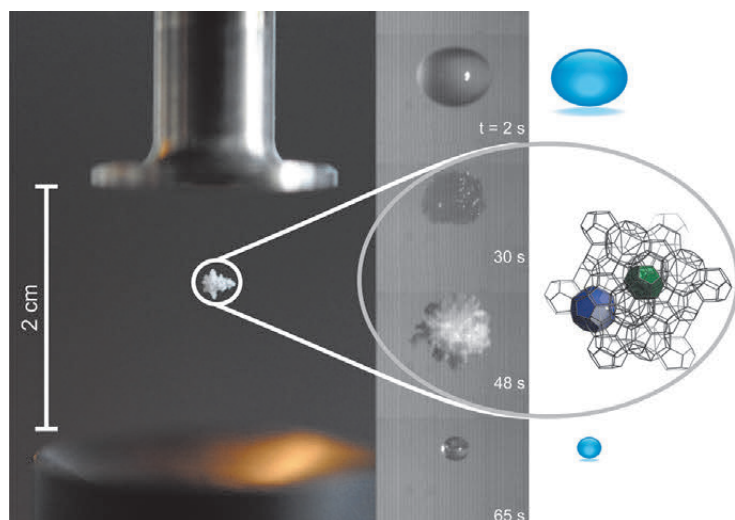


**Fig. 31:** Clathrate hydrate floating on sound: the series of images shows the different steps during formation of clathrates starting from a suspended droplet.

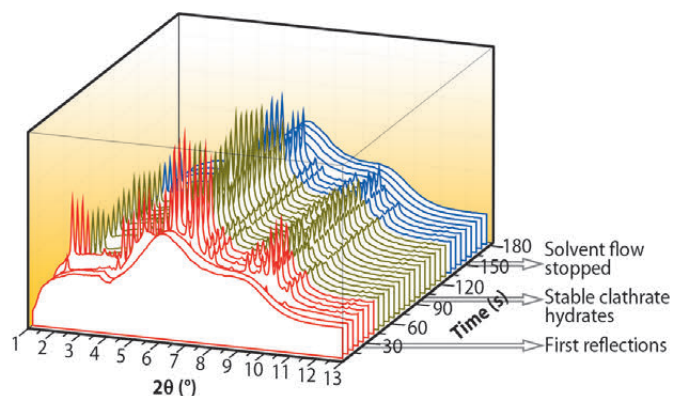


**Fig. 32:** Stabilising clathrates at ambient condition: the time-resolved X-ray diffraction patterns show the initial phase of clathrate formation (red area) with appearance of the Bragg peaks, the stabilisation (green) and the dissolution of the clathrates after stopping the supply of seed solution (blue).

The spontaneous formation of clathrates in the acoustic levitator is promoted by a combination of the following ideally suited conditions. The high vapour pressure of the seed solution leads to a low surface temperature. Since the whole surface area of the droplet undergoes fast evaporative cooling, subzero temperatures are reached. Under these conditions atmospheric water condenses on the droplet and an amorphous solid phase is observed. The evaporating seed solution becomes trapped in the amorphous solid that is formed on the surface. The low solubility of the seed solution in water results in rapid supersaturation and clustering of water. Finally, clathrates begin to crystallise and grow. Because of the ambient temperature and pressure





conditions, the clathrate only remains stable for a certain period of time and rapidly transforms to water.

The clathrate hydrates could be stabilised in the suspended droplet by using a piezo-syringe for continuous addition of the seed solution. Hence, using the high time resolution provided by ID11, it was possible to observe the formation process of clathrate hydrates. **Figure 32** shows the evolution of the diffraction pattern while adding the seed solution to the suspended droplet. A diffraction pattern of the amorphous phase can be observed initially. After about 30 seconds, the first

reflections appear and they remain stable as long as the micro syringe adds solvent to the droplet. Finally, upon stopping the supply of the seed solution, the clathrates are no longer stable and an amorphous diffraction pattern is observed.

This novel method for the production of stable clathrates at ambient conditions could be employed extensively in clathrate research. As compared to former methods that involved low temperatures and high pressures, the advantages of this experimental approach is the rapid production of clathrates at ambient conditions.

#### References

- [1] C.E. Taylor and J.T. Kwan, *Advances in the study of gas hydrates*, Springer (2004).
- [2] E.D. Sloan, *Nature* **426**, 353-363 (2003).

## ■ A new dimension in short fatigue crack characterisation

If you bend a piece of metal, like a spoon, just a tiny little bit, so that it returns back to its original shape when you let go, nothing seems to have happened. But on the microscopic scale, unobservable to the naked eye, some permanent deformation will occur in its crystalline structure. If you repeat this process millions of times, the spoon may eventually break. In materials science and engineering this phenomenon is called fatigue. The risk of failure of stressed components due to cyclic loading has great practical importance, for instance in engines, railway wheels and structures such as bridges that vibrate due to traffic or wind. A deep understanding of fatigue mechanisms is needed to increase the reliability of predictions such as the fatigue lifetime and to design materials with greater fatigue resistance.

A fatigue crack in a structural component, such as part of an engine, may spend up to 90% of its lifetime as a “short” fatigue crack. Such cracks are typically smaller than 1 mm, and are quite difficult to detect. Their behaviour is also less well understood than longer cracks. The local effects of the microstructure average out gradually with increasing crack length, so long crack growth rates in response to loading can be predicted by empirical laws. For short cracks the situation is more complex: the elastic and plastic anisotropy of crystalline materials create

heterogeneities in the deformation at the grain and sub-grain level and these govern short-crack growth. The 3D nature of the microstructure, particularly grain shape and crystal orientation, must be taken into account for accurate predictive modelling. The proper characterisation and description of microstructure and the subsequent modelling of short crack behaviour are complicated!

To acquire a full description of short fatigue crack growth, a multi-dimensional dataset is required: for each point in three dimensional space, the three dimensional grain orientation and the three-dimensional crack growth vector with time must be known. Previously, it was only possible to characterise crack growth and microstructure at the surface or through destructive, three-dimensional mapping of the crack shape and microstructure at a single moment in time. Characterisation of the crucial extra dimensions has now been achieved at beamlines **ID19** and **ID11**, due to the development of diffraction contrast tomography [1]. This non-destructive method makes it possible to characterise grain orientations and boundaries within the bulk of polycrystalline materials. Information on the 3D crack evolution with time is gained by observing the crack with phase contrast tomography [2], at intervals with progressive fatigue cycling.

#### Principal publications and authors

- M. Herbig (a,b), A. King (c), P. Reischig (d), H. Proudhon (e), E. M. Lauridsen (f), J. Marrow (g), J.-Y. Buffière (a) and W. Ludwig (a,h), *Acta Mat.* **59**, 590–601 (2011).
- A. King (h), W. Ludwig (a, h), M. Herbig (a, b), J.-Y. Buffière (a), A.A. Khan (i), N. Stevens (j) and T.J. Marrow (g), *Acta Mat.* **59**, 6761–6771 (2011).
- (a) *Université de Lyon, MATEIS, UMR5510 CNRS, Villeurbanne (France)*
- (b) *Present address: Max-Planck-Institut für Eisenforschung, Düsseldorf (Germany)*
- (c) *GKSS-Research Centre, Geesthacht (Germany)*
- (d) *Karlsruhe Institute of Technology, Eggenstein-Leopoldshafen (Germany)*
- (e) *MINES ParisTech, Centre des Matériaux, CNRS UMR 7633, Evry (France)*
- (f) *Risø-DTU, Technical University of Denmark, Roskilde (Denmark)*
- (g) *Department of Materials, University of Oxford (UK)*
- (h) *ESRF*
- (i) *Pakistan Institute of Nuclear Science & Technology, Islamabad (Pakistan)*
- (j) *Manchester Materials Science Centre (UK)*





**Fig. 33:** Short fatigue crack in a polycrystalline sample. The grains and the crack were reconstructed using diffraction and phase contrast tomography.

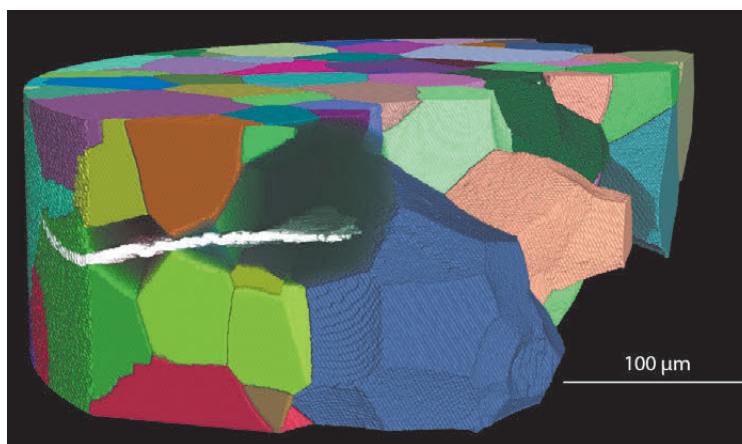
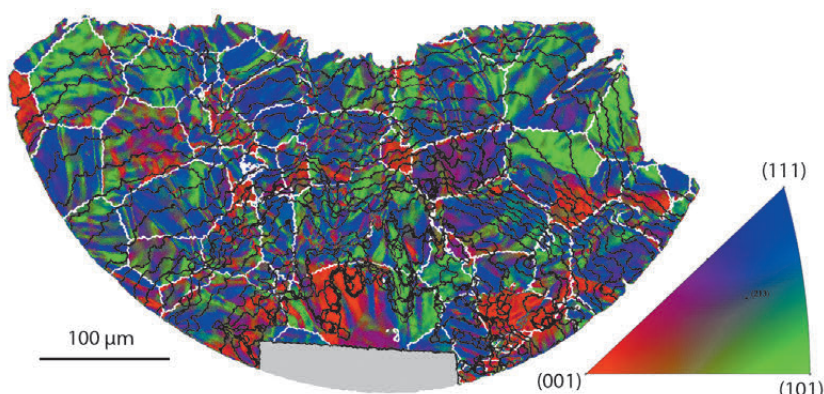


**Fig. 34:** The same crack without visualised grains. Intersections with grain boundaries are marked in white. The black lines show the crack front at a given number of fatigue cycles. The colours represent the fracture surface's local crystallographic orientation.



#### References

- [1] W. Ludwig, P. Reischig, A. King, M. Herbig, E. Lauridsen, T. Marrow and J. Buffière, *Rev. Sci. Instrum.* **80**, 033905 (2009).  
 [2] P. Cloetens, M. Pateyron-Salomé, J.-Y. Buffière, G. Peix, J. Baruchel, F. Peyrin and M. Schlenker, *J. Appl. Phys.* **81**, 5878-5886 (1997).

**Figure 33** shows an example of the combined data.

An approach was developed for the data analysis that presents information as colours on the surface of the 3D crack (**Figure 34**). For each part of the crack, the local crystal orientation, the number of fatigue cycles required to develop the crack to that point and the grain in

which it is situated can be determined. This enables the calculation of local crack growth rates, the crystallographic aspects of the fracture surface and the relative changes in crystal orientation at grain boundaries. Using this toolbox, the interactions between crack and microstructure that control its overall development can be studied for the first time in full depth.

## ■ Shedding light on the heart of a transistor

X-ray diffraction is a powerful tool to determine the structural properties of all manner of materials. The absence of specific requirements for sample preparation makes it one of the most appealing methods to check quickly the sample quality and to gain crucial information on new materials. A limiting factor for nanoscale structures is the lack of spatial resolution, as the diameters of X-ray beams are usually in the range from millimetres down to few tens of micrometres. We used the latest advances in technology for hard X-ray focusing and precise sample positioning available at beamline **ID01** to explore the centre of a

fully processed transistor device, an area size well below one micrometre.

The investigated device was a 'dot-FET' [1], an n-type field-effect transistor with a strained silicon channel as its main active element and a SiGe island (or dot) as stressor. Strain engineering is a versatile tool to enhance the properties of a transistor such as carrier mobility, in this case electrons, and thereby the switching speed. Si and Ge have the same crystal structure with a lattice mismatch of 4.2%, thus a Ge layer can be used to stretch the lattice of Si grown on top. In the dot-FET, a self-organised 3D SiGe island with 250 nm



diameter and 50 nm height is used to apply tensile strain to the Si channel. Its enhanced relaxation compared to 2D layers enables higher strain values while avoiding defects. Such islands are grown on pre-patterned Si (001) substrates as the transistor needs to be aligned with high precision around a single island (see **Figure 35d**). In the completed device this small active area is buried underneath the gate stack, metal contacts and insulation layers, which makes it hard to assess its structural properties while preserving its functionality.

XRD with a focused beam of 400 nm diameter FWHM offers the possibility to probe exclusively this small area. The setup for focusing hard X-ray beams at

ID01 is shown in **Figure 36a**. Via scanning X-ray diffraction (SXD, see **Figure 36b**) [2], we were able to identify the specific island at the transistor core and record reciprocal (004) and (224) space maps to derive parameters such as the average Ge content of the island or the thickness of the Si capping layer. Here, the Si channel was reduced from 30 nm in the as-grown sample to about 24 nm in the completed device due to processing steps including gate stack deposition, etching, implanting and annealing. Combining XRD measurements with finite element simulations, we found tensile strain values of 1% in the Si channel, which are locally reduced due to the influence of the gate stack (see **Figure 36c**).

Such investigations are highly valuable for the development of process flows, as samples from different processing steps can be compared without destructive preparation. Furthermore, the investigation of devices during operation becomes feasible, which is important e.g. for ageing and reliability studies.

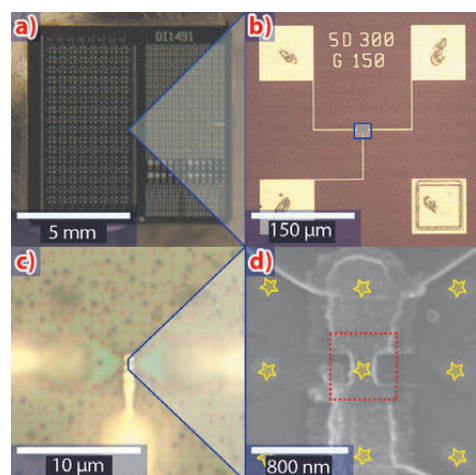


**Fig. 35:** Photograph a) and optical micrographs (b, c) of the sample at different scales. d) shows a SEM image of a transistor sample after gate formation, before source and drain contacts are in place. The gate finger is precisely aligned to the array of SiGe islands (asterisks). The red square marks the area probed by the X-ray beam.

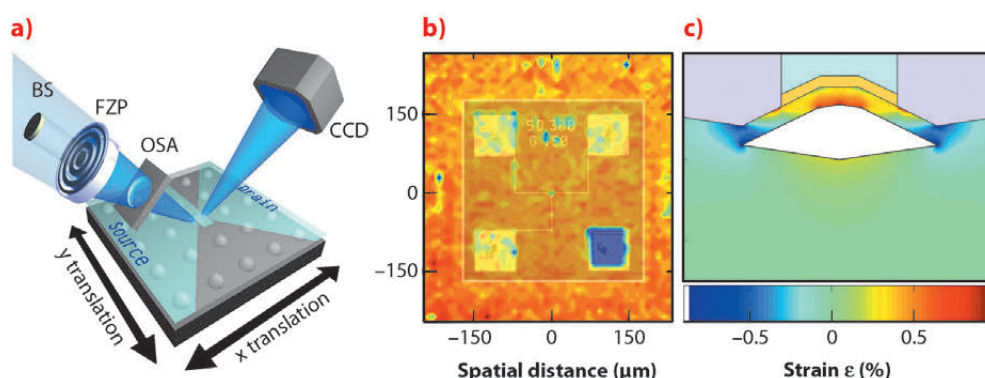


**Fig. 36:** a) Experimental setup at beamline ID01: a beamstop (BS), a Fresnel zone plate (FZP) and an order sorting aperture (OSA) are used to focus the incoming X-ray beam. An SXD map is shown in b) overlaid with a transparent microscope image. c) A map of the in-plane strain in the Si channel.

#### Principal publication and authors

N. Hrauda (a), J.J. Zhang (a,b), E. Wintersberger (a,c), T. Etzelstorfer (a), B. Mandl (a), J. Stangl (a), D. Carbone (d), V. Holý (e), V. Jovanović (f,g), C. Biasotto (f,h), L.K. Nanver (f), J. Moers (i), D. Grützmacher (i) and G. Bauer (a), *Nano Letters* **11**, 2875–2880 (2011).

(a) Institute of Semiconductor and Solid State Physics, JKU Linz (Austria)

(b) IFW Dresden (Germany)

(c) HASYLAB at DESY, Hamburg (Germany)

(d) ESRF

(e) Faculty of Mathematics and Physics, Charles University Prague (Czech Republic)

(f) DIMES, TU Delft (The Netherlands)

(g) FER, University of Zagreb (Croatia)

(h) CCS, State University of Campinas, São Paulo (Brazil)

(i) Halbleiter-Nanoelektronik (IBN-1), Forschungszentrum Jülich GmbH (Germany)

#### References

- [1] V. Jovanović, C. Biasotto, L.K. Nanver, J. Moers, D. Grützmacher, J. Gerharz, G. Mussler, J. van der Cingel, J.J. Zhang, G. Bauer, O.G. Schmidt and L. Miglio, *IEEE Electron Device Letters* **31**, 1083–1085 (2010).
- [2] C. Mocuta, J. Stangl, K. Mundboth, T.H. Metzger, G. Bauer, I.A. Vartanyants, M. Schmidbauer and T. Boeck, *Phys. Rev. B* **77**, 245425 (2008).



### Principal publication and authors

S. Disch (a), E. Wetterskog (b),  
R.P. Hermann (a,c),  
G. Salazar-Alvarez (b), P. Busch (a),  
Th. Brückel (a), L. Bergström (b)  
and S. Kamali (d), *Nano Lett.* **11**,  
1651–1656 (2011).  
(a) JCNS and PGI, JARA-Fit,  
Forschungszentrum Jülich  
(Germany)  
(b) Arrhenius Laboratory,  
Stockholm University (Sweden)  
(c) Faculty of Science, University of  
Liège (Belgium)  
(d) Japan Synchrotron Radiation  
Research Institute (JASRI)

## ■ Shape-induced symmetry in nanoparticle assemblies

The self-assembly of nanocrystals is a widely investigated phenomenon as the understanding of it promises new routes for the formation of large-scale ordered structures for nanotechnology. Most investigations focus on spherical nanoparticles or binary superlattices composed of different particle sizes or compositions. Because the interactions between the nanocrystal facets are important for self-assembly, slight variations in the nanocrystal shape can lead to profound variations of their arrangements on the mesoscale. We have

studied the self-assembly of iron oxide nanocubes with a slight degree of truncation of the corners and report on the influence of the nanoparticle shape on the structure obtained. The resulting mesocrystal structure has been rationalised by evaluation of the van der Waals forces between the adjacent nanoparticle facets.

We studied the magnetically induced assembly of iron oxide nanocubes with an edge length of 8.5 nm and a narrow lognormal size distribution of 6%. The nanocubes are truncated at the corners with a degree of truncation of  $\tau = 0.45$  (derived as  $\tau = 2 t/l$  in **Figure 38**). The presence of a weak magnetic field during evaporation has been shown to promote nanoparticle superlattices with large lateral correlation lengths **[1]**. In this study, we obtained three dimensional mesocrystals with a micrometre lateral size and several hundred nanometres in height. Scanning electron microscopy (SEM) revealed a square lateral with a face to face arrangement of the nanocubes (**Figure 37**).

To obtain depth resolution for the mesocrystal structure, grazing-incidence small-angle X-ray scattering (GISAXS) studies were carried out at beamline **ID01**. The GISAXS pattern obtained revealed sharp reflections which permit a three dimensional crystal structure determination. Purely lateral structural correlations can be assessed in the so called Yoneda line (red line in **Figure 37**). The width of the sharp reflections confirms the high lateral order observed by SEM with a correlation length beyond the instrumental resolution of 65 nm. Reflections with a component perpendicular to the substrate are located above the Yoneda line. The observation of all  $hkl$  reflections in one pattern without rotation of the sample indicates the orientation of the mesocrystals in a two dimensional powder, with a single-crystalline arrangement of the nanoparticles perpendicular to the substrate.

For the nanocube mesocrystals, a body centered tetragonal ( $bct$ ) lattice has been derived from the GISAXS pattern shown

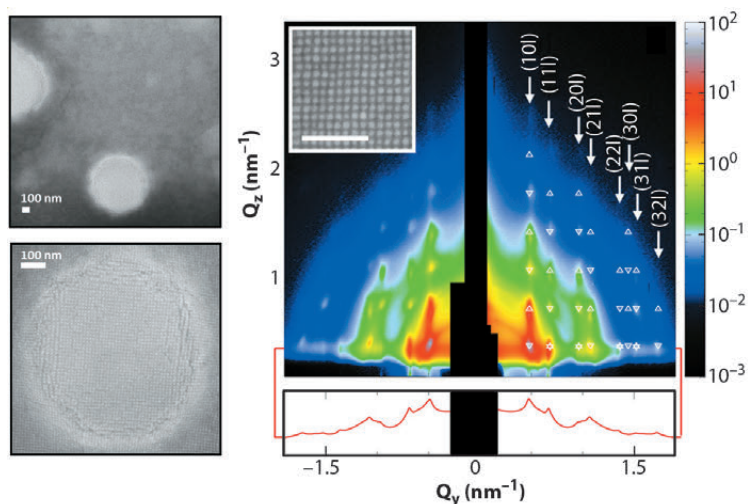
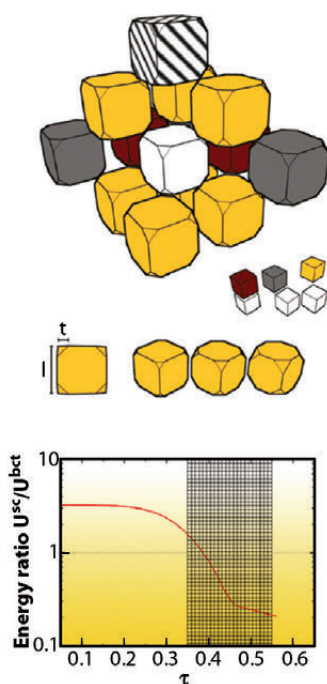


**Fig. 37:** SEM and GISAXS data of the studied mesocrystals.

**Fig. 38:** Illustration of the  $bct$  lattice with different interparticle interaction types (top) and the truncated cubic building blocks (centre). Ratio of the interaction energies in a  $sc$  and  $bct$  lattice (bottom).







in **Figure 37**. This is different from the simple cubic (*sc*) arrangement reported for cubic Fe nanoparticles [2], which can also be inferred from the square symmetry observed by SEM.

To assess the observed preference of the *bct* arrangement against a possible *sc* arrangement, we attempted to model the energy of a particle in both lattice types by comparing the energy needed to remove a nanocube from both lattices. The precise knowledge of interparticle separation distances obtained from GISAXS, TEM, and SEM allowed calculation of the van der Waals energies for the different types of interparticle interactions found in the mesocrystal structure, namely face-face, edge-edge, and corner-corner interactions (**Figure 38**), as a function of the degree of truncation of the nanocubes. In particular, the corner-corner interaction, which depends largely on the degree of truncation of the nanocubes, has been found to dominate the overall interaction

energies. Accordingly, the degree of truncation is an essential parameter for the preference of a *bct* or *sc* lattice. The ratio between the interaction energies calculated for both lattice types presented in **Figure 38** shows that the *sc* lattice is favoured at a low degree of truncation, whereas the *bct* lattice dominates at moderate truncation as observed for the nanocubes under study.

In summary, this work presents the formation and structure determination of large mesocrystals of magnetic nanoparticles of a cuboidal shape. The interaction energy estimates support the observed preference of a *bct* lattice and identify the degree of truncation to be crucial for the mesocrystal structure. The ability to modulate interparticle interactions by a variation of the particle shape is promising for opening a new direction in crystallography, where the mesocrystal structure depends largely on the shape of the primary constituents.

#### References

- [1] A. Ahnizay, Y. Sakamoto and L. Bergström, *PNAS* **104**, 17570-17574 (2007).  
[2] A. Demortière, P. Launois, N. Goubet, P. Albouy and C. Petit, *J. Phys. Chem. B* **112**, 14583-14592 (2008).

## ■ Orientational ordering of non-planar phthalocyanines on Cu(111) revealed by X-ray standing wave experiments

The charge carrier transport across organic semiconductor-metal interfaces depends strongly on the energy level alignment of the two materials. To minimise the resulting energy barrier a controlled manipulation of the interface dipole (ID) would be very effective. In most cases, the complex interaction mechanisms of  $\pi$ -conjugated organic molecules and the rich phenomenology of adsorption geometries make this approach difficult. Detailed, multi-technique characterisations are often necessary to uncover the interplay between the structural and the electronic properties of the organic adlayer [1]. For instance, it has been shown that even planar molecules exhibit surprisingly different bonding distances and sometimes significant distortions of the entire molecule [2,3] because the covalent bonding between the metal substrate and the molecule can be altered by dispersion forces and electron transfer processes [4].

The adsorption behaviour of non-planar organic molecules with permanent dipole moments on metals is highly relevant to our aim of tuning the interface dipole. As these molecules can adsorb in different orientations (**Figure 39**), an (re-)alignment of the molecular dipoles on the surface would allow the work function and energy barrier at the interface to be influenced. In this context, we studied the orientational ordering of chlorogallium phthalocyanine molecules ( $\text{GaClPc}$ ,  $\text{Pc} = \text{C}_{32}\text{N}_8\text{H}_{16}$ ) on Cu(111) using the X-ray standing wave (XSW) technique at beamline **ID32**. The element-specific photoelectron signals of the adsorbate were measured in a narrow energy range around  $E_{\text{Bragg}} = 2.97$  keV in order to determine the bonding distances  $d_{\text{H}}$ . The results reveal that the majority of  $\text{GaClPc}$  molecules adsorb in a Cl-down configuration for coverages below one monolayer (**Figures 40a** and **41**). Small deviations from the gas phase structure, as they were found in the XSW experiments,

#### Principle publication and authors

- A. Gerlach (a), T. Hosokai (a), S. Duhm (b,c), S. Kera (c), O.T. Hofmann (d), E. Zojer (d), J. Zegenhagen (e) and F. Schreiber (a). *Phys. Rev. Lett.* **106**, 156102 (2011).  
(a) Universität Tübingen (Germany)  
(b) Humboldt-Universität zu Berlin (Germany)  
(c) Chiba University (Japan)  
(d) Technische Universität Graz (Austria)  
(e) ESRF (France)





**Fig. 39:** Artist's impression of GaClPc (Pc =  $C_{32}N_8H_{16}$ ) deposition on Cu(111).

A preferential orientation of the molecules on the surface (either Cl-up or Cl-down) with an alignment of the intrinsic dipole moments is essential for the electronic structure of the entire system. X-ray standing wave experiments performed to measure the adsorption geometry and orientation of the molecules distinguish the different elements within molecules, *i.e.* Ga (red), Cl (orange), N (blue), and C (green).

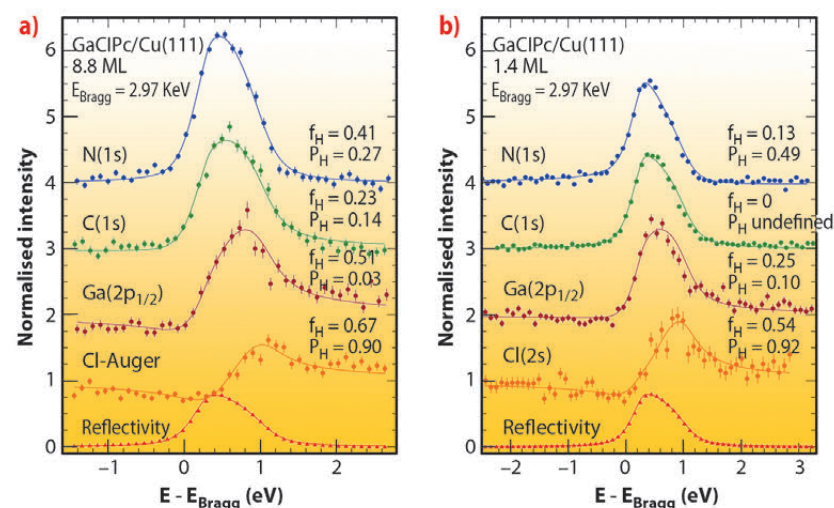
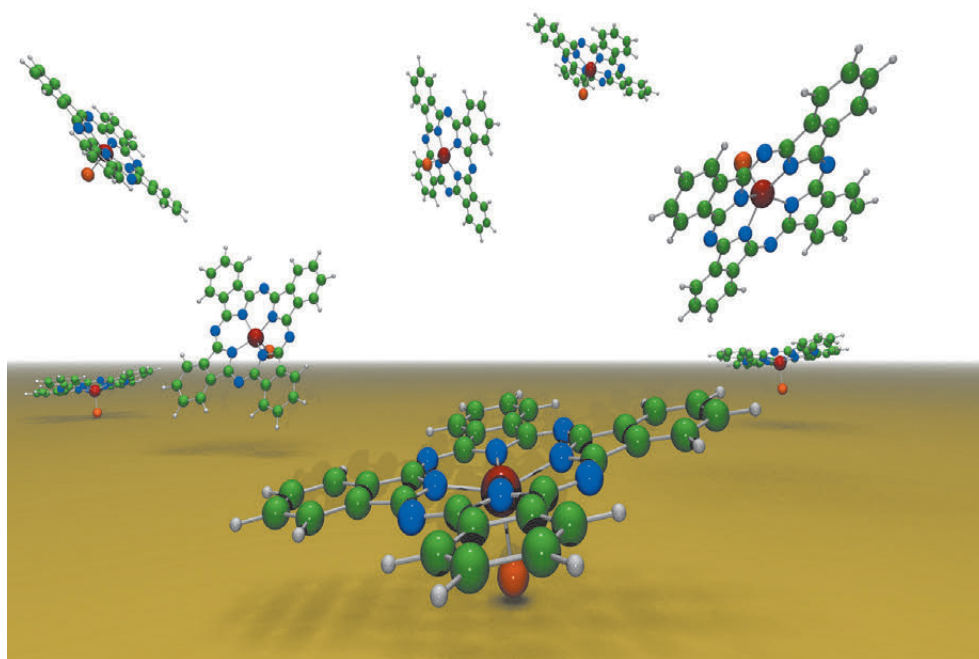


**Fig. 40:** XSW data for GaClPc on Cu(111) taken for two different coverages in back-reflection geometry at an elevated temperature. The photon energy has been scanned around  $E_{\text{Bragg}}=2.97$  keV to measure the photoelectron yield (circles) and reflectivity (triangles). Least-squares fits to the data (solid lines) give the coherent fraction  $f_H$  and coherent position  $P_H$  that are related to the adsorption geometry.

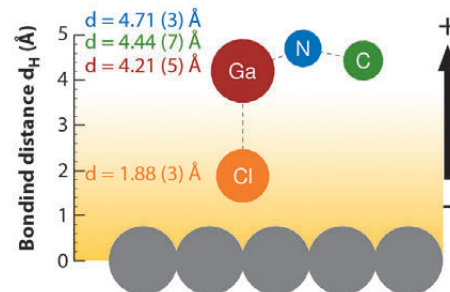


**Fig. 41:** Adsorption geometry of GaClPc as derived from the XSW data for 0.8 ML. The orientation of the molecular dipole leads to a decrease of the work function by  $\sim 0.3$  eV, which is nearly half of the total adsorption induced change  $\Delta\Phi$ . Note that model calculations based on a statistical description of the GaClPc ensemble suggest that thermally activated librational modes of the molecules play an important role.

#### References

- [1] N. Koch, A. Gerlach, S. Duhm, H. Glowatzki, G. Heimel, A. Vollmer, Y. Sakamoto, T. Suzuki, J. Zegenhagen, J.P. Rabe and F. Schreiber. *J. Am. Chem. Soc.* **130**, 7300 (2008).
- [2] H. Yamane, A. Gerlach, S. Duhm, Y. Tanaka, T. Hosokai, Y.Y. Mi, J. Zegenhagen, N. Koch, K. Seki and F. Schreiber. *Phys. Rev. Lett.* **105**, 046103 (2010).
- [3] A. Gerlach, S. Sellner, F. Schreiber, N. Koch and J. Zegenhagen. *Phys. Rev. B* **75**, 045401 (2007).
- [4] L. Romaner, G. Heimel, J. L. Bredas, A. Gerlach, F. Schreiber, R.L. Johnson, J. Zegenhagen, S. Duhm, N. Koch and E. Zojer. *Phys. Rev. Lett.* **99**, 256801 (2007).

can be related to the interaction with the substrate and charge rearrangements at the organic-metal interface. For coverages above one monolayer (**Figure 40b**), the XSW data indicate a co-existence of the Cl-down and Cl-up configurations on the substrate. Eventually, the structural results for different coverage regimes – in particular the parallel/antiparallel orientation of the molecular dipoles – allow one to explain and analyse the observed work function change. DFT-based calculations confirm these findings and help to establish a quantitative picture of the GaClPc adsorption.

This example illustrates the unique potential of XSW measurements, which give precise and chemically-resolved structural information even for relatively complex organic molecules, and thereby help to establish a better understanding of these systems.

## ■ Acids attack: tracing rapid metal etching on the atomic scale

Chemical etching and coating of metals have numerous important industrial applications, ranging from metal mining and refinement to high-tech processes such as the metallisation of ultra large scale integrated microchips. Because of these important applications, the structural changes in materials during etching and coating are intensively studied worldwide. Such studies at present largely fall into two categories. Firstly, studies of the structure of real specimens from the actual technological process analysed *ex situ*, *i.e.*, after the etching or deposition reaction. This is commonly the case in applied research, however, direct insight into the morphological evolution is difficult to obtain and artefacts (*e.g.* changes in the sample structure during sample emersion and transfer) cannot be rigorously excluded. The second category, particularly in the last two decades, includes fundamental studies of growth and etching processes at solid-liquid interfaces that have been performed by high-resolution *in situ* methods. In particular, scanning probe microscopy and synchrotron-based X-ray techniques have contributed enormously to the in-depth understanding of these complex interface processes by revealing in detail the mechanisms of nucleation and growth on the atomic scale. However, all these techniques have been limited to studies at deposition or dissolution rates that are orders of magnitude lower than those employed in industrial processes. Hence, similar to heterogeneous catalysis, a substantial gap exists between atomic-resolution *in situ* studies and the corresponding industrial applications.

In recent years, *in situ* surface X-ray scattering (SXS) studies of electrochemical metal deposition and dissolution in acidic solutions have been pioneered at beamline ID32. The use of electrochemical cells with transmission geometry (see inset in Figure 42) has allowed the study of reactions with unrestricted mass transport. In the initial *in situ* experiments with such cells, the homoepitaxial electrochemical metal deposition and dissolution in Cl-containing electrolytes were studied on the atomic scale at moderate rates of a few monolayers per minute, revealing a

complex growth behaviour that depends on the applied potential and the interface structure [1,2].

Recently, we reported significant advances in this method that allowed studies to be performed at rates close to those employed in technological processes. Key to this improvement was the implementation of a state-of-the-art solid state 1D pixel detector (Dectris Mythen 1K) on the ID32 six-circle diffractometer. This permits single-shot studies of surface structural changes with a time resolution of few milliseconds, which is essential for investigating irreversible processes, such as crystal growth and etching.

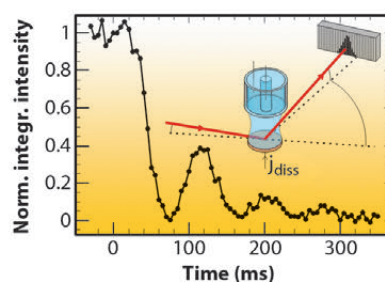


**Fig. 42:** Growth oscillations indicating layer-by-layer growth for Au(001) dissolution in 0.1 M HCl + 0.5 mM  $\text{HAuCl}_4$ , after a potential step from 0.60 to 1.07  $V_{\text{Ag}/\text{AgCl}}$ , where anodic etching commences. The inset illustrates the diffraction geometry.

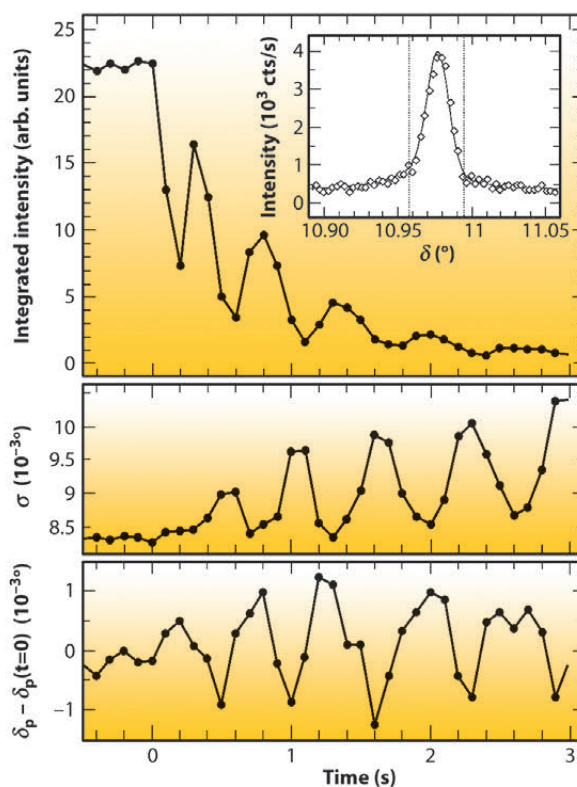


**Fig. 43:** Oscillatory behaviour of intensity (top), peak width  $\sigma$  (middle), and peak position  $\delta_p$  (bottom) of the (1,1,0.1) peak during Au(001) dissolution at 0.99  $V_{\text{Ag}/\text{AgCl}}$ , indicating alternating surface strain and lateral correlations during layer-by-layer etching.

### Principal publications and authors

F. Golks (a,b,c), K. Krug (a,d), Y. Gründer (a,e), J. Zegehnagen (b), J. Stettner (a) and O.M. Magnussen (a), *J. Am. Chem. Soc.* **133**, 3772-3775 (2011).  
 (a) Institut für Experimentelle und Angewandte Physik, Universität Kiel (Germany)  
 (b) ESRF  
 (c) Robert Bosch GmbH, Stuttgart (Germany)  
 (d) Present address: Department of Chemical Engineering, National Cheng University (Taiwan)  
 (e) Present address: The School of Chemistry, University of Manchester (UK)



We studied the anodic electrochemical dissolution of Au(001) in HCl solution by grazing incidence X-ray scattering ( $E_{\text{ph}} = 22.5$  keV). The time-dependent intensity of the crystal truncation rod was recorded close to the anti-Bragg position by the 1D detector (**Figure 42**). After applying a potential step into the regime of anodic gold etching, characteristic growth oscillations are observed that indicate a layer-by-layer dissolution mechanism up to electrochemical currents of  $10 \text{ mA cm}^{-2}$ , corresponding to dissolution rates as high as 20 ML/s. These rates are already comparable to those employed in microchip metallisation. Furthermore, each cycle of the pixel detector contained information on the peak position and width (**Figure 43**), providing insight into strain and lateral correlations at the metal surface. Both position and width exhibit clear oscillations, which are in agreement with a layer-by-layer dissolution mechanism, where the surface alternates periodically between a smooth and a vacancy island covered state.

More recently, we applied this method to the important case of galvanic copper deposition on Cu(100) in chloride-containing acidic electrolytes. Contrary to previous STM studies at low growth rates, potential-dependent transitions to layer-by-layer and even 3D mode were detected, illustrating the need to extend atomic-scale studies into the range of more realistic deposition rates.

In summary, the highly brilliant hard X-ray beam of the ESRF together with fast photon-counting area detectors provide unique opportunities for studying structural changes at deeply buried solid-liquid interfaces under realistic conditions. This approach will also be of great use for in-depth investigations of other (electro-) chemical processes and eventually may help to close the gap between fundamental studies of model systems and applied studies of fast technological or natural reactions.

#### References

- [1] K. Krug, J. Stettner and O.M. Magnussen, *Phys. Rev. Lett.* **96**, 246101 (2006).  
 [2] K. Krug, D. Kaminski, F. Golks, J. Stettner and O.M. Magnussen, *J. Phys. Chem. C* **114**, 18634 (2010).

#### Principal publication and authors

L. Tamam (a), D. Pontoni (b), Z. Sapir (a), S. Yefet (a), E. Sloutskin (a), B. Ocko (c), H. Reichert (b) and M. Deutsch (a), *Proc. Nat. Acad. Sci. USA* **108**, 5522-5525 (2011).

(a) *Physics Department and Institute of Nanotechnology, Bar-Ilan University, Ramat-Gan (Israel)*  
 (b) *ESRF*

(c) *Soft Condensed Matter & Materials Science Department, Brookhaven National Laboratory, Upton NY (USA)*

## ■ When oil and water do mix: the nanoscale structure of a surfactant-modified hydrophobic interface

Hydrophobicity plays a dominant role in fields ranging from the structure of living matter, like cell membrane stabilisation and protein folding, to microemulsion-mediated nano-particle formation [1]. Surfactants can be used to reduce the hydrophobic barrier between oil and water as demonstrated by the use for millennia of detergent-containing water to solubilise and remove oils from fabrics, crockery and the human body. Nevertheless, until recently, the very challenging experiments required have prevented a molecular-resolution determination of the structure of the prime surfactant-modified hydrophobic interface, that between oil and water. Thus, a key ingredient in the fundamental understanding of the relation between surfactants and the hydrophobic interaction was still missing.

Using X-ray reflectivity at the high-energy microfocus beamline **ID15A** and surface tensiometry, the molecular-scale structure

and thermodynamics of deeply buried oil/water interfaces decorated by ionic surfactants have been measured for the first time.

The interface between bulk oil (alkane) and pure water is simple, showing a monotonic transition from the density of oil to that of water over a distance of a few angstroms, determined by the capillary waves decorating all liquid interfaces [2]. When the pure water phase is replaced by a very dilute (sub-millimolar) water solution of an alkyl ammonium bromide cationic surfactant, an intriguingly complex interfacial structure is found. At high temperatures, a liquid-like layer consisting of a mixture of alkane molecules and surfactant tails is found to intrude between the alkane and solution bulk phases. This is manifested by the appearance of a shallow dip in the X-ray reflectivity (**Figure 44a**). The layer has a thickness smaller than the length



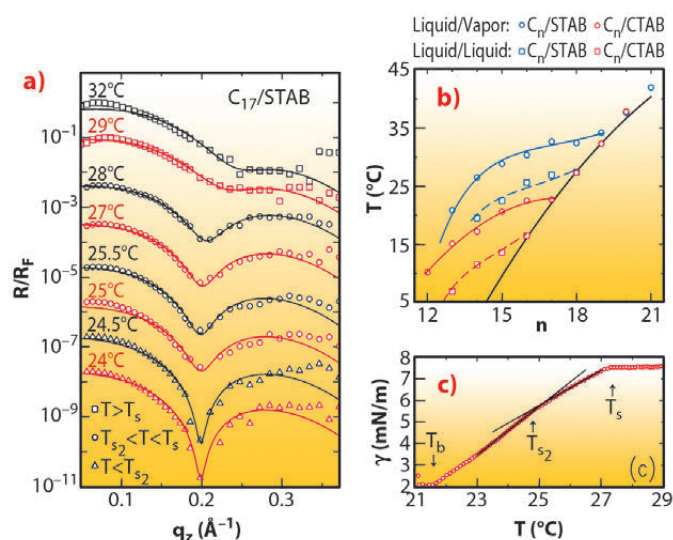


**Fig. 44:** a) Measured (symbols) and modelled (lines) Fresnel-normalised X-ray reflectivity of the interface between a bulk liquid of 17-carbon alkane and a 0.16 mM aqueous STAB surfactant solution. b) Measured (symbols) and modelled (lines) interfacial freezing temperatures  $T_s(n)$  of alkane monolayers at the liquid/vapour (solid lines) and liquid/liquid (dashed lines) interfaces of 0.6 mM CTAB (red) and 0.16 mM STAB (blue) solutions, and the alkane's bulk freezing temperatures  $T_b$  (black line). c) Temperature dependence of the surface tension for the interface in (a). Arrows mark the transitions.

of a single extended alkane molecule. Upon cooling this layer undergoes an abrupt freezing transition at  $T_s$  to a solid monolayer of densely-packed, fully-extended, interface-normal alkane molecules. This transition is observed in **Figure 44a** as a sharpening of the dip at  $T_{s2} \sim 28^\circ\text{C}$  and its shifting to a lower scattering vector  $q_z$ . Moreover, about  $3^\circ\text{C}$  below this transition, a second transition is observed, manifested in an abrupt sharpening of the dip, but no shift in its position. This is a transition from a rotator to a fully crystalline monolayer, as demonstrated also by the magnitude of the entropy loss at the transition, measured from the slope change occurring at the transition in the linear temperature dependence of the surface tension (**Figure 44c**).

The temperature-dependent surface tension measurements, carried out for a range of alkane lengths for two different-length but same headgroup surfactants (CTAB and STAB), determined the phase diagram of the interface, shown in **Figure 44b**. An increasing temperature range of existence is found for the interface-frozen monolayer as the alkane length ( $n$ ) decreases, reaching tens of degrees at low  $n$ . The phase boundaries,  $T_s(n)$ , are similar to, but downshifted from, those observed for alkane monolayers spread on the liquid/vapour interface of the same solutions for both surfactants [3]. The study offers a Mixture Theory based thermodynamic model for the transition, dominated by the interchange energy cost of replacing a surfactant tail with an

alkane molecule. This model reproduces faithfully  $T_s(n)$  at both the bulk alkane/solution and solution/vapour interfaces (**Figure 44b**). The phase sequence and transitions are summarised pictorially in **Figure 45**.

Similar studies on other surfactants should reveal whether the behaviour found here is typical, and will allow a deeper insight into the microscopic origins of hydrophobicity.

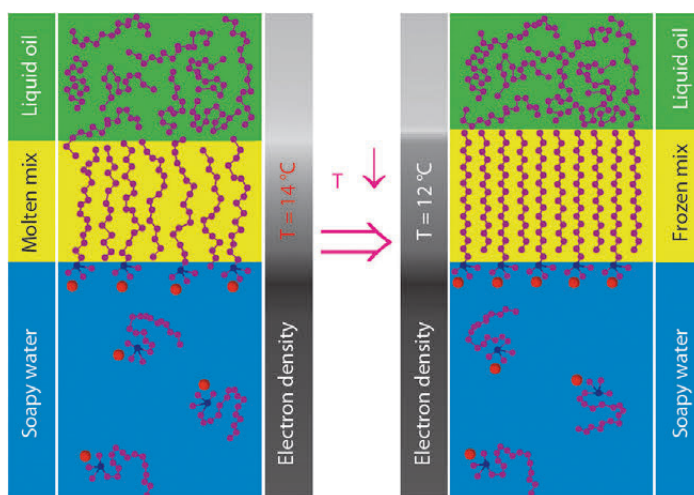


**Fig. 45:** Pictorial summary of the interfacial phase transition for an aqueous CTAB solution/15-carbon liquid alkane interface. At  $14^\circ\text{C}$ , the oil and surfactant molecules intermix at the interface forming a single monolayer of flexible, kinked, and partly aligned chains. At  $12^\circ\text{C}$ , the chains abruptly assume a fully stretched conformation, thus yielding a frozen, solid, two-dimensional interfacial monolayer, while the overlying alkane phase remains liquid.

#### References

- [1] D. Chandler, *Nature* **437**, 640 (2005).
- [2] B.M. Ocko *et al.*, *Phys. Rev. Lett.* **72**, 242 (1994).
- [3] E. Sloutskin *et al.*, *Phys. Rev. Lett.* **99**, 0136102 (2007)



### Principal publication and authors

S.D.M. Jacques (a, b),  
 M. di Michiel (c), A.M. Beale (a),  
 T. Sochi (b), M.G. O'Brien (a),  
 L. Espinosa-Alonso (a),  
 B.M. Weckhuysen (a) and  
 P. Barnes (b), *Angew. Chem. Int. Ed.* **50**, 10148, (2011).  
 M.G. O'Brien (a),  
 S.D.M. Jacques (a,b),  
 M. di Michiel (c), P. Barnes (b),  
 B.M. Weckhuysen (a) and  
 A.M. Beale (a) *Chem. Sci.* **3**, 509-523 (2012).  
 (a) *Inorganic Chemistry and Catalysis, Debye Institute for NanoMaterials Science, University of Utrecht (The Netherlands)*  
 (b) *UCL Chemistry London/Dept. Crystallography, Birkbeck College, London (UK)*  
 (c) *ESRF*

## ■ Observing catalysts in multiple dimensions

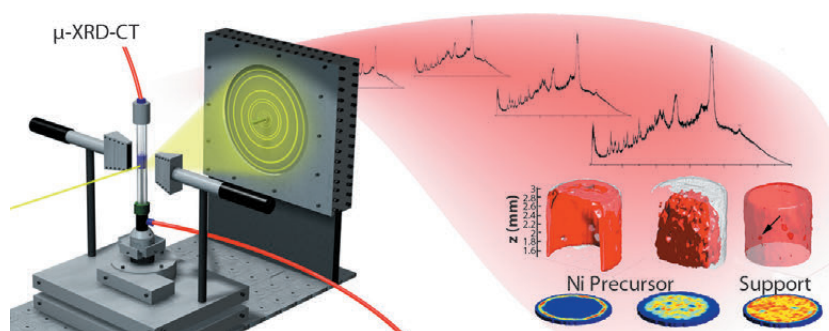
Metals and/or metal oxides anchored to porous support materials are the cornerstone of the industrial heterogeneous catalysis industry. These catalysts owe their activity to the stabilisation of the metals/metal oxides in active electronic and/or coordination states, and are often employed in 3D form (known as catalyst bodies) in fixed bed reactors so as to minimise pressure drops across the reactor vessel. The efficiency of the final catalytic system depends on the nature and distribution of these active species within the catalyst body, although this can be controlled at the preparation stage. However, the evolution of the active species from an initial precursor delivered via liquid phase impregnation is often a highly complex process. In recent times analytical techniques have been developed to obtain real time 2D and 3D spatial information on the distribution of chemical species in catalysts during their preparation in order to unravel the physicochemical processes taking place. Such information enables better control of the distribution of the active phase and therefore the overall performance of the catalyst [1]. Recently we employed the technique of time-resolved X-ray diffraction computed tomography (XRD-CT, **Figure 46**) at beamlines **ID15A** and **ID15B** and demonstrated its capability to image a catalyst body as a function of time to follow the preparation process and to study the catalyst as a reaction (CO methanation) takes place [2].

In the first study, examining the preparation during calcination (in  $N_2$ ) of a Ni supported  $\gamma-Al_2O_3$  catalyst body, we observed the formation of the final cubic (fcc) metallic Ni phase via a complex multi-step process involving a number of crystalline intermediate phases.

Importantly, two different crystalline phases initially form located at the periphery and in the centre of the body accordingly. Although both phases yielded fcc Ni, the precursor at the periphery did so in one step, while the phase in the centre did so via a 3-4 step process (**Figure 47**). This appeared to affect the particle size of the fcc Ni phase with the fcc Ni particles in the centre of the pellet larger than those seen at the periphery. This has important implications for the activity/selectivity of these catalyst bodies in a catalytic reaction.

In a second recent study, we combined XRD-CT with absorption-CT to study the activity of Ni/ $\gamma-Al_2O_3$ , to study again the phase evolution process during the processes of calcination and activation, but more importantly, to study such catalyst bodies for the first time under true catalytic conditions. As with the first study, two different, inhomogeneously distributed precursors result after the impregnation process, although the breakdown of these precursors resulted in the formation more uniformly-sized Ni nanoparticles. Particles located towards the periphery undergo uncontrolled sintering on exposure to  $O_2$  although this appears to be dependent on both the concentration/distribution of the Ni and its form (where it is expected that Ni is present in the sample in both crystalline and diffraction silent forms). Reduction by  $H_2$  does not induce further sintering but results in an active fcc Ni-containing catalyst for CO methanation. Operando catalytic measurements performed during CO methanation, demonstrated the crystalline metallic fcc Ni component to be remarkably stable during the duration of reaction (~3 hours), undergoing no change in phase constitution, spatial distribution or average

**Fig. 46:** In XRD-CT, a series of transmission projection measurements is made at several angles while the sample is exposed to X-ray radiation. A 2D image slice is then reconstructed from these measurements via a suitable algorithm based on the differences in the diffraction signals for the crystalline phases present.



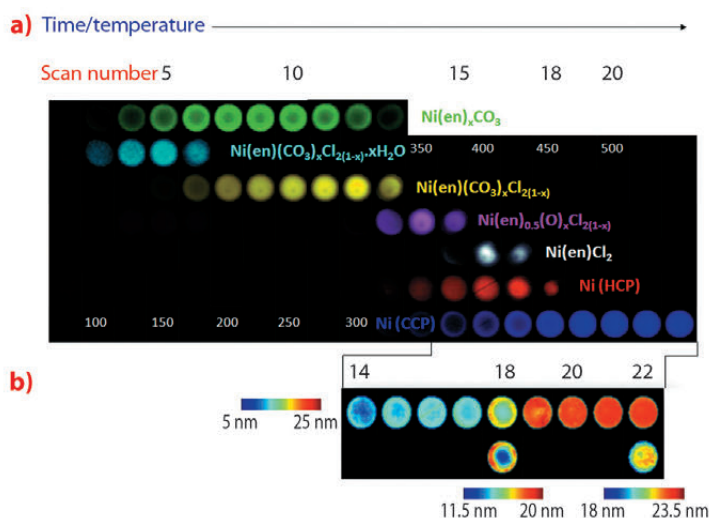


**Fig. 47:** Reconstructed 2D images of crystalline components' features observed in the diffraction patterns as a function of time/temperature during thermal activation of a  $\gamma$ - $\text{Al}_2\text{O}_3$ -supported Ni catalyst precursor. a) The colour maps indicate the following distribution of solid-state phases accordingly: precursor 1 (green), precursor 2 (cyan), subsequent breakdown phases associated with precursor 2 (yellow, magenta, white and red), and fcc Ni (blue). b) The thermal colour maps show the variation in crystallite size (nm). When plotted with a common colour axis (top) these indicate the growth of fcc Ni crystallite size as the growth of the phase proceeds. For slices, 18 and 22, the data have been re-plotted with bespoke colour axes (shown beneath).

particle size, leading us to conclude that metallic fcc Ni is the active component of the catalyst for CO methanation.

#### References

- [1] L. Espinosa-Alonso, A.M. Beale and B.M. Weckhuysen, *Acc. Chem. Res.* **43**, 1279 (2010).  
 [2] P. Bleuet, E. Welcomme, E. Dooryhee, J. Susini, J.L. Hodeau, P. Walter, *Nat. Mater.* **7**, 468 (2008).

## ■ The missing link: surface freezing meets self-assembly

The formation of organic monolayers is of interest both for fundamental science and for applications ranging from biosensors to organic photovoltaic devices. At one end of the organic monolayer spectrum are self assembled monolayers (SAMs), like gold-supported alkyl-thiols and silica-supported alkyl-silanes, where the solution prepared monolayer formation and order are dominated by the strong covalent bond between the head group and substrate while the weaker chain-chain van der Waals (vdW) interactions are less important. At the other end of the spectrum is surface freezing, where a solid monolayer of n-alkane molecules forms at the free surface of their own melt over a temperature range of a few degrees above the bulk melting point. Here the lateral vdW interaction between molecules dictates the frozen monolayer's structure, while the very weak interaction of the molecules with the "substrate" (the vapour) plays only a minor role. The present study is the first to explore the intermediate regime, where both chain-chain and substrate-head group interactions are of equal

strength and importance in determining the lateral structure of the monolayer. This study provides, therefore, a hitherto-missing link between self-assembly and surface freezing.

Using X-ray reflectivity at the high energy microfocus beamline **ID15A**, we have investigated the structure of long-chain alcohol monolayers at the interface of a highly polished sapphire (0001) surface while in contact with either a molten bath or a saturated vapour of the same long-chain alcohol. In **Figure 48** the experimental configuration is shown where the sapphire surface is in contact with the bulk molten alcohol. X-rays of 71 keV were focused to  $<10 \mu\text{m}$  using compound refractive optics lenses and then reflected off the liquid/solid interface.

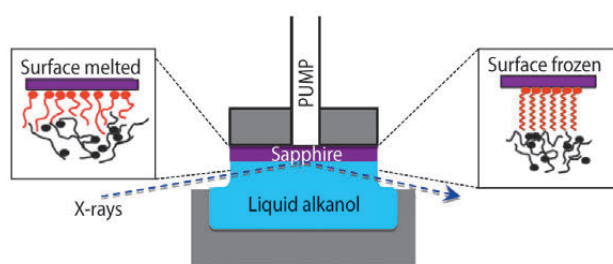


**Fig. 48:** Schematic of the X-ray scattering geometry at the liquid/solid interface (centre). The fit-derived molecular models are shown in the disordered state (left) and in the surface frozen state (right).

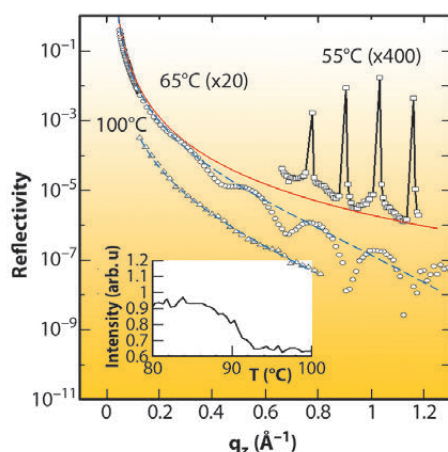
#### Principal publication and authors

- B.M. Ocko (a), H. Hlaing (a), P.N. Jepsen (a), S. Kewalramani (a), A. Tkachenko (b), D. Pontoni (c), H. Reichert (c) and M. Deutsch (d), *Phys. Rev. Lett.* **106**, 137801 (2011).  
 (a) *Condensed Matter & Materials Science Department, Brookhaven National Laboratory, Upton NY (USA)*  
 (b) *Center for Functional Nanomaterials, Brookhaven National Laboratory, Upton NY (USA)*  
 (c) *ESRF*  
 (d) *Physics Department and Institute of Nanotechnology, Bar-Ilan University, Ramat-Gan (Israel)*





**Fig. 49:** Absolute X-ray reflectivity versus  $q_z$  at the sapphire/C18OH interface at 55, 65 and 100°C corresponding to the crystalline ( $\square$ ) monolayer ( $\circ$ ) and disordered ( $\triangle$ ) phases. The calculated Fresnel curves are shown with no roughness (solid line) and a roughness of 1.5 Å (dashed line). (inset) Intensity at  $q_z = 0.55 \text{ \AA}^{-1}$  versus temperature shows the transition between the surface frozen monolayer and disordered phases at a temperature about 30°C above the bulk melting temperature.



The reflectivity recorded as a function of the incidence angle  $\alpha$  expressed as  $q_z = (4\pi/\lambda)\sin\alpha$ , where  $\lambda = 0.175 \text{ \AA}$  is the X-ray wavelength. Using a model for the surface-normal electron density, the monolayer's structure can be extracted from the measured reflectivity.

**Figure 49** shows the reflectivity at the C18OH/sapphire interface at several temperatures along with the Fresnel reflectivity,  $R_F$ , the theoretical reflectivity of an ideally flat and smooth interface. At 62°C, above the bulk freezing point,  $T_f = 59.8^\circ\text{C}$ , the reflectivity exhibits well-defined modulations whose  $q_z$  period corresponds to a single layer of upright molecules. By 100°C, the modulations have nearly vanished suggesting that the monolayer has melted. The melting of the monolayer is clearly visible between 87 and 92°C, as demonstrated by the gradual intensity change that occurs in this interval (see inset to **Figure 49**). The surface melting transition occurs at a

relative transition temperature  $\Delta T = T_b - T_f$ , which is about 30°C higher than the bulk melting transition. This  $\Delta T$  is about an order of magnitude larger than that observed for the surface freezing of alkanes [1] and alcohols [2] at the melt/vapour interface. The reflectivity at 55°C, a temperature below  $T_f$ , exhibits Bragg peaks characteristic of a crystalline bilayer phase.

Additional reflectivity measurements show that the monolayer remains intact with the same structure and density after removal from the liquid. Complementary grazing incidence diffraction measurements show that the monolayer is ordered commensurately with the underlying sapphire lattice. With increasing temperature, this air terminated "self-assembled monolayer" melts. The monolayer thickness decreases from 25 to 20 Å with a decrease in the number of hydrogen bonded alcohol groups.

Our results provide insight into the link between surface freezing and self-assembled monolayers. The thickness change upon melting and the temperature range of the surface frozen layer are consistent with a simple free energy model that only includes the OH-sapphire adsorption energy, and the elastic penalty associated with stretching the chains. On the basis of this model, we expect that surface freezing is a generic property of all self-assembled monolayers. For self-assembled monolayers, the temperature range of surface freezing will depend on the energetics of the surface bond, the entropy change upon melting, and the availability of surface bonding sites.

#### References

- [1] X.Z. Wu *et al.*, *Phys. Rev. Lett.* **70**, 958 (1993).  
 [2] M. Deutsch *et al.*, *Europhys. Lett.* **30**, 283 (1995).

#### Principal publication and authors

R. Algra (a,b), V. Vonk (a),  
 D. Wermeille (c), W. Szweryn (a),  
 M. Verheijen (b),  
 W. van Enckevort (a), A. Bode (a),  
 W. Noorduyn (a), E. Tancini (c),  
 A. de Jong (a), E. Bakkers (b) and  
 E. Vlieg (a), *Nano Lett.* **11**, 44–48  
 (2011).  
 (a) Radboud University Nijmegen,  
 Institute for Molecules and  
 Materials (The Netherlands)  
 (b) Philips Research Laboratories  
 Eindhoven (The Netherlands)  
 (c) ESRF

## ■ Does liquid-ordering play a role in determining the crystallographic structure of nanowires?

Semiconducting nanowires offer the possibility of nearly unlimited complex bottom-up design, which allows new device concepts that may find use in applications like sensors, solar energy conversion or light-emitting diodes. Essential parameters that determine the electronic and optical properties of a nanowire are its crystal structure and the density of defects.

Nanowires can be grown from nano-sized metal droplets by the vapour-liquid-solid (VLS) growth mechanism. As the name suggests, three phases are involved in this type of nanowire growth. Precursor molecules from the gas phase are decomposed and form an alloy with the metal particle. Nucleation occurs at the solid-liquid interface and the crystalline nanowire grows layer by layer. The crystal

structure of nanowires grown by the VLS mechanism is often different from corresponding bulk crystals. For instance, intrinsic InP nanowires crystallise in the wurtzite structure, while bulk, Czochralski-grown InP crystals have the zinc-blende structure. It has been argued that the shape of the metal particle, and more specifically the contact angle of the droplet with the nanowire side facets, determines the nanowire crystal structure [1], but alternatively the chemical composition and the precise atomic positions at the solid-liquid interface could determine the nanowire crystal structure [2]. We used surface X-ray diffraction at beamline **ID03** to solve the atomic structure at the liquid-solid interface of an AuIn alloy in contact with a (111) InP bulk crystal surface at elevated temperatures, simulating the solid-liquid interface during InP nanowire growth from an initial Au particle.

Two major problems are encountered when studying the solid-liquid interface of genuine nanowires *in situ*. First, the actual area covered by nanowires is quite small, and second, growth conditions are required with highly-toxic precursor gasses. We therefore used a thin alloy film in contact with an InP (111) substrate as a model system. The InP substrate is covered by a 100 nm metal layer, with the eutectic composition of the AuIn alloy. To minimise the decomposition of the InP substrate by phosphorus desorption during heating, a 100 nm SiO<sub>2</sub> layer was deposited on top as a protective layer. The samples are heated to 773K to liquefy the AuIn alloy, similar to the annealing steps prior to nanowire growth. Then, the samples were cooled down to 693K, a typical growth temperature for InP nanowire growth.

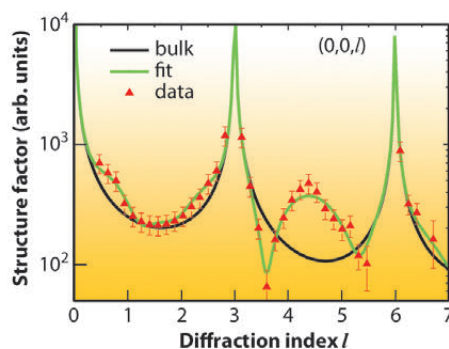


**Fig. 50:** The experimental structure factors (triangles) together with the optimum fit (green curve) that shows the exceptional high degree of liquid ordering in the Au-In eutectic at the measurement temperature of 693 K. The black curve shows the expected shape without liquid ordering. Additional data (not shown) yield the lateral location of the first-layer liquid atoms.

By measuring specular and non-specular rods, both the in-plane and out-of-plane structures of the solid-liquid interface are determined. The experimental data (Figure 50) are fitted to a model (Figure 51a) that describes the entire solid-liquid interface. We find that several of the liquid layers show a surprisingly high degree of order. Moreover, the first layer has an increased In composition and the atoms are positioned in the middle of the InP hexagons of the crystal surface (Figure 51c). This can have important consequences for the structure (stacking) of the next InP layer. When nucleating the next crystalline bilayer, In will always be positioned on top of the P atoms of the previous bilayer. Only the P atoms in the new layer will determine the stacking. There are two possibilities, either continuing the zinc-blende structure or forming a stacking fault, corresponding to the start of the wurtzite structure. Because we find that the hollow sites are preferentially occupied by Au/In alloy atoms, the P atoms will be sterically-hindered for entry into the zinc-blende positions and therefore crystallise preferentially in the wurtzite structure.

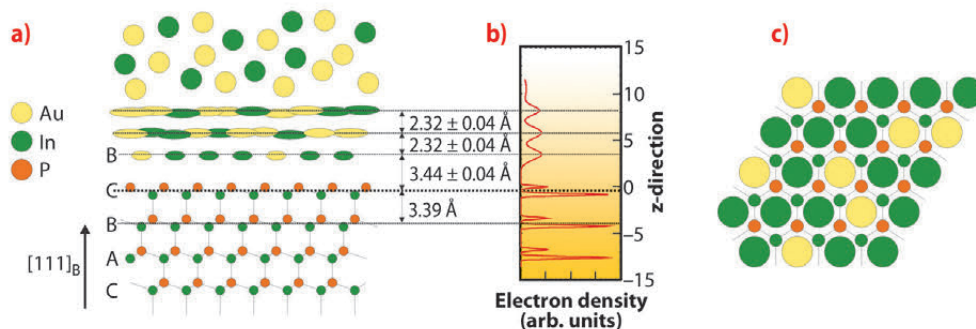


**Fig. 51:** a) A side view of the solid-liquid interface structure of the InP crystal in contact the Au-In eutectic. The first quasi-liquid layer has a B stacking and is enriched in In. b) The z-projected electron density distribution as derived from the data in Figure 50. c) Top-view of the InP surface (small circles) indicating that the first liquid layer (large circles) occupies the centre of the hexagonal InP rings.

#### References

- [1] F. Glas, J. Harmand and G. Patriarche, *Phys. Rev. Lett.* **99**, 146101 (2007).
- [2] R. Algra, M. Verheijen, M. Borgström, L. Feiner, G. Immink, W. van Enckevort, E. Vlieg and E. Bakkers, *Nature* **456**, 369-372 (2008).



## Soft Condensed Matter

This chapter presents a selection of highlights in the soft condensed matter field. The year 2011 was celebrated as the International Year of Chemistry commemorating the achievements of chemistry and its contributions to mankind. As if tuned to this special occasion, this time there are more highlight articles related to chemistry than other disciplines. Similar to last year, some articles have strong emphasis on the complementary techniques.

The first article by Zeng *et al.* illustrates the beauty of soft matter, in this case the ability of X-shaped liquid crystal molecules to overcome geometrical and compositional frustrations by forming complex periodic honeycomb structures. These intriguing molecules may even form a dodecagonal quasicrystalline honeycomb analogous to quasicrystals, for the discovery of which this year's Nobel Prize in Chemistry was awarded to Professor Shechtman. Metal-organic frameworks are another novel class of crystalline materials involving complex self-assembly. The article by Cravillon *et al.* reports the nucleation and growth of these nanocrystals and finds important differences from the classical nucleation process. Hybrid organic-inorganic composite materials are involved in many practical applications. Balmer *et al.* present the dynamics of adsorption and distribution of small silica particles on large polymer latex particles to form remarkably well defined hybrid core-shell morphology. Molecular chirality is the foundation of stereochemistry. Rosenthal *et al.* explored a higher level of chirality in semi-crystalline polyethylene emanating from the twist of the lamellar stacking. In the following article, Sanyal *et al.* report on an *in situ* crystallisation study of a polymer-fullerene blend, a composite material with promising applications. Their results reveal details of the development of the heterojunction that determines the efficiency of power conversion in their potential application in polymer solar cells.

Turning to biologically relevant examples, Ghosh *et al.* investigated the structure and interaction of synaptic vesicles with lipid membranes revealing a collective reorganisation of the monolayer upon site selective binding of these protein-rich vesicles. To shed more light on the photosynthetic reaction centers, Wohri *et al.* probed the conformational changes in tyrosine residues from a bacterial photosynthetic reaction center following photoactivation. The structural changes observed were interpreted in terms of

complementary electron-proton transfer reactions in which excess positive charge following the primary electron transfer induces a proton transfer in the opposite direction.

Complementary techniques are often vital in reaching a better understanding of the results from scattering experiments. The article by Ramachandran *et al.* demonstrates how a combination of time-resolved scattering, nuclear magnetic resonance and double electron-electron resonance spectroscopy captures short-lived transient intermediate states in photoactive yellow protein in solution. Using complementary electron microscopy, spectroscopy and micro diffraction, Hauser *et al.* report on different steps in the self-assembly of a very small peptide to fibrous structures similar to those involved in Alzheimers and other degenerative diseases. Finally, Martinez *et al.* revisit the dynamics of the concentrated hard-sphere colloidal suspensions, first by establishing the equivalence of the results from dynamic light and X-ray scattering experiments, and then reviving the longstanding debate on the scaling of the short-time and long-time diffusion coefficients.

Indeed, as in previous years, this chapter contains only a selective sub-set of many interesting results published during the year and obviously there are many omissions due to lack of space. To mention but a few, the work of Reconditi *et al.* [PNAS 108, 7236 (2011)] on the pathways of skeletal muscle cell activation, and Czakkel and Madsen on the non-equilibrium dynamics of cross-linked polymer gel formation [EPL 95, 28001 (2011)].

Among the technical developments, beamline ID10 is undergoing a major refurbishment and it will no longer be Troika. The new shared beamline "Soft Interfaces and Coherent Scattering Beamline" will be open to users soon after the restart of the ESRF in May 2012. The technical design report for UPBL9a (ID02) has been completed and the upgrade is due to begin in mid 2013. The technical design report for UPBL9b (ID09 Time-Resolved) is in preparation. Finally, the formal collaboration contract for the Partnership for Soft Condensed Matter is nearing completion and full-scale activities are expected to take-off at the end of 2013 when the new science building becomes available.

T. Narayanan





## Complex patterns in liquid crystals

A new way of making small molecules self-assemble into highly complex nanopatterns has been established that will help expand the capabilities of nanopatterning for advanced functional materials. Liquid crystals can form many diverse nanoscale structures. Particularly intriguing are the new liquid crystals honeycombs formed by T- or X-shaped molecules composed of several mutually incompatible rigid and flexible parts. A bee honeycomb can be represented in 2D as a tiling of hexagonal tiles. Here we show how in liquid crystals the tiles can be of many different shapes and colours, forming periodic patterns of high complexity.

T-shaped molecules consisting of a rigid rod aromatic core (II in **Figure 52a**) capped at each end with hydrogen-bonding groups like glycerol (I) and having a flexible non-polar side chain, such as alkyl (III), have been found to assemble in honeycombs with cells of different polygonal cross-sections [1]. The rods, lying perpendicular to the channel axis, form the cell walls (“wax”), while the side-chains (“honey”) fill the cells. The larger the side-chain, the more sides to the polygon; thus compounds with small chains form triangular cells (**Figure 52b**), those with longer chains form square cells (**Figure 52c**), through pentagonal, hexagonal and beyond. If, however, a second chain (IV) is attached to the opposite side of the rod, an X-shaped molecule results (**Figure 52d**). If, moreover, that second chain is incompatible with the first one, we could obtain honeycombs described as two-colour tilings. Two examples are shown in **Figures 52e,f**. Even more elaborate tilings can also be conceived [2].

If the chain volumes are too large for triangular yet too small for square cells then regular structure formation can be highly frustrated. Utilising such geometric and incompatibility frustration, compounds were synthesised giving a range of liquid crystal honeycombs with highly complex self-assembled “multicolour tiling” patterns. Well-aligned thin films of X-shaped liquid crystals on silicon surface were studied using grazing incidence small-angle X-ray scattering (GISAXS) on beamline **BM28** (XMaS).

**Figures 53a** and **b** show GISAXS patterns of two honeycomb phases of a compound with a perfluoroalkyl and a carbosilane side-chain. Superimposed on the GISAXS patterns are the corresponding 2D reciprocal lattices in several orientations. Although the molecules are small (ca 4 nm), the unit cells are large: 21 x 11 nm for the high-temperature phase. By Fourier analysis, electron density maps were constructed (**Figures 53c,f**). To explain the maps, schematic molecules are superposed, bearing in mind that the perfluoro-chains have the highest electron density (blue-purple) and the carbosilane the lowest (red). It emerges that in neither of the two phases is there a clean separation between the two

### Principal publication and authors

X.B. Zeng (a), G. Ungar (a),  
C. Tschierske (b), R. Kieffer (b),  
B. Glettner (b), F. Liu (a),  
C. Nürnberger (b), K. Pelz (b),  
M. Prehm (b), U. Baumeister (b),  
H. Hahn (c), H. Lang (b),  
G.A. Gehring (a), C.H.M. Weber (a)  
and J.K. Hobbs (a), *Science* **331**,  
1302 (2011).  
(a) University of Sheffield, Sheffield  
(U.K.)  
(b) Martin-Luther-University Halle-  
Wittenberg, Halle (Germany)  
(c) TU Chemnitz, Chemnitz  
(Germany)

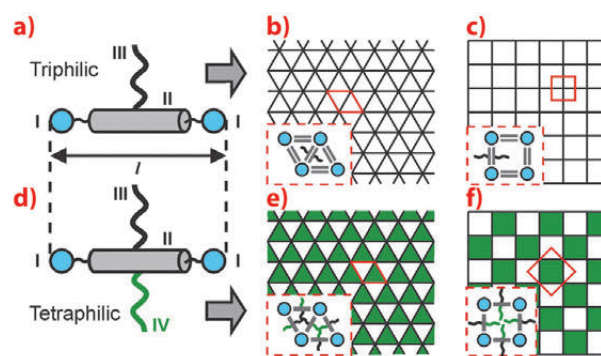


**Fig. 52:** b,c) Schematics of “single-colour” liquid crystal honeycombs formed by T-shaped “triphilic” molecules (a). e,f) “Two-colour” honeycombs formed by X-shaped “tetraphiles” (d).

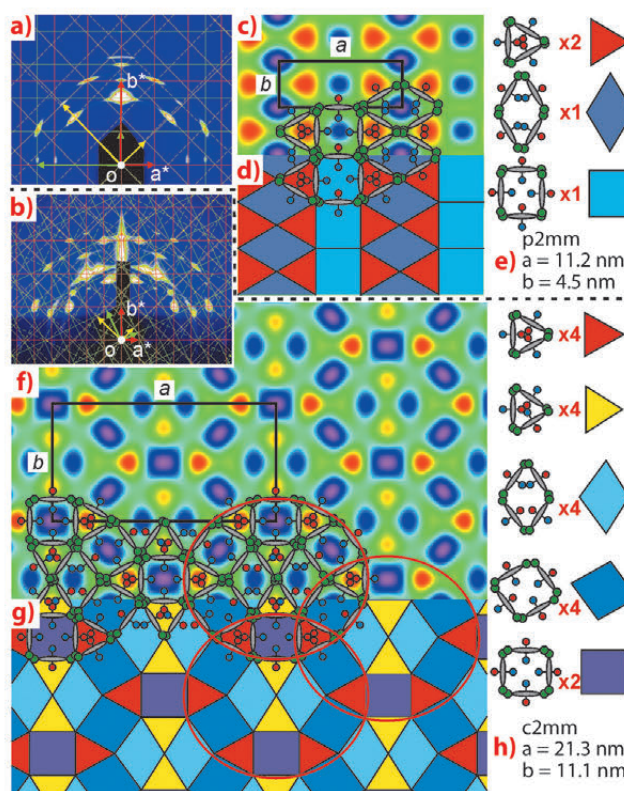


**Fig. 53:** a,b) GISAXS patterns of a thin film of an X-shaped liquid crystal compound in the low- and high-temperature phases. c,f) Corresponding electron density maps (purple high, red low), with schematic molecules partly superposed (red and green side-groups are carbosilane and perfluoroalkyl chains). d,g) Representation of the honeycombs as tilings. e,h) Tile types constituting the two phases and their number in a unit cell.



### References

- [1] G. Ungar, C. Tschierske, V. Abetz, R. Holyst, M. A. Bates, F. Liu, M. Prehm, R. Kieffer, X.B. Zeng, M. Walker, B. Glettner and A. Zywockinski, *Adv. Funct. Mater.* **21**, 1296 (2011).  
 [2] B. Glettner, F. Liu, X.B. Zeng, M. Prehm, U. Baumeister, M.A. Bates, M. Walker, P. Boesecke, G. Ungar and C. Tschierske, *Angew. Chem. Int. Ed.* **47**, 9063 (2008).

types of chains possible. The optimum compromise achieved by the liquid crystal in the low-temperature phase is a honeycomb composed of pure carbosilane triangles (red, **Figure 53e**), pure fluoroalkyl rhombuses (dark blue), and squares in which the two chains are mixed (light blue).

Even more complex is the high-temperature phase. This honeycomb contains eighteen channels in a unit cell. They are of five different colours (compositions) and four different shapes, shown in **Figure 53h**. These structures show the remarkable ability of liquid crystals to find the optimum solution to the problem of geometric and compositional frustration, and the overriding tendency

to form periodic structures. Even so, occasionally there may come a point when the unit cell becomes so large that the system gives up on periodicity and opts for an aperiodic solution. This still does not mean giving up on long-range order. Long-range positional order without periodicity was inconceivable until 1980s, when this year's Nobel laureate Dan Shechtman discovered quasicrystals in metal alloys. This intriguing and mind-boggling condensed state was recently also discovered in liquid crystals. The tiling pattern in **Figure 53g** shows features hinting that a "forbidden" dodecagonal quasicrystalline honeycomb may be round the corner – see the red ellipses in **Figure 53g**. Preliminary results of research in this direction are encouraging.

### Principal publications and authors

J. Cravillon (a), C.A. Schröder (a), R. Nayuk (b), J. Gummel (c), K. Huber (b) and M. Wiebcke (a), *Angew. Chem., Int. Ed.* **50**, 8067-8071 (2011).

(a) *Institut für Anorganische Chemie, Leibniz Universität Hannover (Germany)*

(b) *Department Chemie, Universität Paderborn (Germany)*

(c) *ESRF*

## Fast nucleation and growth of nanocrystals of a porous coordination polymer

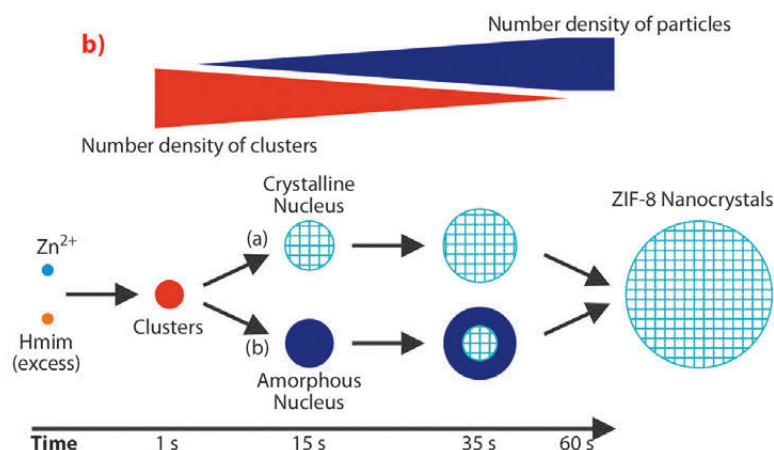
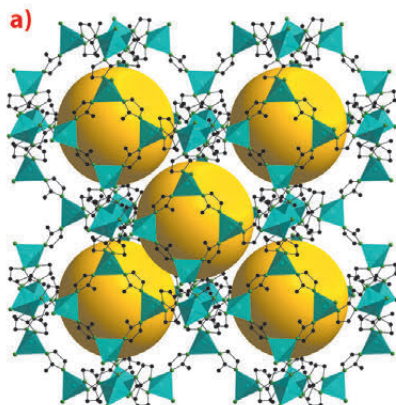
Metal-organic frameworks (MOFs) constitute a novel class of crystalline porous materials with many potential applications in gas storage, separation, catalysis and medical diagnostics. The three-dimensional frameworks of these hybrid materials are assembled from inorganic units and bridging polytopic organic ligands. A widely investigated MOF is the microporous zeolitic imidazolate framework 8 (ZIF-8). ZIF-8 consists of zinc cations and bridging 2-methylimidazolate anions (**Figure 54a**). ZIF-8 exhibits outstanding thermal and chemical stability: it can be heated up to 400°C in air and resists boiling solvents like benzene, water and dilute aqueous NaOH for periods of many hours. The

small pores of ZIF-8 enable the separation of hydrogen from larger gas molecules.

At present, the mechanisms of MOF crystallisation are only poorly understood. This significantly limits the design of new MOF compounds as well as the control of the size and morphology of MOF particles. ZIF-8 nanocrystals with a narrow size distribution can be prepared rapidly by simply combining methanol solutions of zinc salt and organic ligand at room temperature. Monitoring the process *in situ* by time-resolved static light scattering (SLS) revealed nanoparticles with a size of approximately 45 nm at 130 seconds after the start of the reaction [1]. Unfortunately, the very early events

**Fig. 54:** a) ZIF-8 framework structure; the big yellow balls represent large cavities which are connected by small pores that are defined by rings of six zinc-centred tetrahedra and bridging 2-methylimidazolate ligands (free pore diameter approximately 0.34 nm).

b) Species occurring during nucleation and growth of ZIF-8 nanocrystals; two possible alternative crystallisation pathways (a) and (b) are considered.







occurring before 130 seconds could not be followed by SLS. It is this initial phase, which now became accessible by combined *in situ* SAXS/WAXS experiments at beamline ID02 with a time resolution of 1 second. A stopped-flow device available at ID02 was used to rapidly mix the two component solutions and thus defined the onset of the fast reaction as precisely as possible. The diagram in Figure 54b presents the various species detected by SAXS/WAXS and possible alternative crystallisation pathways.

The SAXS patterns (Figure 55a) reveal that small nanoparticles with a diameter of approximately 2 nm (denoted clusters) were present already after 1 second (first measurement), while larger ZIF-8 particles started to form after 15 seconds and had grown to a size of approximately 25 nm at 800 seconds. The SAXS intensities corresponding to the clusters and particles are inversely correlated (Figure 55b) suggesting that the clusters were involved in the particle formation processes. Quantitative SAXS data evaluation indicated that the clusters took part also in particle nucleation. The particles grew by a monomer addition mechanism with the clusters and/or smaller units acting as the monomers but not by coalescence. Bragg peaks are first seen in the WAXS patterns after 35 seconds (Figure 55c) that is 7 seconds after the emergence of the first particles. This may be taken as an indication that the very first ZIF-8 particles were amorphous, and that crystalline order developed later by internal structural rearrangement (pathway b in Figure 54b). A plot of the extent of crystallisation as a function of time (Figure 55d) shows that the fast crystallisation process slowed down after approximately 300 seconds and was followed by a slower process, which most likely is Ostwald ripening.

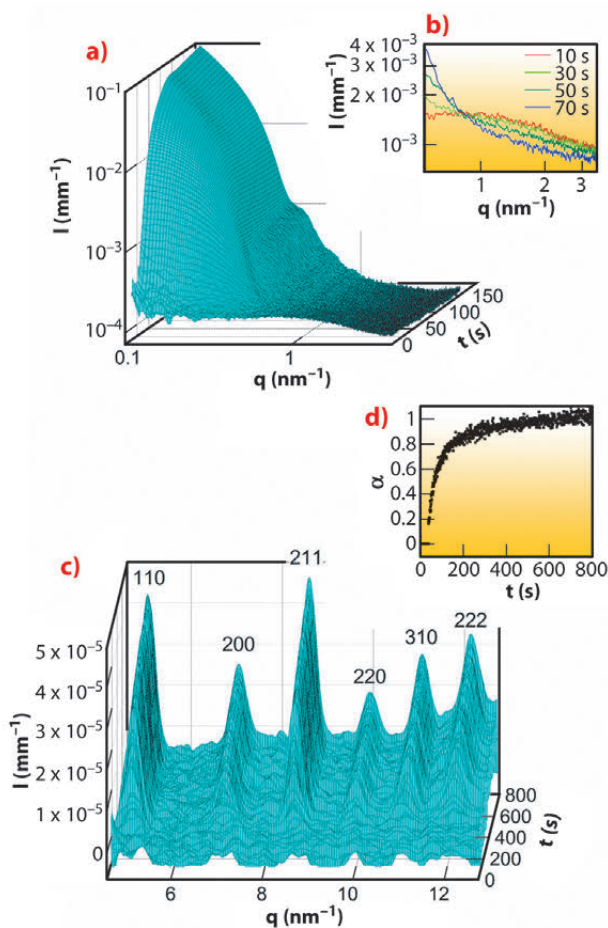


**Fig. 55:** a) SAXS patterns for the first 150 seconds. b) High- $q$  region of selected SAXS patterns originating from the small clusters of approximately 2 nm; the time at which each pattern was measured is indicated. c) WAXS patterns between 1 and 800 seconds; all Bragg reflection belong to the cubic body-centred lattice of ZIF-8. d) Extent of crystallisation ( $\alpha$ ) as a function of time ( $t$ ).

The SAXS/WAXS experiments enabled direct observation of MOF nucleation and early growth in homogeneous solution for the first time. The ZIF-8 nanocrystal formation observed does not follow classical nucleation theory and exhibits similarities with the crystallisation processes of some high-silica zeolites from clear solutions. A number of questions remain to be answered concerning, for example, the chemical composition and structure of the clusters and the detailed mechanism by which the clusters contribute to nucleation and/or growth of the ZIF-8 particles.

#### References

- [1] J. Cravillon, R. Nayuk, S. Springer, A. Feldhoff, K. Huber and M. Wiebcke, *Chem. Mater.* **23**, 2130-2141 (2011).

## ■ Promiscuous particles caught in the act

Colloidal nanocomposites are currently of great interest for both fundamental studies and practical applications. Recently, we reported a route to well-defined core-shell polymer-silica nanocomposite particles based on the physical adsorption (or heteroflocculation) of 20 nm silica nanoparticles onto relatively large sterically-stabilised poly(2-vinylpyridine)

(P2VP) latex particles in aqueous solution [1]. These hybrid organic-inorganic particles exhibit a fascinating phenomenon: addition of excess P2VP latex particles to a colloidal dispersion of P2VP-silica nanocomposite particles leads to the spontaneous redistribution of the silica nanoparticles such that partial coverage of all the latex particles

#### Principal publication and authors

J.A. Balmer (a), O.O. Mykhaylyk (a), S.P. Armes (a), J.P.A. Fairclough (a), A.J. Ryan (a), J. Gummel (b), M.W. Murray (c), K.A. Murray (c) and N.S.J. Williams (c), *J. Am. Chem. Soc.* **133**, 826-837 (2011).  
(a) Department of Chemistry, University of Sheffield (U.K.)  
(b) ESRF  
(c) AkzoNobel, Wexham Road, Slough, Berkshire (U.K.)



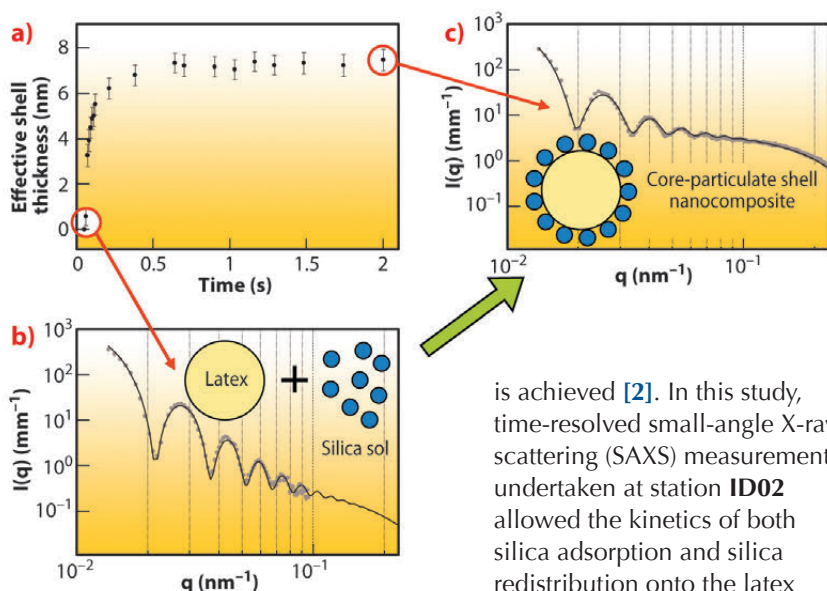


**Fig. 56:** a) Growth of silica shell thickness on the latex core obtained from time-resolved SAXS patterns of the adsorption of 20 nm silica particles onto a 461 nm sterically-stabilised P2VP latex, b) SAXS pattern (experiment - symbols and fit - solid line) corresponding to the binary mixture of latex and silica sol as injected in the stop-flow cell and c) SAXS pattern of the nanocomposite product obtained after 2 seconds.

is achieved [2]. In this study, time-resolved small-angle X-ray scattering (SAXS) measurements undertaken at station ID02 allowed the kinetics of both silica adsorption and silica redistribution onto the latex to be monitored on very short timescales.

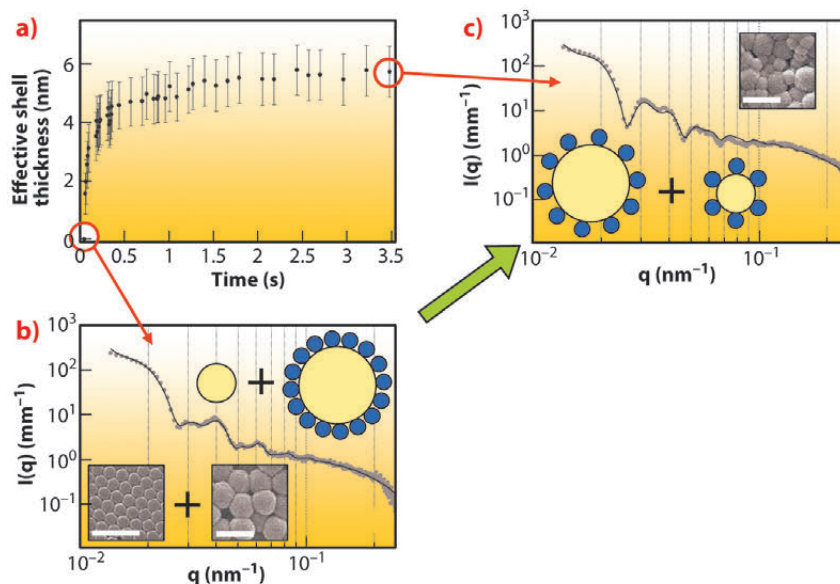
Rapid mixing of two solutions can be achieved with minimal dead time by using a stopped-flow apparatus, thus allowing the early stages of a rapid self-assembly process to be studied with millisecond time resolution. Moreover, the relatively high electron density contrast between the latex core and the silica shell makes SAXS well-suited for time-resolved measurements of the core-shell particle formation *in situ*. A stroboscopic approach was adopted to achieve a resolution of 0.01 seconds.

Time-resolved SAXS confirmed that the silica nanoparticles adsorb onto a 461 nm diameter sterically-stabilised P2VP latex to form a complete monolayer shell approximately 2.0 seconds after mixing

the latex and silica dispersions (Figure 56). The lower time limit of our experimental setup is just sufficient to observe the binary mixture of latex and silica sol before the silica particles begin to adsorb at the latex surface. The effective thickness of the growing silica shell increased rapidly, followed by a period of slower growth until equilibrium was attained after around 0.5 seconds. The shell thickness was obtained by fitting the SAXS patterns using a two-population model [3].

The redistribution of silica nanoparticles that occurs when a P2VP-silica nanocomposite (20 nm silica on a 616 nm sterically-stabilised poly(2-vinylpyridine) latex) is challenged by the addition of a 334 nm sterically-stabilised P2VP latex was also monitored by stopped-flow SAXS (see Figure 57). Here the latex diameters were deliberately chosen to be significantly different because this facilitates the data analysis (Figures 57b and 57c). Silica redistribution is essentially complete within a few seconds after mixing the nanocomposite particles with the sterically-stabilised latex (Figure 57a). There is a rapid initial increase in the

**Fig. 57:** a) Growth of the effective silica shell thickness on a 334 nm sterically-stabilised P2VP latex after mixing with P2VP-silica nanocomposite particles (prepared by the adsorption of silica onto a 616 nm sterically-stabilised P2VP latex). b) SAXS pattern (experiment - symbols and fit - solid line) corresponding to the binary mixture of the core-shell nanocomposite particles and bare latex as injected in the stop-flow cell and c) SAXS pattern of the product obtained after 3.5 seconds. The insets represent scanning electron microscopy images of the components used for heteroflocculation (b) and the resulting product (c). The white scale bar on the images corresponds to 1000 nm.





effective shell thickness, followed by a period of slower growth until equilibrium is attained after around 2.0 s. The effective thickness of the growing shell was obtained by fitting the SAXS patterns using a three-population model (the additional third population accounts for the second population of smaller core-shell particles).

The experimental time-scales for the adsorption and redistribution of silica nanoparticles compare well with that estimated based on the Smoluchowski fast coagulation rate equation. This suggests that silica exchange is mediated by Brownian collisions. This seems reasonable

because the silica nanoparticles are only weakly adsorbed via the steric stabiliser chains, rather than in direct contact with the latex surface (thus avoiding the primary minimum of the potential energy interaction curve).

Our observations are expected to have important implications for the development of nanocomposite paints. Clearly, the performance of such coatings may be compromised if the silica nanoparticles can readily desorb from the latex binder *in situ* and re-adsorb onto the pigment and/or extender particles present in all modern paint formulations.

#### References

- [1] J.A. Balmer, S.P. Armes, P.W. Fowler, T. Tarnai, Z. Gaspar, K.A. Murray and N.S.J. Williams, *Langmuir* **25**, 5339 (2009).
- [2] J.A. Balmer, O.O. Mykhaylyk, J.P.A. Fairclough, A.J. Ryan, S.P. Armes, M.W. Murray, K.A. Murray and N.S.J. Williams, *J. Am. Chem. Soc.* **132**, 2166 (2010).
- [3] J.A. Balmer, O.O. Mykhaylyk, A. Schmid, S.P. Armes, J.P.A. Fairclough and A.J. Ryan, *Langmuir* **27**, 8075 (2011).

## ■ Exploring the chirality of twisted polymer crystals

Most of the semicrystalline polymers exhibit fascinating morphological patterns consisting of regular concentric rings overlaid on the conventional spherulitic structure, which is common to both organic and inorganic compounds (cf. **Figure 58a**). These structural features, the so-called banded spherulites, can be repeatedly formed upon the polymer crystallisation from the melt and are therefore largely independent from the initial processing conditions of the polymer film. The spatial scale pertinent to such structures is undoubtedly the largest that the semicrystalline polymers can ever form: the banded spherulites may be as big as several centimetres in diameter, whereas the height of the band is in the order of micrometres [1]. Although it is now well documented that banded spherulites are due to the formation of nonplanar polymer crystals (see **Figure 58b**), the exact reasons for the appearance of the curved crystals and the details of their microstructure are not known.

Initially, the idea that the lamella twisting results from the surface stresses was put forward in the early 1960s by Geil [1]. Later on, a qualitative model accounting for the existence of unbalanced surface stresses was introduced by Keith and Padden (KP) [2]. The positive and negative sign of the stresses generated on the surface of a twisted lamella according to the KP-model is shown by different colours in **Figure 58b**. Since the very introduction of the KP model, its experimental verification has been essentially missing. Also, the factors controlling the chirality of the crystalline lamellae, which are supposedly adopting the form of left- and right-handed helicoids or helices (see **Figure 58b**) remain unclear.

We used the micro-focus X-ray diffraction facility at beamline ID13 to explore the chirality of the crystalline lamellae of polyethylene, which can be considered as the archetypal semicrystalline polymer with an achiral backbone. In particular,

#### Principal publication and authors

M. Rosenthal (a), G. Bar (b), M. Burghammer (c) and D.A. Ivanov (a), *Angew. Chem: Int. Ed.* **50**, 8881–8885 (2011).  
(a) Institut de Sciences des Matériaux de Mulhouse, CNRS-Université de Haute Alsace, Mulhouse (France)  
(b) Analytical Technology Center, Dow Olefinverbund GmbH, Schkopau (Germany)  
(c) ESRF

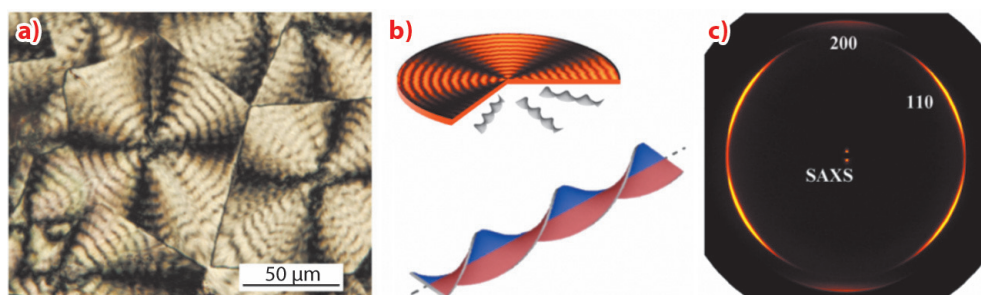
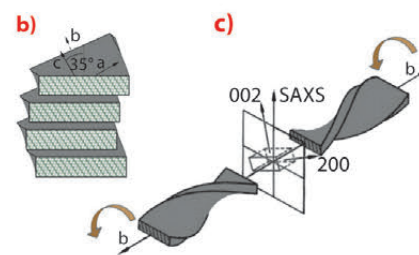
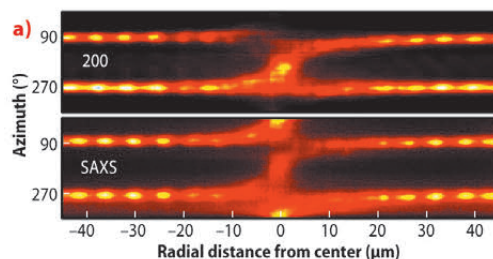


**Fig. 58:** a) Polarised optical micrograph of banded polyethylene spherulites melt-crystallised at 105°C. b) Schematic illustration of the banded spherulite structure, which is composed of lamellar helicoids growing from the spherulitic centre outwards. The origin of lamellar twist is supposed to be due to unbalanced surface stresses of positive or negative sign (indicated by red and blue colour). c) Averaged X-ray pattern recorded during a radial microfocus scan across the whole polyethylene spherulite.



**Fig. 59:** a) Azimuthal position of the meridional 200 reflection and SAXS interference maximum versus radial distance from the spherulite centre. b) Orientation of the polyethylene unit cell with respect to the lamellar basal plane. The crystalline stems are tilted by about 35° about the lamellar normal in the (010) plane perpendicular to the crystal growth direction (b axis). The chain tilt in a lamellar stack has a unique direction in space. c) Model illustrating the rotating unit cell of polyethylene. The *k*01 reflections rotate in the (010) plane. The curved arrows indicate the rotation direction of the unit cell.



we aimed to identify the added chirality parameter imparted to the polyethylene chain by the crystallisation process.

The structure of banded spherulites grown in free-standing polyethylene films was explored by performing radial scans with a microfocus X-ray beam (see **Figure 58c**). We observed that the lamellar twist occurs in a strictly regular and uniform way. The exact orientation of the polyethylene unit cell within the lamella was found from the relative shift of the SAXS signal with respect to the WAXS peaks of the crystalline lattice as displayed in **Figure 59**. The crystalline stems of polyethylene are inclined with respect to the normal to the lamellar surface by 35 degrees, which corresponds to the (201) fold plane. Importantly, the chain direction was found to be unique for the

entire stack of the polyethylene lamellae. The latter observation signifies that, on the local scale, the microstructure of bulk polyethylene is single-crystal-like.

Based on the Ewald sphere construction, we deduced that the polyethylene lamellae with both left and right handed chirality can coexist within the same spherulite. Most importantly, we have shown that the added chiral parameter is the chain tilt direction. Thus, when looking along the crystal growth direction, the lamella having the crystalline stems tilted to the right from the normal to the lamellar basal plane will form a right-handed helicoid, whereas the lamella having the stems tilted to the left will be left-handed (see **Figure 59c**). The latter finding is in agreement with the qualitative model of Keith and Padden.

#### References

- [1] P.H. Geil, *Polymer Single Crystals*, John Wiley and Sons Inc., New York (1963).  
[2] H.D. Keith and F.J. Padden, *Polymer* **25**, 29–41 (1984).

#### Principal publication and authors

- M. Sanyal (a),  
B. Schmidt-Hansberg (b,g),  
M.F.G. Klein (c), C. Munuera (a),  
A. Vorobiev (d), A. Colsmann (c),  
P. Scharfer (b), U. Lemmer (c),  
W. Schabel (b), H. Dosch (e) and  
E. Barrena (a,f), *Macromolecules*  
**44**, 3795–3800 (2011).  
(a) Max Planck Institut für  
Metallforschung, Stuttgart  
(Germany)  
(b) Institut für Thermische  
Verfahrenstechnik, Thin Film  
Technology, Karlsruhe Institute of  
Technology (Germany)  
(c) Lichttechnisches Institut,  
Karlsruhe Institute of Technology  
(Germany)  
(d) ESRF  
(e) Deutsches Elektronen-  
Synchrotron (DESY), Hamburg  
(Germany)  
(f) Institut de Ciencia de Materials  
de Barcelona, Bellaterra (Spain)  
(g) Present address: Cavendish  
Laboratory, Department of Physics,  
University of Cambridge (UK)

## ■ *In situ* observation of polymer-fullerene blend crystallisation for organic photovoltaics

Polymer solar cells are very promising as light-weight and potentially low cost devices for solar energy conversion. Most polymer solar cells are based on the bulk heterojunction device structure, in which a polymer (donor) and a fullerene-derivative (acceptor) are deposited from a common solvent. As solvent evaporates, crystallisation and phase separation take place and give rise to an interpenetrating network of donor and acceptor materials. The energy conversion efficiency depends critically on the nanomorphology that develops dynamically during solidification of the wet film. Hence, there is need to gain knowledge of the phase behaviour and crystallisation of polymer/fullerene blends as basis for a rational search of material combinations and fabrication methods.

We have developed a novel setup at **ID10B** for the real-time observation of

film crystallisation from solution. We obtained structural information by *in situ* grazing incidence X-ray scattering (GIXS) and monitored simultaneously the film thickness evolution by laser reflectometry as schematically depicted in **Figure 60a**. By this powerful approach we are able to investigate the dynamics of bulk heterojunction blend crystallisation in conjunction with the evolution of solvent fraction during film drying. We studied the well-known material combination of P3HT:PCBM dissolved in *o*-dichlorobenzene and probed the influence of parameters such as blending ratio [1] and drying conditions [2].

The GIXS real-time study presented here reveals a remarkable effect of the PCBM content in the development and evolution of P3HT ordering during blend drying. **Figure 60b** shows the time evolution of the mosaicity obtained from the (100)



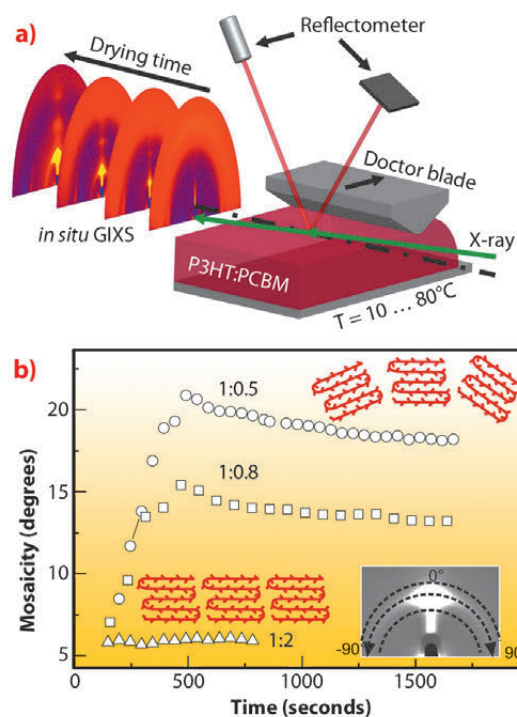
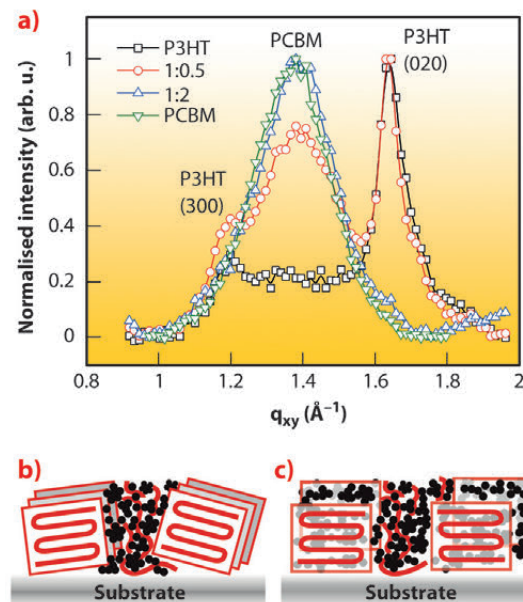


**Fig. 60:** a) Scheme of simultaneous *in situ* grazing-incidence X-ray scattering (GIXS) and optical reflectivity for film thickness monitoring of P3HT:PCBM films during solvent evaporation [1]. b) Time evolution of mosaicity for blends with P3HT:PCBM ratios 1:0.5 (circles), 1:0.8 (rectangles) and 1:2 (triangles) obtained from the P3HT (100) peak. The inset shows the azimuthal integration of the first order Bragg peak to calculate the mosaicity.

reflection which provides information about the orientation distribution of P3HT crystallites. For the P3HT:PCBM ratios of 1:0.5 and 1:0.8, the mosaicity increases considerably during the solvent evaporation, for the blend with highest PCBM content studied here, *i.e.* a P3HT:PCBM blend ratio of 1:2, the small angular distribution of the initially nucleated P3HT crystallites remains constant during crystallisation. We suggest that disorientation provides increased hole mobility perpendicular to the substrate as required for efficient solar cells [2]. Additionally GIXS reveals that PCBM hinders the development of P3HT interlayer  $\pi$ - $\pi$  stacking for the P3HT:PCBM

**Fig. 61:** a) In-plane data obtained by GIXD using a point detector for the films. The in-plane (020) peak is related with the P3HT  $\pi$ - $\pi$ -stacking, which is suppressed by an excessive amount of PCBM for 1:2 blending ratio. The structural characteristics of the dry films are schematically shown in b) for the P3HT:PCBM blending ratio of 1:0.5 and 1:0.8 and c) for the 1:2 blending ratio.



blend with 1:2 ratio (Figure 61). The lack of  $\pi$ - $\pi$  packing is identified here a possible cause for the reported poorer power conversion efficiency for 1:2 blends.

This work increases the microscopic understanding of the structure formation during film drying influenced by the blend ratio and process conditions. This experimental strategy shows great potential for other solution-processed organic systems, such as organic light emitting diodes, organic thin film transistors or polymer membranes.

#### References

- [1] M. Sanyal, B. Schmidt-Hansberg, M.F.G. Klein, C. Munuera, A. Vorobiev, A. Colsmann, P. Scharfer, U. Lemmer, W. Schabel, H. Dosch and E. Barrena, *Macromolecules* **44**, 3795–3800 (2011).  
 [2] M. Sanyal, B. Schmidt-Hansberg, M.F.G. Klein, A. Colsmann, C. Munuera, A. Vorobiev, U. Lemmer, W. Schabel, H. Dosch and E. Barrena, *Adv. Energy Mater.* **1**, 363-367 (2011).

## Interaction with synaptic vesicles induces structural changes in a lipid monolayer

Synaptic vesicles are small, membrane-bound organelles that are found in the synaptic terminal of neurons. The fusion of synaptic vesicles (SVs) with the plasma membrane in neurons is a crucial step in the release of neurotransmitters, which are responsible for carrying signals between nerve cells. After a rise in intracellular  $\text{Ca}^{2+}$  during neuronal stimulation, vesicles fuse at discrete sites on the plasma membrane (active zones) releasing their

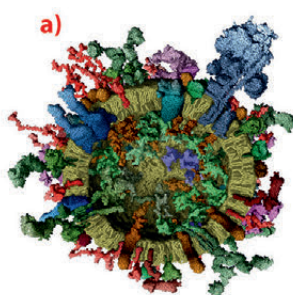
neurotransmitter content, which then passes the signal to neighbouring neurons. While many of the molecular players involved in this fusion process have been identified, a precise description of the structural mechanisms is still lacking. To this end, we have first carried out a small-angle X-ray scattering study on the structure and polydispersity of synaptic vesicles purified from rat brain. In contrast to electron microscopy, the samples can

#### Principal publications and authors

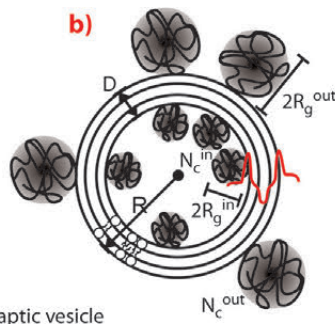
- S.K. Ghosh (a), S. Castorph (a), O. Konovalov (b), R. Jahn (c), M. Holt (c) and T. Salditt (a), *New Journal of Physics* **12**, 105004 (2010); S. Castorph (a), D. Riedel (c), L. Arleth<sup>3</sup>, M. Sztucki (b), R. Jahn (c), M. Holt (c) and T. Salditt (a), *Biophysical Journal* **98**, 1200-1208 (2010).  
 (a) Institut für Röntgenphysik, Universität Göttingen (Germany)  
 (b) ESRF  
 (c) Max-Planck Institut für biophysikalische Chemie, Göttingen (Germany)



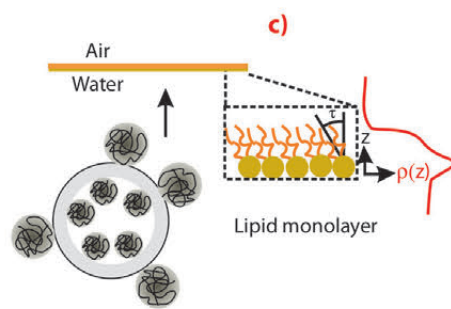
**Fig. 62:** a) Synaptic vesicle containing neurotransmitters with the densely packed layer of proteins, which control the fusion reaction, from [1]. The visualisation is based on the lipid and protein stoichiometry from biochemical analysis.



b) Structural model used to parameterise the protein layers with vesicle radius, and the protein radii of gyration and densities as free fitting parameters in the SAXS analysis. c) Schematic of the monolayer experiments probing the interaction of synaptic vesicles with the lipid film.



Synaptic vesicle



be kept in physiological buffer during the structural characterisation, carried out at beamline **ID02**. The resulting vesicle diameters, as well as the density and width of the vesicle's bilayer and the attached native protein layers as quantified by least-square fits to the SAXS curve have confirmed the standard SV model based on biochemical studies [1], see **Figure 62**.

As a next step, we have probed the interaction of SVs with lipid membranes both in the form of bilayers and monolayers, as a simple model of the pre-synaptic membrane. This  $Ca^{2+}$  dependent interaction is thought to be controlled by the vesicular protein synaptotagmin [2] in combination with the "effector" lipid phosphatidylinositol 4,5-bisphosphate ( $PIP_2$ ), a highly negatively charged lipid which resides in the plasma membrane, and acts as a calcium sensor. To test this idea by a structural method, we have carried out X-ray reflectivity and grazing incidence diffraction experiments on a monolayer of dipalmitoyl-*sn*-glycero-3-phosphatidylcholine (DPPC) with and without addition of  $PIP_2$ . Using the Langmuir trough setup at beamline

**ID10B**, we observed systematic changes in the lipid film structure at the molecular level after SV injection in the subphase. Along with the pressure increase, a small decrease in the area per lipid as well as the tilt angle (from acyl chain diffraction) in the DPPC film were induced by SV association, along with corresponding changes in the density profile. A collective reorganisation of the lipid film was thus observed, *i.e.* local binding of a SV leads to a non-local response of acyl chain tilt and film density. Importantly, the relative changes were much more pronounced in the presence of  $PIP_2$ , see **Figure 63**. Furthermore, the association was further intensified by a physiologically relevant amount of  $Ca^{2+}$  ions in the subphase of the monolayer, as revealed by the corresponding structural changes and the increase in interfacial pressure [2,3]. The results led us to conclude that the collective structural changes in the lipid induced by only 5% mol. concentration of  $PIP_2$  may well modulate vesicle fusion *in vivo*, and that collective degrees of freedom of the lipid membrane must be taken into account in addition to the specific interactions of fusion proteins.

**References**

- [1] S. Takamori *et al.*, *Cell* **127**, 831-846 (2006).
- [2] E.R. Chapman, *Annu. Rev. Biochem.* **77**, 615-641 (2008).

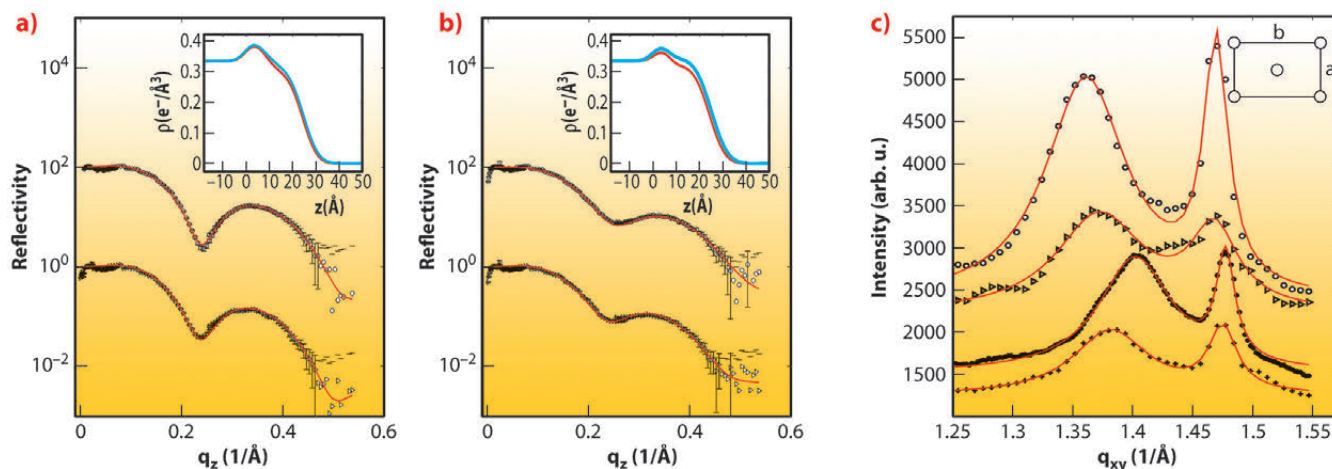


**Fig. 63:** a,b) X-ray reflectivity measurements (fits indicated by solid red line) indicate small structural changes between a) DPPC monolayer before (top) and after (bottom) injection of SVs into the subphase, but relatively large changes for b) DPPC/ $PIP_2$ , see also the corresponding electron density profiles shown in the inset. c) Grazing incidence diffraction results indicating the acyl chain ordering in the film (shifted for clarity), from top to bottom): pure DPPC monolayer, DPPC after injection of SVs, DPPC/ $PIP_2$ , and DPPC/ $PIP_2$  with SVs. The Bragg peaks are fitted by two Lorentzians (solid lines). The centred rectangular unit cell is illustrated in the inset.





## ■ Snapshots of a photosynthetic reaction centre

Nature harvests the energy content of light, the major source of energy for the biosphere, primarily via photosynthetic reaction centres. These integral membrane protein complexes are found in plants and photosynthetic bacteria and function by driving the transport of electrons across an energy transducing biological membrane in response to the absorption of a photon by a special pair of chlorophyll molecules.

Using the method of time-resolved Laue diffraction, we have successfully observed structural changes occurring in connection with the primary light driven reactions of a bacterial photosynthetic reaction centre (Figure 64). This work builds upon earlier developments at ID09B where the light driven reactions of myoglobin with bound carbon-monoxide, and photoactive yellow protein, were studied by time-resolved Laue diffraction. The new discovery described here is the first reproducible electron density changes in an integral membrane protein complex.

Figure 65 shows the difference Fourier electron density map (red: negative density; green: positive density) captured 3 milliseconds following laser photo-activation of crystals of the reaction centre. Paired positive and negative changes in electron density can be observed that are associated with a fully conserved tyrosine residue (TyrL162). This key residue plays an important functional role by bridging the special pair ( $P_{960}$ , which is photooxidised in the primary light conversion event of photosynthesis) to Heme 3 (which reduces  $P_{960}^+$ ).

These experimental observations were interpreted as due to a change in the conformation of TyrL162, which moves approximately 1.3 Å towards the special pair (Figure 65: blue: conformation photo-activated state; grey: conformation resting state) in response to light. Molecular dynamics simulations and free energy calculations suggested that this motion arises because Tyr162 becomes deprotonated following the primary electron transfer event of an electron away from the special pair ( $P_{960}$ ). This supports the concept of complementary electron-proton transfer reactions,

whereby the excess positive charge on  $P_{960}^+$  induces a proton transfer away from TyrL162 in a direction opposite to that of the electron transfer. This principle may find application in the future design of energy transducing systems of artificial photosynthesis.

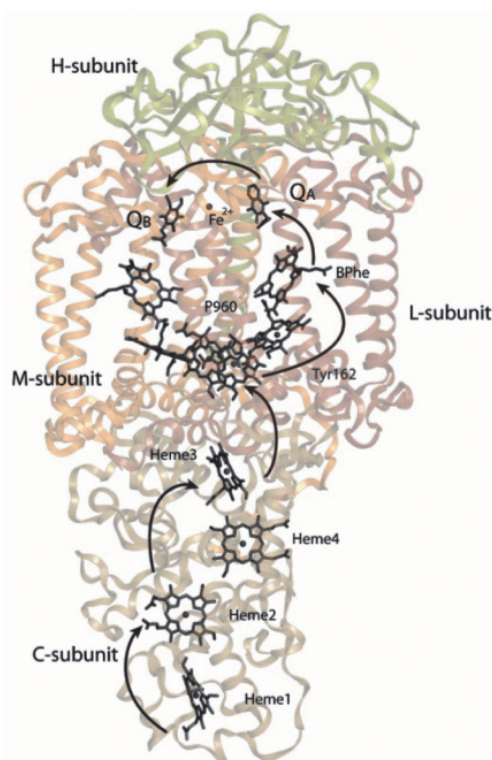
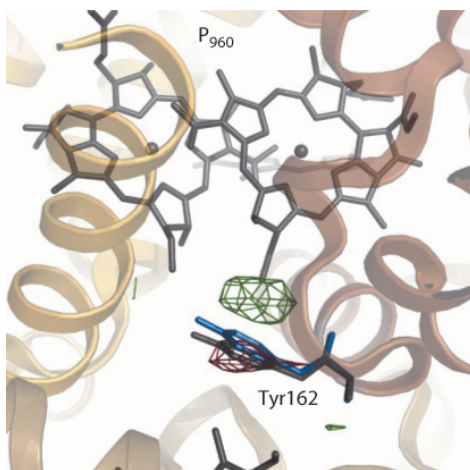


**Fig. 64:** Overview of the structure and energy transfer reactions of the bacterial photosynthetic reaction centre of *Blastochloris viridis*. Light causes electrons to move from the special pair ( $P_{960}$ ) to quinone molecules ( $Q_A$  and  $Q_B$ ) on the opposite side of the membrane.  $P_{960}^+$  is, in turn, reduced from the tetra-heme cytochrome subunit.



### Principal publication and authors

A.B. Wöhri (a,b), G. Katona (c), L.C. Johansson (c), E. Fritz (c), E. Malmerberg (c), M. Andersson (a), J. Vincent (d), M. Eklund (d), M. Cammarata (e,f), M. Wulff (e), J. Davidsson (d), G. Groenhof (g) and R. Neutze (c), *Science* **328**, 630-633 (2010).

(a) Department of Chemical and Biological Engineering, Chalmers University of Technology, Göteborg (Sweden)

(b) Present address: AstraZeneca Research and Development, Cell, Protein, and Structural Sciences, Mölndal (Sweden)

(c) Department of Chemistry, Biochemistry and Biophysics, University of Gothenburg, Göteborg (Sweden)

(d) Department of Photochemistry and Molecular Science, Uppsala University (Sweden)

(e) ESRF

(f) Present address: SLAC National Accelerator Laboratory, Menlo Park, California (USA)

(g) Computational Biomolecular Chemistry Group, Department of Theoretical and Computational Biophysics, Max Planck Institute for Biophysical Chemistry, Göttingen (Germany)

**Fig. 65:** Difference Fourier electron density changes (red: negative density; blue: positive density) captured by using time-resolved Laue diffraction. TyrL162 is observed to move 1.3 Å (grey: resting conformation; blue: photo-activated conformation) towards the special pair ( $P_{960}$ ) 3 milliseconds following photo-activation.





### Principal publication and authors

P.L. Ramachandran (a),  
J.E. Lovett (b,c), P.J. Carl (d),  
M. Cammarata (e), J.H. Lee (f),  
Y.O. Jung (f), H. Ihee (f),  
C.R. Timmel (b) and  
J.J. van Thor (g), *J. Am. Chem. Soc.*  
**133**, 9395-9404 (2011).

(a) Laboratory of Molecular  
Biophysics, University of Oxford  
(UK)

(b) Inorganic Chemistry Laboratory,  
University of Oxford (UK)

(c) EaStCHEM School of Chemistry,  
University of Edinburgh (UK)

(d) Bruker BioSpin GmbH

(Germany)

(e) ESRF

(f) Center for Time-Resolved  
Diffraction, Department of  
Chemistry, KAIST (Republic of  
Korea)

(g) Division of Molecular  
Biosciences, Imperial College  
London (UK)

## ■ Catching a short-lived photoreceptor intermediate with pulsed X-rays

Protein structural changes in photoreceptors are initiated by the absorption of light. For the photoactive yellow protein (PYP) photoreceptor, structural changes in solutions are much stronger than in the crystalline state [1,2]. We used pump-probe solution X-ray scattering as a structural probe of the photointermediate. By combining the scattering data together with short and long range information from NMR and double electron electron resonance spectroscopy (DEER) data of spin labelled PYP, we have revealed the structural changes.

Extensive investigations have addressed the structural aspects of the signalling mechanism of the PYP photoreceptor. Yet, the details of these structural rearrangements for the signalling state  $I_2'$  ( $pB_2$ ) in solution have remained unresolved. In solution,  $I_2'$  has the characteristics of a partially unfolded protein, as judged from NMR observations, the loss of secondary structure elements monitored by FTIR and CD spectroscopy, time resolved ORD spectroscopy and

altered hydrophobic dye binding and thermodynamic observables. From NMR spectroscopy of  $I_2'$  a picture of a partially disordered state has emerged [2].

We used DEER to obtain long-range distance information between selected sites within the protein (including the N-terminal domain) both in the ground and photointermediate  $I_2'$  states. Measurement of distance distributions for doubly spin-labelled photoreceptor constructs suggests that the signalling state is well ordered and show that inter-spin-label distances change reversibly by up to 19 Å upon illumination.

Next, we performed pump-probe TR-SAXS/WAXS measurements at beamline ID09B to probe the  $I_2'$  intermediate. The SAXS/WAXS difference signal for the signalling state, with a 10-ms delay between the optical pump and the X-ray probe, indicates the transient formation of an ordered and rearranged conformation, which has an increased radius of gyration, an increased maximum dimension and a reduced excluded volume. Dynamical annealing calculations using the DEER derived long-range distance restraints in combination with short-range distance information from  $^1\text{H}$ - $^{15}\text{N}$  HSQC perturbation spectroscopy give strong indication for a rearrangement that places part of the N-terminal domain in contact with the exposed chromophore binding cleft while the terminal residues extend away from the core (Figure 66). Time-resolved global structural information from pump-probe TR-SAXS/WAXS data supports this conformation and allows subsequent structural refinement that includes the combined energy terms from DEER, NMR and SAXS/WAXS (Figure 67). The resulting ensemble simultaneously satisfies all restraints and the inclusion of TR-SAXS/WAXS effectively reduces the uncertainty arising from the possible spin label orientations. The observations are essentially compatible with reduced folding of the  $I_2'$  state that is widely reported. However, from direct transformations of both the TR-SAXS/WAXS data as well as the DEER data, there is indication that the intermediate is well ordered, comparable to the ground state.

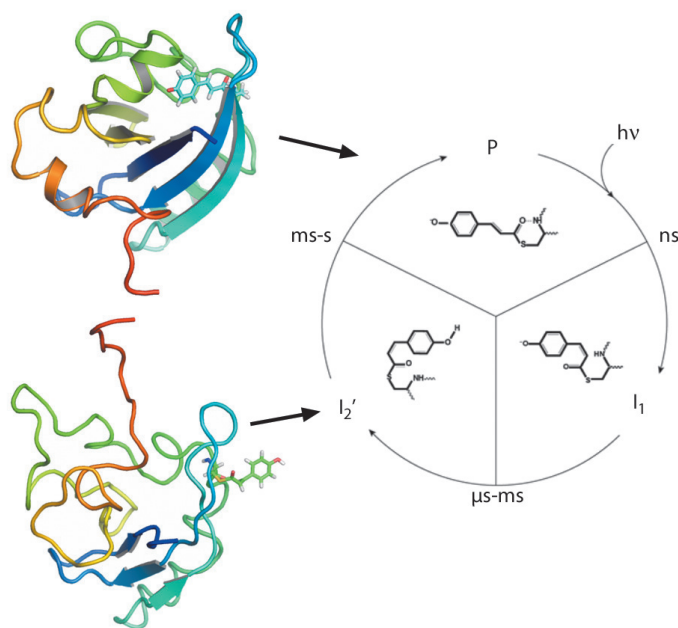


**Fig. 66:** The photocycle of the photoactive yellow protein is triggered by blue light excitation ( $\lambda_{\text{max}} = 446 \text{ nm}$ ), which initiates photoisomerisation of the p-coumaric acid chromophore. Subsequent proton transfer reactions and protein structural changes result in the formation of the signalling state ( $I_2'$ ). In solution, the structural changes are significant and fully reversible. Representative structures for the ground state (P) and the intermediate ( $I_2'$ ) are shown, coloured from N-terminus (red) to C-terminus (blue).

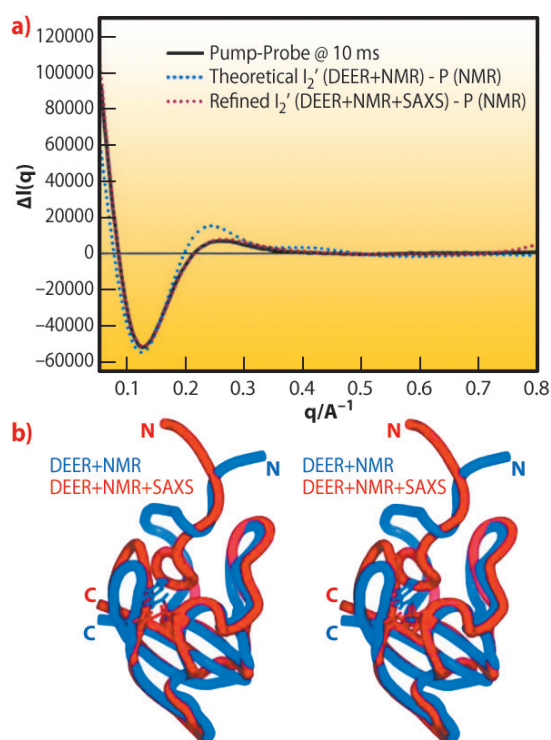


**Fig. 67:** Time-resolved pump-probe SAXS/WAXS of full length wild type PYP. Black: Experimental pump-on minus pump-off difference X-ray scattering data on PYP as a function of  $q$ . The X-ray probe pulse is applied 10 ms after the 460 nm pump pulse that probes the  $I_2'$  transient population. Blue: Theoretical difference scattering curve obtained using the DEER and NMR derived ensemble for the illuminated form minus the ground state. Red: Theoretical difference scattering curve obtained using the DEER, NMR and SAXS/WAXS derived ensemble for the illuminated form minus the ground state, after dynamical annealing calculations that included all experimental data simultaneously. The bottom panel shows a stereo image of the comparison of the average structures refined with DEER and NMR (blue) and combined DEER, SAXS/WAXS and NMR (red, PDB accession code: 2KX6) restraints simultaneously.

#### References

- [1] H. Ihee, S. Rajagopal, V. Srajer, R. Pahl, S. Anderson, M. Schmidt, F. Schotte, P.A. Anfinrud, M. Wulff and K. Moffat, *Proc Natl Acad Sci USA* **102**, 7145 (2005).
- [2] C. Bernard, K. Houben, N.M. Derix, D. Marks, M.A. van der Horst, K.J. Hellingwerf, R. Boelens, R. Kaptein and N.A. van Nuland, *Structure* **13**, 953 (2005).

To the best of our knowledge, here we show the first application that uses simultaneous structure refinement from TR-SAXS/WAXS, DEER and NMR derived restraints. Furthermore, we have applied it to the problem of transient structural change of the PYP photoreceptor.

## Simple ultrasmall peptides self-assemble into fibrous structures found in Alzheimer's and other degenerative diseases

A large number of fatal degenerative diseases including Alzheimer's exhibit fibrous amyloid aggregates as a common pathological feature. Despite decades of investigations, how pathogenic amyloid structures develop out of naturally occurring proteins remains a mystery. Structural changes of the proteins by misfolding have been identified as one of the most likely causes of amyloid formation. We have rationally designed a novel class of ultrasmall aliphatic peptides of only 3 to 7 amino acids in length that can self-assemble to typical fibrous amyloid structures, see **Figure 68** [1].

Each of these tri- to heptapeptides contains a water-soluble 'polar head' and a water-insoluble 'tail' with decreasing hydrophobicity. This specific motif enables the molecules to self-assemble spontaneously in water to form hydrogels—stiff gels held together by stable fibrous aggregates. The honeycomb-like structures of the peptide scaffolds enable them to

entrap large amounts of water. We observed a complex stepwise mechanism of aggregation involving at least three different steps. The process of self-assembly to fibres and condensed amyloid aggregates is most likely driven by unexpected  $\alpha$ -helical intermediates during the transition to cross- $\beta$  fibres. Investigations using electron microscopy, spectroscopy and X-ray microdiffraction at the **ID13** beamline confirmed these conformational changes (**Figure 69**). Interestingly, the highly-

#### Principal publication and authors

- C.A.E. Hauser (a), R. Deng (a), A. Mishra (a), Y. Loo (a), U. Khoe (a), F. Zhuang (a), D.W. Cheong (b), A. Accardo (c,d), M.B. Sullivan (b), C. Riekel (c), J.Y. Ying (a) and U.A. Hauser (a), *Proc. Natl. Acad. Sci. USA* **108**, 1361-1366 (2011).  
 (a) Institute of Bioengineering and Nanotechnology (Singapore)  
 (b) Institute of High Performance Computing (Singapore)  
 (c) ESRF  
 (d) Center of BioNanotechnology and Engineering for Medicine (BIOMEMS), University Magna Graecia of Catanzaro (Italy)  
 (e) Institute of Physics I, University of Cologne (Germany)

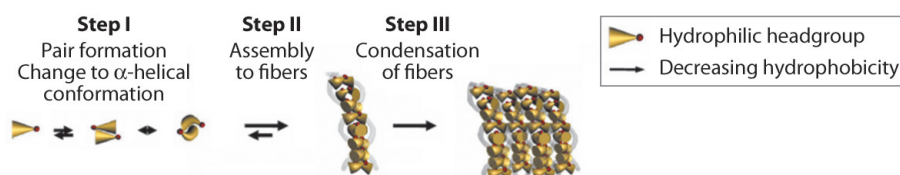


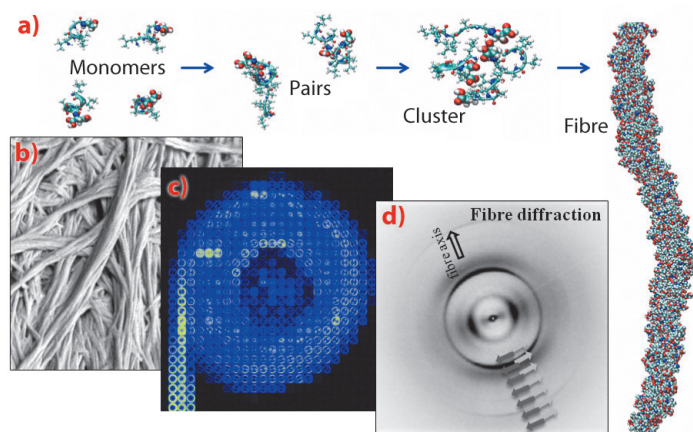
**Fig. 68:** Hypothetical self-assembly of peptide monomers into supramolecular networks of condensed fibres. Self-assembly is initiated by antiparallel pairing of two peptide monomers by changing to  $\alpha$ -helical conformation. Subsequently, peptide pairs assemble to nanostructures and fibres and condense to fibrils resulting in hydrogel formation.



### References

- [1] A. Mishra, Y. Loo, R. Deng, Y.J. Chuah, H.T. Heeb, J.Y. Ying and C.A.E. Hauser, *Nano Today* **6**, 232-239 (2011).  
 [2] A. Lakshmanan and C.A.E. Hauser, *Int. J. Mol. Sci.* **12**, 5736-5746 (2011).

**Fig. 69:** a) Molecular dynamics simulation of assembly of hexamer-peptide monomers into a fibre. b) The aggregated fibres imaged by scanning electron microscopy. c) Scanning X-ray microdiffraction image of a hydrogel solute drop dried on a superhydrophobic surface. d) Fibre diffraction pattern showing schematically the orientation of the  $\beta$ -strands.



oriented X-ray fibre diffraction pattern resembled the earlier observed pattern of natural amyloids. It was obtained with a new aggregation technique of peptide solution drops on a superhydrophobic surface, developed in collaboration with the group of E. Di Fabrizio at IIT (Genova). Molecular dynamics simulation of peptide behaviour in water revealed antiparallel pairing of monomers and stable, condensed and coiled fibres.

A particularly challenging aspect of bioengineering is the design of biomimetic materials that closely resemble and reproduce the native three-dimensional architecture and functions occurring in living species. Such a biomimetic material is in great demand for a wide range of biomedical applications such as tissue engineering, *in vivo* devices for controlled drug delivery or even biochips. Our ultrasmall peptides are designed to self-assemble into a surprisingly

wide variety of structures of nano- to supramolecular dimensions [1]. Altering the amino acid sequence of the peptides creates nanostructures, including hollow nanospheres, short, flat fibres, elongated helical fibres and spider web-like structures [2]. Although these hydrogels are soft materials, they possess surprisingly remarkable mechanical strength, far exceeding that of soft tissue in the human body, such as collagen or nucleus pulposus cells (the jelly-like material of the spinal discs). More importantly, the strength can be tuned for applications from injectable therapies to repair and replacement of damaged tissues. To offer an injectable therapy that would render invasive surgery obsolete, the peptides are currently being tested for treatment of degenerative spinal disc disease. Use of these peptide-based gels in cartilage and joint repair as well as wound healing and skin treatment is being explored.

These peptides which closely resemble natural polypeptides can serve as excellent model systems to study the onset and progression of amyloid diseases, its prevention and treatment. An ongoing study investigates ultrasmall peptide therapeutics specifically targeted at the prevention and control of amyloid formation. Furthermore, studying the self-assembly of these peptides, made of simple aliphatic amino acids believed to have existed in the 'primordial soup', could provide important clues to the origin of life and the mechanisms underlying evolution.

### Principal publication and authors

V.A. Martinez (a,b), J.H.J. Thijssen (a), F. Zontone (b), W. van Meegen (c) and G. Bryant (c), *J. Chem. Phys.* **134**, 054505 (2011).  
 (a) School of Physics and Astronomy, The University of Edinburgh (UK)  
 (b) ESRF  
 (c) Applied Physics, School of Applied Sciences, RMIT University (Australia)

## ■ Dynamics of concentrated colloidal suspensions revisited

Suspensions of colloidal particles are valuable experimental model systems for exploring phase behaviour and dynamics in condensed matter. Hard-sphere-like colloidal particles can form colloidal crystals or colloidal glasses at volume fractions above  $\phi_f = 0.494$  or  $\phi_g \sim 0.57$ , respectively, allowing the investigation of the dynamics of the freezing and glass transitions.

Colloidal particles are much bigger and slower than atoms, thus the metastable state can be studied in real-time using the

well-established technique of dynamic light scattering (DLS), or the more recently developed technique of X-ray photon correlation spectroscopy (XPCS). The fundamental quantity accessible via both DLS and XPCS is the intermediate scattering function (ISF),  $f(q, \tau)$ , which describes the dynamics (or time evolution) of particle number density, where  $q$  is the scattering vector and  $\tau$  is the delay time.

For concentrated suspensions, the dynamics are often divided into three regimes: a short-time regime, where



particles diffuse within their neighbour cages; a non-diffusive crossover regime or plateau, where the interactions between a particle and its neighbours are most clearly exposed; and a long-time diffusion regime where the particles have escaped their neighbour cages. The short- and long-time diffusion coefficients,  $D_s(q)$  and  $D_L(q)$ , are usually used to quantify these processes [1]. The long-time regime is difficult to access experimentally, and ambiguities in interpretation can arise depending on the method of data analysis.

Using DLS, Segré & Pusey [1] measured the short- and long-time diffusion coefficients of sterically-stabilised hard spheres and found that the ratio  $D_s(q)/D_L(q)$  is independent of  $q$ , exposing a scaling of the dynamics. However, Lurio *et al.* [2] did not observe this scaling when applying XPCS to charge-stabilised pseudo-hard spheres. Possible explanations for this discrepancy are: (i) there is a fundamental difference between XPCS and DLS; (ii) X-ray damage contributes to the results using XPCS; (iii) the charge-stabilised pseudo-hard sphere system is not equivalent to the steric-hard-sphere; and/or (iv) different analysis methods lead to ambiguities in interpretation.

To elucidate this discrepancy, we directly compared XPCS (at ID10A) and DLS (at RMIT) on colloidal suspensions of hard-sphere particles, thus eliminating sample preparation as a variable. We conducted analyses similar to those in [1, 2], and compared the results.

Figure 70 shows the ISFs obtained from XPCS and DLS for several volume fractions  $\phi$ . Good sample statistics are harder to obtain with XPCS but very good agreement is observed, demonstrating the equivalence of the techniques.

We also investigated the scaling of the dynamics by calculating the time-dependent quantity,  $D(q, \tau)$ , from the numerical derivative of the ISF [1]. This quantity describes the evolution from short- to long-time processes. The observation of plateaux in  $D(q, \tau)$  allows the identification of diffusive regimes at short- and long-times characterised by  $D_s(q)$  and  $D_L(q)$ .

Figure 71 shows  $D(q, \tau)/D_s(q)$ , for several scattering vectors at  $\phi = 0.531$ .

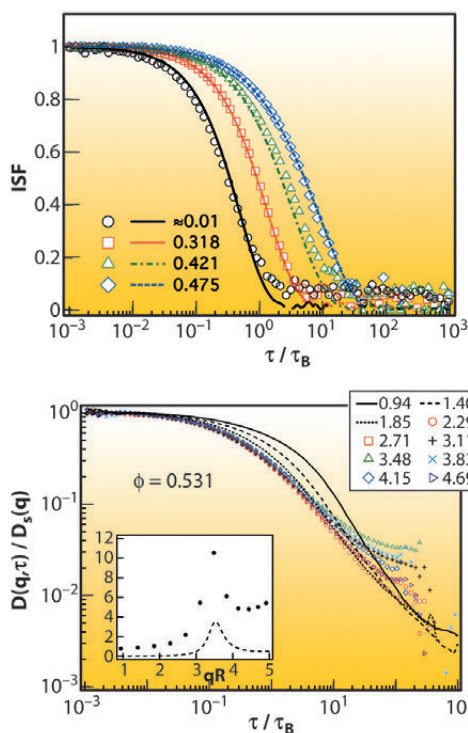


**Fig. 70:** ISF from XPCS (symbols) and DLS (lines) at  $qR = 3.48$  and  $\phi$  values indicated.  $\tau_B \sim 0.013$  s is the Brownian (diffusion) time and  $R \sim 0.190$   $\mu\text{m}$  is the particle radius.

**Fig. 71:**  $D(q, \tau)/D_s(q)$  at  $\phi = 0.531$  for the  $qR$  values indicated. Inset shows  $D_0/D_s(q)$  (symbol) and the static structure factor  $S(q)$  (line) as functions of  $qR$ .  $D_0$  is the free diffusion coefficient.

The coincidence of the curves at low delay time in Figure 71 confirms the short-time scaling behaviour found by Segré & Pusey [1]. The short-time diffusion regimes exist at all volume fractions and scattering vectors, and  $D_s(q)$  scales with the structure factor  $S(q)$  (see inset Figure 71). However in the long-time regime there is significant  $q$ -dependence, and long-time diffusive regimes are only observed near the peak of the structure factor at high volume fractions.

Thus the existence of a collective long-time diffusive regime is rather questionable. The constant ratio  $D_s(q)/D_L(q)$  observed by Segré & Pusey [1], but not by Lurio *et al.* [2], is not observed. We argue that the absence of a long-time diffusive regime is due to the fact that particles are unable to move sufficiently far for number density fluctuations, at least for scattering vectors away from the main maximum in the static structure factor, to forget packing constraint effects during accessible time scales.

As far as we are aware, this work forms the first comprehensive comparison between DLS and XPCS on concentrated colloidal samples. We found that the two techniques are equivalent, but that DLS provides better statistics. However, DLS is only possible for suspensions that are carefully refractive-index matched to minimise multiple scattering (like ours). As most concentrated suspensions have significant multiple scattering, XPCS would be the ideal choice for many samples.

#### References

- [1] P.N. Segre and P.N. Pusey, *Phys. Rev. Lett.* **77**, 771 (1996).
- [2] L.B. Lurio, *et al.*, *Phys. Rev. Lett.* **84**, 785 (2000).



## Electronic Structure and Magnetism

At the time of writing this introduction the major construction works for the ESRF upgrade are in full swing. The electrons are no longer circulating in the ring and the laboratory has become a construction site with the scientific visitors replaced by workers with hard hats. The creation of new experimental facilities and long beamlines will be possible in 2013 when the buildings are handed over to the facility. By then we will be well into phase I of the upgrade. These new facilities will be crucial to the long term success of the ESRF allowing us to carry out experiments not possible today.

As the upgrade is reaching its peak activity, we are seeing the first fruits of the programme in terms of new beamlines appearing on the floor. The XAFS beamline (BM29) has been refurbished and moved to BM23 to be next to its sister beamline ID24. We envisage new highlights coming from the better performance of the new beamline and continuing the impressive history of BM29. More importantly, ID24 has been fully upgraded with two branches and has started commissioning. It was inaugurated at the November Scientific Advisory Committee (SAC) meeting as the first Upgrade beamline. The new facility provides optimised X-rays for small and large spot activities, improved stability, and a 1000-fold increase in time resolution for single shot studies.

Within the Electronic Structure and Magnetism group the next step in upgrading the beamlines will come with the closure of the ID08 soft X-ray beamline in the second half of 2013 and the construction of the new upgrade beamline on ID32. The new beamline will extend to 120 m making full use of the new building.

Its scientific programme will centre on the use of two techniques: very high energy resolution soft X-ray resonant inelastic X-ray scattering (RIXS) and state-of-the-art soft X-ray dichroism.

However, recent budget cuts have impacted on the group beamlines and the magnetic scattering beamline ID20 has closed during the past year: this was not before producing some very interesting results on multiferroics as can be seen in these Highlights.

The challenge now is to produce new exciting proposals for a much anticipated phase II of the ESRF upgrade which will be one of the main objectives for the coming year. If a phase II were funded then it would also be an opportunity for new upgrade beamlines. These could be, for instance, in the areas covered until recently by the magnetic scattering beamline and the hard X-ray circular polarisation beamline (ID12) which have not been part of the phase I upgrade, or they could be something totally new.

The upgrade will allow us to improve our experimental facilities and offer better possibilities to our user community. This will be true for the group beamlines already being upgraded and we hope for the other beamlines in phase II. Despite the difficulties, we have to think to the future and, once they have finished the concrete work, to move forward with a scientific programme taking full advantage of the new facilities in order to strengthen our activities in the areas of magnetism and electronic structure research.

*N.B. Brookes*



**Ribbons were cut during the inauguration ceremony of ID24 to mark the opening of two new beamline branches.** Left: High-pressure/extreme conditions branch. From left to right: Francesco Sette, ESRF Director General, Sakura Pascarelli, Scientist in charge of ID24, Harald Reichert, ESRF Research Director. Right: Chemistry branch. From left to right: Michel van der Rest, vice-chairman ESRF Council, Geneviève Fioraso, Députée de l'Isère et Adjointe au Maire chargée de l'Economie, l'Emploi, l'Université, la Recherche, Rafael Abela, Chairman ESRF SAC.

Credit: C. Argoud / ESRF



## Aharonov-Bohm interferences from local deformations in graphene

Since graphene was first isolated in a controlled way, it has been an optimal playground to test the most exciting ideas in condensed matter. Its curvature and elastic deformations can be modelled by means of fictitious gauge fields as if the system were in the presence of a magnetic field [1]. These fields have become an experimental reality after the observation of strain-induced Landau levels in graphene with effective fields up to 300 T [2]. We have theoretically explored the opposite (low-field) geometrical limit, where the electronic excitations can still be described in terms of plane waves rather than Landau levels. In particular, we have discussed a realisation of the Aharonov-Bohm effect due to mechanical deformations in graphene that can be used to detect stresses at the nanometre scale.

The Aharonov-Bohm effect is one of the hallmarks of quantum physics, widely established as the textbook illustration to explain the physical content of the electromagnetic gauge fields [3]. In the context of quantum transport in meso- and nanoscopic devices, in particular, it was found that the Aharonov-Bohm effect gives rise to a peculiar magnetoresistance behaviour due to the specific way in which it touches on the phenomenon of weak localisation [4]. More recently, a scanning-tunnelling-microscopy (STM) setup has been put forward to visualise directly the Aharonov-Bohm effect through oscillations in the local density of states (LDOS) [5]. The STM is a very convenient tool for studying the properties of the 2D electron gases that form at the close-packed surfaces of noble metals such as Cu(111) or Ag(111), where the proposed Aharonov-Bohm setup can easily be implemented. The main idea is to replace the open electron paths of the standard Aharonov-Bohm interferometers by the closed loops depicted in Figure 72. Thus, in the presence of a time-reversal symmetry-breaking gauge field, electrons scattering along these loops pick up different phases depending on whether the scattering is clockwise or anticlockwise. This further affects the interference contribution to the LDOS measured by the STM tip, which eventually exhibits oscillations as a function of the magnetic flux. More

specifically, the LDOS can be written as  $N = N_0 + N_{\text{loop}} [\cos(\pi\Phi/\Phi_0) - 1]$ , where  $N_0$  is the LDOS in the absence of the gauge field,  $N_{\text{loop}}$  is its interference contribution along the loops,  $\Phi$  is the magnetic flux through the area enclosed by the loop, and  $\Phi_0$  is the flux quantum. This simple setup can be of potential use to detect space variations of the magnetic field at the nanometre scale as discussed in [5].

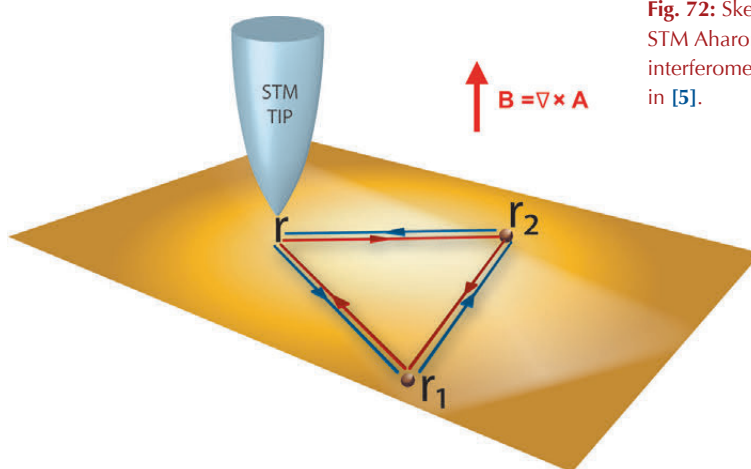


**Fig. 72:** Sketch of the STM Aharonov-Bohm interferometer proposed in [5].

In the case of graphene, electrons are described by an effective Dirac Hamiltonian that can be derived from a microscopic tight-binding model. Then, when the graphene sheet deforms, and the tight-binding parameters change accordingly, the effective Hamiltonian becomes  $H = -i\hbar v_F \sigma_i (\partial_i - iA_i)$ , where the effective gauge field  $\mathbf{A}$  traces back to the change of the electron hopping with the lattice deformations [ $\mathbf{A} = (\kappa\Phi_0/\pi)(u_{xx} - u_{yy} - 2u_{xy})$ , with  $u_{ij}$  being the strain tensor] [1]. This brings out the possibility of having Aharonov-Bohm interferences without real magnetic fluxes since, in the case of graphene, having a certain landscape of deformations is analogous of having the system in the presence of a magnetic field. The emergent gauge field  $\mathbf{A}$ , however, preserves time-reversal symmetry and therefore seems to give no net Aharonov-Bohm effect. In reality, in each of the two different Dirac points, the electrons feel an effective symmetry breaking that is restored only once the system is considered as a whole (because the coupling with the gauge field has

### Principal publication and authors

F. de Juan (a), A. Cortijo (b), M.A.H. Vozmediano (c) and A. Cano (d), *Nature Phys.* **7**, 810 (2011).

(a) Department of Physics, Indiana University, Bloomington (USA)

(b) Departamento de Física Teórica, Universidad Autónoma de Madrid (Spain)

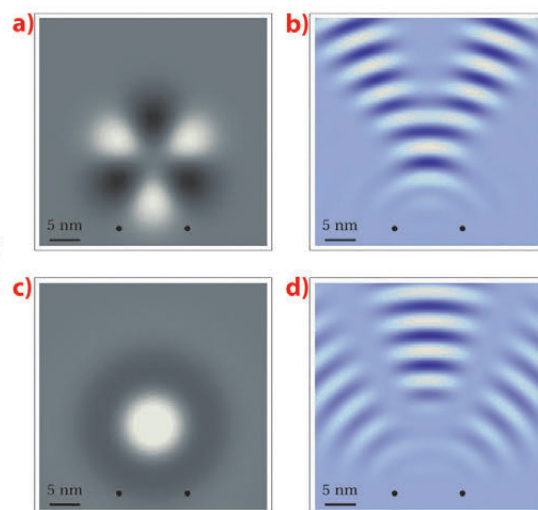
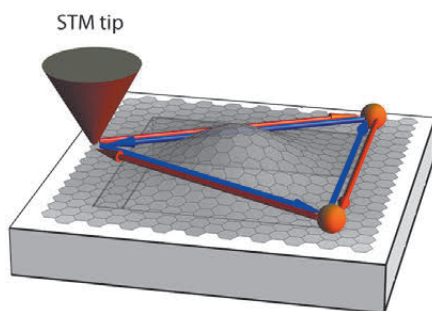
(c) Instituto de Ciencia de Materiales de Madrid (CSIC) (Spain)

(d) ESRF





**Fig. 73:** (Left panel) Proposed STM setup for measuring Aharonov-Bohm oscillations due to deformations in graphene. (Right panels) Distribution of pseudo magnetic fields generated by (a) out-of-plane Gaussian bump and (c) in-plane displacements with  $C_3$  symmetry, and corresponding patterns of Aharonov-Bohm oscillations in the LDOS (b and d respectively). The black dots indicate the position of the scatterers.



#### References

- [1] M.A.H. Vozmediano, M.I. Katsnelson and F. Guinea, *Phys. Rep.* **496**, 109-148 (2010).
- [2] N. Levy *et al.*, *Science* **329**, 544-547 (2010).
- [3] Y. Aharonov and D. Bohm, *Phys. Rev.* **115**, 485 (1959).
- [4] G. Bergmann, *Phys. Rep.* **107**, 1 (1984).
- [5] A. Cano and I. Paul, *Phys. Rev. B* **80**, 153401 (2009).

opposite signs in the two different Dirac points). As long as the two Dirac points are independent, this suffices to generate Aharonov-Bohm interferences in the LDOS as we have demonstrated in [5]. The result

is illustrated in **Figure 73**, which shows that the above STM setup can also be used to probe tiny deformations of graphene sheet by means corresponding Aharonov-Bohm oscillations.

#### Principal publication and authors

H.C. Walker (a), F. Fabrizi (a,b,c), L. Paolasini (a), F. de Bergevin (a), J. Herrero-Martin (a), A.T. Boothroyd (c), D. Prabhakaran (c) and D.F. McMorrow (b), *Science* **333**, 1273 (2011).  
 (a) ESRF  
 (b) University College London (UK)  
 (c) University of Oxford (UK)

## ■ Femtoscale magnetoelastic distortions in multiferroic $TbMnO_3$

$TbMnO_3$  is the canonical spin-cycloid multiferroic where a strong cross coupling between ferroelectric and magnetic long-range order exists, as demonstrated by the onset of ferroelectricity at a magnetic phase transition, and the magnetic field control of the ferroelectric polarisation axis [1]. Although numerous experiments have provided a comprehensive description of the magnetic structure, the driving mechanism behind the ferroelectricity has proved more elusive, with two competing theoretical scenarios: one purely electronic [2], and the other based on ionic displacements arising due to antisymmetric exchange interactions [3]. Our experiments decisively support the ionic displacement mechanism in  $TbMnO_3$ , revealing that both symmetric and antisymmetric interactions need to be included into the microscopic models; and thus our results represent an important step forward towards the goal of realising the technological potential of these materials.

A non-resonant X-ray scattering investigation of  $TbMnO_3$  under applied magnetic field has revealed the possibility of finding magnetic and charge dispersive

amplitudes of the same order of magnitude superposed at the same reflection. By analysing the interference between the magnetic and charge dispersive amplitudes, we are able to obtain detailed information regarding the nature of the displacements as a function of applied magnetic field. Our experimental setup (inset **Figure 74a**) applies an electric field along the c-axis and a magnetic field along the b-axis of the sample. The incident X-rays are converted to a circular polarisation state using a diamond crystal as a quarter-wave phase plate. The scattered X-ray polarisation state is determined by performing a complete Stokes polarimetry analysis using appropriate analyser crystals.

As shown in **Figure 74a**, it was found that the intensity of the scattering varies as a function of applied magnetic field, below the critical field for the polarisation flop transition. In particular the amplitudes of the scattering for left and right circularly polarised (LCP and RCP) incident X-rays become more equal and the minima are approaching zero, indicating that the scattering process is effectively converting

the incident circular polarisation state into a linear polarisation state.

There are no reports in the literature of a change in the magnetic structure below the transition field, and indeed the data shown in **Figure 74a** could only be fitted by including charge scattering into our calculations for the scattering cross-section. The physical origin of the charge scattering is the magnetostrictive atomic displacements due to interactions between the zero field moments and those induced by the applied magnetic field, which have the same periodicity as the magnetic ordering (**Figure 74b**).

A specific feature of these experiments is that they were performed at three different energies to enable the separation of the signals arising from the Tb and Mn ions through the changing ratio of the dispersion corrections for the atomic scattering factors. By analysing the results for two reflections  $(4, \tau, \pm 1)$  at the three energies we have established different displacement modes. One of the dominant modes responsible for the charge scattering is the Tb motion of  $19 \pm 2$  fm/T along the c-axis. It is the symmetric interaction between the Tb induced moment along b with the zero field parallel component of the Mn moment which leads to this displacement (**Figure 74c**). These displacements are in anti-phase and therefore sum to give zero net electric polarisation.

By relating the size of the induced moment along b on the Tb ions in a magnetic field,

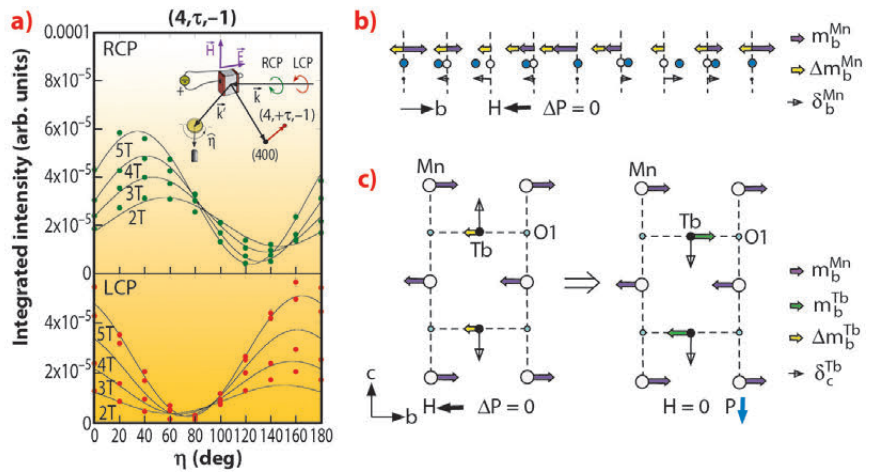


**Fig. 74:** a) Magnetic field and polarisation dependence of the interference scattering. The inset describes the experimental setup. b) Mn displacements arising due to an imbalance in neighbouring magnetisation densities resulting from the b-component of the spin cycloid and the uniform induced moment in a magnetic field. c) Magnetoelastic distortions of the Tb atoms along the c-axis due to the symmetric interaction between the Tb moment and the alternating Mn moment in an applied magnetic field and zero field, giving rise to a spontaneous ferroelectric polarisation in zero magnetic field.

with the magnitude of the b-component of the moment in zero field, we can estimate the magnitude of the zero field atomic displacements, obtaining  $21 \pm 3$  fm for the Tb displacements along c. However, in contrast to the magnetic field situation, in zero field these displacements are in phase along c (**Figure 74c**), giving an electric polarisation of  $\sim 150$   $\mu\text{C}/\text{m}^2$ . Thus we have revealed a mechanism concurrent to the Dzyaloshinskii-Moriya interaction, due to a symmetric interaction between parallel moments, which produces an electric polarisation which accounts for one quarter of that observed in bulk measurements.

#### References

- [1] T. Kimura *et al.*, *Nature* **426**, 55 (2003).
- [2] H. Katsura, N. Nagaosa and A.V. Balatsky, *Phys. Rev. Lett.* **95**, 057205 (2005).
- [3] I.A. Sergienko and E. Dagotto, *Phys. Rev. B* **73**, 094434 (2006).

## Strong coupling of Sm and Fe magnetism in SmFeAsO

The discovery of high temperature superconductivity in the fluorine doped pnictide compound  $\text{LaFeAsO}_{1-x}\text{F}_x$ , with a  $T_c = 26$  K has reinforced the idea that the electronic correlations pairing mechanism for superconductivity in iron-based pnictides is mediated by antiferromagnetic spin fluctuations. This was suggested by the discovery of a strong increase of  $T_c$  by replacing lanthanum with magnetic rare-earth (R) elements, and  $\text{SmFeAsO}_{1-x}\text{F}_x$  reached the highest superconducting transition temperature  $T_c \sim 55$  K [1].

However, conflicting experimental reports have opened an intense debate about the role of magnetic coupling between the Fe and the magnetic R ions in the enhancement of the superconducting transition temperature [2,3]. Elucidating the nature and strength of this interaction between the two magnetic sublattices in the non-superconducting parent compound is an important endeavour in understanding the interplay between magnetism and superconductivity in the RFeAsO family.



**Principal publication and authors**

S. Nandi (a), Y. Su (b), Y. Xiao (a), S. Price (a), X.F. Wang (c), X.H. Chen (c), J. Herrero-Martín (d), C. Mazzoli (d), H.C. Walker (d), L. Paolasini (d), S. Francoual (e), D.K. Shukla (e), J. Stempfer (e), T. Chatterji (f), C.M.N. Kumar (a), R. Mittal (g), H.M. Rønnow (h), C. Rüegg (i,j), D.F. McMorrow (j) and T. Brückel (a,b), *Phys. Rev. B* **84**, 054419 (2011).

(a) Jülich Centre for Neutron Science JCNS and Peter Grünberg Institut PGI, JARA-FIT, Forschungszentrum Jülich GmbH (Germany)

(b) Jülich Centre for Neutron Science JCNS-FRM II, Forschungszentrum Jülich GmbH, Outstation at FRM II (Germany)

(c) Hefei National Laboratory for Physical Science at Microscale and Department of Physics, University of Science and Technology of China (China)

(d) ESRF

(e) Deutsches Elektronen-Synchrotron DESY (Germany)

(f) ILL, Grenoble (France)

(g) Solid State Physics Division, Bhabha Atomic Research Centre (India)

(h) Laboratory for Quantum Magnetism, Ecole Polytechnique Fédérale de Lausanne (EPFL) (Switzerland)

(i) Laboratory for Neutron Scattering, Paul Scherrer Institut (Switzerland)

(j) London Centre for Nanotechnology and Department of Physics and Astronomy, University College London (UK)

**Fig. 76:** a) Temperature dependence of the (1 0 6.5) reflection measured in both resonant and nonresonant conditions near Fe K edge in polarisation channel  $\sigma$ - $\pi$ . The inset shows the change of Fe magnetic order below 5 K in  $\pi$ - $\sigma$  channel. b) Temperature dependencies of the (3 0 7.5) and (-2 0 6) reflections measured in resonant condition at the Sm  $L_2$  edge. The inset shows the Sm phase transition below 5K.

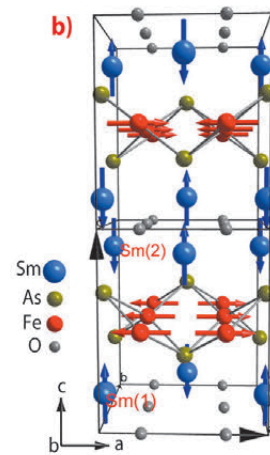
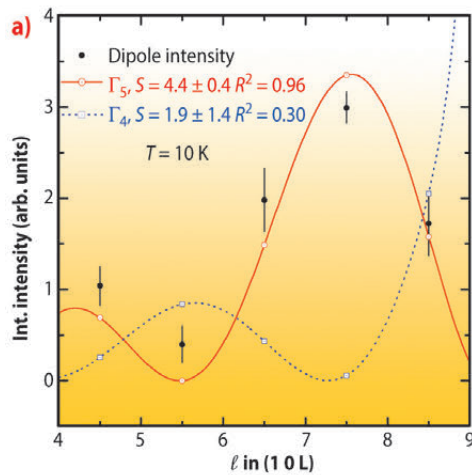
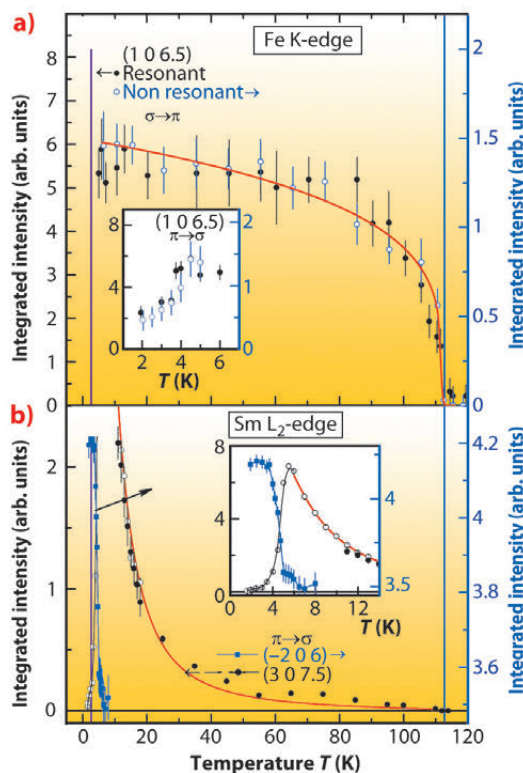


**Fig. 75:** a)  $l$  dependence of the integrated intensity at the Sm  $L_2$  edge along with the fits for the (1 0  $l/2$ ) reflections. Open symbols are the calculated intensities. Lines serve as guides to the eye. b) Proposed magnetic structure of SmFeAsO determined in the temperature range 5 K  $\leq T \leq$  110 K.

We have used element-specific X-ray resonant magnetic scattering (XRMS) and nonresonant X-ray magnetic scattering (NRXMS) to disentangle the two magnetic moment sublattice contributions in the parent compound SmFeAsO, and to investigate in detail their orientation within the unit cell. The experiments were performed at beamline ID20 for the Sm  $L_2$ ,  $L_3$  and Fe K absorption edges and at beamline P09 of PETRA III for the Fe K edge. Below  $T = 110$  K, both Sm and Fe magnetic moments order with a magnetic propagation vector (1 0 1/2), as observed by the enhancement of XRMS intensities at Sm  $L_{2,3}$  and Fe K edges, respectively. By exploiting the peculiar polarisation dependence and site

selectivity of XRMS we have determined the magnetic structure of the Sm, by collecting integrated intensities of a series of magnetic reflections measured at the Sm  $L_2$ -edge, as shown in **Figure 75a**. Similarly, the magnetic structure of Fe sublattice was determined in the temperature range 5 K  $\leq T \leq$  110 K and the final magnetic structure is shown in **Figure 75b**.

The temperature dependence of the two magnetic sublattices is represented in **Figure 76**, where the Fe shows a typical magnetisation curve and Sm follows a quite unusual behaviour, with a sharp increase of the intensity below 50 K, followed by a second magnetic phase transition at 5 K. This unusual temperature dependence of the Sm sublattice can be explained with a ground-state doublet crystal-field level, split by an exchange field, and can be modelled by taking into account only the ground-state doublet and a splitting  $[\Delta(T)]$  proportional to the effective field  $[B_{\text{eff}}(T)]$  produced by the Fe sublattice (see **Figure 76b**, red line). We obtained  $B_{\text{eff}}(T = 0) = (56.4 \pm 1.9)$  Tesla characterising the strength of interaction between the two







sublattices, which is comparable or even higher than the value for Ce-Fe interaction in CeFeAsO, indicating a strong coupling between these two sublattices. Below 5 K a magnetic phase transition arises on both the sublattices, as deduced by a drop of the Fe XRMS intensity (inset of **Figure 76a**) and the switch of the XRMS intensities at Sm  $L_2$  edge from (3 0 7.5) reflection to the charge (-2 0 6) reflection, signalling

a change in the magnetic order of Sm with the magnetic unit cell equal to the chemical unit cell.

Our finding reveals that the magnetism of Sm and Fe in the SmFeAsO compound are strongly correlated, and shed light on the currently debated importance of the R-Fe interaction in the family of iron-based superconductors.

#### References

- [1] Y. Kamihara *et al.*, *J. Am. Chem. Soc.* **130**, 3296 (2008).
- [2] H. Maeter *et al.*, *Phys. Rev. B* **80**, 094524 (2009).
- [3] W. Tian *et al.*, *Phys. Rev. B* **82**, 060514 (2010).

## ■ Observation of a zero-magnetisation ferromagnet in exchange-coupled systems

Magnetic materials possessing long range ferromagnetic order with zero magnetisation are of considerable interest for applications in spintronics devices. To date, there has been only one experimental realisation of such a ferromagnet, obtained by substituting a small amount of Sm atoms by Gd atoms in the  $\text{SmAl}_2$  intermetallic compound. The pure spin contribution from Gd atoms leads to complete cancellation of the small magnetisation resulting from antiparallel spin and orbital contributions of Sm atoms at a certain temperature  $T_{\text{comp}}$  (compensation point), while individual magnetic moments maintain a long-range ferromagnetic order [1]. Exchange-coupled systems with such an unusual ferromagnet as pinned layer may be interestingly compared to conventional ferromagnetic/antiferromagnetic exchange bias systems, with the advantage that the remaining spin ferromagnetic order enables specific studies by electronic selective techniques such as X-ray magnetic circular dichroism (XMCD). This permits important issues relating to the exchange bias phenomena

to be addressed, especially the influence of the ferromagnetic reversal on the biasing layer.

We have successfully developed the growth of  $\text{Sm}_{1-x}\text{Gd}_x\text{Al}_2$  single crystalline thin films by molecular beam epitaxy [2] and confirmed the existence of a zero-magnetisation ferromagnetic state using XMCD [3-4].

The bilayers studied in this work combine a ferromagnetic material ( $\text{SmAl}_2$ ), dominated by the Sm orbital contribution, and the unusual ferromagnet ( $\text{Sm}_{1-x}\text{Gd}_x\text{Al}_2$ ). The compensation point of the latter is about 64 K and its large coercivity inhibits the magnetisation reversal over the -7/+7 T field range below 80 K. Exchange bias phenomenon has been investigated by complementary macroscopic magnetisation and XMCD measurements.

**Figure 77** presents the hysteresis loops (SQUID) measured for  $\text{SmAl}_2/\text{Sm}_{1-x}\text{Gd}_x\text{Al}_2$  at 20 K and at 64 K ( $T_{\text{comp}}$ ). The loops are obviously shifted along the field axis, as a

#### Principal publication and authors

M. Ungureanu (a), K. Dumesnil (a), C. Dufour (a), N. Gonzalez (a), F. Wilhelm (b), A. Smekhova (b) and A. Rogalev (b), *Phys. Rev. B* **82**, 174421 (2010).

(a) Institut Jean Lamour (UMR 7198), Nancy Université, Vandoeuvre les Nancy (France)  
(b) ESRF

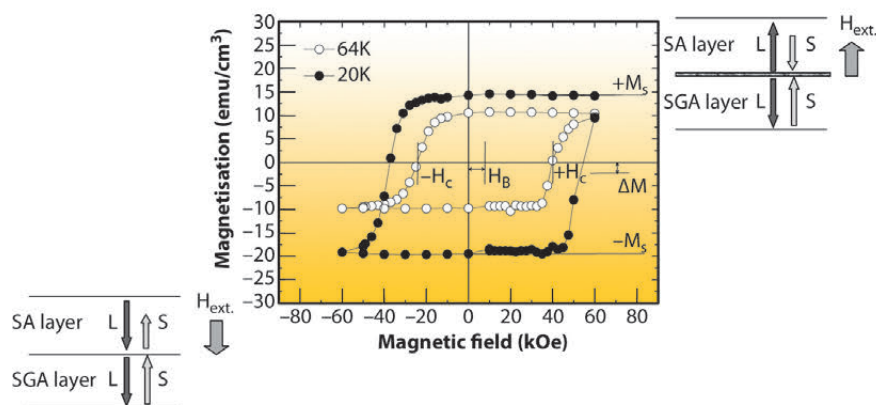


**Fig. 77:** Magnetisation measurements of  $\text{Sm}_{1-x}\text{Gd}_x\text{Al}_2/\text{SmAl}_2$  at 20 K and 64 K. The sketches present the magnetic configurations expected for large positive and negative magnetic fields.



result of the interface exchange coupling between  $\text{SmAl}_2$  and  $\text{Sm}_{1-x}\text{Gd}_x\text{Al}_2$ . The large bias field yields an interface energy of the order of  $10 \text{ erg/cm}^2$ . The positive sign of the bias field arises from opposite orientations between spin moments of both compounds at  $+7 \text{ T}$ . At  $20 \text{ K}$ , the shift of the loop along the magnetisation axis implies a pinned magnetic contribution.

XMCD experiments (beamline **ID12**) have been carried out to unravel the behaviour of the zero magnetisation ferromagnet during the  $\text{SmAl}_2$  magnetisation reversal. XMCD signals at the  $\text{Gd L}_{2,3}$  absorption edges permit to selectively probe

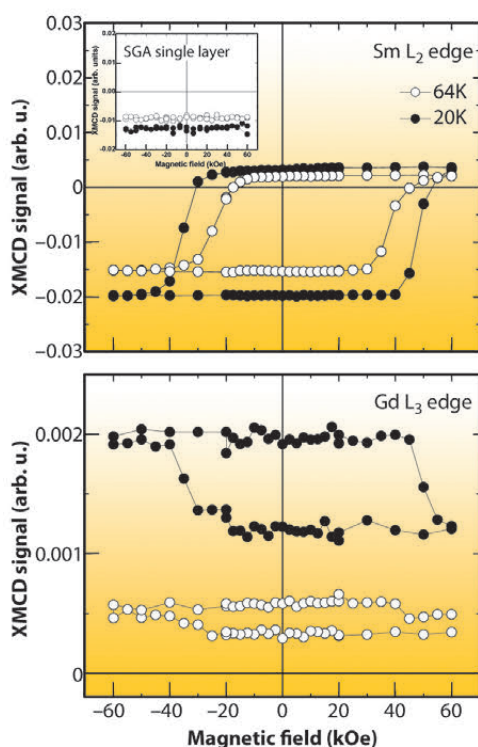
$\text{Sm}_{1-x}\text{Gd}_x\text{Al}_2$ , even in its compensated state.

Results obtained for the uncovered  $\text{Sm}_{1-x}\text{Gd}_x\text{Al}_2$  film confirmed the pinned magnetisation over the  $-7/+7 \text{ T}$  field range (inset **Figure 78**). In the bilayer, the hysteresis loops recorded at the  $\text{Sm L}_2$  edge (**Figure 78**, top) exhibit strong horizontal and vertical shifts, in agreement with magnetometry results. The specific investigation of the biasing layer (**Figure 78** bottom) reveals that a certain proportion of it rotates with field. The close coercive fields recorded at both edges confirm that  $\text{Sm}_{1-x}\text{Gd}_x\text{Al}_2$  partial reversal is driven by exchange coupling to ferromagnetic layer. This reversal also occurs at compensation, although the external field has no effect on the zero magnetisation state.

The proportion of rotatable moments in  $\text{Sm}_{1-x}\text{Gd}_x\text{Al}_2$  is approximately 20% at both temperatures, corresponding to an effective thickness of  $60 \text{ nm}$ . Given the large amount of rotatable moments compared to the wall thickness expected in this material, the scenario of an interface domain wall has been ruled out and the presence of lateral domains in  $\text{Sm}_{1-x}\text{Gd}_x\text{Al}_2$  is strongly suggested.

In summary,  $\text{SmAl}_2/\text{Sm}_{1-x}\text{Gd}_x\text{Al}_2$  bilayers are an original exchange bias system. At the compensation point, a large bias field is observed that can be tuned by the magnetic configurations in  $\text{Sm}_{1-x}\text{Gd}_x\text{Al}_2$ . XMCD experiments offer the possibility to investigate the influence of the reversal of ferromagnetic layer on the compensated biasing layer. They reveal that a significant proportion of the zero magnetisation layer is driven to reverse by exchange-coupling to the ferromagnetic layer.

**Fig. 78:** Hysteresis loops measured by XMCD for  $\text{Sm}_{1-x}\text{Gd}_x\text{Al}_2/\text{SmAl}_2$  at  $20 \text{ K}$  and  $64 \text{ K}$ , for incident photons energy tuned to the  $\text{Sm L}_2$  (top) and  $\text{Gd L}_3$  (bottom) absorption edges. The inset corresponds to XMCD at the  $\text{Sm L}_2$  edge for the  $\text{Sm}_{1-x}\text{Gd}_x\text{Al}_2$  single layer.



#### References

- [1] H. Adachi and H. Ino, *Nature* **401**, 148-150 (1999).
- [2] A. Avisou, C. Dufour, K. Dumesnil and D. Pierre, *J. of Crystal Growth* **297**, 239 (2006).
- [3] A. Avisou, K. Dumesnil and C. Dufour, *J. Mag. Mag. Mat.* **316**, 317 (2007).
- [4] A. Avisou, C. Dufour, K. Dumesnil, A. Rogalev, F. Wilhelm and E. Snoeck, *J. of Phys.: Cond. Matter.* **20**, 265001 (2008).

#### Principal publication and authors

V. Kapaklis (a), P.T. Korelis (a), B. Hjörvarsson (a), A. Vlachos (b), I. Galanakis (b), P. Pouloupoulos (b), K. Özdoğan (c), M. Angelakeris (d), F. Wilhelm (e) and A. Rogalev (e), *Physical Review B* **84**, 0244411 (2011).  
 (a) Uppsala University (Sweden)  
 (b) University of Patras (Greece)  
 (c) Yildiz Technical University (Turkey)  
 (d) Aristotle University of Thessaloniki (Greece)  
 (e) ESRF

## Violation of Hund's third rule in structurally-disordered ferromagnets

Hund's rules were formulated for atomic physics and refer to the coupling of the spin and orbital moments of atoms. These rules have also been shown to generally hold for solid magnetic materials, alloys and molecules. In the past decade a number of experimental works report on the violation of Hund's third rule,

which is observed for metallic multilayers (Fe/W) [1] and for bulk  $\text{ErCo}_2$  in a narrow temperature range [2]. Theoretical calculations have been suggesting a dependence of the observation of the break down of Hund's third rule and the structure and chemical environment.

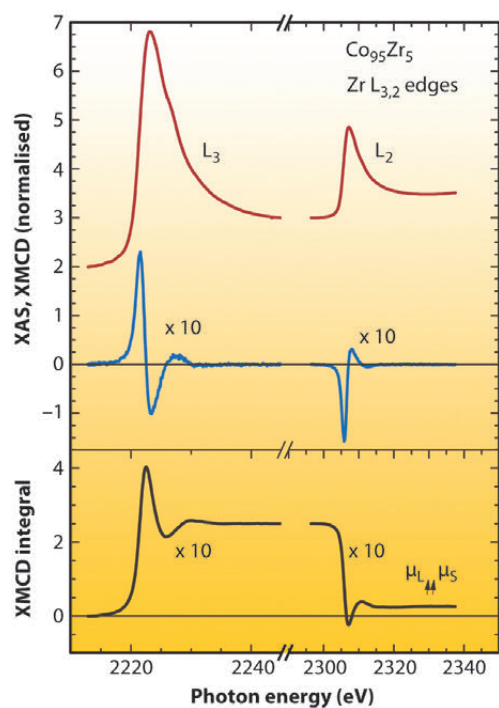


**Fig. 79:** XANES and XMCD spectra at the  $L_{2,3}$  edges of Zr in amorphous  $\text{Co}_{95}\text{Zr}_5$ . The XMCD integral in the lower part of the figure reveals a parallel alignment of the spin and orbital magnetic moment.

Amorphous materials present an interesting playground to test such ideas, as the atomic arrangement differs vastly from their crystalline counterparts. In this work, we probed the induced spin and orbital moment of Zr in amorphous Fe- and Co- based alloys with XMCD and compared them to crystalline alloys. The experimental data and a theoretical analysis prove that by altering the coordination number and bond length, a violation of Hund's third rule can be obtained.

**Figure 79** presents normalised XANES spectra of amorphous  $\text{Co}_{95}\text{Zr}_5$  for the  $L_{2,3}$  edges of Zr, at the temperature of 300 K. The data were recorded at the **ID12** beamline using the total fluorescence yield detection mode in a backscattering geometry. A clear and sizeable XMCD signal for Zr was detected, revealing an induced magnetic moment for Zr. Knowing the direction of the magnetic field and the helicity of the beam we were able to determine the alignment of the Zr moment with respect to Co or Fe. In all cases the Zr moment was aligned antiparallel to the Co or Fe magnetic moment.

Application of the sum rule analysis on the XAS and XMCD results allows the determination of the spin and orbital contributions to the magnetic moment of Zr. Only for the case of amorphous  $\text{Fe}_{91}\text{Zr}_9$  or  $\text{Co}_{95}\text{Zr}_5$ , the spin and orbital magnetic

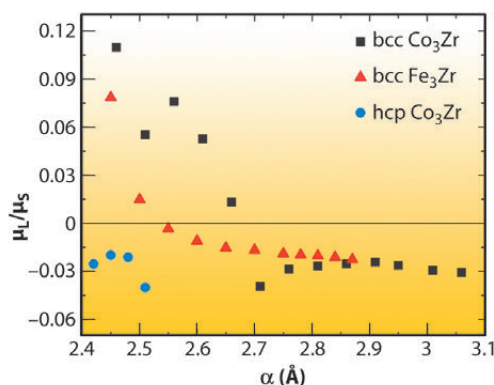


**Fig. 80:** First-principles calculation of the induced orbital and spin magnetic moment ratio for Zr, as a function of the lattice parameter and for various crystallographic structures.

moments for Zr are found to be parallel, as can also be seen in the lower part of **Figure 79**.

First-principles calculations were performed in order to elucidate this effect. The results, which are summarised in **Figure 80**, clearly indicate a sign reversal of the orbital magnetic moment occurs as the interatomic distance between Co(Fe) and Zr decreases. Recent experimental results have demonstrated the reduction of the interatomic distances between dissimilar atoms and chemical short-range order in amorphous alloys [3,4].

In summary, a violation of Hund's third rule is observed as a consequence of changes in the local atomic structure. These changes can be obtained in amorphous materials, in which both the electron and atomic structure can be adjusted through the composition of the material. Further experimental and theoretical efforts are needed to enhance our understanding of the complex and unique properties of amorphous materials.

#### References

- [1] F. Wilhelm, P. Pouloupoulos, H. Wende, A. Schertz, K. Baberschke, M. Angelakeris, N. K. Flevaris and A. Rogalev, *Phys. Rev. Lett.* **87**, 207202 (2001).
- [2] J. Herrero-Albillos, L. M. García, F. Bartolomé, A. T. Young, *Europhys. Lett.* **93**, 17006 (2011).
- [3] X. Liu, X.D. Hui, H.Y. Hou, T. Liu and G.L. Chen, *Phys. Lett. A* **372**, 3313 (2008).
- [4] A. Hirata, P. Gua, T. Fujita, Y. Hirotsu, A. Inoue, A.R. Yavari, T. Sakurai and M. Chen, *Nat. Mater.* **10**, 28 (2011).





### Principal publications and authors

R. Torchio (a,b), A. Monza (c),  
F. Baudelet (c), S. Pascarelli (a),  
O. Mathon (a), E. Pugh (d),  
D. Antonangeli (e) and  
J. Paul Itié (c), *Phys. Rev. B* **84**,  
060403(R) (2011);  
R. Torchio (a,b), Y.O. Kvashnin (a),  
S. Pascarelli (a), O. Mathon (a),  
C. Marini (a), L. Genovese (a,f),  
P. Bruno (a), G. Garbarino (a),  
A. Dewaele (g), F. Occelli (g) and  
P. Loubeyre (g), *Phys. Rev. Lett.*  
**107**, 237202 (2011).

(a) ESRF

(b) Dipartimento di Fisica,  
Università di Roma Tre (Italy)

(c) Synchrotron SOLEIL, Gif-sur-  
Yvette (France)

(d) Cavendish Laboratory,  
University of Cambridge (UK)

(e) Institut de Minéralogie et de  
Physique de Milieux Condensés,  
UMR CNRS 7590, Université Pierre  
et Marie Curie, Paris (France)

(f) Laboratoire de Simulation  
Atomistique, SP2M, UMR-E CEA /  
UJF-Grenoble 1, INAC (France)

(g) CEA, Bruyères le-Châtel,  
Arpajon (France)

## ■ Suppression of ferromagnetism in compressed 3d metals

The appearance of ferromagnetism in iron, cobalt and nickel is one of the most interesting phenomena currently under investigation in solid-state physics. In these transition metals, the magnetic properties arise from the partially filled spin-polarised 3d band which in turn is strongly related to the crystal structure and external factors such as temperature, magnetic field and pressure. The application of pressure is thus an effective way to study the complex interplay between magnetic, structural and electronic degrees of freedom. The compression of interatomic distances leads to a reduction of the density of states at the Fermi level to below the Stoner critical limit: suppression of ferromagnetism is therefore expected, as well as possible associated structural transitions.

The iron phase diagram has been widely investigated because of its geophysical interest. Upon compression, its ferromagnetic order vanishes around 16 GPa corresponding to the body centred cubic (bcc) to hexagonal close packed (hcp) structural transition. Similar investigations in the case of cobalt and nickel are far more challenging due to the higher pressures involved.

In cobalt, the ferromagnetic hcp phase is stable up to around 100-150 GPa where a structural phase transition to the face centred cubic (fcc) phase, predicted to be non-magnetic, occurs over an extended pressure range. Although estimated to

occur at 150 GPa – *i.e.* at the end of the structural transition [1] – total suppression of ferromagnetism in Co had not yet been observed.

In nickel, no structural transitions have been reported up to 150 GPa and theory predicts fcc Ni to be stable up to 34 TPa. Being structurally stable over such a large pressure range, Ni offers a unique opportunity to investigate how magnetism is affected by the simple compression of interatomic distances. Previous experiments show a weak reduction of ferromagnetism with pressure, and theory predicts Ni to be still magnetic at 300 GPa [2]. Other calculations predict a transition to a paramagnetic state to occur around 160 GPa.

K-edge X-ray magnetic circular dichroism (XMCD) is nowadays the only magnetic probe allowing measurements on a sample under pressures of Mbars, while providing simultaneous structural information through the X-ray absorption near-edge spectrum (XANES). However, while the existence of a non zero K-edge XMCD signal clearly indicates the presence of ferromagnetic order, a complete understanding of the information carried by the signal is still required.

Our new results for cobalt (**Figure 81a**) provide the first experimental evidence of the pressure-induced extinction of ferromagnetism in Co and indicate that

**Fig. 81:** K-edge XMCD data for a) cobalt and b) nickel.

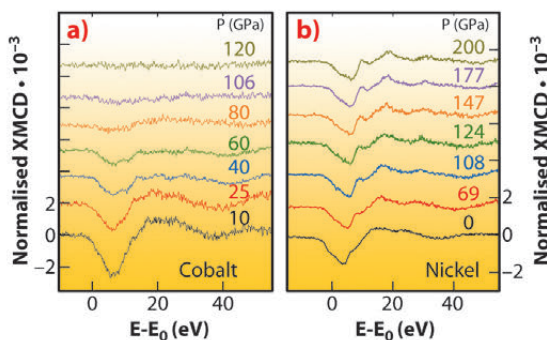
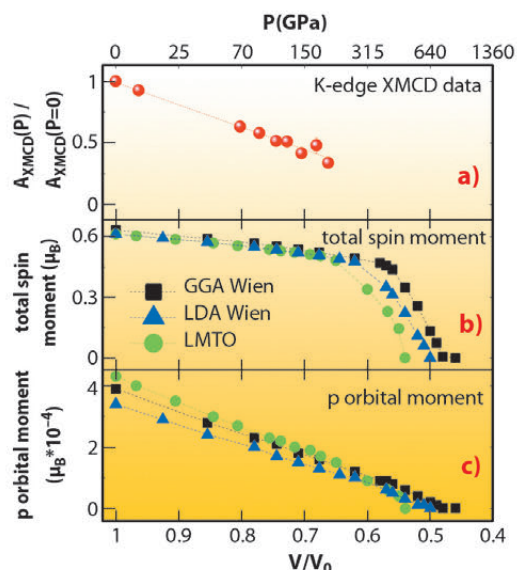


**Fig. 82:** a) Volume evolution of the XMCD integral for nickel and b,c) comparison to DFT calculations.





the magnetic response is somewhat independent of the structural transformation. The XMCD signal starts decreasing as soon as pressure is applied, whereas the onset of the hcp-fcc transition only occurs around 80 GPa. Moreover, extinction of ferromagnetism is observed around 120 GPa where simulations of the XANES spectra suggest that the structural transition is only half way through.

In the case of nickel, we find persistence of ferromagnetism at 200 GPa (Figure 81b), a record pressure for XAS, in contradiction to the prediction of a paramagnetic state.

New density functional theory (DFT) calculations (Figure 82) show that the pressure evolution of the Ni K-edge XMCD closely follows that of the  $p$  projected orbital moment and not that of the total spin magnetisation, as was previously assumed [1]. The calculations also predict that the disappearance of magnetism in Ni will not occur below 400 GPa.

These results provide an important input to the interpretation of the K-edge XMCD and add benchmarks to the 3d metals phase diagrams.

#### References

- [1] V. Iota, J.H.P. Klepeis, C.S. Yoo, J. Lang, D. Haskel and G. Srajer, *Appl. Phys. Lett.* **90**, 042505 (2007).
- [2] T. Jarlborg, *Physica C* **385**, 513 (2003).

## ■ Organising single-molecule magnets on surfaces while preserving their magnetic properties

Device miniaturisation pushes towards the single-molecule level. Single molecule magnets (SMMs) are molecules presenting a high spin ground state and a high magnetic anisotropy, therefore exhibiting slow relaxation of magnetisation which translates to the occurrence of hysteresis in the magnetisation at low temperature. The ability to retain its magnetic state is the main characteristic of a memory unit, and occurs in SMMs at the single-molecule level. A lot of effort has been dedicated over the past few years to the preparation of new SMMs, trying to push-up their blocking temperatures, with the idea that they might prove useful for data storage or spintronic applications. Before this could happen, it is imperative to check that the properties of the SMMs can be preserved when deposited on a surface.

For this reason, we carried out a detailed experimental and theoretical study of the 2D supramolecular organisation on graphite of  ${}^1\text{Pc}_2\text{Tb}$ , a well known double-decker phthalocyanine Tb(III) complex that exhibits SMM behaviour in the crystalline state.

When drop cast from a toluene solution onto highly-oriented pyrolytic graphite (HOPG),  ${}^1\text{Pc}_2\text{Tb}$  self-assembles into anisotropic two dimensional nanocrystals one molecule thick and aligned along the graphite symmetry axes, as shown by atomic force microscopy (see Figure 83). This morphology was rationalised by molecular dynamics simulations which provided excellent agreement with the experiment, showing that – after diffusion on the graphite surface – the molecules

#### Principal publication and authors

M. Gonidec (a,b), R. Biagi (c,d), V. Corradini (d), F. Moro (e), V. De Renzi (c,d), U. del Pennino (c,d), D. Summa (f), L. Muccioli (f), C. Zannoni (f), D.B. Amabilino (a) and J. Veciana (a,b), *J. Am. Chem. Soc.* **133**, 6603–6612 (2011).  
(a) Institut de Ciència de Materials de Barcelona (ICMAB-CSIC), Bellaterra (Spain)  
(b) Networking Center on Bioengineering, Biomaterials and Nanomedicine (CIBER-BBN), Bellaterra (Spain)  
(c) Dipartimento di Fisica, Università di Modena e Reggio Emilia, Modena (Italy)  
(d) S3 Istituto Nanoscienze-CNR, Modena (Italy)  
(e) School of Chemistry, University of Nottingham (UK)  
(f) Dipartimento di Chimica Fisica e Inorganica and INSTM, Università di Bologna (Italy)

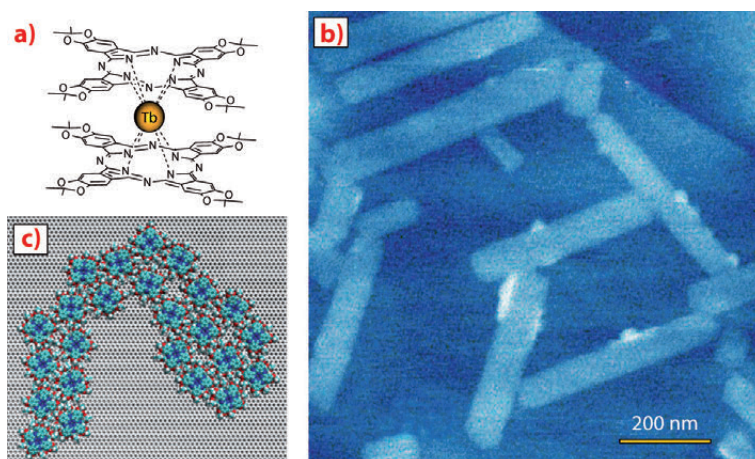


**Fig. 83:** a) Structure of the  ${}^1\text{Pc}_2\text{Tb}$  complex, b) AFM image of the rectangular 2D islands formed by drop casting  ${}^1\text{Pc}_2\text{Tb}$  on HOPG from a toluene solution, and c) self assembled 2D aggregates obtained from the MD simulations.



### References

- [1] R. Biagi, J. Fernandez-Rodriguez, M. Gonidec, A. Mirone, V. Corradini, F. Moro, V. De Renzi, U. del Pennino, J.C. Cezar, D.B. Amabilino and J. Veciana, *Phys. Rev. B* **82**, 224406 (2010).  
 [2] S.J. Gong, Z.Y. Li, Z.Q. Yang, C. Gong, C.-G. Duan and J.H. Chu, *J. Appl. Phys.* **110**, 043704 (2011).

self-assemble into nanoscopic islands which align preferentially along the three main graphite axes, and in which the molecules lie flat on the surface. These low dimension assemblies of independent magnetic centres are ideal to study the influence of the surface on the properties of those SMMs, since all of the molecules are in interaction with the graphite substrate and could therefore be perturbed by it.

Due to the very small amount of magnetic material in the sample, the detection of the magnetic properties of the self-assembled bar-shaped islands of  ${}^i\text{Pc}_2\text{Tb}$  on HOPG was not a trivial experiment, and was made possible by using beamline **ID08** to perform X-ray absorption (XAS) and

the related magnetic circular dichroism (XMCD) spectroscopy at the  $M_{4,5}$  edge of terbium at low temperature (7 K) and high magnetic field (5 T). We were able to reproduce the experimental spectra by means of multiplet calculations and validate the applicability of sum rules to the present case, which allowed us to determine the orbital and spin moments of the molecules [1]. The comparison of XAS measurements with the spectra simulation as a function of the molecule orientation led us to ascertain the adsorption geometry of the molecules. They lay flat when adsorbed on graphite, as suggested by the microscopy and molecular dynamics results. The magnetisation curves as a function of the applied magnetic field were recorded as well (Figure 84b).

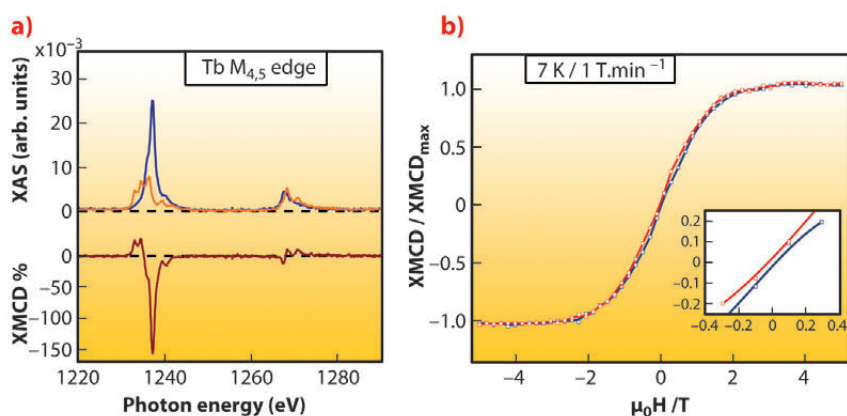


**Fig. 84:** a) Polarised XAS and resulting XMCD spectra and b) XMCD intensity hysteresis loop of the submonolayer samples of  ${}^i\text{Pc}_2\text{Tb}$  on HOPG at 7 K.

Our experiments showed that the  ${}^i\text{Pc}_2\text{Tb}$  complexes preserve their spin and orbital moments despite the interaction with the graphite substrate. Furthermore, the magnetisation hysteresis, although slightly narrower, is preserved also at  $T = 7$  K, which was not the case with different substrates. Therefore the  ${}^i\text{Pc}_2\text{Tb}$  molecules on graphite widely retain their SMM behaviour, demonstrating their potential for future applications in hybrid organic/inorganic spintronic systems when associated with suitable substrates. These results, in particular, pave the way for the use of  $\text{Pc}_2\text{Tb}$  compounds with graphene, to prepare novel spintronic devices [2].

### Principal publication and authors

F.Y. Bruno (a), J. Garcia-Barriocanal (a,b), M. Varela (c), N.M. Nemes (d), P. Thakur (e), J.C. Cezar (e), N.B. Brookes (e), A. Rivera-Calzada (a), M. Garcia-Hernandez (d), C. Leon (a), S. Okamoto (c), S.J. Pennycook (c) and J. Santamaria (a). *Phys. Rev. Lett.* **106**, 147205 (2011).  
 (a) GFMC. Dpto. Física Aplicada III, Universidad Complutense de Madrid (Spain)  
 (b) SpLine Spanish CRG Beamline at the ESRF, Grenoble (France)  
 (c) Materials Science and Technology Division, Oak Ridge National Laboratory, Oak Ridge (USA)  
 (d) Instituto de Ciencia de Materiales de Madrid ICMM- CSIC, Madrid (Spain)  
 (e) ESRF

## Spin reconstruction at $\text{La}_{0.7}\text{Sr}_{0.3}\text{MnO}_3/\text{SrTiO}_3$ interfaces

The appearance of emergent phenomena, resulting from the orbital and electronic reconstruction at the lattice discontinuity at complex oxide interfaces, is gathering much research interest. Since spin ordering is largely determined by the orbital structure in these correlated oxides with quenched orbital magnetism, the modified bonding at the interface may determine its magnetic ground state. In experiments at beamline **ID08** using X-ray magnetic circular dichroism (XMCD) we have examined the magnetic structure of  $\text{La}_{0.7}\text{Sr}_{0.3}\text{MnO}_3$  (LSMO)/ $\text{SrTiO}_3$  (STO) epitaxial interfaces in the light of its modified orbital structure. We found

a magnetic moment induced at the Ti, resulting from the orbital reconstruction, which couples magnetically to the LSMO layers when the STO layer is thin enough. This finding constitutes direct evidence on how macroscopic properties of a heterostructure may be controlled by the interface orbital and spin reconstruction.

Using a high-pressure pure oxygen sputtering technique, we have grown  $[\text{LSMO}_M/\text{STO}_N]_8$  superlattices consisting of 8 bilayers of  $M = 2, 6, 14$  LSMO unit cells (u.c.) and  $N$  STO u.c. (with  $N_{\text{STO}} = 0, 1, 2, 5, 6, 12, 18, 24$ ), on (100) STO substrates. STEM imaging



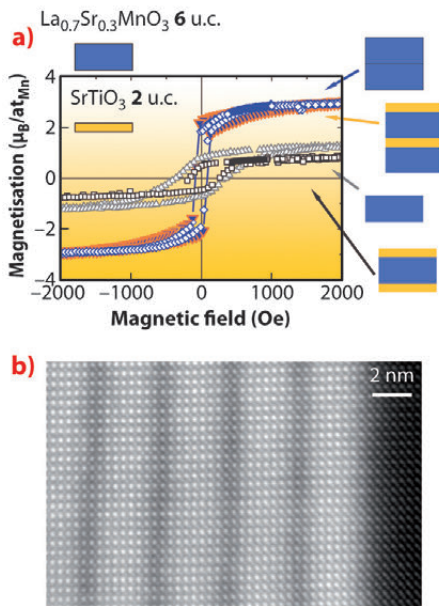


**Fig. 85:** a) VSM Hysteresis loops measured at  $T = 10\text{K}$  of a thin film of 6 u.c. (grey triangles), 12 u.c. (blue diamonds), a thin film of 6 u.c. with a buffer and a capping layer of 2 u.c. STO (black squares) and a heterostructure formed by two LSMO 6 u.c./STO 2 u.c. bilayers (inverted triangles). Schematics of the “building blocks” used to make the samples to illustrate magnetic coupling. b) High magnification Z-contrast image of a  $[\text{LSMO}_6/\text{STO}_2]_8$  superlattice from a VG Microscope HB501UX.

displayed in the bottom panel of **Figure 85** provides evidence of sharp interfaces. Atomic column resolution EELS shows the presence of  $\text{Ti}^{3+}$  at the interface plane indicating a charge transfer mechanism as previously found in LMO/STO interfaces [1]. Multilayers with thick STO ( $N > 6$ ) behave magnetically as the superposition of isolated LSMO layers showing reduced values of the saturation magnetisation and Curie temperature  $M_S = 1.5 \mu_B/\text{at}_{\text{Mn}}$  and  $T_C = 150\text{K}$  characteristic of the presence of dead layers. Whereas, heterostructures with thin STO spacers showed  $M_S = 3.2 \mu_B/\text{at}_{\text{Mn}}$  and  $T_C = 280\text{K}$  indicating that substantial magnetic coupling may exist between the layers (see top panel of **Figure 85**). This is a striking result in view of the insulating and non-magnetic nature of the STO and suggests that a significant interface reconstruction may be taking place. XMCD spectra showed clear Ti dichroic signals (see **Figure 86**) which closely tracked the Mn signal when temperature was varied evidencing that Ti moment originates at the Mn-O-Ti superexchange interaction at the interface. The negative value of the Ti moment indicates that its direction is opposite to the magnetic field, and hence that the Mn-Ti coupling is antiferromagnetic.

As a result of the lattice mismatch between STO and LSMO and the reduced electron density in LSMO compared with undoped  $\text{LaMnO}_3$ , the hybridised “down”  $d_{xz,yz}$  bonding orbitals reside lower in energy than hybridised “up”

bonding  $d_{3z^2-r^2}$  orbital. Because of charge transfer Ti is in a mixed  $3+/4+$  oxidation state at the interface, resulting in the antiferromagnetic coupling with Mn.

These electrons residing in  $d_{xz,yz}$  orbitals at the interface provide a mechanism for the magnetic coupling of the manganite layers if the STO layer is thin enough. The effect of coupling is to order the interface spins and hence to increase the saturation magnetisation and Curie temperature and to reduce the low temperature magnetoresistance. The physical mechanism of the coupling could be through direct exchange by free carriers of the STO spreading into 1-2 unit cells, suggesting that in fact the interfacial STO layer might be in a metallic ground state, consistent with the observed presence of  $\text{Ti}^{3+}$  at the interface.

In summary we have found a magnetic coupling between LSMO layers through (nominally insulating and diamagnetic) STO spacers driven by an induced magnetic moment at the Ti atoms resulting from the Mn-O-Ti superexchange interaction at the interface. This provides the channel for the magnetic interaction between LSMO layers when the STO is thinner than 1 nm resulting in the magnetic coupling of the manganite layers and a suppression of the magnetic dead layer.

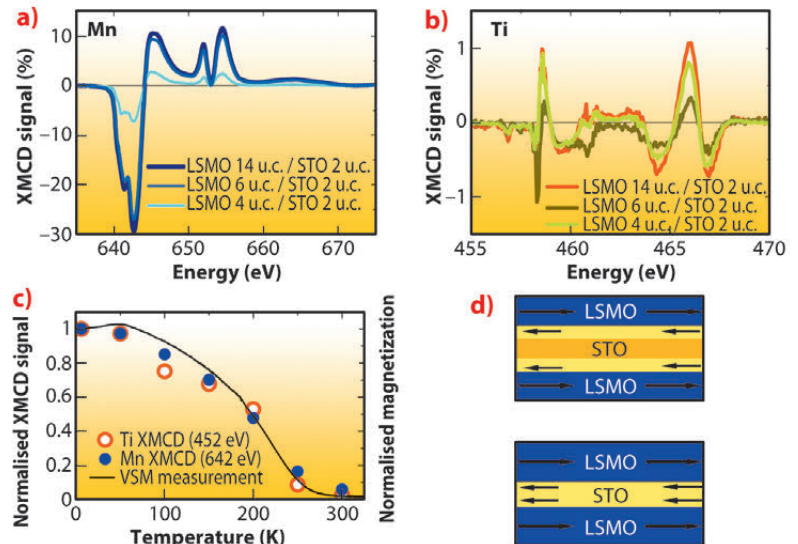


**Fig. 86:** XMCD spectra at the a) Mn and b) Ti L edge of  $[\text{LSMO}_M/\text{STO}_2]_8$  at 6 K in a 1 T magnetic field. c) Temperature dependence of Ti and Mn dichroic signals. d) Sketch illustrating the possible magnetic coupling through thin STO layers mediated by the interfacial Ti moments.

#### References

[1] J. Garcia-Barriocanal *et al.*, *Nature Comm.* **1**, 82 (2010).



### Principal publication and authors

A.F. Lee (a), C.V. Ellis (a),  
J.N. Naughton (b), M.A. Newton (c),  
C.M.A. Parlett (a) and K. Wilson (a),  
*J. Am. Chem. Soc.* **133**, 5724–5727  
(2011).

(a) Cardiff Catalysis Institute,  
School of Chemistry, Cardiff  
University (UK)

(b) Department of Physics,  
University of York, York (UK)

(c) ESRF

**Fig. 87:** a) Schematic of operando catalyst cell. b) Time-resolved, synchronous DRIFTS/EDE/MS results showing crotonaldehyde formation, and desorption, under alternating  $O_2$ /crotyl alcohol pulses over partially oxidised Pd nanocatalysts.

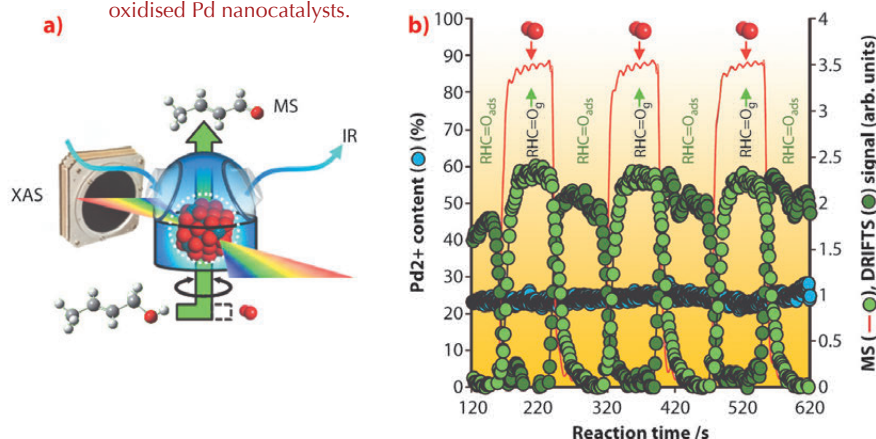
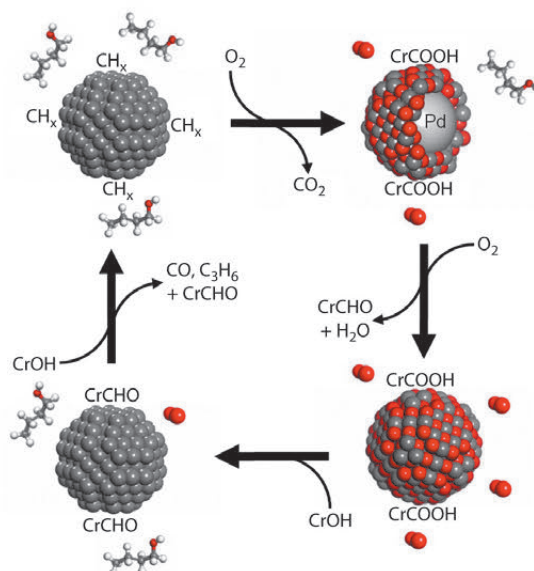


**Fig. 88:** Reaction-induced surface restructuring of Pd nanocatalysts elucidated during aerobic selective oxidation of crotyl alcohol to crotonaldehyde.



### References

- [1] C.P. Vinod, K. Wilson and A.F. Lee, *J. Chem. Technol. Biotechnol.* **86**, 161–171 (2011).  
[2] M.A. Newton, C. Belver-Coldeira, A. Martinez-Arias and M. Fernandez-Garcia, *Nat. Mater.* **6**, 528–532 (2007).

## Visualising clean catalytic technologies in action

Catalysis is a rich, multidisciplinary field with a global socio-economic impact ranging from improved air quality to the design of new HIV therapies, and creation of bulletproof fabrics. Heterogeneous catalysis is currently experiencing a global renaissance, with interest soaring in new predictive quantum chemical models and experimental synthetic and analytical methodologies able to deliver tailored catalyst formulations for diverse chemistries. However, the rational design of new heterogeneous catalysts for sustainable chemical technologies requires molecular level insight into surface chemistry, and nanoengineering approaches to achieve precise control over the structure and reactivity of

novel functional materials. Critical to this success is correct identification of the active centre participating in the catalytic cycle, and recognition that such active sites are responsive to changing reaction environments. Aerobic selective oxidation (selox) of alcohols offers an environmentally-benign synthetic route to key chemical intermediates used across the fine and agrochemical industries, notably in flavouring and fragrance preparation [1]. Despite their commercial importance, the nature of the active species within palladium catalysts used to drive these transformations has remained shrouded in mystery.

Operando techniques (wherein measurements are made under realistic reaction conditions mimicking those of practical catalytic processes) provide a powerful means to visualise catalysts in action, and derive critical mechanistic insight impossible to obtain by conventional means. We therefore utilised an experiment developed on ID24, in which dispersive EXAFS, diffuse-reflectance IR and mass spectrometry are coupled in a synchronous fashion [2], to enable time-resolved studies of vapour phase, allylic alcohol selective oxidation over Pd nanoparticles (Figure 87). By carefully pulsing either alcohol or oxygen reactants over our catalysts, we were able to simultaneously determine the palladium oxidation state, and quantify the surface and gas phase concentrations of the desired, reactively-formed aldehyde product, along with undesired secondary products such as propene, CO and  $CO_2$ . Contrary to the popular belief of the last century's published literature, our operando measurements have conclusively revealed that partially oxidised palladium surfaces, and not palladium metal, are active towards selective oxidation, with *in situ* catalyst reduction under alcohol-rich environments responsible for undesired decarbonylation and combustion chemistry (Figure 88). Such insight is helping to direct the design of next-generation, tunable nanocrystalline and nanoporous clean technologies for the aerobic selox of diverse organic molecules.



## Size influence on Pd catalysis for pollutant abatement

Pd-based three-way catalysts are a paradigmatic example of a technology for controlling pollutant emissions, specifically the removal of noxious NO<sub>x</sub> emissions and the complete oxidation of hydrocarbons and CO to CO<sub>2</sub> in gasoline engine powered vehicles. Catalyst operation under light-off or isothermal conditions has been exhaustively evaluated but in recent years the focus has shifted to more realistic, dynamic, cyclic conditions. Among the major issues targeted by early studies under cycling conditions, the key role of redox chemistry processes in controlling catalytic activity was clearly established. More recent studies have however revealed a significantly richer chemistry than may have been previously supposed. Particularly for CO elimination, there is intensive activity both at basic and applied levels that indicates that CO oxidation can involve a series of unexpected steps. For CO/NO cycling conditions, a role for a Pd carbide phase resulting from CO dissociation has been recently demonstrated [1]. Also, studies concerning the dynamics of the oscillatory catalytic behaviour upon CO/O<sub>2</sub> mixtures have triggered a debate as to whether the most active phase relates to a surface Pd oxide layer or is a metallic one dominated by chemisorbed oxygen [2]. All these studies confirm that Pd chemistry in pollutant elimination processes needs to be further clarified from a basic perspective. A basic understanding of how supported noble metal size affects the catalytic performance was thus investigated here using cycling CO/(NO+O<sub>2</sub>) conditions.

To derive a new way of seeing into the dynamic behaviour of such systems, experiments at ID24 (dispersive EXAFS) and ID15 (hard X-ray diffraction - HXRD) were carried out. Figure 89 collates XANES spectra of Pd chemical species and corresponding concentration profiles (obtained through a factorial analysis approach) during a single CO/(NO+O<sub>2</sub>) cycle at 673 K for two Pd-based three-way catalyst materials having different Pd loading (2 and 4 wt.%) on alumina and corresponding to a particle size of ca. 1.5 and 2.5-3.0 nm in the fully metallic

state. Most apparent differences are related to the presence of an intermediate Pd(I)-like species in the lower Pd loading case. In particular, these species delay the appearance of Pd(0) under the CO atmosphere with respect to the higher loaded sample. Such differential behaviour is confirmed using two additional techniques, EXAFS and HXRD (see principal publication). The combined utilisation of these X-ray techniques shows that this Pd(I) phase corresponds to a surface oxide-containing layer or patch and has a distinctive electronic structure which retains a certain metallic character obviously based in the existence of Pd-Pd contacts.

Catalytically speaking, the presence of such Pd(I) phase is rather important.

Figure 90 plots the normalised (per surface active centre as measured by XRD/EXAFS) activity for CO<sub>2</sub> production for the two Pd-based materials under study. This provides the evidence that both Pd(I) and Pd(0) species are highly active species in CO

### Principal publication and authors

I. Iglesias-Juez (a), A. Kubacka (a), M. Fernández-García (a), M. Di Michiel (b) and M.A. Newton (b), *J. Am. Chem. Soc.* **133**, 4484 (2011).  
(a) Instituto de Catálisis y Petroleoquímica, CSIC, C/Marie Curie 2, Madrid (Spain)  
(b) ESRF

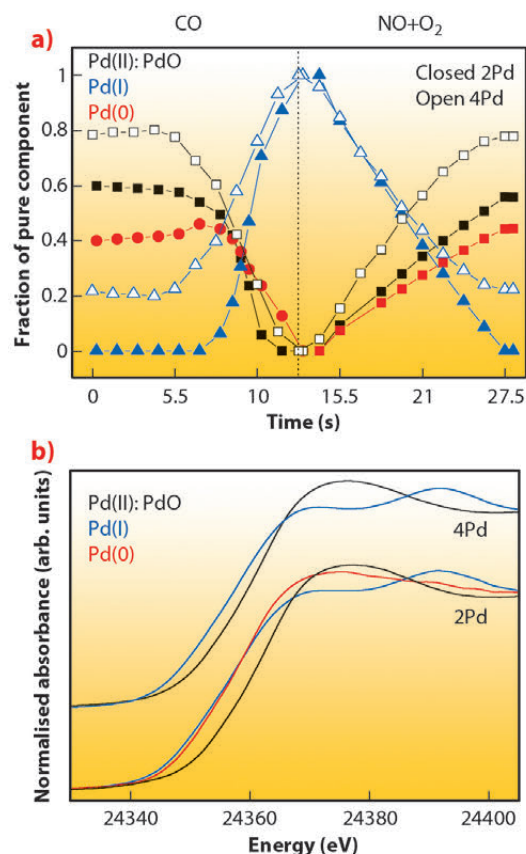


Fig. 89: XANES spectra (top) and concentration profiles (bottom) corresponding to pure chemical species present during a single CO/(NO+O<sub>2</sub>) cycling treatment at 673 K.





### References

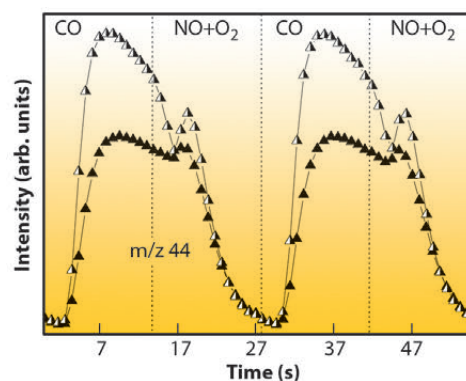
- [1] M.A. Newton, M. Di Michiel, A. Kubacka and M. Fernández-García, *J. Am. Chem. Soc.* **132**, 4540 (2010); A. Kubacka, A. Martínez-Arias, M. Fernández-García, M. Di Michiel and M.A. Newton, *J. Catal.* **270**, 275 (2010).
- [2] B.L.H. Hendriksen, M.D. Ackermann, R. van Rijn, D. Stolz, I. Popa, O. Balmes, A. Resta, D. Werneille, R. Felici, S. Ferrer and J.W.M. Frenken, *Nat. Chem.* **2**, 730 (2010); F. Gao, Y. Cai, K.K. Gath, Y. Wang, M.S. Chen, Q.L. Guo and D.W. Goodman, *J. Phys. Chem. C* **113**, 182 (2009).

elimination but the superior performance of Pd(I) is clearly established.

Summarising, the multitechnique XAS/HXRD/DRIFTS/MS analysis of Pd-Al<sub>2</sub>O<sub>3</sub> systems have revealed a series of size-dependent phenomena at Pd nanoparticles upon CO/(NO+O<sub>2</sub>) cycling conditions. The most important is that both Pd(I) and Pd(0) species can be present in Pd surface layers but this is strongly dependent on the size of the nanoparticles. Both species appear to be highly active species in CO elimination but our results suggest a higher activity for the Pd(I) species. A Pd(I) chemical nature can be thus associated to the CO elimination “active” surface Pd oxide

**Fig. 90:** Normalised mass spectrometry profile for CO<sub>2</sub> (m/z 44) production during CO/(NO+O<sub>2</sub>) cycling treatment at 673 K. Half-closed symbols: 2Pd; closed symbols; 4Pd.

layers, at least in nanoparticulate materials below ca. 2-3 nm in diameter. Above this size limit, we detected the exclusive presence of Pd(0) as active species for CO elimination at the surface of Pd nanoparticles. These results would point to the ability to tune and maintain Pd nanoparticles of a certain size as being crucial to the most efficacious oxidation of CO during catalyst operation.



### Principal publication and authors

R. Kirsch (a,b), D. Fellhauer (c), M. Altmaier (d), V. Neck (d), A. Rossberg (a), T. Fanghänel (c), L. Charlet (b) and A.C. Scheinost (a) *Environ. Sci. Technol.* **45**, 7267–7274 (2011).  
 (a) Institut für Radiochemie, Helmholtz Zentrum Dresden Rossendorf, Dresden (Germany)  
 (b) Institute des Sciences de la Terre, Université Joseph Fourier, CNRS, Grenoble (France)  
 (c) European Commission, Joint Research Center, Institute for Transuranium Elements, Karlsruhe (Germany)  
 (d) Institut für Nukleare Entsorgung, Karlsruhe Institute of Technology, Karlsruhe (Germany)

## ■ Plutonium redox chemistry on corroding steel surfaces

Nuclear waste has to be safely stored for geological time scales, even though current developments like fuel recycling and transmutation may substantially reduce the amount of waste in the future. The repository concepts of most countries utilising nuclear power foresee storage in the deep geological underground, which is commonly an anoxic environment unlike that exposed to our oxygen-rich atmosphere. Under such conditions, iron occurs predominately in its divalent oxidation state, and is able to reduce a number of radionuclides like selenium or uranium from higher to lower oxidation states, with important consequences for their chemical and migration behaviour.

Studying chemical reactions under such anoxic conditions requires the almost complete exclusion of oxygen from our oxygen-rich atmosphere down to levels of < 1 ppmv O<sub>2</sub>. While it is already a challenge to maintain such conditions from the laboratory to a public beamline for non- or low-radioactive samples, the effort required to do this safely with transuranium actinides is much

higher. Plutonium in particular is of high interest since it occurs in relatively high quantity in burnt-up nuclear fuel and its nuclides have long half-lives (up to 80 million years) and a very high radiotoxicity. In this current study, we were able to study the redox chemistry of plutonium under anoxic conditions at the surface of three Fe(II)-bearing minerals for the first time. The mineral samples are representative of (anoxically) corroding steel containers and natural (anoxic) aquifers, they were the oxide magnetite, the sulfide mackinawite, and the hydroxo-carbonate chukanovite. The nanoparticulate mineral samples were prepared under anoxic conditions at the University of Grenoble, then reacted with Pu in an anoxic glovebox designed for radionuclides at KIT, transported from Karlsruhe to Grenoble in a special LN<sub>2</sub> transport container developed by PSI, and finally measured at **BM20**, the HZDR-owned Rossendorf Beamline, where a custom-designed closed-cycle He cryostat as sample environment helped to exclude oxygen as well as to avoid photon-induced redox changes previously



observed for plutonium. The purified  $^{242}\text{Pu}$  was provided by ITU.

Using Pu-L<sub>III</sub> edge XANES, we found that the initial Pu(V) aquocomplex with transdioxo coordination symmetry was reduced by magnetite at pH 6 and 8 to Pu(III) with tricapped trigonal-prismatic (TTP) coordination symmetry (Figure 91a). A relatively long equilibration period of 40 days as well as a cross-check with initial Pu(III) aquocomplex suggests that the trivalent oxidation state is thermodynamically stable. The radial structure function presented by the Fourier transform magnitude of the Pu-L<sub>III</sub> EXAFS spectrum (Figure 91b) shows a strong symmetric peak typical for the quasi-equidistant arrangement of oxygen atoms in the TTP coordination shell of Pu(III). The smaller, asymmetric peak at about 3.25 Å (uncorrected for phase shift) is due to Pu-Fe backscattering as verified by Morlet wavelet analysis, while Pu-Pu backscattering could be excluded. To test the hypothesis of formation of an inner-sphere sorption complex at the magnetite surface, we applied a Monte-Carlo FEFF simulation method. Seven positions around a model slab of magnetite at the octahedrally terminated {111} face gave the lowest error and a very close fit of the experimental spectrum (Figure 91c,d). The matching structure is a trinuclear tridentate (with respect to surface Fe-octahedra), monomeric surface complex as shown in Figure 91e.

This is the first experimental evidence for the formation of such a trivalent Pu sorption complex. The few authors who previously studied Pu sorption reactions found formation of PuO<sub>2</sub> colloids. By using higher surface loadings, we were able to replicate these older results (Figure 92, path 3). In terms of the safety assessment of nuclear waste repositories, both Pu(III) sorption and Pu(IV) precipitation have to be taken into account. Interestingly, both processes lead to similar, low Pu solubilities (<10<sup>10</sup> M) – and both may be prone to colloidal transport under worst case scenarios.

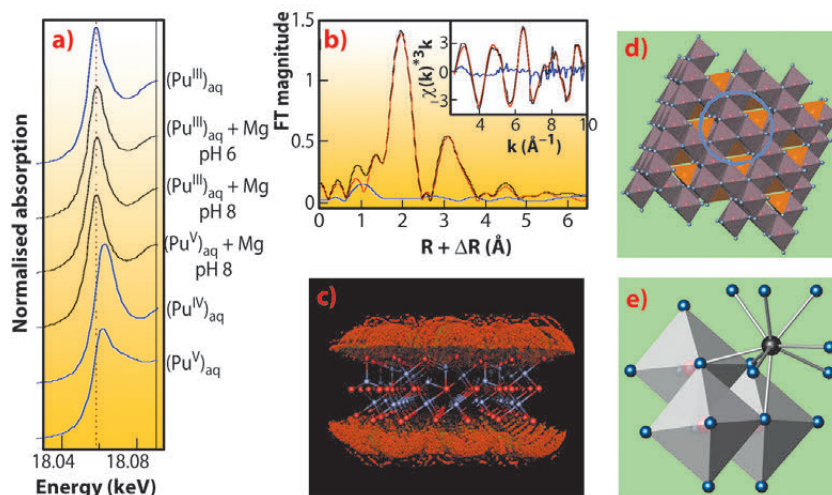
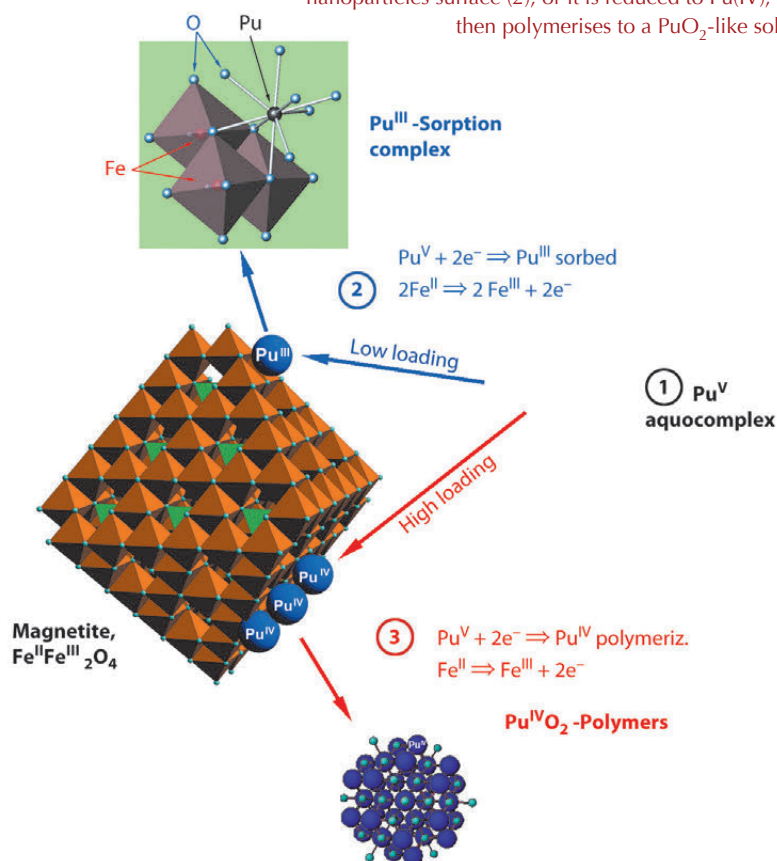


**Fig. 91:** Pu-L<sub>III</sub> XAS analysis of Pu redox processes at the magnetite/water interface. a) XANES. b) Best fit (red) of experimental EXAFS (black) as obtained by Monte-Carlo simulation. c) Probability of Pu positions at the surface of a magnetite slab (red: lower, green: higher likelihood). d) One of 7 best positions is marked with blue circle. e) Molecular structure of Pu(III) surface complex.

**Fig. 92:** Depending on the loading at the magnetite surface, aqueous Pu(V) (1) is either reduced to Pu(III), which forms a so-called inner-sphere sorption complex at the magnetite nanoparticles surface (2), or it is reduced to Pu(IV), which then polymerises to a PuO<sub>2</sub>-like solid (3).





### Principal publication and authors

F. Giannici (a), M. Shirpour (b),  
A. Longo (c), A. Martorana (a),  
R. Merkle (b) and J. Maier (b),  
*Chem. Mater.* **23**, 2994-3002  
(2011).

(a) *Università di Palermo, Palermo  
(Italy)*

(b) *Max-Planck-Institut für  
Festkörperforschung, Stuttgart  
(Germany)*

(c) *Istituto per lo Studio dei  
Materiali Nanostrutturati, CNR,  
Palermo (Italy)*

### References

[1] K.-D. Kreuer, *Annu. Rev. Mater.  
Res.* **33**, 333-359 (2003).

[2] F. Giannici, A. Longo,  
A. Balerna, K.-D. Kreuer and  
A. Martorana, *Chem. Mater.* **19**,  
5714-5720 (2007).

## The elusive structure and symmetry of the proton conducting oxide Y:BaZrO<sub>3</sub>

Proton-conducting oxides are the most studied electroceramics for hydrogen technology such as fuel cells, membranes for hydrogen purification and hydrogen sensors [1]. Their advantage over zirconia electrolytes for fuel cells relies on the lower operating temperature range (500-700°C). Among proton-conducting perovskite oxides, yttrium-doped barium zirconate BaZr<sub>1-x</sub>Y<sub>x</sub>O<sub>3-y</sub> (BZY) has been proposed as the best candidate for technological applications, combining both high proton mobility and chemical stability.

In the last decade, many crystal structures have been proposed for BZY compounds using X-ray or neutron diffraction: cubic, tetragonal, orthorhombic, or an intrinsically two-phase regime with different cation compositions. Moreover, the yttrium dopant atoms are a potential source of local distortions, or even of preferential attraction for protonic defects: in this respect, the local structure approach has been overlooked in the past, and only recently applied to proton-conducting perovskites [2].

To unravel the finer structural details of BZY, we used X-ray diffraction, exploiting the exceptional resolution of beamline **ID31** to probe long-range symmetry, and X-ray absorption spectroscopy at beamline **BM29**, to explore the local structure around zirconium and yttrium: these were complemented with Raman spectroscopy to probe the local symmetry.

We have determined that BZY forms a single crystalline phase for Y<sup>3+</sup> content up to 15%. If probed with XRD, undoped BaZrO<sub>3</sub> shows a perfectly cubic perovskite structure, but the high oxygen vibration amplitudes and the Raman peaks suggest that incoherently mutual tilting of ZrO<sub>6</sub> units appears throughout the lattice (not affecting the overall cubic symmetry). This dynamical distortion of the anion sublattice is an unexpected and interesting feature, possibly present also in other cubic perovskites.

When Y<sup>3+</sup> dopants are inserted in the perovskite lattice they act as rigid inclusions, maintaining their larger ionic radius with respect to the host Zr<sup>4+</sup> cations. However, the cation and anion sublattices respond very differently to provide sufficient space for the YO<sub>6</sub> octahedra: the O<sup>2-</sup> shells are much expanded around the dopant, while the Y-Ba and Zr-Ba bond lengths are equal (see **Figure 93**), like Y-Zr and Zr-Zr. This peculiar configuration is attained through a local tilting of the YO<sub>6</sub> units with respect to the rest of the lattice, resulting in local Y-O-Zr configurations with angles of about 160°. The tilting of the YO<sub>6</sub> octahedra causes a reduction of symmetry throughout the structure, with an extremely slight tetragonal distortion (< 0.1%) appearing, as proved by the splitting of many XRD peaks (see **Figure 94**).

**Fig. 93:** Interatomic distances of first and second shell around different sites as a function of Y<sup>3+</sup> dopant content, represented as bond length change with respect to undoped BaZrO<sub>3</sub>. a) First shell distances Y-O (red), Zr-O (blue) and average M-O (black), as derived by both EXAFS and XRD analysis. b) Y-Ba (red), Zr-Ba (blue) and average M-Ba (black).

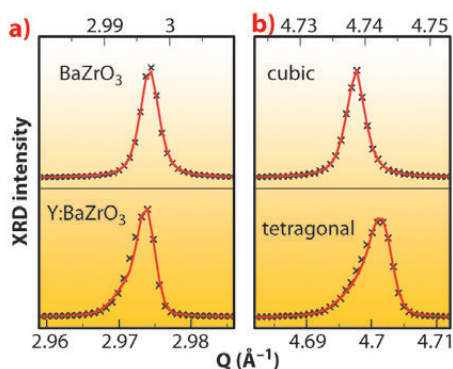
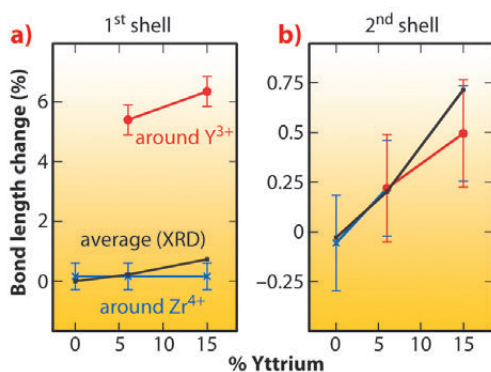


**Fig. 94:** XRD data (black crosses) and Rietveld refinement (red line) of undoped BaZrO<sub>3</sub> and BZY with 15% Y<sup>3+</sup>. a) The (310) reflection of the cubic cell splits into (113) and (331) reflections in the case of a tetragonal cell. b) The (200) reflection of the cubic cell splits into (002) and (220) reflections in the case of a tetragonal cell.

These structural distortions around Y<sup>3+</sup> are most likely the reason of its limited solubility in the BaZrO<sub>3</sub> lattice. However, they are not large enough to create two inequivalent oxygen sites, and therefore not reducing the possible hopping pathways for protons.





## ■ Molecular near-infrared to visible light upconversion

Near-Infrared to visible photon upconversion is a process in which photoexcitation at a certain wavelength in the near infrared is followed by luminescence at a shorter wavelength in the visible. In this process, low energy photons are “converted” to higher energy photons. This phenomenon could be of potential use in liquid solar cell applications in order to take advantage of the infrared part of the solar spectrum or in biological imaging to design visible emitting bio-luminescent probes which are excited with infrared radiation. Using a longer excitation wavelength than in the visible range, infrared presents several advantages such as less phototoxicity and a deeper penetration depth into living tissues. Moreover, compared to classical fluorescence spectroscopy, up-conversion microscopy does not suffer from noise due to the auto-luminescence of the sample [1].

The minimum prerequisite for the generation of upconversion luminescence by a material is the existence of two metastable excited states, the first serving as an excitation reservoir, and the second as the emitting state. Different possible processes of up-conversion have been described [2], the two most common being excited-state absorption (ESA) and energy transfer upconversion (ETU). ESA is a single ion mechanism which involves two sequential absorption processes. In the ETU process, at least two closely spaced ions are required. A sensitizer, which is excited to an intermediate excited state, transfers its energy to a neighbouring chromophore called acceptor, also in an intermediate excited state, promoting it to the upper emitting level (Figure 95). The existence of several excited states located between the ground state and the target excited state in lanthanide complexes makes them good candidates for such an upconversion mechanism, although it has long been thought that the vibrational oscillation of the organic ligands would quench this process for trivalent lanthanide ions [3]. However, with the development of the supramolecular chemistry of lanthanide complexes, using specially designed ligands, assemblies can be made

where the geometry of the metal centre is controlled. This control enables chemists to synthesise assemblies with specific structural properties in order to tune the physical properties.

With a two-photon excitation model in mind, we therefore designed a molecular complex which can maximise the probability of the ETU process. It consists of the connection of two chromium(III) sensitizers around a central erbium(III) acceptor in a linear self-assembled cation (see Figure 95). This system presents several characteristics that can favour the ETU upconversion mechanism such as the high local concentrations of sensitizers, the choice of metals that gives a high efficiency for the Cr-Er energy transfer, and the wrapping of the helical ligand strands around the metal ion that protects them from the solvent.

The structure of such highly paramagnetic slow-relaxing complexes is difficult to assess without the use of X-ray diffraction. NMR and EPR techniques are difficult to

### Principal publication and authors

L. Aboshyan-Sorgho (a), C. Besnard (b), P. Pattison (c,d), K.R. Kittilstved (e), A. Aebischer (f), J-C. G. Bünzli (f), A. Hauser (e) and C. Piguet (a), *Angew. Chem. Int. Ed.* **50**, 4108–4112 (2011).

(a) Department of Inorganic, Analytical and Applied Chemistry, University of Geneva (Switzerland)

(b) Laboratory of Crystallography, University of Geneva (Switzerland)

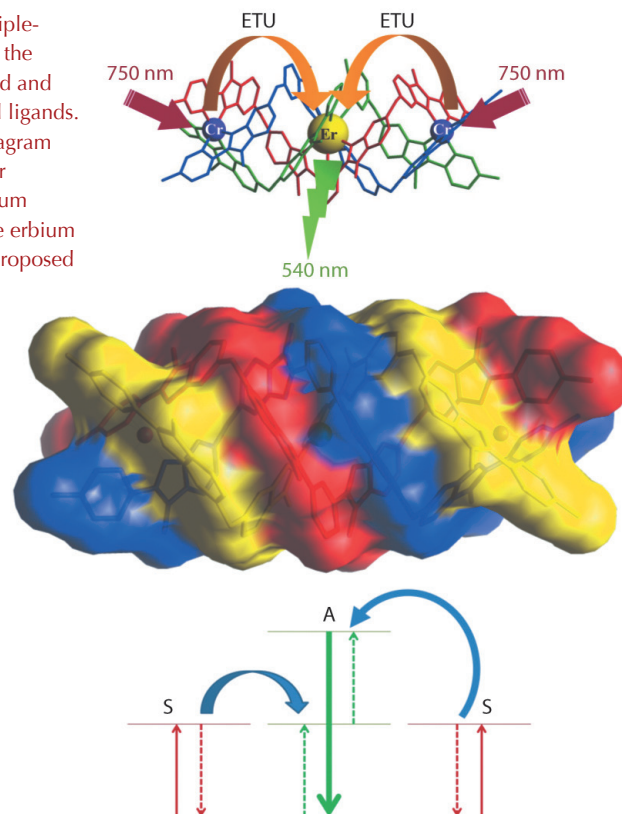
(c) Laboratory of Crystallography Ecole Polytechnique Fédérale de Lausanne (Switzerland)

(d) Swiss Norwegian Beamline (SNBL), ESRF

(e) Department of Physical Chemistry University of Geneva (Switzerland)

(f) Laboratory of Lanthanide Supramolecular Chemistry Ecole Polytechnique Fédérale de Lausanne (Switzerland)

**Fig. 95:** The molecular triple-metallic complexes with the three metal atoms aligned and wrapped by three helical ligands. The simplified energy diagram shows the energy transfer between the two chromium atoms (sensitizer) and the erbium atom (acceptor) for the proposed ETU mechanism.





### References

- [1] D.H. Kim and J.U. Kang in *Microscopy: Science, Technology, Applications and Education* **1**, 571-582 (2010).
- [2] F. Auzel, *Chem. Rev.* **104**, 139-173 (2004).
- [3] C. Reinhard and H.U. Güdel, *Inorg. Chem.* **41**, 1048-1055 (2002).

use in these systems: NMR suffers from large line widths due to chromium(III) and EPR suffers from complications due to zero-field splitting, TIP effects and large line widths due to erbium(III). But as this compound crystallises with two complexes in the asymmetric unit, the unit-cell is large (volume 47200 Å<sup>3</sup>). Moreover, disordered solvent molecules occupy channels inside the crystal, and the diffraction data from conventional sources in our laboratory were of poor quality. The higher quality of the data obtained from **BM01A**, the Swiss-Norwegian beamline, allowed us to unambiguously solve the structure and proved the organisation of the molecule.

The carefully chosen molecular design permitted green emission to be observed upon NIR irradiation of the sample, characteristic of the Er(<sup>4</sup>S<sub>3/2</sub> → <sup>4</sup>I<sub>15/2</sub>) transition. This first example of upconversion in an isolated molecular complex opens a new playground for synthetic chemists. New molecular designs connecting three Cr ions to the Er ion could for instance lead to unprecedented molecular three-photon upconversion luminescence.



# Structural Biology

The productivity of the ESRF's Structural Biology facilities is currently unmatched within Europe. The basis of our success is the provision of many of the complementary techniques required to study complex problems. In this context, the ESRF Structural Biology Group provides tools, and crucially, access mechanisms, for experiments combining X-ray crystallography and bioSAXS (this may also be extended to bioSANS where appropriate); for experiments combining X-ray crystallography and spectroscopy; for experiments requiring the routine use of micro-focus X-ray beams in an automated fashion; for the collection of high quality diffraction data at both very high and very low resolutions. The provision of robust & reliable facilities for the experiments described above is coupled with the development of innovative methods. Most of the developments currently deployed result from the high quality in-house research carried out in the Group, examples of which are included in this chapter.

A brief perusal of the highlights selected here makes it clear that we continue to facilitate extremely high-quality research over a broad range of topics of fundamental biological interest. As usual, the space available means that we limit ourselves to highlighting some general themes and have not been able to include a very large number of deserving cases. That approximately 30% of the articles presented in the chapter concern the crystal

structures of membrane proteins illustrates the growing importance of this research area throughout Europe. Until recently, the elucidation of a membrane protein structure was a notable event in its own right. Today, however, we see sophisticated sets of experiments that provide an understanding, at an atomic level, of how these crucial cellular components function.

Despite the excellent Science summarised in this chapter, the years 2011 and 2012 may be most remembered for the construction work required for an upgraded ESRF which will ultimately provide many new opportunities for more advanced research. During this period the Structural Biology Group will do its utmost to maintain the quality of the service we provide while, at the same time, we manage the decommissioning of the ID14 complex of beamlines and the construction and commissioning of its replacement on ID30. The latter is well under way with key goals and targets met.

While the construction of a new set of beamlines will lead to a number of short-term inconveniences for our User Community - not least of which will be a loss of beamtime capacity - we are confident that the upgraded facilities will provide the tools necessary for a radical change in the way structural biology research is supported at the ESRF. The practice of sample screening will be greatly

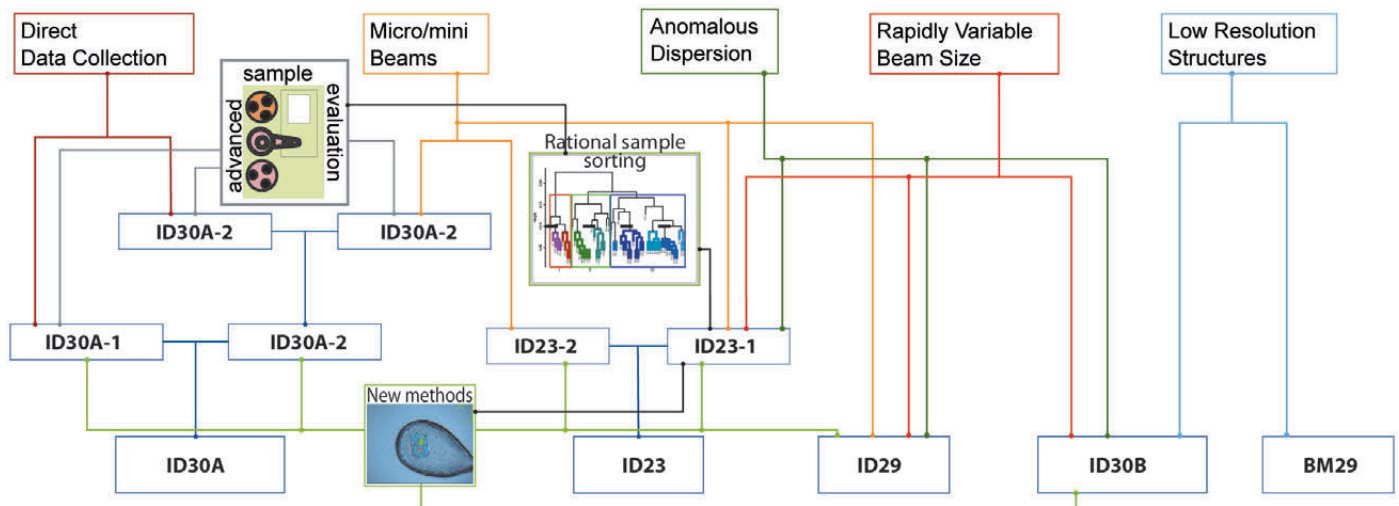


Fig. 96: The suite of coordinated, multidisciplinary beamlines for Structural Biology research that will result from Phase I of the ESRF Upgrade.





enhanced and simplified, it will be possible to investigate samples in a completely automated fashion with precise control over the nature of the screening carried out and the development of optimal diffraction experiment plans. Where appropriate, enhanced automatic data collection and treatment will be available. Access to microfocus beams will be extended both in capacity and smallest beam size available. This process has already been started through the tuneable aperture sizes available on ID29 and ID23-1. Greatly improved automation will also be made available through a combination of new hardware and software, data tracking and selection of the most appropriate sub-sets of data – leading to the possibility to collect highest resolution, most isomorphous, data sets from multiple crystals. The quality

of the operation of the facilities at long wavelength and the flexibility of beam (size) provision will also be improved. Finally, by the end of the construction of ID30, users will be able to collect very low resolution diffraction data with microbeams of a very low divergence. Thus, we expect to deliver a suite of coordinated, multidisciplinary beamlines for researchers (see [Figure 96](#)) that will enable a paradigm shift in the way that Structural Biology problems are approached.

We hope you will bear with us until the upgrade of our facilities has been successfully completed.

S. McSweeney and G. Leonard

#### Principal publication and authors

R. Rocha (a), P.J. Barbosa Pereira (a), M.A. Santos (b) and S. Macedo-Ribeiro (a), *Proc Natl Acad Sci USA*. **108**, 14091-6 (2011).

(a) *IBMC – Instituto de Biologia Molecular e Celular, Porto (Portugal)*

(b) *CESAM and Universidade de Aveiro, Aveiro (Portugal)*

## ■ Ser or Leu: Structural impact of a genetic code alteration in *C. albicans*

A 200-million year old alteration to the standard genetic code resulted in the appearance of a novel serine tRNA [1], allowing the human pathogen *Candida albicans* and other CTG-clade fungi to translate the otherwise universal leucine CUG codon as serine. Due to a mutation in the anticodon loop, this unusual serine tRNA recognises the CUG codon, but additional changes in its sequence allow

recognition both by the seryl- and the leucyl-tRNA synthetases ([Figure 97](#)). Therefore, the serine-tRNA<sup>CAG</sup> can be aminoacylated either with serine (97%) or leucine (3%), so that proteins encoded by a CUG-containing gene incorporate either of these amino acids at the CUG-encoded positions, with a significant bias towards serine. This ambiguous CUG decoding affects approximately 67% of the *C. albicans* ORFome and leads to proteome expansion. Curiously, *C. albicans* can be engineered to increase the percentage of leucine misincorporation up to 28%, leading to impressive phenotypic alterations. However, these show no changes in growth rates, implying that this pathogenic yeast has the ability to survive with significant CUG ambiguity.

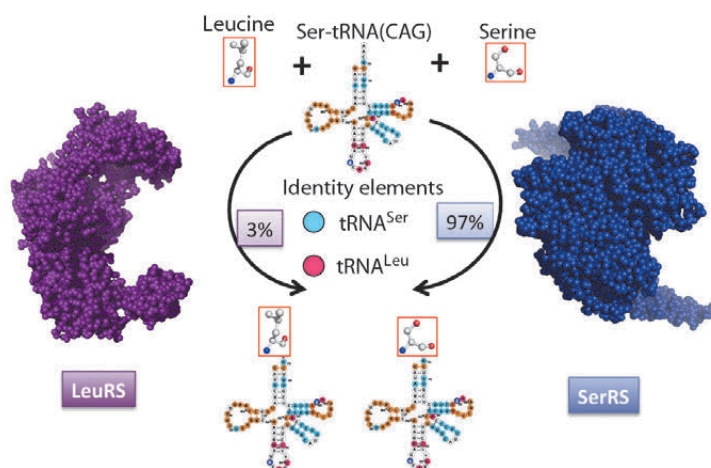


**Fig. 97:** The molecular determinants of genetic code ambiguity in *Candida* spp. *C. albicans* serine-tRNA<sup>CAG</sup> is a hybrid molecule with specific identity elements, which allow the recognition both by seryl- and leucyl-tRNA synthetases. This tRNA is predominantly charged with serine (97%) highlighting the predominant role of SerRS in ambiguous CUG decoding.

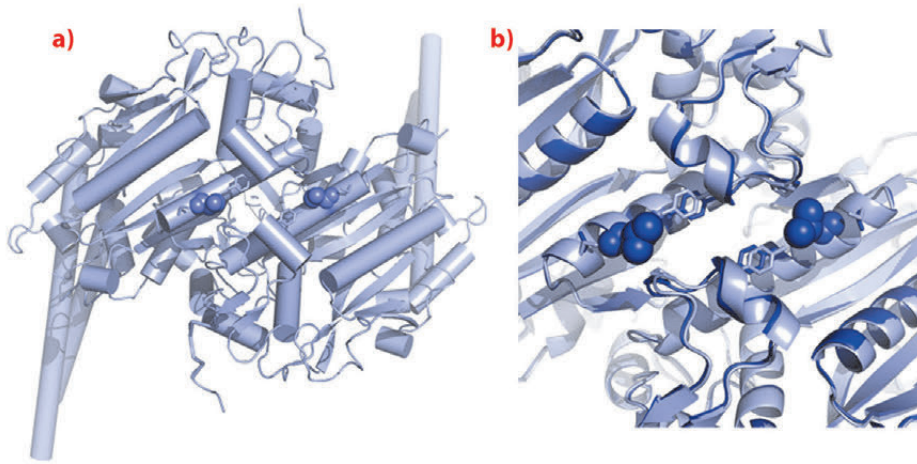


**Fig. 98:** Crystal structures of *C. albicans* seryl-tRNA synthetase isoforms. a) Structure of the SerRS\_Ser197 dimer with Ser197 shown as spheres. b) Local structural changes at the CUG-encoded position in the SerRS\_Leu197 isoform.

This *Candida* Spp. serine/leucine ambiguity generates an intriguing question from a structural biology perspective: how can the 4168 CUG-encoded *C. albicans* proteins cope with incorporation of serine or leucine at the same position without significant protein misfolding and consequent cell dysfunction? Previous data showed that CUG codon ambiguity in CTG-clade fungi resulted in the relocation of the CUG codons to novel positions: 98% of the ancestral CUGs disappeared and were replaced by other leucine codons (UAA, UAG) and new CUGs were located in positions occupied by codons coding for serine or other polar amino acids in homologous genes from related fungal species. A large-scale analysis of the location of CUG-encoded residues in CTG-clade proteins showed that they reside predominately in non-conserved regions of the sequence, avoiding the buried protein core. Consequently, it is expected that the structure and function of protein isoforms with serine or leucine at CUG positions does not differ significantly and that increased incorporation of leucines at these positions does not result in massive protein misfolding.

Nevertheless, the substitution of serine for leucine (and *vice versa*) in CUG-containing genes is unlikely to be completely neutral, since surface residues are often involved in macromolecular interactions, which might be compromised upon modification of the molecular surface. Moreover, structural and functional changes can be predicted for a small number of proteins containing CUG-encoded residues in functionally conserved positions, possibly explaining the phenotypic and morphological changes accompanying increased leucine incorporation in *C. albicans* [2].

The seryl-tRNA synthetase (SerRS) is the main player in CUG-decoding ambiguity in *C. albicans*, and itself contains a CUG-encoded residue in a position where polar amino acids are preferred in homologous yeast SerRSs. The three-dimensional structures of the two isoforms of the enzyme were determined, showing that no large structural change results from serine replacement by leucine at the CUG position. The CUG-encoded residue is located at the dimer interface, partially exposed at the protein surface, and it is not involved in inter-monomer interactions (Figure 98). Nonetheless, the presence of the bulkier hydrophobic leucine side chain induces local rearrangements in the adjacent monomer in the vicinity of the C-terminal tail, unique in cytoplasmic eukaryotic SerRSs and required for enzyme stability and function [3]. These small structural changes are associated with functional differences between the two isoforms, indicating that although the placement of serine or leucine at the CUG-encoded position does not induce major structural changes or protein misfolding, the two isoforms have small but significant differences in function.

Similar functional alterations could be expected for the fungal proteins containing CUG-encoded residues in functionally relevant positions, namely those playing a role in pathogenesis-associated signalling cascades. Therefore, besides providing a deeper insight into the molecular basis of CUG codon relocation in the CTG clade fungi and highlighting the intrinsic link between natural codon ambiguity and protein multifunctionality, our results also provide new perspectives for future research in *Candida* virulence pathways.

#### References

- [1] M.A. Santos, G. Keith and M.F. Tuite, *Embo J* **12**, 607-616 (1993).
- [2] I. Miranda, R. Rocha, M.C. Santos, D.D. Mateus, G.R. Moura, L. Carreto and M.A. Santos, *PLoS ONE* **2**, e996 (2007).
- [3] M. Mociobob and I. Weygand-Durasevic, *Arch Biochem Biophys* **470**, 129-138 (2008).



### Principal publications and authors

K. Lammens (a,b), D. Bemeleit (b),  
C. Möckel (b), E. Clausing (b)  
A. Schele (b), S. Hartung (b),  
C.B. Schiller (b), M. Lucas (b),  
C. Angermüller (b), J. Söding (b),  
K. Sträßer (b) and  
K.P. Hopfner (a,b), *Cell* **145**, 54-66  
(2011);  
C. Möckel (b), K. Lammens (a,b),  
A. Schele (b) and  
K.P. Hopfner (a,b), *Nucleic Acids  
Res.* **39**, 1-14 (2011).  
(a) Center for Integrated Protein  
Science Munich (CIPSM)  
(b) Gene Center, Ludwig-  
Maximilians-University Munich  
(Germany)

## The Mre11/Rad50 complex - an ATP dependent molecular clamp in DNA double strand break repair

The DNA in our cells is continuously exposed to DNA damaging agents such as radiation and mutagenic chemicals. Amongst the various forms of damage, probably the most cytotoxic are DNA double strand breaks (DSBs) which can lead to gross chromosomal aberrations and cancer. DSBs arise during chromosomal replication but can also be products of ionising radiation and genotoxic chemicals. In addition, enzymatically induced DSBs are intermediates in V(D)J recombination, immune globulin class switching and meiosis. Both sporadic and programmed DSBs need careful and prompt repair to maintain genome stability and allow cell survival.

DSBs elicit a complex cellular response and induce predominantly two different repair pathways: homologous recombination (HR) and non-homologous end joining (NHEJ). In HR, DNA ends are resected and paired with the sister chromatid to prime repair synthesis, resulting in error-free repair. In contrast, in NHEJ the DNA ends are directly ligated without a template, making NHEJ potentially mutagenic.

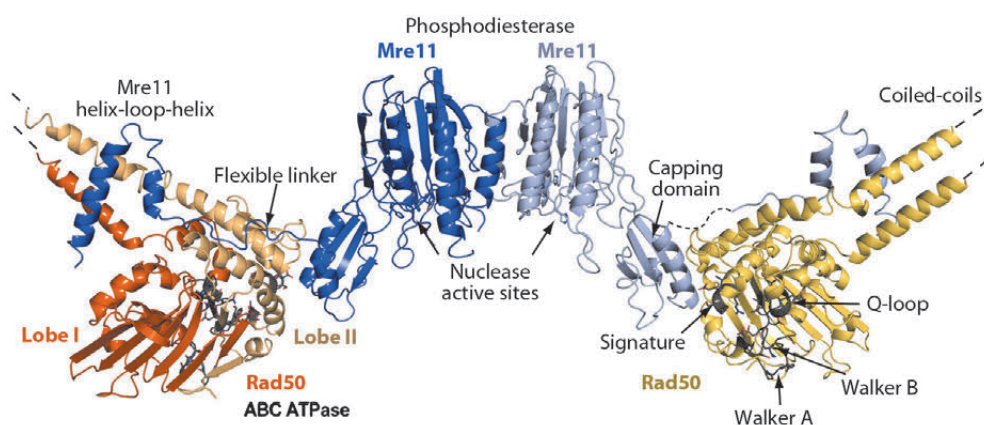
The Mre11/Rad50/Nbs1 complex (MRN; Mre11/Rad50/Xrs2 in *Saccharomyces cerevisiae*) is an evolutionarily conserved key player in the detection and repair of DNA double strand breaks. Mutations in MRN subunits lead to a defective DSB repair response and can result in cell death or chromosomal aberrations. Hypomorphic mutations in the MRN-ATM axis are linked to diseases that are

characterised by neurological disorders and/or cancer predisposition. The MRN complex functions in both the HR and NHEJ repair pathways and is involved in DSB detection, DNA tethering, damage signalling via ATM, structural organisation of repair and checkpoint foci, as well as nucleolytic processing of the DNA ends. These diverse functions suggest that the MRN complex possesses multiple activities, including not only enzymatic, but also architectural and structural roles. Whereas enzymatic activities are required to prepare DNA ends for repair, architectural functions maintain these in close proximity. Homologs of the Mre11/Rad50 complex are found in every kingdom of life, suggesting that this core enzyme complex is fundamental for genomic stability. To understand the interplay between Mre11 and Rad50, we determined the crystal structure of the catalytic head of the *Thermotoga maritima* (*Tm*) Mre11/Rad50 complex (SbcCD).

The structure reveals important information about the architectural organisation of Mre11 homodimerisation and the interaction of Mre11 with Rad50. The *Tm*MR catalytic head (*Tm*MR<sup>NBD</sup>) is an elongated crescent shaped complex and its core is formed by a dimer of the two Mre11 nuclease domains, with the two nuclease active sites located near the centre of the concave face (Figure 99). The Rad50 NBDs each attach to the outside of the nuclease dimer and form the tips of the crescent. The Rad50 coiled-coils protrude from the convex side of the catalytic head, opposite to the nuclease active sites, at

an angle of approx. 120° from each other. The overall structure explains two poorly understood functional characteristics of MR. The widely separated, outward placement of the Rad50 NBDs allows unobstructed access of DNA to the Mre11 active sites, even if the DNA ends are blocked by large proteins. In addition, our structure together with SAXS and chemical crosslinking analysis of the MR head complex, with and

**Fig. 99:** Overall structure of the Mre11:Rad50 catalytic head complex in its "open" nucleotide free conformation.





without nonhydrolysable ATP analogues, shows that the complex undergoes major conformational changes upon ATP binding to Rad50 [1].

Recently we determined the crystal structure of the closed ATP bound *Tm*Mre11/Rad50 head complex (*Tm*MR<sup>NBD</sup> ATP) and on the basis of both structures we have derived a precise structural framework for ATP induced conformational changes in the *Tm*MR<sup>NBD</sup> complex. We find that ATP binding induces a large structural change from the open form with accessible *Tm*Mre11 nuclease sites into a closed form (Figure 100a). Most remarkably, ATP repositions the engaged Rad50 NBDs into the dsDNA binding groove of the Mre11 active site, suggesting an ATP induced blocking of Mre11's active site. While this conformation is incompatible with dsDNA binding to Mre11, unwound or single-stranded DNA may still reach Mre11's nuclease sites and could offer a structural explanation of how MR promotes endonucleolytic cleavage of single-stranded DNA or hairpins (Figure 100b). Additionally, the extended coiled-coil domains of Rad50 undergo an extensive conformational reorientation, which could prevent intramolecular MR interaction after ATP dependent engagement and allow intermolecular interaction between different MR complexes via the zinc hook. This raises the possibility that DNA tethering functions of the complex and ATP dependent DNA binding are allosterically coupled (Figure 100c).

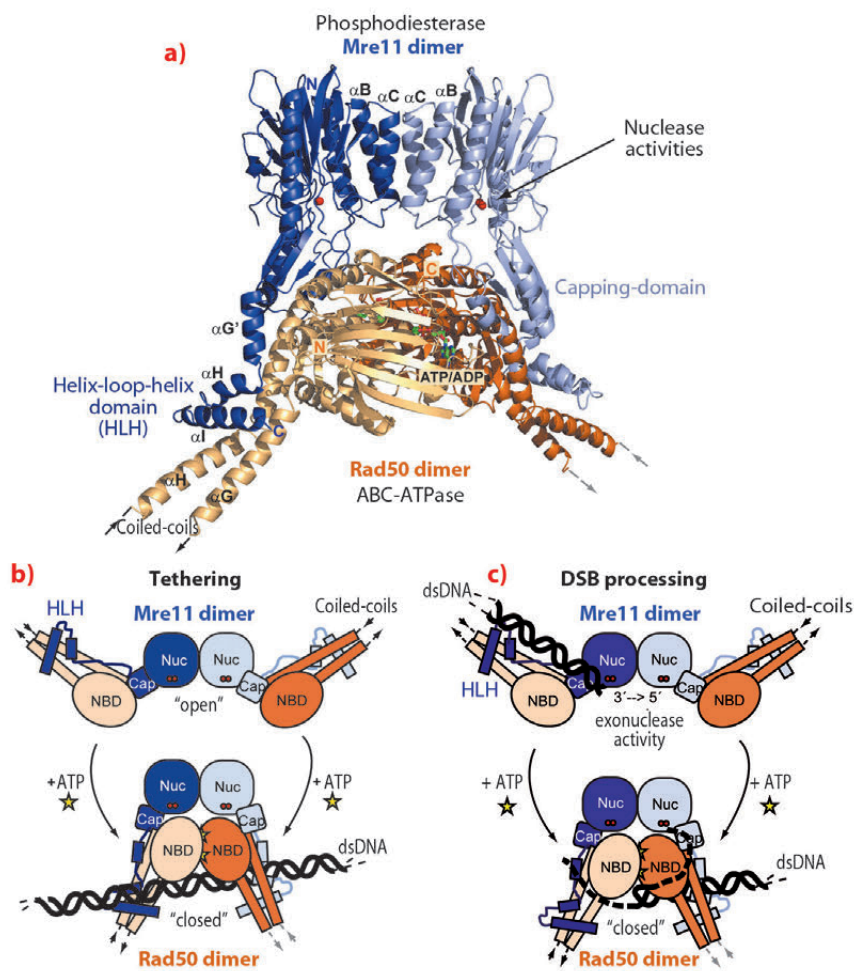


**Fig. 100:** a) The *Tm*MR<sup>NBD</sup> complex structure in its ATP bound “closed” conformation. b) and c) show, respectively, the proposed clamp model for the DSB processing and DNA tethering functions of the *Tm*MR<sup>NBD</sup> complex.

#### References

[1] C. Wyman, J. Lebbink and R. Kanaar, *DNA Repair* **10**, 1066-1070 (2011).

## ■ The molecular mechanism of pain relief

General anaesthetics are one of the classes of medicine that have reduced human suffering more than any other drug. Despite widespread use, their exact mode of action is not well understood, but a growing body of evidence suggests that they bind specifically to membrane bound receptors in the synapses of nerve cells. These receptors, called pentameric ligand gated ion channels, send an electrical signal in response to a chemical signal. Two crystal structures of a bacterial homologue of these receptors, in complex with two general anaesthetics, have recently been solved (electrophysiological tests showed that this bacterial homologue

is also sensitive to general anaesthetics). The results reveal a specific cavity in which the drugs are bound, offer insights into their molecular mechanism, and have the potential to allow the development of improved anaesthetics in the future.

Nerve impulses control processes in the body from movement to sight and thought. They are propagated between nerve cells by chemical signals transmitted across synapses. When an electrical potential arrives at a synapse in response to a stimulus, it must be transmitted across the synaptic cleft – the gap between nerve cells. This is an entirely chemical process,

#### Principal publication and authors

H. Nury (a,b,c,d),  
 C. Van Renterghem (a,b), Y. Weng (e),  
 A. Tran (e), M. Baaden (f),  
 V. Dufresne (a,b), J. Changeux (b,g),  
 J.M. Sonner (e), M. Delarue (c,d) and  
 P. Corringer (a,b), *Nature* **469**, 428-431 (2011).  
 (a) *Group Récepteurs-Canaux, Institut Pasteur, Paris (France)*  
 (b) *CNRS URA 2182, Paris (France)*  
 (c) *Unité de Dynamique Structurale des Macromolécules, Institut Pasteur, Paris (France)*  
 (d) *CNRS URA 2185, Paris (France)*  
 (e) *University of California, San Francisco (USA)*  
 (f) *CNRS UBPC UPR 9080, Paris (France)*  
 (g) *Collège de France, Paris (France)*

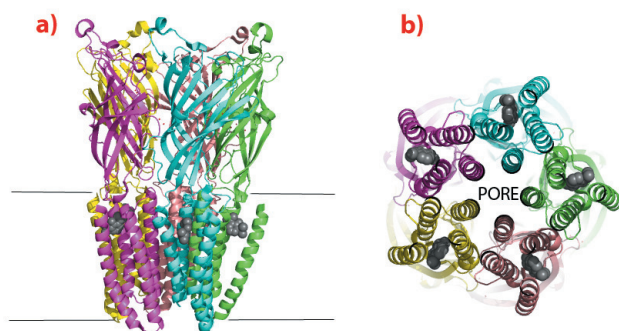


**Fig. 101:** The structure of a bacterial pLIGIC bound to the anaesthetic propofol. a) The channel is shown as a ribbon with each pentamer coloured differently, the position of the protein within the cell membrane is indicated by the two lines. Neurotransmitters bind in the extracellular domain and cause the opening or closing of the cation channel located in the membrane domain. Propofol is shown as Van der Waals spheres (grey) and is bound within the membrane domain of the protein. b) View of the channel from inside the cell. The cation pore is formed at the interface of the five subunits and is in the open conformation. Propofol (grey spheres) binds in a hydrophobic pocket between helices and interferes with the opening and closing of the channel.

#### References

- [1] N. Bocquet *et al.*, *Nature* **457**, 111-114 (2009).  
 [2] R.J.C. Hilf *et al.*, *Nature* **457**, 115-118 (2009).

where the change in electrical potential triggers the release of neurotransmitters. These molecules then bind to pentameric ligand-gated ion channels (pLIGICs) in the membrane of the adjoining nerve cell. The binding of the molecules stimulates the opening of pLIGICs allowing the rapid influx of cations into the cell, which in turn propagates an electrical impulse along the nerve, thereby transmitting the stimulus. The channels produce local permeability changes in the membranes that are directly correlated to both the concentration of neurotransmitter and its lifetime in the synaptic cleft - changing a self amplifying electrical transmission into a highly-sensitive, graded response. Their receptors are the target of many psychoactive drugs and are probably also the targets of general anaesthetics, but, as they are membrane proteins, structural studies are challenging. Recently, a bacterial homologue of human pLIGICs was discovered and its structure solved [1,2], showing the first molecular details of this class of membrane protein and

providing an excellent model for studies of neurotransmission.

We have now crystallised a bacterial pLIGIC in complex with two commonly used general anaesthetics, desflurane and propofol. The crystal structures were solved using diffraction data collected on beamline **ID14-2**. They reveal a common binding cavity for the drugs in the membrane bound domain of the “cation channel open” conformation of the protein with interactions between residues that form the cation channel and phospholipids bound to the protein. The cation channel is formed at the interface of the pentamers and the anaesthetics bind in a hydrophobic cleft between four transmembrane helices of each monomer (**Figure 101**). In order to confirm that this is a physiological relevant binding site, we conducted electrophysiological tests to show that the anaesthetics alter the ion permeability of the channel and that mutations to the residues that form the pocket identified in the crystal structure also alter the response to the drugs. As the pore is opened and closed by relative movements of the helices to which the anaesthetics are bound, their interaction at this site will affect the channels ability to open and close in response to neurotransmitters. The identification of a binding cavity for two of the most commonly used general anaesthetics opens the possibility to develop a new generation of this important class of analgesics with enhanced characteristics.

## ■ TBL1, a tetrameric scaffold at the heart of the SMRT/NCoR transcriptional repression machinery

Transcriptional repression complexes play important roles in both repressing gene transcription and in “resetting” genes after rounds of active transcription.

SMRT and NCoR are homologous corepressor proteins that are recruited to many repressive transcription factors. They are large “platform” or “hub” proteins (c.2500 amino acids) that assemble a complex containing a number of histone deacetylase enzymes. These enzymes

remove acetyl groups from histone tails causing chromatin condensation.

The conserved “core” of the SMRT/NCoR repression complexes (called repression domain 1 or RD1) recruits HDAC3, TBL1 (and/or its homologue TBLR1) as well as a protein called GPS2 (also known as AMF1). SMRT, GPS2 and TBL1 form a ternary complex in a three-way interaction.



In this study we sought to understand the mode of assembly of SMRT with TBL1 and GPS2. We mapped the regions in the three proteins required for interaction and demonstrated that the amino-terminal domain of TBL1 (TBL1-NTD) is able to bind both GPS2 and SMRT forming a ternary complex. Adjacent interaction regions in SMRT and GPS2 form a binary complex.

We were unable to obtain crystals of the SMRT:TBL1:GPS2 ternary complex. However, using NMR spectroscopy we were able to determine the structure of the binary complex between SMRT and GPS2. The structure revealed that the two proteins interact through a tight antiparallel coiled-coil (**Figure 102a**). The antiparallel nature of the coiled-coil positions the regions that interact with TBL1 at the same end of the complex suitable for simultaneous interaction with TBL1 immediately suggesting an arrangement for the ternary complex. The heterodimerisation of SMRT and GPS2 allows them to form a higher affinity complex with TBL1 than could be formed with either alone.

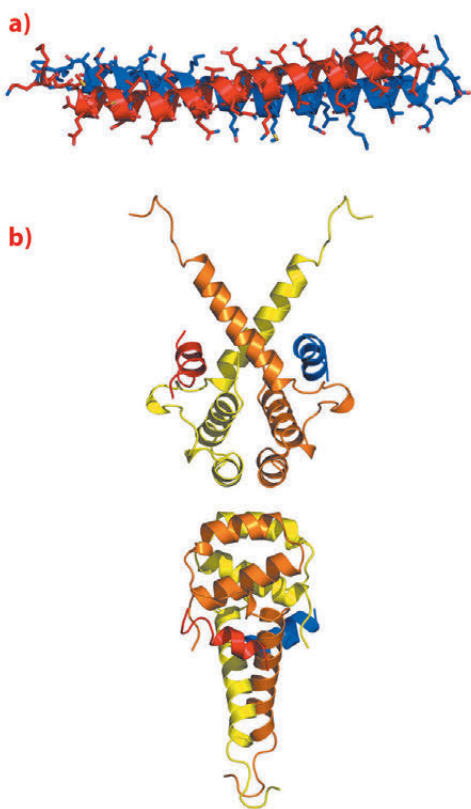


**Fig. 102:** a) NMR structure of the anti-parallel coiled-coil interaction between GPS2 (red) and SMRT (blue). b) Cartoon representation of the crystal structure of tetrameric oligomerisation domain of TBL1 (yellow and orange) with modelled helices binding from GPS2 (red) and SMRT (blue).

The amino terminal domain of TBL1, that mediates interaction with both SMRT and GPS2, crystallised in three different forms that diffracted to between 2.2 Å and 5 Å resolution.

Unexpectedly this domain formed a tetramer (a dimer of dimers) in all three crystal lattices, with a number of non-polar amino acids interdigitating at the interface between two TBL1 dimers (**Figure 102b**). Tetramerisation in solution was confirmed by comparing the mobility of wild-type protein and protein with a mutation at the tetramer interface on a size exclusion column. Thus it seems very likely that the tetramer is the physiologically relevant form of TBL1 *in vivo*. We also showed that each dimer of TBL1 is able to bind a heterodimer of SMRT and GPS2 and thus the physiological relevant stoichiometry of the TBL1:SMRT:GPS2:HDAC3 complex is 4:2:2:2.

A striking feature of the structure of the TBL1-NTD is that each TBL1 dimer has a pair of non-polar grooves on either side of the structure. These grooves were suggestive of an interaction surface with the SMRT:GPS2 heterodimer. Indeed mutations in the grooves abolished interaction with both SMRT and GPS2. Examination of the GPS2 and SMRT sequences adjacent to the coiled-coil identified a common  $\alpha$ -helical sequence motif that could mediate interaction with TBL1. The motif is  $A \times \times \varphi H/K/R \times \varphi$  (where  $\varphi$  is a non-polar amino acid). Mutations in this motif in both proteins abolished recruitment to TBL1. Docking an alpha helix with this motif (using HADDOCK software) indicated a unique mode of binding to the non-polar groove in TBL1 with the key residues making important interactions at the interface.

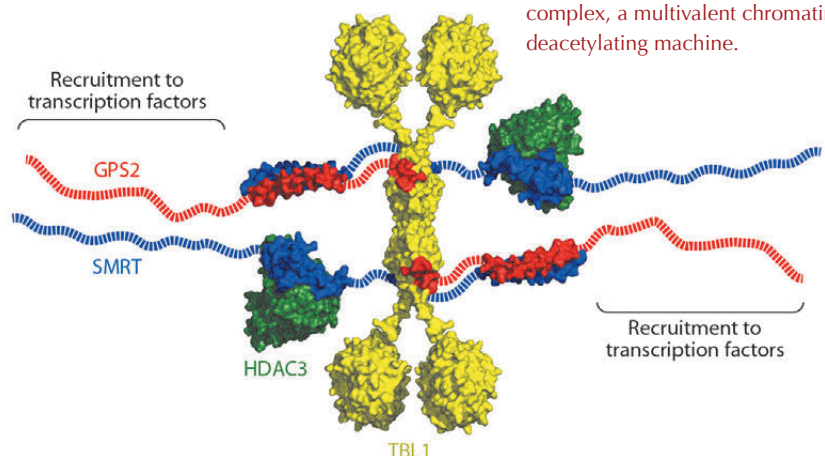


**Fig. 103:** Schematic of the overall arrangement of the SMRT repression complex, a multivalent chromatin deacetylating machine.

#### Principle publication and authors

J. Oberoi (a,b), L. Fairall (a), P. Watson (a), J.-C. Yang (b), Z. Czimmerer (c), T. Kampmann (a), B. Goult (a), J.A. Greenwood (a), J. Gooch (b), B.C. Kallenberger (b), L. Nagy (c), D. Neuhaus (b) and J.W.R. Schwabe (a), *Nature Structural and Molecular Biology* **18**, 177-85 (2011).  
(a) Henry Wellcome Laboratories of Structural Biology, Department of Biochemistry, University of Leicester (UK)  
(b) Medical Research Council-Laboratory of Molecular Biology, Cambridge (UK).  
(c) Apoptosis and Genomics Research Group of the Hungarian Academy of Sciences, Department of Biochemistry and Molecular Biology, University of Debrecen (Hungary).

#### Acknowledgements

The Wellcome Trust and UK Medical Research Council for funding. Beamlines used for data collection: Beamline ID14-2 at the ESRF; IO3 & IO4 at Diamond Light Source, UK.





### References

- [1] P.J. Watson, L. Fairall and J.W.R. Schwabe, *Mol Cell Endocrinol* **348**, 440–449 (2012).  
 [2] A. Codina, J.D. Love, Y. Li, M.A. Lazar, D. Neuhaus and J.W.R. Schwabe, *Proc Natl Acad Sci USA* **102**, 6009–6014 (2005).

Taken together, the crystal structure of the TBL1-NTD tetramer, the NMR structure of the SMRT:GPS2 heterodimer, along with mutagenesis and docking experiments give us considerable insight into the assembly of the core SMRT/NCoR:TBL1:GPS2:HDAC3 repression complex. A schematic is shown in **Figure 103**. In addition to the amino-terminal tetramerisation domain, TBL1

contains a C-terminal WD40 domain that could potentially bind to histone tails and to intact nucleosomes, since such domains have been observed in this role in other proteins. Hence the tetrameric nature of the TBL1 suggests that the protein may serve as a scaffold for a multivalent chromatin-targeted repression machine that contains multiple co-repressor proteins and histone deacetylase enzymes.

### Principal publication and authors

S. Stefer (a), S. Reitz (b),  
 F. Wang (c), K. Wild (b),  
 Y.-Y. Pang (b), D. Schwarz (d),  
 J. Bomke (d), C. Hein (a),  
 F. Löhr (a), F. Bernhard (a),  
 V. Denic (c), V. Dötsch (a) and  
 I. Sinning (b), *Science* **333**, 758–762 (2011).

(a) Institute for Biophysical Chemistry, Centre for Biomolecular Magnetic Resonance, Goethe University, Frankfurt am Main (Germany)

(b) Heidelberg University Biochemistry Center (BZH), Heidelberg (Germany)

(c) Department of Molecular and Cellular Biology, Harvard University, Northwest Laboratories, Cambridge (USA)

(d) Merck KGaA, Merck Serono, Molecular Interactions and Biophysics, Darmstadt (Germany)

## ■ Tail-anchored protein targeting to the endoplasmic reticulum membrane

Eukaryotic cells contain a complex system of membrane surrounded organelles and delivery of newly-synthesised membrane proteins to their specific destinations is of vital importance. Diverse mechanisms for chaperoning membrane proteins have evolved. These include cytosolic factors that identify targeting signals, transiently associate with the hydrophobic regions, and escort their cargo to the designated location.

The best understood targeting machinery is the signal recognition particle (SRP)/Sec61 translocon system at the endoplasmic reticulum (ER) membrane, which accepts membrane proteins with a N-terminal signal [1]. Membrane proteins with a single C-terminal transmembrane helix, the so-called tail-anchored (TA) proteins, utilise

the recently identified GET system (guided entry of TA proteins) [2]. The central player in the latter process is the Get3 ATPase, a dimeric protein in which each subunit comprises a nucleotide binding (NBD) and TA binding (TABD) domain. The dimer is held together by a zinc ion and switches between an ‘open’ and a ‘closed’ state by a nucleotide-dependent rotation of the two subunits. At the ER membrane, Get3 interacts with the cytoplasmic domains of the two receptor proteins Get1 and Get2, which are necessary and sufficient for TA protein insertion [3]. To dissect the mechanism of TA protein insertion we studied the structure and function of the Get3 ATPase in complex with its receptors Get1 and Get2.

Due to the inherent flexibility of a molecular targeting machine, crystal growth proved difficult and the success of the project relied on the brilliant beamlines **ID14-4**, **ID23-1** and the microfocus **ID23-2** coupled with regular access via the BAG scheme.

The crystal structure of Get3 in complex with the cytoplasmic domain of Get1 (Get1 for simplicity), determined at a resolution of 3.0 Å, revealed Get1 to form a typical coiled-coil stabilised by a hydrophobic zipper in a heptad repeat. The Get1/Get3 complex forms a symmetrical heterotetramer with a central Get3 homodimer and two Get1 molecules wedging into the Get3 dimer interface (**Figure 104b**). Get1 stabilises nucleotide-

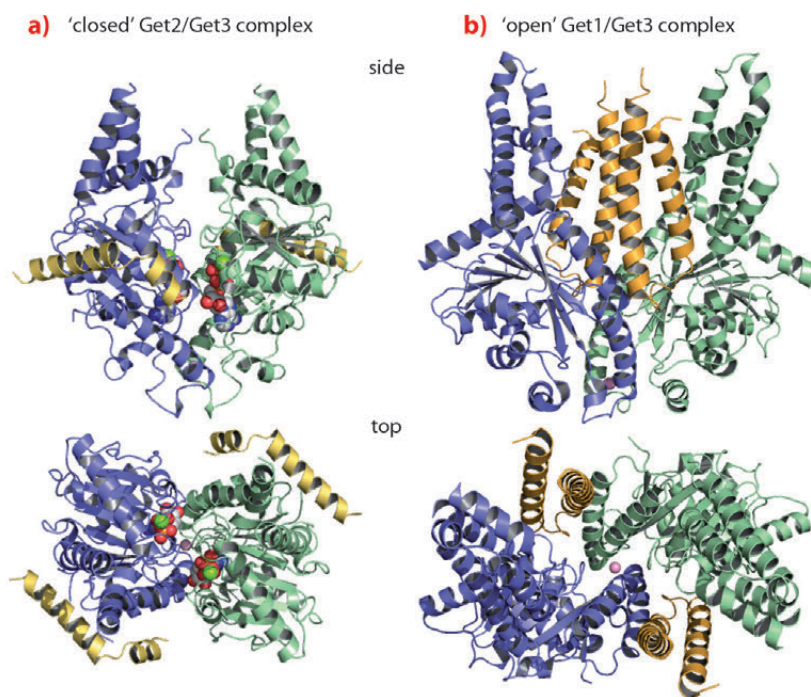


**Fig. 104:** TA protein targeting by the GET system. a) The ‘closed’ Get2/Get3 complex; b) the ‘open’ Get1/Get3 complex.



free 'open' conformations of Get3 by directly interfering with nucleotide binding and rendering the active site highly solvent accessible. Each Get1 molecule binds to both Get3 subunits, however, the interactions are different in size and strength. While the larger interface performs a structural role and seems independent of Get3 closure, the smaller interface 'slides' along the second Get3 subunit during opening to finally convey nucleotide exchange activity in the 'open' conformation.

Since both Get1 and Get2 are necessary for TA protein insertion, we solved the structure of the Get2 N-terminal cytoplasmic domain in complex with Get3 at 4.6 Å resolution. The Get2/Get3 complex is also a symmetric heterotetramer with two Get2 molecules bound to the nucleotide-loaded 'closed' Get3 homodimer (Figure 104a). The Get2 interaction region comprises two amphipathic, positively charged helices connected by a flexible glycine linker. Each Get2 molecule interacts laterally with a negatively charged surface patch of a single Get3 subunit, and does not interfere with nucleotide binding. Interestingly, this binding site partially overlaps with the binding site described for Get1 as also confirmed by NMR titration experiments. Thus, sequential binding of Get2 and Get1 to the Get3/TA protein complex might be envisaged, which is accompanied by structural rearrangements in the targeting complex at the membrane.

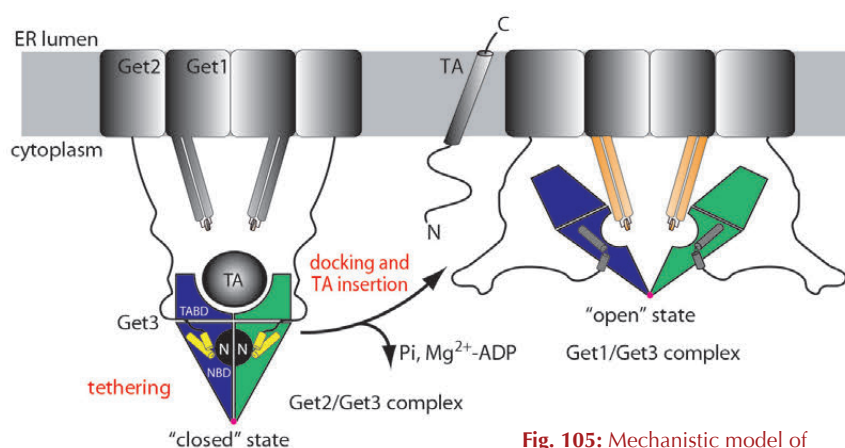


**Fig. 105:** Mechanistic model of TA protein targeting by the GET system. Coloured parts correspond to structures shown in Figure 104: Get3 dimer (blue/green), Get2 (yellow), and Get1 (orange).

The integration of the crystal structures with biochemical data suggests the following mechanistic model for TA protein delivery to the ER (Figure 105): The Get3/TA protein complex is tethered to the membrane by the N-terminus of Get2. Docking of Get1 to the tethering complex partially displaces Get2, which results in an insertion competent complex. Insertion of the TA protein allows for  $P_i$  release and the stored energy of ATP hydrolysis drives Get3 from the 'closed' to the 'open' state as observed in the Get1/Get3 structure with a concomitant loss of  $Mg^{2+}$ -ADP. As the cytoplasmic domain of Get1 is rigidly linked to its transmembrane regions, the rearrangements during opening of Get3 may create a force, which could be directly exploited for TA protein insertion by a mechanism reminiscent of ABC transporters. Finally, Get3 dissociates from the membrane by ATP binding and adopts the 'closed' conformation, ready for the targeting of the next TA protein.

#### References

- [1] P. Grudnik, G. Bange and I. Sinning, *Biol Chem* **390**, 775-782 (2009).
- [2] P.J. Simpson, B. Schwappach, H.G. Dohlman and R.L. Isaacson, *Structure* **18**, 897-902 (2010).
- [3] F. Wang, A. Whynot, M. Tung and V. Denic, *Mol Cell* **43**, 738-750 (2011).

## ■ A RAF-induced allosteric transition of KSR stimulates KSR and RAF phosphorylation of MEK

The RAS-RAF-MEK-ERK signalling pathway relays extracellular stimuli to changes in cellular function and gene expression. Aberrant activation of this pathway through oncogenic mutations is responsible for a large proportion of human cancers. KSR (kinase suppressor of RAS) functions as an essential scaffolding protein to coordinate the assembly of the protein kinases RAF, MEK and ERK into dynamic signalling complexes [1,2]. Such complexes facilitate the sequential

phosphorylation of MEK by RAF and then ERK by MEK. Although the role of KSR as a scaffolding molecule to coordinate the assembly of RAF, MEK and ERK is well established, how KSR promotes stimulatory RAF phosphorylation of MEK is less well defined. Moreover, there has been significant debate as to whether KSR is an authentic protein kinase or, instead, represents a pseudo-kinase, that is, a protein with structural similarity to a protein kinase, but without catalytic activity.

#### Principal publication and authors

D.F. Brennan (a), A.C. Dar (b), N.T. Hertz (b), W.C. Chao (a), A.L. Burlingame (c), K.M. Shokat (b) and D. Barford (a), *Nature* **472**, 366-9 (2011).  
(a) Division of Structural Biology, Institute of Cancer Research, Chester Beatty Laboratories, London (UK)  
(b) Howard Hughes Medical Institute and Department of Cellular and Molecular Pharmacology, University of California San Francisco (USA)  
(c) Department of Pharmaceutical Chemistry, University of California San Francisco (USA)



To address these questions we determined the crystal structure of a complex of the kinase domain of KSR2 (KSR2<sup>KD</sup>) with MEK.

KSR2<sup>KD</sup> and MEK1 dimerise, and the crystal structure of the KSR2<sup>KD</sup>:MEK1 dimer was determined using data collected at beamline **ID14-4**. KSR2<sup>KD</sup>:MEK1 assemble into a tetramer through a KSR2<sup>KD</sup> homodimer interface centred on Arg718<sup>K</sup> of KSR2<sup>KD</sup> (superscripts 'K' and 'M' refer to KSR2 and MEK1, respectively). KSR2<sup>KD</sup> and MEK1 molecules interact with their catalytic sites facing each other through their activation segments and  $\alpha$ G helices (**Figure 106**). MEK's activation segment, incorporating RAF phosphorylation sites Ser218<sup>M</sup> and Ser222<sup>M</sup>, comprises a short  $\alpha$ -helix connected to a segment of extended chain that forms an anti-parallel  $\beta$ -sheet with the KSR2 activation segment (**Figure 106**). The integrity of the complex is likely conferred by the more extensive interface created by engagement of their respective  $\alpha$ G helices.

The KSR2<sup>KD</sup>:MEK1 crystal structure indicated that KSR has the potential for catalytic activity possibly necessary for KSR function. Electron density maps reveal well-defined density for ATP-Mg<sup>2+</sup> at the KSR2<sup>KD</sup> catalytic site. Although Asp803<sup>K</sup> of the DFG motif is shifted slightly out of position, the metal coordinating Asn791<sup>K</sup> and the general base Asp786<sup>K</sup> of the catalytic loop adopt conformations typical of conventional protein kinases.

However, due to the position of its  $\alpha$ C helix, KSR2<sup>KD</sup> adopts an inactive conformation in this crystal structure.

To examine putative KSR2 catalytic function we conducted *in vitro* kinase assays using an analogue-specific (as1) mutant of KSR2 incubated with the modified ATP analogue (A\*TP $\gamma$ S) and found clear evidence for MEK phosphorylation. These data, together with results using a range of kinase inhibitors with wild type KSR2, demonstrated that KSR is an authentic protein kinase.

KSR assembles MEK-KSR-RAF ternary complexes responsible for promoting RAF phosphorylation of MEK. A model for how KSR and RAF interact through a KSR-RAF heterodimer interface was proposed based on similarities between the KSR homodimer interface and the BRAF homodimer interface. Both KSR and RAF homo-dimer interfaces are centred on an equivalent and conserved residue (Arg718 in KSR), therefore we proposed that KSR and RAF dimerise through the same interface. Formation of a KSR2:BRAF heterodimer would be accompanied by a shift of the KSR2  $\alpha$ C helix to an active conformation. A BRAF-induced conformational shift of the KSR2  $\alpha$ C helix into the active position would enhance KSR2 kinase activity and influence its interaction with the activation segment of MEK, thereby affecting RAF's capacity to phosphorylate MEK. Consistent with this notion, RAF was found to allosterically stimulate KSR kinase activity.

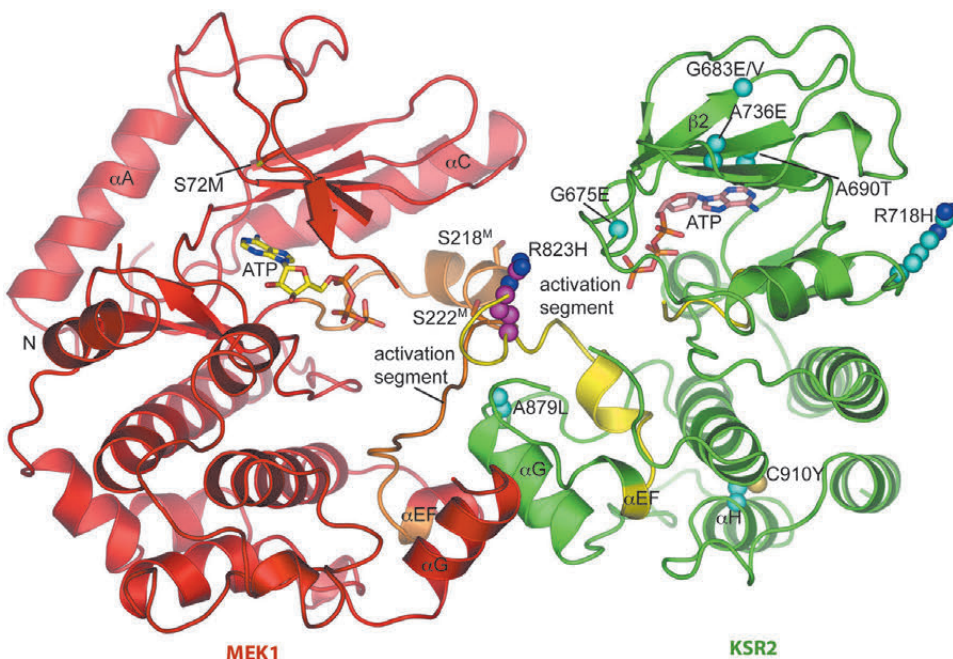
Moreover, the change of KSR tertiary structure modulates the structure of the MEK activation segment, facilitating its phosphorylation by RAF *in trans*.

This work reveals KSR as an effector molecule, receiving a stimulatory signal from an activated regulatory RAF molecule and relaying this to modulate the accessibility of the MEK activation segment for phosphorylation by catalytic RAF.

**Fig. 106:** Overall view of the KSR2<sup>KD</sup>:MEK1 heterodimer showing the face-to-face configuration of KSR2 (green) and MEK1 (red). Activation segments of KSR2 and MEK1 shown in yellow and orange, respectively. KSR loss of function mutations are shown with C-atoms as cyan spheres.

#### References

- [1] A. Claperon and M. Therrien, *Oncogene* **26**, 3143-58 (2007).  
 [2] W. Kolch, *Nat Rev Mol Cell Biol* **6**, 827-37 (2005).







## Snapshot of a bacterial transporter in action

The human urinary tract is one of the most common sites of bacterial infection and most of them are caused by uropathogenic *Escherichia coli* (UPEC). During the infection, UPEC adhere to host epithelial cells by using specific extracellular adhesive organelles termed pili. Despite a wealth of other structural and biochemical information, little is known about how pilus formation is orchestrated at the bacterial cell surface. We present here a crystal structure capturing the pilus assembly platform in the act of secreting its cognate substrate. This new breakthrough provides new insights into the molecular details of pilus assembly.

Uropathogenic *Escherichia coli* (UPEC) attach specifically to human bladder cells using surface structures known as type 1 pili. These are assembled by the so-called chaperone-usher (CU) pathway, one of the best-characterised secretion systems in Gram-negative bacteria [1]. Type 1 pili consist of many individual subunits that are polymerised at the outer membrane by

a specific assembly platform, the usher. In the periplasm, each subunit is stabilised by a dedicated molecular chaperone, FimC, which protects it from aggregation. The chaperone:subunit complexes are then targeted differentially to the usher FimD, which catalyses their assembly. The first subunit to be engaged is FimH, the adhesin at the very tip of the pilus, and subsequent subunits are added one at a time from the base up.

Over the last two decades, some of the molecular details of pilus biogenesis through the CU pathway have been provided [1]. However, little is known about how the usher works. We have recently solved a new crystal structure describing the first step in pilus biogenesis – the FimD usher bound to its cognate FimC:FimH substrate – using diffraction data collected at beamline ID23-1 (Figure 107). This structure, solved at 2.8 Å resolution, shows the full-length usher FimD in its active state. Along with the crystal structure of the closed state of

### Principal publication and authors

G. Phan (a), H. Remaut (a,b), T. Wang (c), W.J. Allen (a), K.F. Pirker (a), A. Lebedev (d), N.S. Henderson (e), S. Geibel (a), E. Volkan (f), J. Yan (a), M.B.A. Kunze (a), J.S. Pinkner (f), B. Ford (f,g), C.W. McKay (a), H. Li (c,h), S. Hultgren (f), D.G. Thanassi (e) and G. Waksman (a), *Nature* **474**, 49–53 (2011).

(a) *Institute of Structural and Molecular Biology, UCL and Birkbeck (UK)*

(b) *Structural Biology Brussels (Belgium)*

(c) *Biology Department, Brookhaven National Laboratory (USA)*

(d) *Department of Chemistry, University of York (UK)*

(e) *Center for Infectious Diseases, Stony Brook University (USA)*

(f) *Department of Molecular Microbiology and Center for Women's Infectious Disease Research, Washington University School of Medicine (USA)*

(g) *Department of Pathology and Immunology, Washington University (USA)*

(h) *Department of Biochemistry and Cell Biology, Stony Brook University (USA)*

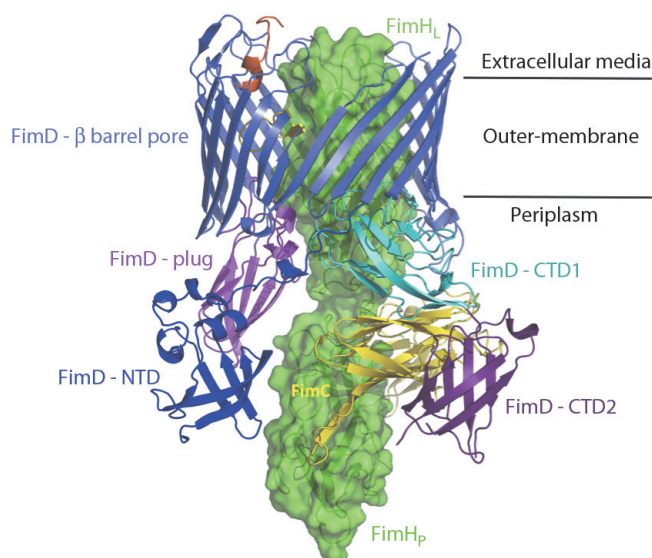


**Fig. 107:** Crystal structure of the FimD:FimC:FimH complex shown as side view and ribbon/surface representation. The adhesin subunit FimH is in green (FimH<sub>L</sub> and FimH<sub>P</sub> stand for the lectin and the pilin domains respectively) and the periplasmic chaperone FimC is in yellow. The usher FimD comprises 5 domains: the N-terminal domain (NTD), the C-terminal domains (CTD1 and CTD2), the plug domain and the  $\beta$ -barrel pore domain. The usher NTD,  $\beta$ -barrel, plug, CTD1 and CTD2 are in blue, slate, magenta, cyan and purple, respectively. Two black lines indicate the position of the usher within the bacterial outer-membrane.

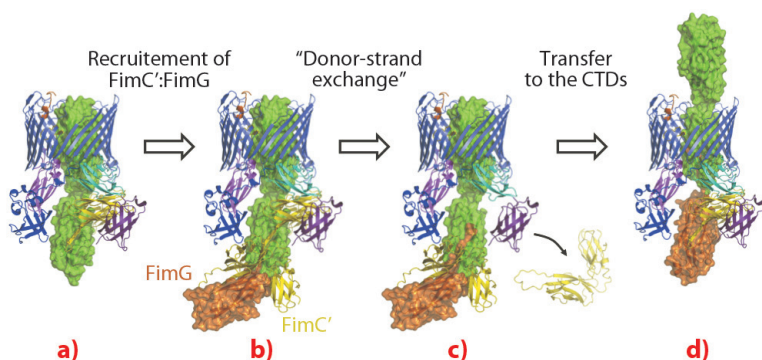


**Fig. 108:** Structural model of the subunit incorporation cycle at the FimD usher, represented as in Figure 107. a) The FimD:FimC:FimH complex. In the described conformation, the FimD NTD is in an ideal position for the recruitment of the next chaperone:subunit complex FimC':FimG. b) FimC':FimG (in yellow and orange, respectively) bound at the NTD of the usher (model based on PDB deposition 1ZE3 [2]). c) The FimG subunit polymerises with FimH via the "donor-strand exchange" mechanism, leading to the dissociation of FimC from FimH and from the usher CTDs. d) Transfer to the FimD CTDs and translocation of FimH through the FimD pore. This frees up the FimD NTD for the next round of subunit incorporation.



### References

- [1] G. Waksman and S.J. Hultgren, *Nature Review Microbiology* **7**, 765-767 (2009).  
 [2] M. Nishiyama *et al.*, *EMBO Journal* **24**, 2075-86 (2005).

the FimD pore domain, this structure sheds new light on the mechanism of usher activation.

A striking feature of the active usher conformation is that the FimC:FimH complex is bound to a newly identified site on the C-terminal domains (CTDs) of FimD. This frees the N-terminal domain (NTD), which is known to bind chaperone-subunit complexes [2],

to recruit the next subunit. Furthermore, this binding positions the two subunits in an ideal position for the polymerisation mechanism to take place (Figure 108). We thus conclude that the usher has two binding sites (NTD and CTDs) that act in concert, such that the growing pilus remains anchored to one, while the next subunit in assembly is recruited by the other (Figure 108).

### Principal publication and authors

A. Nuccitelli (a), R. Cozzi (a), L.J. Gourlay (b), D. Donnarumma (a), F. Necchi (a), N. Norais (a), J.L. Telford (a), R. Rappuoli (a), M. Bolognesi (b), D. Maione (a), G. Grandi (a) and C.D. Rinaudo (a), *Proc. Natl. Acad. Sci. USA*, **108**, 10278-10283 (2011).  
 (a) Novartis Vaccines and Diagnostics, Siena (Italy)  
 (b) Department of Biomolecular Sciences and Biotechnology, and Centro Interdisciplinare Materiali e Interfacce Nanostrutturati, University of Milan (Italy)

## ■ Development of a universal vaccine for *Streptococcus agalactiae*

Several regions of a foreign protein antigen are the target of immune responses, however protective epitopes, the part of an antigen that is recognised by the immune system, are confined within a limited number of protein domains. Structural vaccinology involves the elucidation of domains embedding protective properties in order to design highly efficacious synthetic vaccines exclusively constituted by protective epitopes.

We have recently applied structural vaccinology to develop a universal anti-*Streptococcus agalactiae* (Group B Streptococcus (GBS)) vaccine. Like many other Gram-positive organisms, GBS features the pilus-like structures on its surface. These are known to play a crucial role in the interaction with the human host as they are involved in bacterial aggregation, adhesion to the host tissues and in biofilm formation.

GBS pili are constituted by three protein subunits, one forming the shaft of the organelle (also known as backbone protein (BP)), an ancillary protein (AP1) which decorates the pilus stem, and a second ancillary protein (AP2) often found at the base of the pilus and which has the role of anchoring the pilus to the cell wall. All three proteins are covalently linked to each other through a sortase-mediated transpeptidation reaction.

Sequence analysis of a large panel of GBS isolates revealed the existence of three pilus islands, PI-1, PI-2a and PI-2b, with all strains having at least one, and more frequently two, of the three islands.

Although structurally similar, the BP subunit from one island shares relatively low homology with its counterparts in the other two islands. However, amino acid sequences of BP in strains carrying the same island are highly conserved, with the exception of the backbone subunit of PI-2a (BP-2a), which is grouped into six immunologically distinct variants.

GBS pili were discovered by serendipity while searching for protective antigens using reverse vaccinology. This and subsequent investigations demonstrated that AP1 and BP subunits elicit protective opsonophagocytic antibodies, with BP having the strongest immunogenic properties. From a vaccine standpoint, the fact that virtually all GBS isolates carry pili opens exciting perspectives for the design of universal pilus-based vaccines. However, the existence of eight immunologically different variants of the highly protective BP protein (one from PI-1, one from PI-2b and six from PI-2a) poses a severe challenge in vaccine manufacture.

With the aim of simplifying the final vaccine formulation, the 3D structure of one of the six BP variants of PI-2a was resolved using diffraction data collected on beamline ID23-1. The structure revealed a four-domain organisation (D1 - D4, Figure 109a) with the 100 amino acid long D3 facing the external side of the pilus shaft. When each domain was independently expressed in *E. coli* and tested for protective activity only D3 induced high titers of opsonophagocytic antibodies protecting mice against a lethal challenge with GBS isolates expressing the



homologous PI-2a pilus variant. When the 3D structure of the PI-2a BP variant was used to model the structures of the other five PI-2a BP variants, not surprisingly, it was found that all BPs share a similar four-domain structural organisation. In line with this observation, the D3 domains of the other variants also proved to be highly protective against homologous challenge.

Taking advantage of the limited size of D3, the six PI-2a D3 variants were fused in a single polypeptide chain (**Figure 109b**), which was efficiently expressed in *E. coli*. The recombinant chimera conferred strong protection in mice challenged with any of the GBS strains carrying PI-2a pilus variants.

This work paves the way for the development of a universal, broadly protecting GBS vaccine. GBS infections still represent a serious threat for newborns despite the intrapartum antibiotic prophylaxis of GBS-colonised pregnant women adopted by most industrialised countries. Since children delivered from women with high titers of anti-GBS opsonophagocytic antibodies are protected from GBS infections, vaccination of women of child bearing age and/or pregnant women appears to be the ideal

long-lasting solution to infections of newborn babies. However, an effective anti-GBS vaccine is not yet available. One of the reasons for this is the existence of ten different GBS serotypes and therefore, for a vaccine to be broadly protective, antigens conserved in all serotypes must be identified. The fact that (i) all GBS isolates carry pili, (ii) their BP subunits induce protective antibodies, and (iii) the combination of three proteins (the PBs from PI-1 and PI-2b and the PI-2a chimeric protein) can potentially protect against all GBS isolates, offers a once-and-for-ever solution to the prophylaxis of this important human pathogen.

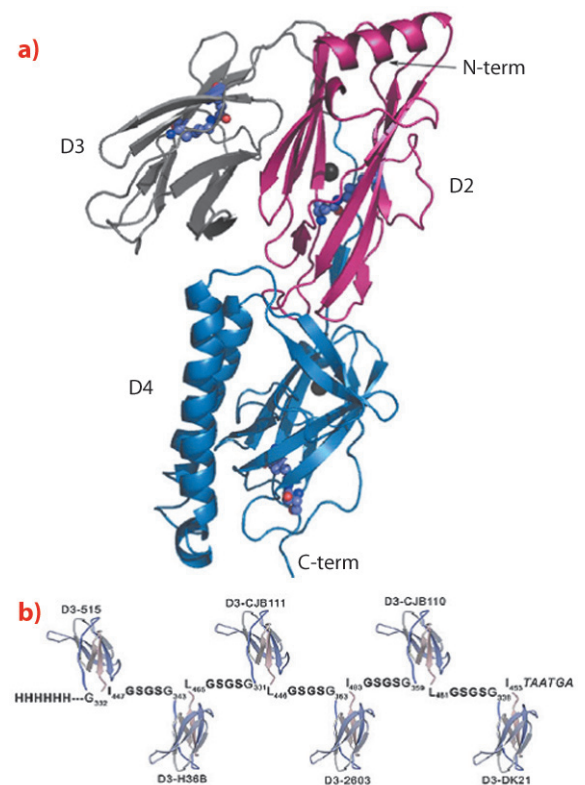


**Fig. 109:** a) Ribbon representation of the crystal structure of the BP subunit of GBS 515 strain carrying type 2a pili. The structure illustrates the four-domain organisation of the pilus protein. b) Schematic representation of the recombinant chimeric protein carrying the D3 domains of all six BP variants of type 2a pili.

## ■ The structural basis of modularity in ECF-type ABC transporters

Energy coupling factor (ECF) transporters form a subgroup of the ATP-binding cassette (ABC) transporter family. The members of this family are involved in the transport of a wide variety of substrates across biological membranes at the expense of ATP hydrolysis [1]. The core-architecture of ABC transporters is conserved and consists of four subunits/domains: two identical or structurally related transmembrane domains (TMDs) that form a single membrane pore through which the substrate is transported and two nucleotide binding domains (NBDs) that hydrolyse ATP. NBDs are well conserved and are considered the hallmark of the ABC transporter family. In contrast, the TMDs from different ABC transporters display a large variation in both structure and amino acid sequence.

Additional subunits/domains are present in some ABC transporters (e.g. “classical” importers found in prokaryotes rely on a water-soluble substrate binding protein domain (SBP) for the recognition of their substrates [1]).

ECF transporters are a group of ABC transporters involved in the uptake of vitamins and other micronutrients in prokaryotes [2]. These proteins are widespread among Gram-positive bacteria, many of which are pathogens (e.g. *Staphylococcus aureus*). ECF transporters contain two NBDs, typical for ABC transporters, and two transmembrane subunits, the EcfT subunit and S-component, which are not related in sequence. ECF transporters do not make use of SBPs for substrate binding. Instead,

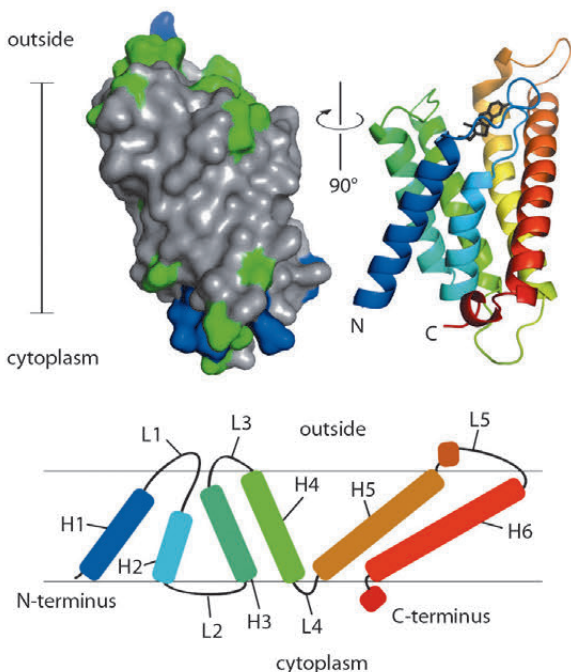
### Principal publication and authors

G.B. Erkens, R.P.-A. Berntsson, F. Fulyani, M. Majsnerowska, A. Vujčić-Žagar, J. ter Beek, B. Poolman and D.J. Slotboom, *Nature Structural and Molecular Biology* **18**, 755-60 (2011). Groningen Biomolecular Science and Biotechnology Institute, University of Groningen (The Netherlands)





**Fig. 110:** Surface (left) and secondary structure cartoon representation (right) of ThiT. In the surface model, hydrophobic residues are coloured grey, hydrophilic green, positively charged blue. The cartoon is coloured from N-terminal blue to C-terminal red. The bar indicates the location of the membrane (35 Å). The topology of ThiT within the membrane is depicted at the bottom. H1-H6: helices 1-6; L1-L5: loops 1-5.



the integral membrane S-component binds the transported substrate with high affinity. S-components for different substrates, such as RibU (specific for riboflavin), ThiT (thiamin) and BioY (biotin), are unrelated in amino acid sequence, but intriguingly, they form active complexes with the same EcfT-NBD assembly [2,3] (the ‘energising module’). The sharing of a single energising module between many (up to 15) different S-components is unique for ECF transporters.

The structural basis of the modular S-component/energising module interactions has been unclear because of the absence of detectable sequence similarity between the different S-components. The high-resolution (2.0 Å, beamline ID23-1) crystal structure of ThiT that we determined together with the crystal structure of RibU [4] allowed us to elucidate how different S-components interact with the same energising module.

ThiT contains six hydrophobic helical segments that cross the membrane (Figure 110). A part of the loop connecting membrane helices 1 and 2 is also embedded in the lipid bilayer, and may play an important mechanistic role in the translocation of thiamin across the membrane.

Comparison of ThiT with the structure of RibU (determined to 3.6 Å resolution) showed that the two proteins have a similar fold in spite of the lack of sequence similarity (14% identity). Membrane-spanning segments 1, 2 and 3 superimpose well, whereas segments 4 and 5 adopt different conformations. The latter are intimately involved in substrate binding, and we hypothesise that structural divergence in this region is required to bind different, chemically-unrelated substrates with high affinity (Figure 111). The structural similarity between the membrane-embedded helices 1-3 of ThiT and RibU suggests that this region is involved in the interaction with the energising module subunit EcfT. The structural alignment revealed a previously unnoticed conserved motif (AxxxA, where x is any amino acid) in transmembrane helix 1 (Figure 111). Similar motifs (e.g. GxxxG) have been shown to mediate interactions between transmembrane helices. We showed that the AxxxA motif in the S-components is important for interaction with the membrane embedded EcfT subunit: mutation of either alanine into tryptophan completely disrupted the interaction between ThiT and the energising module.

Further structural and biochemical studies on the entire complexes will now be necessary to elucidate the complete mechanism of transport. ECF transporters are exclusively prokaryotic and numerous human pathogens are dependent on the uptake of ECF substrates for survival. Structural and mechanistic understanding of ECF transporters may therefore enable the development of new antibiotics that target these proteins.

**References**

[1] A.L. Davidson, E. Dassa, C. Orelle and J. Chen, *Microbiol. Mol. Biol. Rev.* **72**, 317-64, table (2008).  
 [2] D.A. Rodionov, P. Hebbeln, A. Eudes, J. ter Beek, I.A. Rodionova, G.B. Erkens, D.J. Slotboom, M.S. Gelfand, A.L. Osterman, A.D. Hanson and T. Eitinger, *J. Bacteriol.* **191**, 42-51 (2009).  
 [3] J. Ter Beek, R.H. Duurkens, G.B. Erkens and D.J. Slotboom, *J. Biol. Chem.* **286**, 5471-5 (2011).  
 [4] P. Zhang, J. Wang and Y. Shi, *Nature* **468**, 717-720 (2010).

	<<	helix 1	>>	
ThiT	---	MSNSKFNVRLLTEIAFMALAFIISLIPNTVYG--	33	
RibU	-----	MSKTRRMVLIAMLAALSSTILL-PILQFPL-	29	
BioY	----	MTNNQKVRTLYSAFMTAFIILGFLPGIPIGF-	33	
PanT	-----	MKRKASDVAILAIFIAIMVVQLFTQFVINV-	32	
HmpT	--	MKLMNDNKNIKKLTLLAIWTALTFVLGRLTFPI---	33	
QeuT	-----	MKKSPTYDIVTIAIYAALYVILTMTPGLSAIS-	32	
NiaX		TQMTQTKKAKVRNLIIAAMLTLGLIPMMPVKLIIG	38	
BioY2	----	MQN-TKLYSLTLIALGAAITAVLSPLA-IPIGI-	31	
		: : * : * : ::		

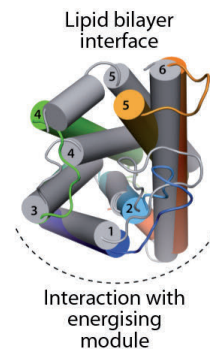


**Fig. 111:** Multiple-sequence alignment of the first transmembrane helices from all S-components in *L. lactis*. Highlighted in red is an alanine motif that is exposed to the predicted EcfT interface in ThiT. Right: Superposition of the RibU (grey; PDB entry 3P5N, [4]) and ThiT crystal structures.



## ■ The molecular details of receptor-drug interactions in the treatment of asthma and heart conditions

The ‘fight-or-flight’ response allows one to deal with abnormally stressful situations and is mediated predominantly by the hormones adrenaline and noradrenaline that are released from the adrenal gland. These hormones are the core of the physiological responses observed under stress. For example, noradrenaline binds to a specific receptor on the surface of heart cells, the  $\beta_1$ -adrenergic receptor ( $\beta_1$ AR), and increases the rate of the heartbeat. Adrenaline binds to a very similar receptor in the lungs, the  $\beta_2$ -adrenergic receptor ( $\beta_2$ AR), where it acts to dilate the airways, thus allowing easier breathing. Both adrenaline and noradrenaline are known as agonists, as they activate their respective receptors, but how this happens at the molecular level was unclear until 2011, when a series of papers were published that showed for the first time how agonists interact with receptors.

$\beta_1$ AR and  $\beta_2$ AR are both G protein-coupled receptors (GPCRs), which are characterised by having seven transmembrane regions and extracellular N-terminus. Although only 35–45 kDa in size, these receptors have proven very difficult to crystallise because they are extremely dynamic, undergoing a conformational change between an inactive R state and the active R\* state even in the absence of ligands. This dynamism undoubtedly contributes to their instability in detergents, which are necessary to purify and crystallise any membrane protein. Unfortunately, the most useful detergents for crystallisation are often those that are most likely to denature the protein. We developed a thermostabilisation strategy that significantly improved the stability of receptors in short chain detergents. This allowed us to crystallise  $\beta_1$ AR for the first time [1]. Subsequently, we crystallised the same receptor mutant bound to eight different ligands that either mimic the actions of noradrenaline, *i.e.* agonists, or block the binding of noradrenaline, *i.e.* antagonists. Most of the compounds we used are either already prescribed as drugs for the treatment of heart

conditions (antagonists of the  $\beta_1$ AR), *e.g.* beta blockers, or are used to treat asthma (agonists of  $\beta_2$ AR).

The high-resolution structures of the thermostabilised  $\beta_1$ AR mutant bound to the agonist isoprenaline highlights how little conformational change is required by the receptor to increase the probability of formation of the activated state. The initial binding of the agonist causes a contraction of the ligand binding pocket of the receptor by 1 Å, which, combined with a change in rotamer conformation of a single serine residue (Ser215), is sufficient to induce the formation of the activated receptor. Once activation has occurred, a G protein can bind and be activated, which initiates a cascade of further reactions in the cytoplasm, ultimately leading to a physiological response by the cell. The small changes involved in receptor activation are exactly what would be expected for a sensitive system that can detect and amplify signals from the binding of a low molecular weight ligand.

The biological insights from the structures are paralleled by the insights that may help

### Principal publication and authors

T. Warne (a),  
R. Moukhametzianov (a),  
J.C. Baker (b), R. Nehmé (a),  
P.C. Edwards (a), A.G.W. Leslie (a),  
G.F.X. Schertler (a,c) and  
C.G. Tate (a), *Nature* **469**, 241–244  
(2011).

(a) MRC Laboratory of Molecular  
Biology, Cambridge (UK)

(b) Institute of Cell Signalling,  
University of Nottingham (UK)

(c) Present address: Paul Scherrer  
Institut, Laboratory of Biomolecular  
Research, Villigen (Switzerland)

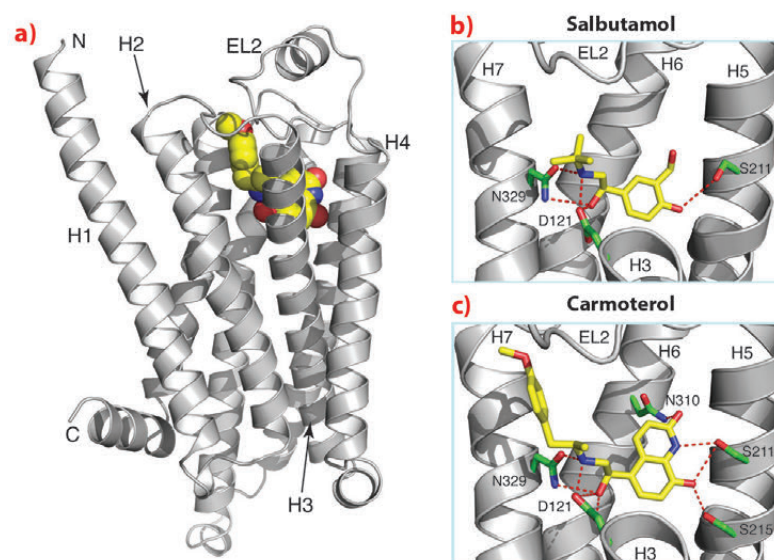


**Fig. 112:** Structure of  $\beta_1$ AR bound to agonists used for the treatment of asthma. a) Overall structure of the receptor, b) structure with salbutamol (Ventolin) and c) structure with carmoterol. Parts of helices H2, H3 and H4 have been removed in (b) and (c) for clarity.



in the design of new ligands that may be more effective treatments for asthma or heart conditions. For example, one of the structures we have determined of  $\beta_1$ AR is bound to carmoterol, which was in phase III clinical trials as a one-shot per day treatment for asthma. Comparison of the carmoterol-bound  $\beta_1$ AR structure with that with salbutamol (Ventolin, currently used for treating millions of asthmatics worldwide) bound shows that there are additional interactions in the former that may decrease the rate of dissociation of carmoterol from the receptor and may, therefore, be instrumental in prolonging its biological activity (**Figure 112**).

GPCRs comprise an exciting group of receptors with regard to their huge potential for developing new therapeutics to a wide variety of diseases and

afflictions. Determining their structures will accelerate the development of new therapeutics. The microfocus beamline **ID23-2** is an essential tool in this process, as the crystals obtained are invariably small and very radiation sensitive. The implementation of user-friendly scanning procedures for defining the best-diffracting part of a crystal or, in the case of lipidic cubic phases, to actually find the crystal in an opaque background, has been essential to improve throughput and to allow efficient screening of the hundreds of crystals that is typically required to collect a complete data set to high-resolution. None of the structures of GPCRs determined to date would have been possible without the technological advances and dedicated personnel that make these facilities available to structural biologists.

#### References

[1] T. Warne, M.J. Serrano-Vega, J.G. Baker, R. Moukhametzianov, P.C. Edwards, R. Henderson, A.G.W. Leslie, C.G. Tate and G.F.X. Schertler, *Nature* **454**, 486-491 (2008).

#### Principal publication and authors

R.G. Efremov (a,b) and L.A. Sazanov (a), *Nature* **476**, 414-420 (2011).

(a) Medical Research Council Mitochondrial Biology Unit, Cambridge (UK)

(b) Present address: Max-Planck Institute for Molecular Physiology, Dortmund (Germany)

## ■ Structure of the membrane domain of respiratory complex I

Mitochondria are “cellular power plants” supplying energy for the organism. They contain their own DNA, about half of which codes for proteins of mitochondrial complex I, the first and largest enzyme in the respiratory “power chain”. Defects in mitochondrial DNA are one of the most common types of human genetic disorder. They occur in about 1 in 5,000 of the population and the majority involve respiratory complex I. So far there is no treatment for the debilitating diseases resulting from these disorders, which include neurological impairment, deafness, blindness, muscle weakness and cardiovascular disease.

To understand the molecular basis of such diseases, as a starting point for drug development, we need to know the structure of Complex I. Complex I transfers two electrons from NADH to quinone and couples this process to the translocation of four protons across the membrane. It plays a central role in cellular energy production, providing about 40% of the proton flux required for ATP synthesis. Mitochondrial complex I consists of 45 subunits, whilst the prokaryotic enzyme is simpler, consisting of 14 “core” subunits with a total mass of about 550 kDa.

The prokaryotic enzyme represents an important ‘minimal’ model of human complex I.

Complex I, due to its sheer size, resisted the efforts to determine its structure for a long time. Our earlier crystal structures of the hydrophilic domain of complex I from *Thermus thermophilus* established the electron transfer pathway from NADH through flavin mononucleotide (FMN) and seven iron-sulfur (Fe-S) clusters to the likely quinone binding site [1]. Recently we have determined the architecture of the entire complex at 4.5 Å resolution [2]. Now, we have succeeded in the determination of the crystal structure of the membrane domain, at 3.0 Å resolution. Most of the data was collected at beamline **ID29**. The membrane domain includes six subunits containing a total of 55 transmembrane (TM) helices and represents, to date, one of the largest membrane proteins for which the structure has been solved using X-ray crystallography.

The crystal structure reveals that the fold of three largest subunits (NuoL/M/N; homologous to Mrp antiporters) is novel, with two inverted structural repeats of five

#### References

[1] L.A. Sazanov and P. Hinchliffe, *Science* **311**, 1430-1436 (2006).  
[2] R.G. Efremov, R. Baradaran and L.A. Sazanov, *Nature* **465**, 441-445 (2010).



TM helices arranged, unusually, face-to-back. Each repeat includes a discontinuous TM helix, containing essential charged residues, and forms half of a channel across the membrane. A network of conserved polar residues connects the two half-channels, which completes the proton translocation pathway. Unexpectedly, lysines rather than carboxylate residues appear to act as the main elements of the proton pump in these subunits. The fourth likely proton-translocation channel is found at the interface of subunits NuoN/K/J/A and contains two conserved glutamates in the middle of the membrane.

Antiporter-like subunits are connected linearly, like carriages in a train. Due to their internal symmetry, functionally important residues interact between the subunits, allowing communication of conformational changes (Figure 113). The subunits are held together on one side of the domain by an unusual long amphiphatic helix HL and on the other side by a  $\beta$ H motif consisting of connected in series  $\beta$ -hairpins and helices. Both structural elements interact with flexible discontinuous TM helices, containing essential lysine residues.

Thus, the crystal structure shows that the enzyme functions by connecting different parts of the protein through mechanical coupling elements, akin to the piston coupling rods in a steam engine (Figure 114). The crystal structure also elucidates, for the first time, how the most common mutations in the membrane subunits lead to human disorders. The mutations are found in areas of the protein critically important for energy transduction. This structural knowledge should greatly help scientists developing drugs against mitochondrial diseases.

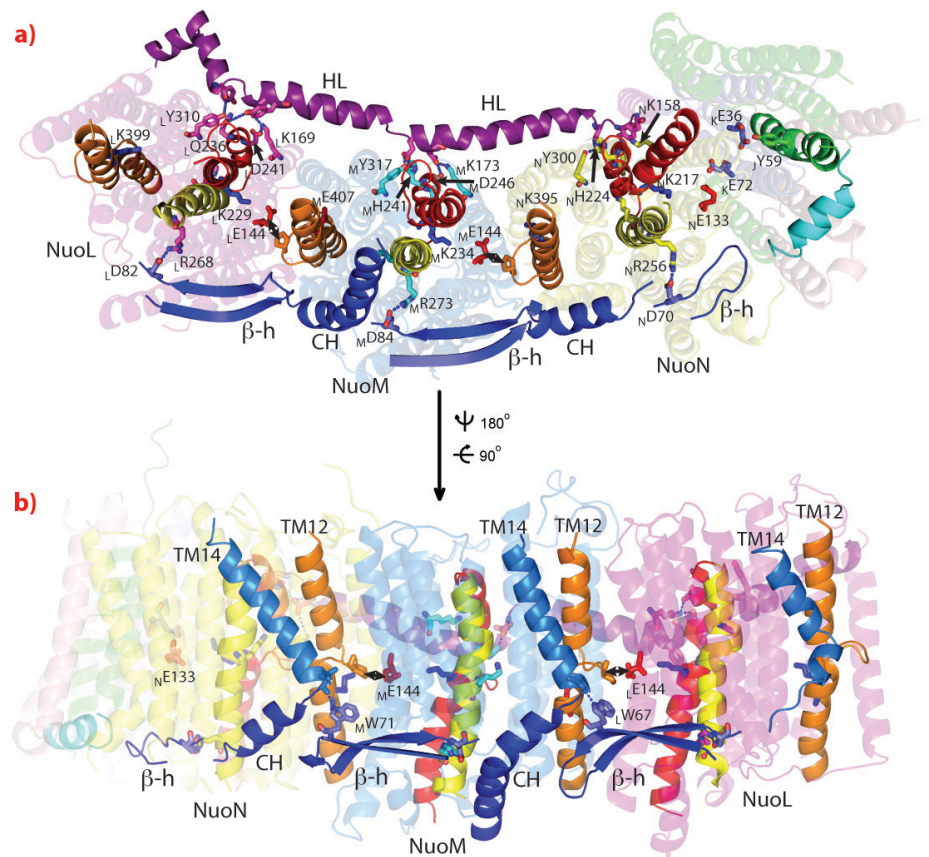
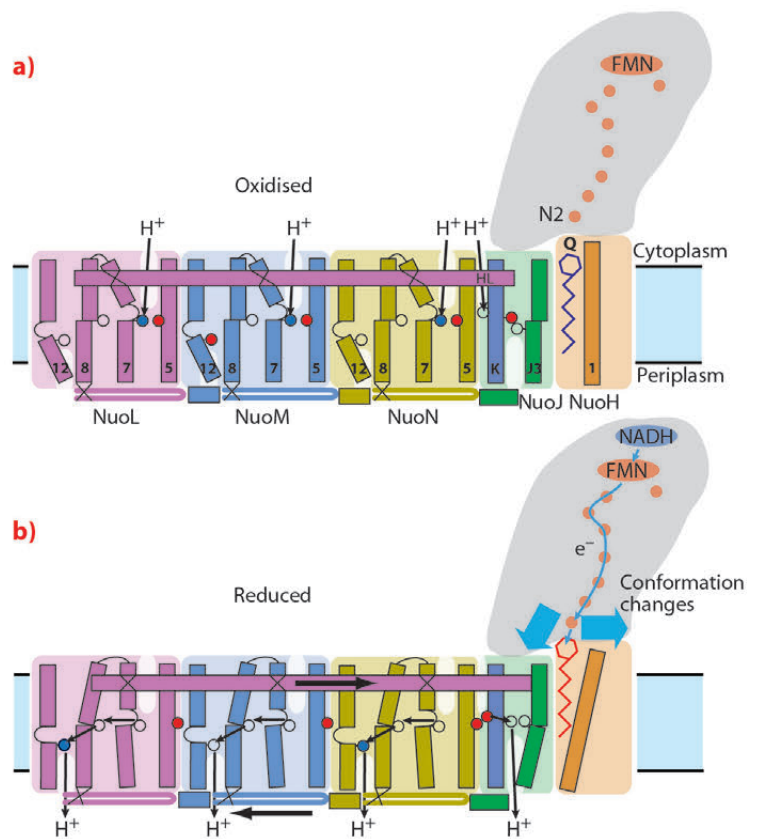


**Fig. 113:** Interactions between subunits of the membrane domain of Complex I. a) View from the periplasm; b) view in the membrane. Helix HL is in purple and the  $\beta$ -hairpin-helix element ( $\beta$ -h and CH) in blue. Helices likely involved in conformational changes are shown in red ( $_{LMN}$  TM7), orange (TM12), yellow (TM8) and green ( $_J$  TM3). Essential residues are shown as sticks and labelled (prefix indicates subunit).

**Fig. 114:** Proposed mechanism of complex I. a) Oxidised state. b) Reduced state. Conformational coupling between electron transfer and proton translocation is mediated by helix HL (cytoplasmic side) and the  $\beta$ H element (periplasmic side). TM helices are numbered. Crucial charged residues are indicated by red/empty circles (Glu) and empty/blue circles (Lys) for unprotonated/protonated residue, respectively. In NuoL/M/N, LysTM7 from the first half-channel is assumed to be protonated in the oxidised state. Upon reduction it donates its proton to the connecting Lys/HisTM8 and then onto Lys/GluTM12 from the second half-channel. Lys/GluTM12 ejects its proton into periplasm upon return from reduced to oxidised state. A fourth proton per cycle is translocated at the interface of NuoN, K and J.





### Principal publication and authors

K. Domanska (a,b),  
S. Vanderhaegen (a,b),  
V. Srinivasan (a,b), E. Pardon (a,b),  
F. Dupeux (c), J.A. Marquez (c),  
S. Giorgetti (d), M. Stoppini (d),  
L. Wyns (a,b), V. Bellotti (d) and  
J. Steyaert (a,b), *Proc Natl Acad Sci U S A*, **108**, 1314-9 (2011).

(a) Department of Molecular and Cellular Interactions, Vlaams Instituut voor Biotechnologie, Brussels (Belgium)

(b) Structural Biology Brussels, Vrije Universiteit Brussel (Belgium)

(c) Grenoble Outstation, European Molecular Biology Laboratory and Unit of Virus Host-Cell Interactions, Grenoble (France)

(d) Department of Biochemistry, University of Pavia (Italy)

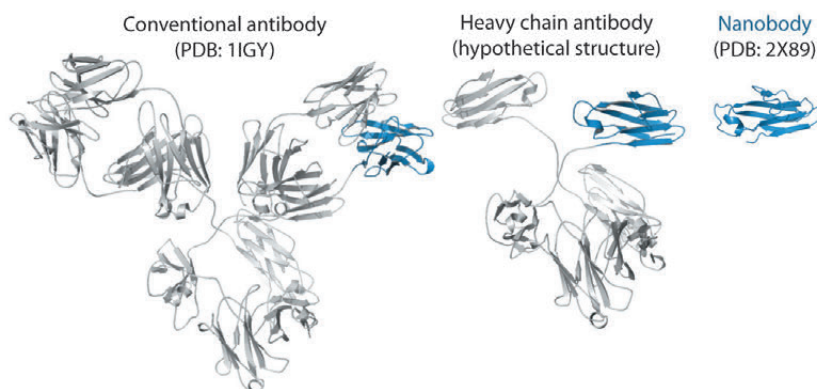
## Nanobody aided crystallisation of $\beta$ 2m amyloidogenic intermediate

A number of severe contemporary diseases including Alzheimer's disease, Parkinson's disease, type 2 diabetes and dialysis related amyloidosis (DRA) are associated with the structural conversion of initially innocuous proteins into insoluble amyloid fibrils. Understanding the molecular basis of this process is crucial for the development of drugs that prevent and/or cure amyloid diseases. However atomic-level investigation of the key intermediates of amyloidogenesis remains one of the supreme challenges of structural biology. This is due to the nature of the process, which may be described as a dynamically evolving equilibrium between large numbers of structural species. These intermediates have highly diverging sizes and are present in uneven amounts and timeframes.  $\beta$ 2-microglobulin ( $\beta$ 2m) is a well-documented amyloidogenic protein involved in onset of DRA. This type of amyloidosis develops in patients with kidney failure undergoing long-term hemodialysis. Amyloid fibrils are composed mostly of full-length  $\beta$ 2m but an N-terminally truncated variant also accumulates in the protein deposits in the musculoskeletal system of DRA patients.

To trap and characterise the early intermediates of  $\beta$ 2m fibril assembly, we used single domain antibodies. The antigen-binding site of these antibodies consists of a single domain, referred to as VHH or nanobody (**Figure 115**). Nanobodies are derived from heavy chain only antibodies that along with conventional antibodies naturally occur in camelids [1]. We generated a panel of anti- $\beta$ 2m nanobodies and found that some of the nanobodies stabilise the amyloidogenic  $\beta$ 2m variant ( $\Delta$ N6 $\beta$ 2m)

abolishing its propensity to fibrillate. One of these nanobodies proved to be instrumental in solving the crystal structure of a dimeric intermediate of  $\beta$ 2m fibrillation process (**Figure 116a**). This high-resolution structure (2.2 Å; beamline ID29) confirms the predicted domain swapped nature of the early amyloidogenic intermediate and explains the many local structural perturbations (mutations, deletions, ligand binding) that have been associated with the transition of the soluble  $\beta$ 2m into insoluble fibrils. The properties of the swapped dimer provide new insights on the elongation mechanism by self-templated growth, leading to protofibrils and ultimately amyloids. During the self-association of  $\Delta$ N6 $\beta$ 2m, two hinges that correspond to the heptapeptide NHVTL SQ, refold into extended  $\beta$ -strands and stack into a novel two-stranded anti-parallel  $\beta$ -sheet. This heptapeptide forms amyloids in isolation demonstrating that this peptide by itself has a high propensity to form amyloid structure upon exposure [2]. In the newly formed two-stranded sheet, the backbone donor and acceptor sites of Val85 and Leu87 are exposed to solvent (**Figure 116b**) and are prone to stack with other  $\beta$ -strands in a parallel or antiparallel configuration. Indeed, other strands may associate perpendicular to build large intermolecular  $\beta$ -sheets that run parallel to the axis of the growing oligomers (**Figure 116c**). It thus appears that the swapped dimer can serve as a structural nucleus for the growth of the cross- $\beta$  spine of elongating fibrils by templating the hydrogen-bonding network connecting the strands. The remaining core domains may decorate the spine and protect it from solvent.

**Fig. 115:** Ribbon representations of a conventional antibody, a heavy chain antibody and a nanobody. The variable domain of the heavy chain is depicted in blue.





Most remarkably,  $\Delta N6\beta 2m$  swapped dimer meets many characteristics that have been attributed to prefibrillar intermediates of  $\beta 2m$  fibrillogenesis. Phe30, His31 and Pro32, three residues particularly involved in amyloidogenesis are located on the tip of the first loop that connects strands B and C. In the native monomer, parts of all three connecting loops are shielded from solvent by the N-terminal peptide that is missing in  $\Delta N6\beta 2m$  variant, explaining why the truncated species is less stable and unlike wild-type protein has a higher tendency to self-associate and forms amyloid fibrils even at physiological pH [3].

The identification and characterisation of oligomers preceding the formation of fibrils is of particular interest because evidence is growing that these species are likely to play a critical role in the pathogenesis of protein deposition diseases. The use of nanobodies to trap a single oligomeric intermediate of a dynamically evolving equilibrium between large numbers of conformational species

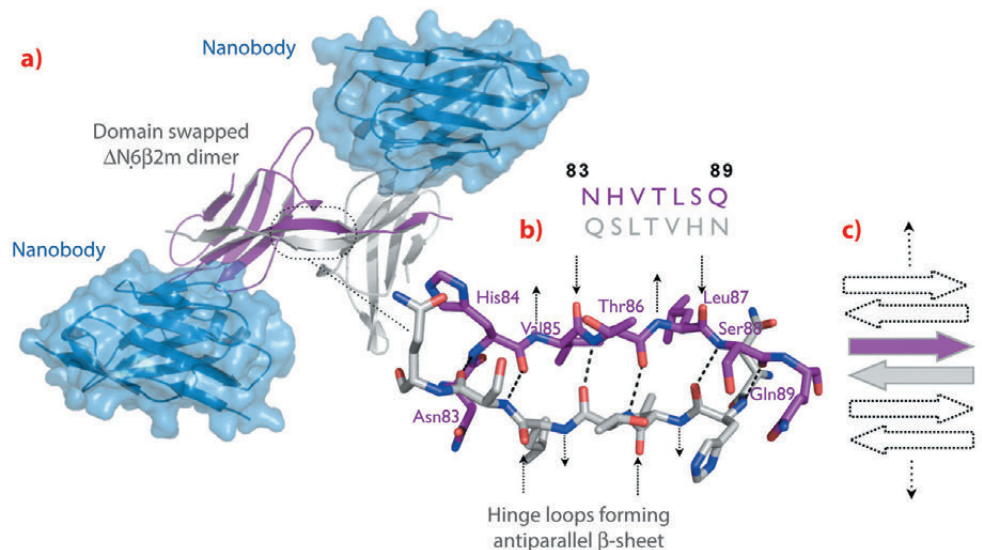


**Fig. 116:** Structure of the  $\Delta N6\beta 2m$  swapped dimer. a)  $\Delta N6\beta 2m$  swapped dimer stabilised by two nanobody molecules. b) Atomic structure of the open interface of the  $\Delta N6\beta 2m$  dimer. The main chain NH and CO groups of His84, Thr86, and Ser88 are hydrogen-bonded to the carbonyls and the amides of Ser88, Thr86, and His84 on the adjacent strand, respectively. The backbone donor and acceptor sites of Val85 and Leu87 are exposed to solvent (indicated by arrows). c) Cartoon presenting the possible association of  $\beta$ -strands causing self-templated growth of the fibril core.

along the amyloidosis pathway may be broadly applicable in the study of other dynamic systems characterised by structural diversity or in the prevention or treatment of amyloid diseases.

#### References

- [1] Hamers-Casterman *et al.*, *Nature* **363**, 446–448 (1993).
- [2] Ivanova *et al.*, *Proc Natl Acad Sci USA* **103**, 4079–4082 (2006).
- [3] Esposito *et al.*, *Protein Sci* **9**, 831–845 (2000).

## Structures of SAS-6 suggest its organisation in centrioles

Centrioles are nine-fold symmetric, cylinder-shaped organelles that organise centrosomes and that are strictly required as a template for cilia and flagella. Abnormalities in these structures can result in numerous human diseases like ciliopathies or infertility. Thus, a detailed understanding of centriole architecture and formation is an important goal [1].

The diameter of centrioles and their symmetry is determined early on in their assembly by a so-called cartwheel structure [2]. This cartwheel consists of a central ring-like hub and nine spokes that radiate outwards to the periphery of centrioles where centriolar microtubule triplets (Figure 117a) are found. Through an elongation process and further additions of components, mature centrioles are subsequently formed.

Since the cartwheel structure provides a scaffold involved in the establishment of the symmetry and diameter of centrioles, understanding the structural organisation of cartwheels should reveal important aspects of centriole formation. A prime candidate for a key player in this respect is the centriolar protein SAS-6. SAS-6 is found at the hub of the cartwheel and is required for its formation. It is found in all organisms that have centrioles and, in all systems tested so far, is essential for proper centriole formation [2].

To understand how SAS-6 might organise the centriolar cartwheel, we obtained high-resolution crystal structures of SAS-6 fragments at beamlines ID29 and BM14. These structures show that SAS-6 consists of a globular N-terminal head domain and a rod like coiled-coil domain that follows

#### Principal publication and authors

M. van Breugel (a), M. Hirano (b), A. Andreeva (a), H.-a. Yanagisawa (b), S. Yamaguchi (b), Y. Nakazawa (b,d), N. Morgner (c), M. Petrovich (a), I.-O. Ebong (c), C.V. Robinson (c), C.M. Johnson (a), D. Veprintsev (a,e) and B. Zuber (a), *Science* **331**, 1196 (2011).  
(a) Medical Research Council – Laboratory of Molecular Biology, Cambridge (UK)  
(b) Department of Biological Sciences, University of Tokyo (Japan)  
(c) Chemistry Research Laboratory, University of Oxford (UK)  
(d) Current Address: Department of Biosciences, School of Science, Kitasato University, Sagamihara (Japan)  
(e) Current Address: Paul Scherrer Institut, Villigen (Switzerland)





### References

- [1] E.A. Nigg and J.W. Raff, *Cell* **139**, 663 (2009).  
 [2] P. Strnad and P. Goczy, *Trends Cell Biol* **18**, 389 (2008).

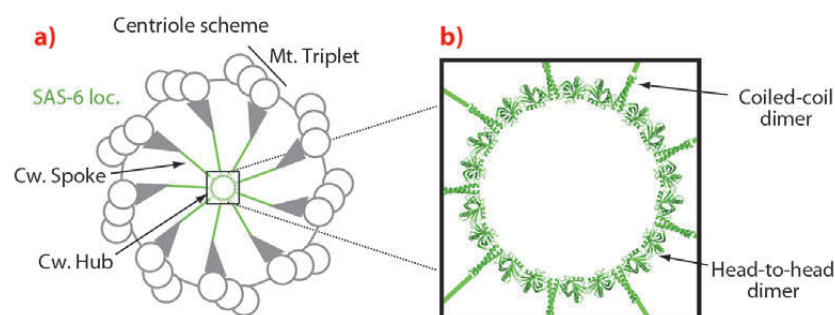
**Fig. 117:** a) Centriole scheme with peripheral microtubule triplets (Mt. Triplet) and central cartwheel structure (Cw.) with hub and spokes. In green is the location of SAS-6. A 9-fold symmetric SAS-6 ring model is placed at the cartwheel hub. b) A close-up view of the cartwheel hub. Solid green lines indicate that the SAS-6 coiled-coil domain could, theoretically, protrude to the cartwheel periphery if it is fully extended.

in sequence. Both domains were found to form homodimers: The N-terminal domain formed a slightly curved head-to-head dimer while the coiled-coil domain formed a canonical elongated coiled-coil dimer. We confirmed these interactions in solution and showed that the coiled-coil dimer is stable while head-to-head dimerisation occurs with a rather low affinity. Both interactions are biologically relevant and are essential for SAS-6 function *in vivo*.

Modelling these interactions in SAS-6 resulted in curved oligomers that were compatible with a 9-fold ring with similar dimensions to that of cartwheel hubs observed *in vivo* (Figure 117b).

Consistent with this model, we found that recombinant SAS-6 constructs do indeed form higher-order oligomers in solution and that they, as judged by cryo-EM, can adopt structures similar to centriolar cartwheels.

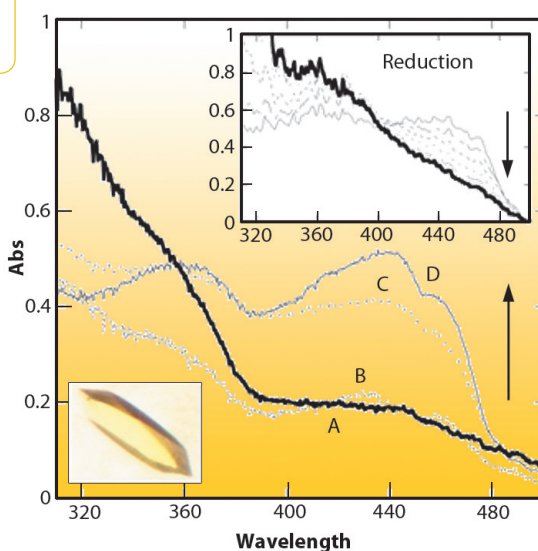
In summary, we have shown that, through self-association, a single protein – SAS-6 – can account for the organisation of centriolar cartwheel centres and thereby contribute to the establishment of centriolar symmetry and dimensions. The challenge ahead is to determine how the other key components of centriole assembly contribute to this process. High-resolution crystal structures of these components will undoubtedly play a decisive role in this.



### Principal publication and authors

R. Orru (a), H.M. Dudek (b),  
 C. Martinoli (a),  
 D.E. Torres Pazmino (b),  
 A. Royant (c,d), M. Weik (c,d),  
 M.W. Fraaije (b) and A. Mattevi (a),  
*J. Biol. Chem.* **286**, 29284 (2011).  
 (a) University of Pavia (Italy)  
 (b) University of Groningen (The Netherlands)  
 (c) Institut de Biologie Structurale, Grenoble (France)  
 (d) ESRF

**Fig. 118:** Microspectrophotometry of PAMO crystals (inset) measured at 100 K. X-ray exposure of the crystals leads to the reduction of the flavin moiety (spectrum A, bold line and inset). Reduced crystals can then be re-oxidised by soaking at room-temperature in aerated solutions as shown by spectra B, C, D which were collected from crystals that were cryo-cooled 2, 4, and 6 minutes after starting the re-oxidation process.



## Structural and spectroscopic observation of an enzyme at work

At the end of the 19<sup>th</sup> century, Baeyer and Villiger discovered that cyclic ketones react with oxidants such as peroxymonosulphuric acid to yield

lactones. Baeyer-Villiger reactions are of enormous value in synthetic organic chemistry and the number of their applications is countless. Several microorganisms produce enzymes able to catalyse Baeyer-Villiger reactions. Amongst these, Baeyer-Villiger monooxygenases are FAD-dependent proteins that use NADPH and molecular oxygen to insert an oxygen atom into their substrate. In this context, it must be emphasised that oxygen biocatalysis and regulation is crucial to a variety of biochemical processes in Nature. Despite extraordinary research progress, the structural and biochemical determinants of specific and efficient oxygen reactivity remain poorly understood [1]. In recent years, we have identified a microbial Baeyer-Villiger enzyme, phenylacetone monooxygenase, which offers several unique and attractive features: it is thermostable, tolerant



towards organic solvents, and catalyses enantioselective Baeyer-Villiger oxidations and sulfoxidations. We were able to generate several intermediate states of this coloured enzyme and to characterise them by X-ray crystallography and single-crystal microspectrophotometry both at the synchrotron beamline (ID14-1, online) and at the dedicated Cryobench laboratory (ID29S, offline [2]).

The experimental strategy recruited otherwise detrimental X-ray induced changes to biomolecules to trigger reduction of the X-ray sensitive flavin moiety of phenylacetone monooxygenase (Figure 118). The resulting intermediate state was captured and structurally characterised by X-ray crystallography using diffraction data collected at 100K. These studies highlight the fascinating ability of Baeyer-Villiger monooxygenases to catalyse a complex, multi-step catalytic reaction. The reaction includes the concerted action of two cofactors (NADPH and FAD) and the protein active site to subsequently promote flavin reduction, oxygen activation, tetrahedral intermediate formation (Figure 119), and product synthesis and release.

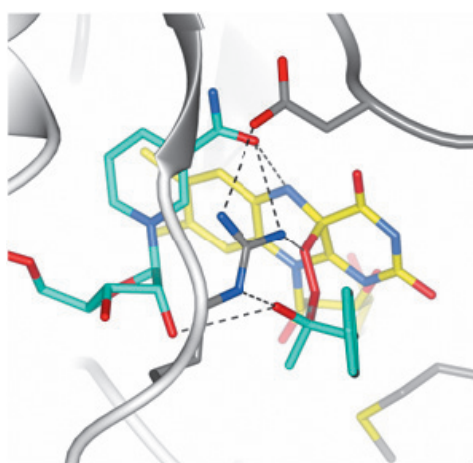


**Fig. 119:** Three-dimensional structural model of the crucial oxygenating “Criegee” intermediate of phenylacetone monooxygenase (PAMO).

The emerging picture is that these enzymes are mainly oxygen-activating “Criegee-stabilising” catalysts that act on any chemically suitable substrate that can diffuse into the active site. This emphasises their potential value as toolboxes for biocatalytic applications.

A movie related to this research is available at [www.unipv.it/biocry](http://www.unipv.it/biocry).

#### Acknowledgements

This research is part of a more comprehensive effort aimed at exploiting Baeyer-Villiger enzymes for applications in industrial biocatalysis and green chemistry within the framework of a project “Oxygreen”, supported by the EU-FP7.

#### References

- [1] R. Baron, J.A. McCammon and A. Mattevi, *Curr. Opin. Struct. Biol.* **19**, 672-679 (2009).
- [2] J. McGeehan, R.B. Ravelli, J.W. Murray, R.L. Owen, F. Cipriani, S. McSweeney, M. Weik and E.F. Garman, *J. Synchrotron Radiat.* **16**, 163-172 (2009).

## ■ Structure of human complement iC3b revealed by 3D-electron microscopy and small-angle X-ray scattering

The complement system comprises over thirty soluble and membrane-associated proteins that constantly monitor the blood and tissue interstitial fluids on the lookout for pathogens, apoptotic cells and immune complexes. Central to the innate immune system, complement also plays a role in the modulation of the adaptive immune system. Activation of the central complement component 3 (C3) by the alternative pathway C3 convertase, a transient protease complex formed by the active forms of C3 (C3b) and factor B, results in an amplification cascade that leads to massive deposition of C3b onto the targeted surface, typically a bacterium surface. Surface covalent attachment of C3b upon activation involves a dramatic conformational change that exposes a highly-reactive thioester group that is

sterically masked in C3. Ultimately, C3b deposition at high density contributes to the recruitment of the so-called membrane attack complex (MAC) leading to cell lysis and clearance. Protection of self-surfaces from excessive complement activation, which would result in unwanted organ damage, is achieved by fast inactivation of the C3 convertase by complement regulators. A prime route for C3 convertase inactivation is the proteolytic cleavage of C3b to iC3b, catalysed by factor I (FI) and appropriate cofactors. A final proteolytic cleavage converts iC3b into two independent molecules, C3c and C3dg, the latter of which remains attached to a membrane. Interestingly, C3b inactivation by FI-mediated proteolysis not only prevents complement consumption and collateral damage to self-cells but

#### Principal publication and authors

M. Alcorlo (a), R. Martínez-Barricarte (a,b), F.J. Fernández (a), C. Rodríguez-Gallego (a), A. Round (c), M.C. Vega (a), C.L. Harris (d), S. Rodríguez de Córdoba (a,b) and O. Llorca (a), *Proc Natl Acad Sci USA* **108**, 13236–13240 (2011).  
(a) CAM Complement Programme (S2010/BMD-2316), Centro de Investigaciones Biológicas (CIB-CSIC), Madrid (Spain)  
(b) Centro de Investigación Biomédica en Enfermedades Raras, Madrid (Spain)  
(c) European Molecular Biology Laboratory (EMBL), Grenoble (France)  
(d) Cardiff University School of Medicine, Cardiff (UK)



### References

- [1] N. Nishida, T. Walz and T.A. Springer, *Proc Natl Acad Sci USA* **103**, 19737-19742 (2006).  
 [2] D.E. Isenman, *J Biol Chem* **258**, 4238-4244 (1983).

also generates active molecules, such as iC3b and C3dg, that can interact with leukocytes and stimulate phagocytic clearance of pathogens.

The prevailing model considers iC3b as a partially unfolded intermediate without a defined conformation [1], portrayed as two stable molecular fragments (C3c and C3dg) tethered to one another by an extended linker. This view is, however, at odds with early spectroscopic data [2] and the known role of iC3b as a specific ligand for the leukocyte complement receptors (CR), CR2, CR3 and CR4. Since a high-resolution structure of iC3b has remained elusive, we decided to piece together a medium-resolution structure using a combination of two powerful imaging techniques: single-particle electron microscopy, also known as three-dimensional electron microscopy (3D-EM), and small-angle X-ray scattering (SAXS). SAXS data were collected at the ESRF's BioSAXS station (ID14-3) using homogenously purified proteins at concentrations ranging from 1 to 5 mg/ml. We now show using 3D-EM that the overall architecture of iC3b at low resolution (24 Å) has a distinct, defined structure (Figure 120), in contrast with previous assumptions. Powerful 3D image reconstruction techniques and in-solution shape restoration methods independently converge upon the same overall structure (Figure 121), which reveals an unforeseen

conformational change. In stark contrast to the downward movement of the thioester-containing domain (TED) seen during C3 activation to C3b, in the iC3b 3D-EM structure this domain bounces back to relocate closer to its original position in C3. The macroglobulin (MG) ring at the core of iC3b however remains essentially unchanged with respect to C3b, indicating that it acts as a rigid scaffold while other domains are reoriented and translated. These features define a unique conformation that differentiates iC3b from C3 and C3b in overall shape and which has the potential for establishing distinctive protein-protein interactions with other complement components, regulators and receptors.

The iC3b structure that emerges from the 3D-EM and SAXS analysis explains an array of biochemical observations that were hard to reconcile with the more flexible 'beads-on-a-string' model of iC3b. In contrast to C3b, the conformational rearrangement observed in iC3b removes surfaces that had been previously identified in C3b as critical for the assembly of the C3 convertase and for recognition of FH and MCP, two complement regulators. Thus, distinctive C3b biological properties (such as the ability to form a C3 convertase) are notably absent in iC3b. Furthermore, the rearrangement exposes surface patches that are partially or totally occluded in C3b and absent in downstream fragments (C3c or C3dg), thereby creating new opportunities for iC3b to engage in interactions with receptors such as CR2, CR3 and CR4. This iC3b-specific interaction profile provides an underpinning for the biomedically relevant roles of iC3b in mediating adaptive immunological responses, stimulating B cell-mediated immunity, down-regulating inflammation and aiding the phagocytic clearance of pathogens.

**Fig. 120:** Molecular architecture of iC3b as obtained by 3D-EM compared to crystal structures of C3 (PDB 2A73) and C3b (PDB 2I07) after filtering to a resolution similar to that of the structure of iC3b. For clarity, structural regions have been coloured differently.

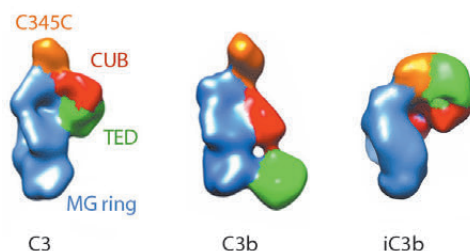
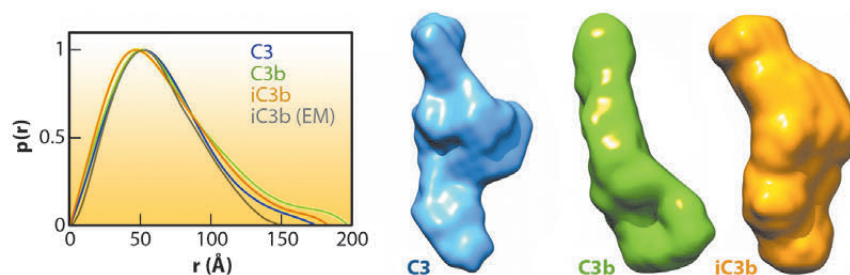


**Fig. 121:** The global shapes of C3, C3b and iC3b computed from experimental SAXS data and the associated pair distance distribution functions,  $P(r)$  (normalised to unity at their maxima). For comparison the  $P(r)$  for the 3D-EM structure of iC3b, as calculated from an equivalent bead model, is also shown (grey).







## Tracking the protein motions that harvest energy

Glycolysis is a metabolic pathway common to all organisms that breaks down sugar to release energy. The pathway is very ancient, does not require oxygen and is likely to have evolved before the accumulation of oxygen in the earth's atmosphere around 3 billion years ago. Phosphoglycerate kinase (PGK) catalyses the seventh step in glycolysis and is the first enzyme in the pathway to produce energy, rather than consume it, by the creation of adenosine triphosphate (ATP), a molecule that is a universal 'energy currency' used to do work in cells. PGK is a target for drugs against anaerobic pathogens, such as the causative agents of sleeping sickness and malaria, that depend solely on glycolysis for energy metabolism. Additionally, the phosphoryl-transfer activity of PGK is important in the processing of anti-retroviral pro-drugs effective against HIV and hepatitis. More recently, it has been found that PGK activity is also used as a signalling mechanism in oncogenesis. A complete understanding of the mechanism of this enzyme is thus essential to improve the processing of pro-drugs and to define its signalling activity in cancer. PGK is composed of two domains that bind two substrates separately (**Figure 122**). Crystal structures have defined both open and closed conformations for PGK [1] and suggest that a significant closure of the enzyme via a "hinge-bending" mechanism is required for catalysis to occur. By combining high resolution crystal structures solved from data collected on **ID14-2** with solution small angle X-ray scattering (SAXS) data collected on **ID14-3**, the extent and timing of the domain motions that lead to catalysis in PGK have now been elucidated.

SAXS measurements were used to examine the resting, open state of the enzyme when no substrates are bound as well as various states of the enzyme in catalytic turnover. By comparing the SAXS envelope determined for the protein in solution to the crystal structures we have obtained it was found that the apo-enzyme adopts a more open conformation than previously thought. During catalysis, the relative contribution of each state defined by a crystal structure to a SAXS scattering curve

can be obtained. Surprisingly, it was found that, during catalytic turnover, the enzyme spends only 7% of its time in the fully closed, catalytically active conformation and is in the fully open conformation most of the time. In order to define the origin of the stability of the open state, a model of the molecular interactions in this state was required. However, as SAXS data provide structural features to around only 15 Å resolution, the details necessary in such a model are missing. By refining the atomic positions of a crystal structure against SAXS data and applying deformable

### Principal publication and authors

L. Zerrad (a), A. Merli (b), G.F. Schröder (c), A. Varga (d), E. Graczer (d), P. Pernot (a), A. Round (e), M. Vas (d) and M.W. Bowler (a), *J. Biol. Chem.* **286**, 14040-14048 (2011).

(a) ESRF

(b) University of Parma (Italy)

(c) Forschungszentrum Jülich (Germany)

(d) Hungarian Academy of Sciences (Hungary)

(e) EMBL, Grenoble (France)

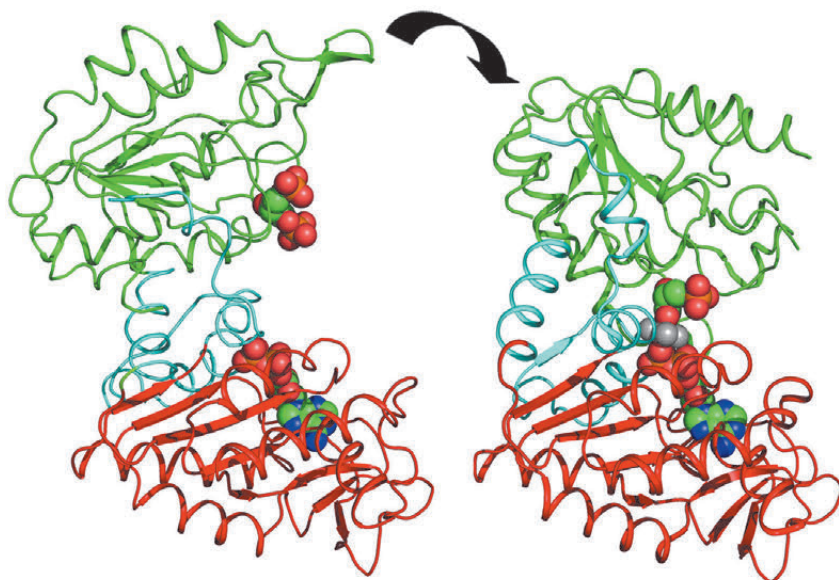


**Fig. 122:** Domain movements during PGK catalysis. The fully open resting state of the enzyme defined by DEN refinement against SAXS data (left) binds the substrates 1,3BPG in the N domain (green) and ADP in the C-domain (red). A rotation of 56° about a hinge region (blue) brings the substrates together. Here, catalysis occurs and ATP is produced (right).



**Fig. 123:** A hydrophobic spring regulates domain movement and catalysis in PGK. Surface representation of the transition from fully open to fully closed (left to right) conformations of PGK. Residues involved in hydrophobic interactions are coloured yellow. As the enzyme moves to the fully closed conformation a hydrophobic patch is progressively exposed to solvent.



elastic network (DEN) protocols [2], a molecular model of the fully open conformation observed in solution was obtained. Analysis of this model revealed that a large, solvent-exposed hydrophobic patch present in the closed conformation is masked from solvent in the open conformation (Figure 123). The occlusion of this hydrophobic region from solvent could account for the preference of PGK to adopt an open conformation, as this will be thermodynamically more stable and implies that, while the enzyme constantly moves between the open

and closed states, it has an energetic preference for the open conformation. The hydrophobic patch thus acts as a 'spring', constantly applying pressure to the closed conformation and leading to efficient release of products after catalysis. A model of cycling and catalysis may therefore be proposed where unliganded PGK remains open (ready to bind substrates, or release products) most of the time. The interpolation of crystal structures and SAXS data has allowed a high resolution time resolved model of catalysis to be proposed.

#### References

- [1] M.J. Cliff *et al.* *J. Am. Chem. Soc.* **132**, 6507-6516 (2010).  
 [2] G.F. Schröder *et al.* *Nature* **464**, 1218-1222 (2010).

#### Principal publication and authors

R.M.F. Leal (a), G.P. Bourenkov (b), O. Svensson (a), D. Spruce (a), M. Guijarro (a) and A.N. Popov (a), *J. Synchrotron Radiat.* **18**, 381-386 (2011).

(a) ESRF

(b) EMBL Hamburg Outstation, c/o DESY, Hamburg (Germany)

## Experimental procedure for the characterisation of radiation damage in macromolecular crystals

Radiation damage caused by ionising radiation is a constant source of concern when collecting X-ray diffraction data from crystals of biological macromolecules. As the dose absorbed by the crystal increases, changes in the unit cell parameters and crystal mosaicity, along with reduction in diffraction intensity of high-angle spots are observed. These radiation-induced

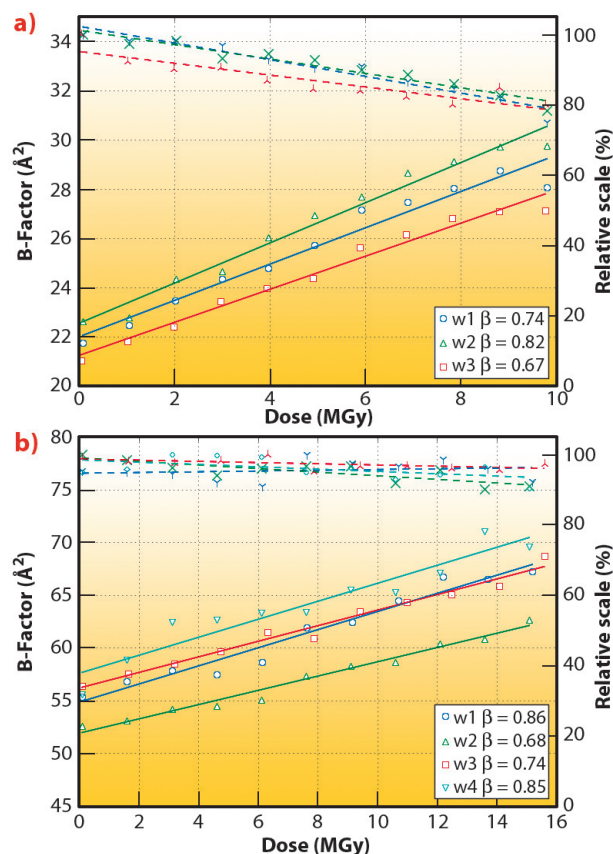
effects are sample-dependent and are proportional to the absorbed dose. Accurate dose estimation is thus essential to determine crystal tolerance to X-rays and consequently to determine an optimal data collection strategy.

When the sample sensitivity or X-ray beam calibration (flux, size, etc.) are

**Fig. 124:** Illustration of the plots resulting from the automated 'burn strategy' procedure for the determination of the radiation damage rate as applied to two protein crystals. Relative scales (overall scale normalised to the maximum value for all the wedges) and B-factors against nominal dose.

A linear fit of the B-factors vs dose is used to calculate the decay rate (or sensitivity coefficient). Full lines represent B-factors and dashed lines relative scales. For a thermolysin crystal (a), the procedure was applied three times yielding crystal sensitivity coefficients between 0.62 and 0.67  $\text{\AA}^2\text{MGy}^{-1}$ .

For a crystal of RecR from *Deinococcus radiodurans* (b), the sensitivity coefficients from the four collected wedges was found to vary between 0.68 and 0.86  $\text{\AA}^2\text{MGy}^{-1}$ .





uncertain, a reliable standardised procedure to calibrate a linear damage model is necessary through a preliminary experiment, sacrificing the whole or part of a crystal. We have therefore established a new procedure to determine crystal sensitivity to radiation damage that involves the measurement of the degree of damage in a sample or in part of it. The procedure describes the variation in scattering power (diffracted intensity and isotropic B factors) as a function of X-ray exposure time in a reliable and reproducible way. To achieve this, the data collection strategy planning software BEST [1], has been modified so that it can carry out a “burn strategy”: eleven successive data collection wedges, interleaved with long X-ray exposures to “burn” the crystal. The data wedges are collected from a relatively narrow crystal rotation range in order to minimise the influence of non-homogeneous irradiation. The data are finally analysed and interpreted to provide both a calibration and a linear B-factor decay model.

The method has been implemented at the ESRF MX beamlines in an automated procedure using the EDNA online data analysis framework [2] and the MxCuBE data collection control interface [3]. The EDNA framework provides an automated crystal characterisation and data collection protocol whereas MxCuBE allows the user to monitor and, if desired, to drive the whole process. To minimise the computing time, the diffraction images from the eleven successive data collection wedges are submitted to the ESRF batch scheduler and thus processed in parallel. The resulting plots and crystal decay coefficients are displayed to the user a few seconds after the last X-ray diffraction image is collected. The information extracted from this procedure can be directly used for optimal planning of data collection by the strategy software program BEST [1]. Using test crystals with well known radiation sensitivity, the procedure can also be used at the beamlines to verify and calibrate X-ray flux and beam size.

The observed dependency of the scale and B-factor on the X-ray dose presented in **Figure 124** clearly confirms the practical applicability of this method. The linearity in the observed B-factor dependency on dose strongly supports the choice of the decay rate as a generalised metric of

radiation damage. Such experiments are not critically dependent on an accurate knowledge of sample composition (and hence the absorbance), nor on the precise calibration of beam parameters. The method itself has proven to be easy to use and requires minimal user interaction. In practice, the time required for decay characterisation is defined by the incident photon flux density, *i.e.*, a complete procedure could be accomplished in about a minute or two on a modern undulator beamline.

#### References

- [1] G.P. Bourenkov and A.N. Popov, *Acta Cryst. D* **66**, 409-419 (2010).
- [2] M.-F. Incardona *et al.*, *J. Sync. Rad.* **16**, 872-879 (2009).
- [3] J. Gabadinho *et al.*, *J. Sync. Rad.* **17**, 700-707 (2011).





## X-ray Imaging

X-ray imaging techniques at third-generation synchrotron radiation facilities are continuously providing original scientific results for a wide variety of scientific topics. This is reflected by the content of the present chapter, which includes contributions from areas ranging from biology and biomedical applications to environment, materials and cultural heritage.

New science often relies on new technical developments: most of the ESRF scientists devote a substantial part of their research to new developments. This has resulted in an extended, state-of-the-art portfolio of synchrotron radiation based X-ray imaging techniques. The present Upgrade Programme of the ESRF will lead to the most advanced versions of both nano-imaging and nano-analysis (UPBL4, NINA) and of coherent and parallel beam imaging, with special emphasis on palaeontological applications.

This effort towards new and improved techniques is exemplified by a contribution that describes the development of a new two-dimensional X-ray grating interferometer for biomedical applications. But the technical enhancements are also, implicitly, present in most of the other contributions, where the improvement in spatial (in the few tens of nm range) and temporal resolution (a complete microtomographic image with a recording time in the second range), as well as the increasing use of “tailored” pink beam for microtomographic purposes, appear to be key ingredients to reach the desired scientific results. Let us point out, in addition, the continuous progress of techniques combining imaging and Bragg diffraction, which allow the limitations of classical “diffraction topography” to be overcome. Examples resulting from this combination are given

in recent publications. Scanning transmission X-ray image of the deformation structure inside a single grain in a polycrystalline Ni foil were, for instance, obtained at ID22 by using a submicrometre spot [1]. The combination of Bragg diffraction with a 3D approach [2] provided images allowing one to follow the inception of the deformation process of a grain in ice, as shown in the figure below, by the image corresponding to a “virtual slice” located in the middle of this crystal. This combination of diffraction and imaging also gives access to the study, in 3D, of the most deformed grains, which are of particular interest, by using the latest enhancements of the diffraction contrast tomography (DCT) technique [3].

In the first section on **biology and biomedical applications**, the direct investigation of the localisation of antimalaria drugs in red blood cells was made possible by the spatial resolution, in the few tens of nm range, now available on ID22. This trend will be pursued through the NINA project, mentioned above. The second contribution to this section studies vessel resistance to microbeam radiation as a function of vascular maturation, which is of high importance in order to prepare the clinical applications of microradiation therapy (MRT), a technique that takes full advantage of synchrotron radiation’s characteristics. Finally, a non invasive virtual extraction of entire teeth by using synchrotron radiation based microtomography with a coherent beam allowed an insight into the evolutionary biology of special present-day mammals that display continuous dental replacement.

The second section on **materials** shows the same variety of applications, which range from the microtomographic study of the multiphase network providing high-temperature strength to metallic alloys of industrial interest, to the combined use of several X-ray imaging techniques to characterise structured catalysts, and to the nano X-ray absorption spectroscopy investigation of Co in ZnO nanowires.

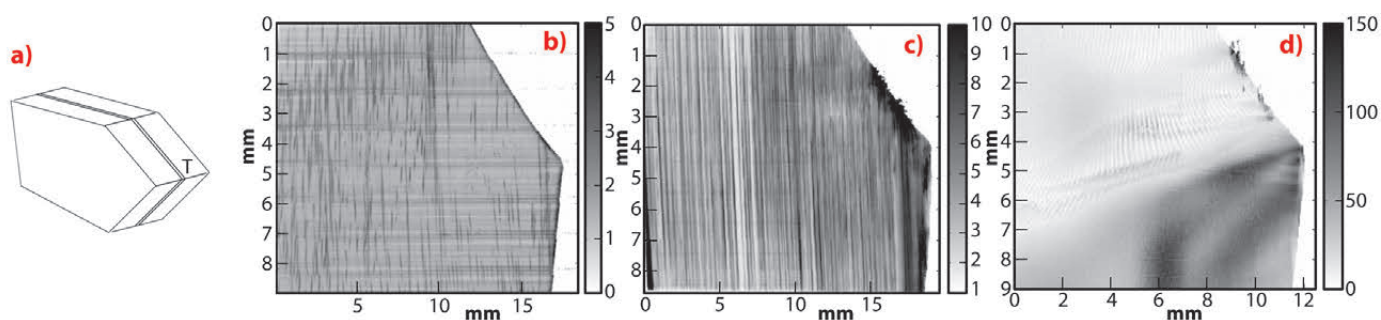


**Fig. 125:** a) Schematic drawing of the single grain of ice, indicating the central virtual slice which is at the origin of the images of the local FWHM values shown on b, c, and d; this virtual slice cuts the triple junction where three grains meet on T. b) Initial state of the ice crystal, exhibiting individual dislocations in a nearly perfect crystalline matrix. c) Intermediate state, after a first application of an external stress, showing slip bands. d) Final state, showing the inception of the formation of a subgrain boundary. Note that the scale, in arc seconds, is very different for the three images (Courtesy of A. Philip and J. Messonnier, LGGE Grenoble).



X-ray imaging is increasingly being used for **cultural heritage** studies. Synchrotron X-ray spectromicroscopy coupled with related methods, on ID21, allowed the degradation process of yellow pigment in Van Gogh paintings to be understood. Synchrotron radiation microtomography with a high energy and/or coherent beam makes it possible to reach elusive information that can completely change our understanding of a palaeontological subject. A very important study, performed at ID17, of the large fossil skull *Australopithecus sediba*, recently discovered in South Africa, and aged 1.9 million years, shows that whereas the brain volume is still the one of a typical *Australopithecus*, the anterior part of the brain already displays a complex reorganisation similar to that observed in the genus *Homo*. Another study, performed at ID19, led to evidence about the diet of one of the most important group of ammonites, distant relatives of squid, octopuses and cuttlefish, which sheds a new light on the reason for their extinction 65.5 million years ago.

All these investigations will be fostered by the refurbishment of the ID17 and ID19 beamlines, which aims to provide the palaeontological community with specially designed facilities, and, of course, these facilities will also be beneficial for many other scientific communities. The upgrade/refurbishment programme presently developing at the ESRF will provide new and unique opportunities on long beamlines both for imaging at high resolution of large samples (ID19, ID17), and for nano-imaging and nano-analysis on the new ID16 beamline (NINA).

J. Baruchel

#### References

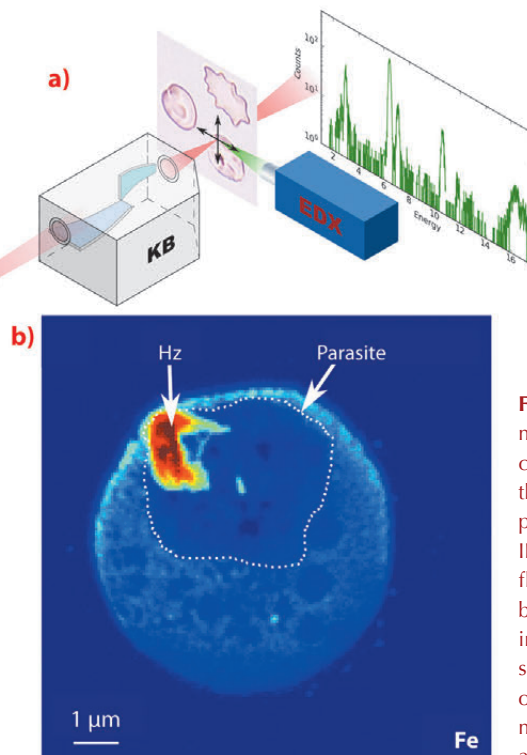
- [1] B. Abbey, F. Hofmann, J. Belnoue, A. Rack, R. Tucoulou, G. Hughes, S. Eve, A.M. Korsunsky, *Scripta Materialia* **64**, 884–887 (2011).
- [2] R.T. Kluender, A. Philip, J. Meyssonier, J. Baruchel, *Phys. Stat. Sol. A* **208**, 2505–2510 (2011).
- [3] A. King, P. Reischig, S. Martin, J. Fonseca, M. Preuss, W. Ludwig, *31st Risø International Symposium on Materials Science*, ed. N, Hansen et al. (2010).

## ■ Biology and biomedical imaging

### Imaging of antimalarial drugs in *Plasmodium falciparum* infected red blood cells

Few strategies are available for label-free imaging in biological systems with high spatial resolution and high sensitivity. We report for the first time the *in vitro* localisation of antimalarial drugs in malaria-infected erythrocytes using synchrotron nanochemical imaging. We demonstrate the ability to measure quantitatively the drug distribution inside the parasite that invades red blood cells, particularly in the food vacuole of the parasite. This approach opens new possibilities to improve the understanding of the action mechanisms of antimalarial drugs and resistances.

With approximately 250 million cases and 781,000 deaths reported in 2009, malaria remains the most important human parasitic disease. Among the five *Plasmodium* species that infect human, *P. falciparum* is responsible for most cases of severe disease and death, mainly in children under five years of age in Africa. An acute need for new drugs exists as resistance has developed to all antimalarial drugs. Thus, overcoming the problem of drug resistance



#### Principal publication and authors

F. Dubar (a), S. Bohic (b,c), C. Slomianny (a), J.C. Morin (d), P. Thomas (d), H. Kalamou (d), Y. Guérardel (a), P. Cloetens (c), J. Khalife (d) and C. Biot (a), *Chem. Commun.* **48**, 910–12 (2012).  
(a) Université Lille 1, Villeneuve d'Ascq (France)  
(b) Grenoble Institute of Neurosciences, Grenoble (France)  
(c) ESRF  
(d) Institut Pasteur de Lille, Lille (France)

**Fig. 126:** X-ray fluorescence microscopy of individual red blood cells. a) The sample is scanned through the nanofocus beam produced by the KB optics of the ID22NI station while the X-ray fluorescence signal is being collected. b) Iron fluorescence signal of an infected red blood cell revealing sub-cellular features. The boundary of the parasite is delineated. The malaria pigment (hemozoin Hz) has an increased iron content.



### References

F. Dubar et. al., *ACS Chem Biol.* **6**, 275-87 (2011).

is an essential goal of antimalarial drug discovery. The new synthetic compound ferroquine (or SSR97193) provides new hope in the fight against malaria. We have used a synchrotron-based nano-imaging technique to localise unlabelled antimalarial drugs inside single red blood cells infected by *P. falciparum*. The nanoprobe endstation of beamline **ID22** allows simultaneous acquisition of the fluorescence signature of most elements of biological interest. Thanks to its exceptionally fine and bright focussed X-ray beam, the end-station permits the imaging of trace elements with a spatial resolution of 50 nm at detection limits down to the attogram level (see **Figure 126**).

The parasite digests hemoglobin in the food vacuole, where degraded compounds, potentially toxic to the

parasite itself, are crystallised into hemozoin, an insoluble, brown pigment (also called the malaria pigment) that contains different iron species (see **Figures 126b** and **127b**). It is impossible to distinguish the iron atoms of ferroquine, heme, hematin, and hemozoin. Therefore, ruthenoquine, a cold tracer of ferroquine in which the iron atom was substituted by a ruthenium atom, was used as a means to follow the cellular uptake of ferroquine in the infected red blood cells. Ruthenoquine has similar antimalarial activities as ferroquine and accumulates preferentially in infected cells rather than in non-infected cells. We were able to show that ruthenium atoms accumulate in the parasitic food vacuole close to its membranes. **Figure 127c** shows the distribution of chlorine (blue), iron (green) and ruthenium (red) in an infected red blood cell. It can clearly be seen that the ruthenium atoms are located in the malarial pigment inside the food vacuole. Also, the chlorine atom within antimalarial drugs can be used to image the drug's uptake without labelling. This was demonstrated not only for ferroquine and ruthenoquine, but also for the long-lived drug chloroquine. Comparing the elemental distributions for the different drugs, the researchers proposed that ferroquine selectively targets the food vacuole through another transport mechanism than the one for chloroquine. This study provides the first demonstration of the localisation of unlabeled antimalarial drugs at pharmacological doses with high spatial resolution. This strategy improves the understanding of the action mechanisms of already available and novel antimalarial drugs. Moreover, this approach may be applied to a wide range of domains where the quantitative chemical imaging of drugs at the sub-cellular level is critical.

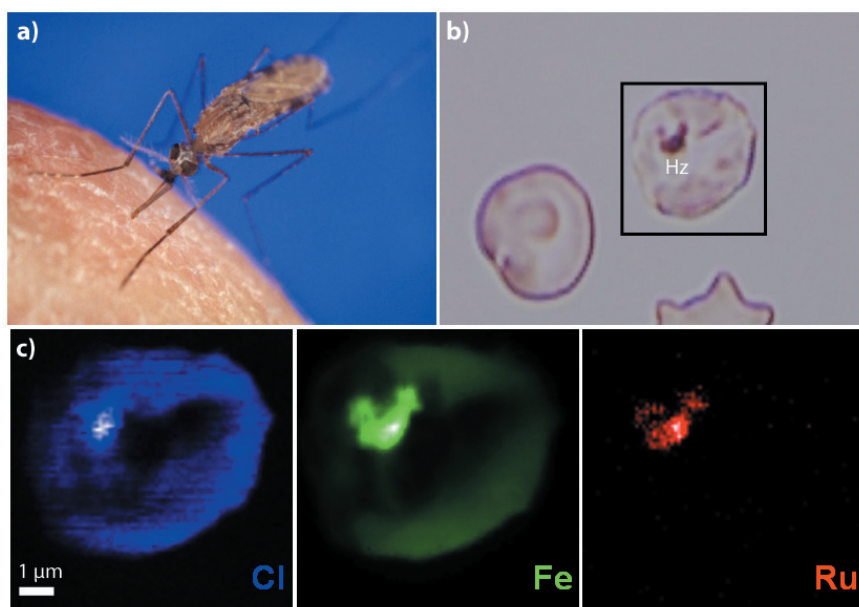


**Fig. 127:** Nanochemical imaging of an antimalarial drug in an infected red blood cell. a) Mosquito vector of the malaria infectious disease, b) visible light micrograph of the analysed cell showing the brown malaria pigment (hemozoin Hz), c) Sub-cellular distribution of the chlorine (blue), iron (green) and ruthenium (red) atoms. The antimalarial drug ruthenoquine is located in the malaria pigment.

## The stage of vascular maturation is crucial for tissue damage after microbeam radiation

Microbeam radiation has been developed for therapeutic purposes and has been preclinically tested. It is capable of delivering high doses (~150-4000 Gy) of radiation. It involves synchrotron X-rays conditioned as an array of parallel beams of 25-75 µm wide, spaced 100 to 400 µm apart. Compared to broad-beam

seamless radiation, currently used in clinical protocols, microbeam radiation has a tissue-sparing effect because of its particular geometry, which produces peak and valley zones of dose deposition [1]. Small vessels have been shown to play an important role in mediating the tissue-sparing effect of microbeam radiation [2].





We have investigated the vascular effects of microbeam radiation relative to the stage of vascular maturation. Moreover, we have evaluated the temporal pathophysiological changes induced by microbeam radiation, compared to those caused by seamless radiation. We chose chick chorio-allantoic membrane (CAM) as the experimental model as it represents an almost pure vascular system, in which maturation of immature capillaries at day 8 (CAM8) of development to mature capillaries at day 12 (CAM12) can be observed [2].

*In vivo* monitoring (Figure 128) of CAM8 vasculature 6 h after 200 Gy microbeam radiation revealed a near total destruction of the immature capillary plexus. Conversely, a higher dose (300 Gy) barely affected CAM12 mature microvasculature (Figure 128b - d). The quantification revealed that the relative density of preserved microvessels was significantly higher in CAM12 than in CAM8. The fraction of unperfused microvascular areas was significantly lower in CAM12 than in CAM8.

For CAM8, using light and electron microscopy, we observed an increased thickness in the irradiated region 6 h after delivery of 200 Gy microbeam radiation, with a damaged capillary plexus in the beam path (Figure 129). In contrast, for CAM12, the larger blood and lymph vessels were preserved, the capillary plexus remained intact, with only the occasional congested and unperfused capillary.

Dynamic morphological evaluation by light and electron microscopy revealed that the effects of microbeam radiation occur very rapidly: as soon as 15 minutes after 300 Gy, opened interendothelial cell junctions were revealed, which could explain the transient mesenchymal edema with increased CAM thickness. After 30 minutes the capillary plexus displayed a striated metronomic pattern of lesion, alternating damaged and intact zones, corresponding to the beam and the interbeam paths within the array. At 60 minutes, CAM started regaining its normal thickness.

For comparison, a 10 Gy dose of seamless radiation caused growth retardation, while 40 Gy damaged the entire CAM vasculature [2].

Based on our observations, we conclude that the effects of microbeam radiation are mediated by capillary damage, with

**Principal publication and authors**

S. Sabatasso (a,c), J.A. Laissue (b), R. Hlushchuk (a,c), W. Graber (c), A. Bravin (d), E. Bräuer-Krisch (d), S. Corde (d,e), H. Blattmann (b,e), G. Gruber (f) and V. Djnonov (a,c), *Int J Radiat Oncol Biol Phys.* **80**, 1522-32 (2011).

(a) Institute of Anatomy, University of Fribourg (Switzerland)

(b) Institute of Pathology, University of Bern (Switzerland)

(c) Institute of Anatomy, University of Bern (Switzerland)

(d) ESRF

(e) Radiotherapy Service, Centre Hospitalier Universitaire A.

Michallon, Grenoble (France)

(f) Radio Oncology Unit, Clinic Hirslanden, Zürich (Switzerland)

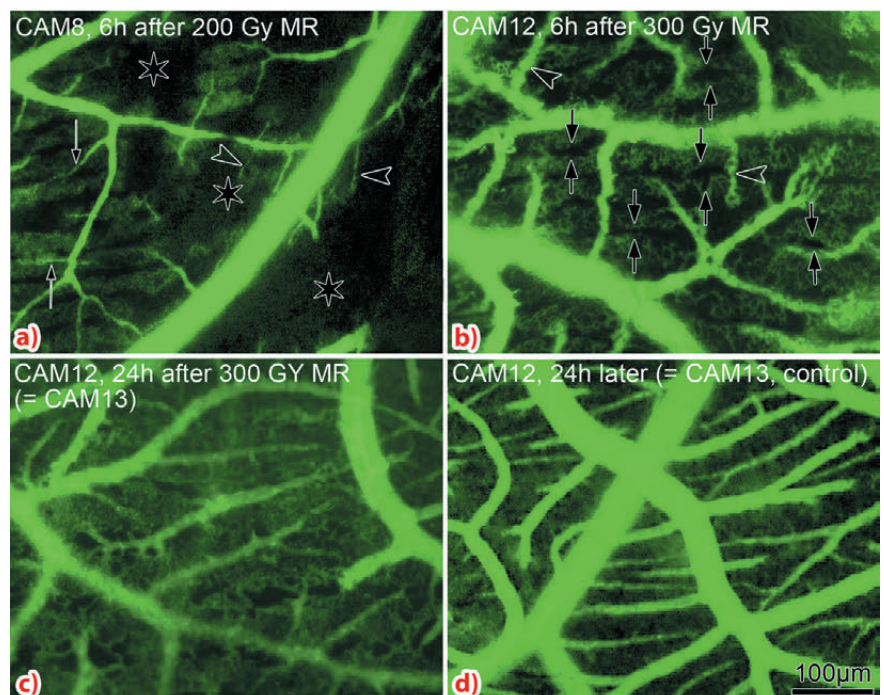
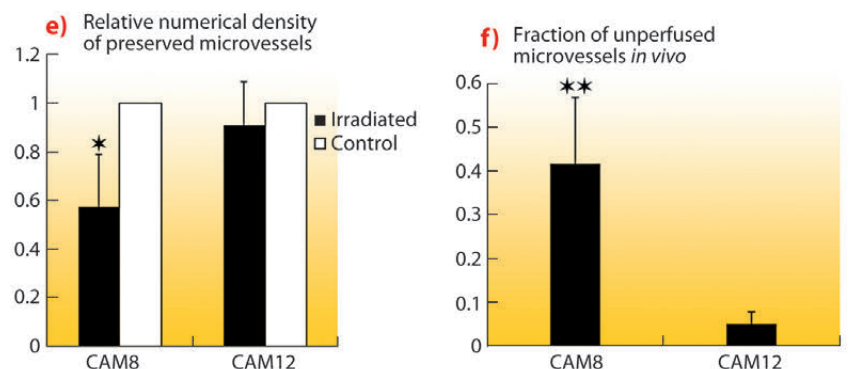


**Fig. 128:** Intravital microscopy of CAM8 (a) and CAM12 (b – d). a) Extensive degeneration of the capillary plexus, identified as large unperfused areas (asterisks) and damaged small supplying vessels (arrowheads) in the beam path. Few capillary areas remain occasionally perfused by small arteries (arrows). b) Microbeam radiation effects are limited to the microvasculature, where the capillary plexus is cut by an array of tiny, unperfused dark stripes (double arrows). Few small supplying vessels are barely affected (arrowheads). c) The vasculature nearly recovered, showing a supplying vessel density similar to that of controls (d). e, f) CAM8 and CAM12, 6 h after 200 Gy MR. Relative numerical density of preserved microvessels (e) and fraction of unperfused microvascular areas (f).







tissue injury caused by insufficient blood supply. Vascular toxicity and physiological effects of microbeam radiation depend on the stage of capillary maturation and

appear in the first 15 to 60 minutes after irradiation. Conversely, the effects of seamless radiation, due to the arrest of cell proliferation, persist for a longer time.

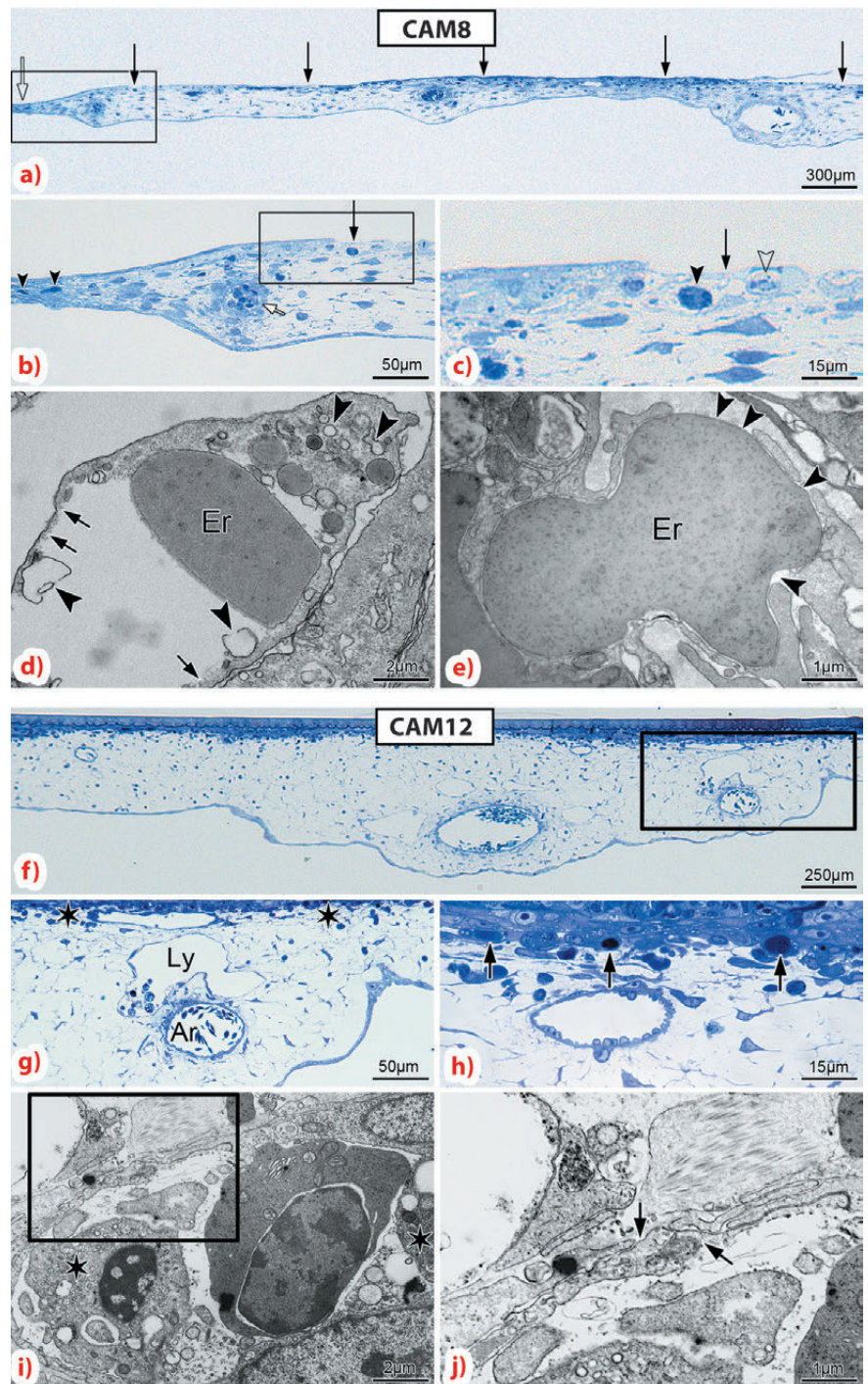


**Fig. 129:** CAM histopathology 6 h after 200 Gy microbeam radiation. a) CAM8. Overview showing the irradiated, thickest part (beam entrances indicated by closed arrows) and the nonirradiated, thinner part (open arrow). b) Preserved capillaries in the nonirradiated region (arrowheads). c) Missing capillary plexus in the irradiated part, with few microvessels containing intact (closed arrowhead) or fragmented (open arrowhead) blood cells. d, e) Transmission electron microscopy. Endothelial cytoplasmic vacuolisation (d, closed arrowheads), disrupted luminal endothelial cell membrane (arrows) and endothelial remains with large gaps in between (e, closed arrowheads). Er = erythrocyte. f) CAM12. Overview of the irradiated region. g) Preserved capillary plexus (asterisks), supplying artery (Ar) and lymph vessel (Ly). h) Blood cells stuck in unperfused capillaries (arrows). i) Transmission electron microscopy of the beam path region. Blood cells show signs of impending cell death (i, asterisks) and the endothelium is partially disrupted (j, arrows).

#### References

- [1] E. Bräuer-Krisch, R. Serduc, E.A. Siegbahn, *et al.*, *Mutat Res* **704**, 160-166 (2010).
- [2] S. Sabatasso, J.A. Laissue, R. Hlushchuk, *et al.*, *Int J Radiat Oncol Biol Phys* **80**, 1522-32 (2011).

## Investigating the continuous dental replacement of mammals through a new rodent model

Continuous dental replacement is an exceptional mechanism in mammals because they usually have only two generations of teeth, contrary to their reptilian ancestors. In continuous dental replacement there is constant addition of teeth at the rear of the jaw. Up to now, this characteristic has been only found in the pygmy rock-wallaby and in manatees, and it remains barely documented. However, we recently discovered an African mole-rat displaying unusual dentition, which reopens the debate concerning tooth replacement and the origin of supernumerary teeth in mammals.

The silvery mole-rat (*Heliophobius argenteocinereus*) is a solitary African rodent that spends most of its lifetime digging burrows in order to find food (Figure 130a). Occurrence of only a few supernumerary teeth has already been mentioned for this rodent, but continuous dental replacement had never been proposed, nor investigated. By means of the X-ray synchrotron microtomography, using beamlines ID19 and BM05 (at 25 keV, cubic voxel of 5.06  $\mu\text{m}$ ), the dental characteristics of this African mole-rat were accurately imaged to highlight the various properties of its dental replacement mechanism. Among 55 investigated skulls of *H. argenteocinereus*, one juvenile and one adult were chosen to be scanned. Comparisons have also been drawn with the dentitions of manatees and the pygmy rock-wallaby. The dental characteristics of the wallaby have also been investigated using beamline ID19 (at 60 keV, cubic voxel of 7.46  $\mu\text{m}$ ).

While the molar number never exceeds three in placental mammals, the silvery mole-rat can bear up to seven molars (Figure 130b-c). Indeed, the molars of this rodent are continuously replaced, since new teeth regularly erupt at the rear of the jaw, pushing the anterior teeth, which become extremely worn, and finally resorbed inside the bone (Figure 130c). The very high quality and precision of synchrotron reconstructions permitted us to visualise the resorption of both root and crown (Figure 131a), which is led by the compressive action of erupting molars on anterior molars. The originality of this dentition also relies

on its high-crowned teeth. As a result, the occurrence of continuous dental replacement coupled to high-crowned teeth constitutes an excellent “escalator-like” dental mechanism (Figure 131b), necessary to withstand the effects of severe wear on teeth. This solitary rodent actively digs with its incisors irrespective of the hardness of the soil, therefore, we hypothesised that high wear of the molars could be linked to severe dental friction occurring during both digging and feeding.

What do the comparisons with other mammals having continuous dental replacement reveal? Manatees and the small wallaby display low-crowned teeth contrary to this mole-rat. Moreover, their dental resorption is only efficient for the roots of their teeth. Synchrotron reconstruction of the wallaby's dentition also allowed us to clearly show that the

### Principal publications and authors

H. Gomes Rodrigues (a), P. Marangoni (a), R. Šumbera (b), P. Tafforeau (c), W. Wendelen (d) and L. Viriot (a), *Proc. Natl. Acad. Sci.* **108**, 17355-17359 (2011).  
 (a) IGFL-ENS Lyon-UCBL1 (France)  
 (b) PrF, University of South Bohemia, České Budejovice (Czech Republic)  
 (c) ESRF  
 (d) Royal Museum for Central Africa, Tervuren (Belgium)

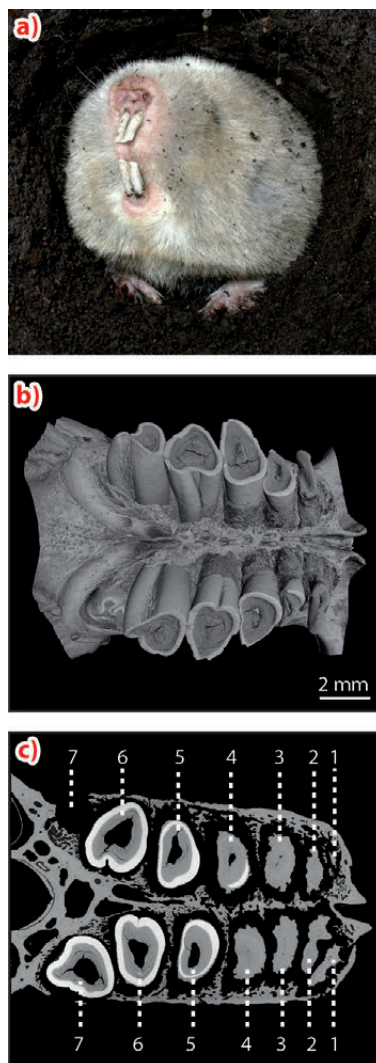


**Fig. 130:** a) Foreside of a captive silvery mole-rat, b) 3D reconstruction and c) Virtual cross-section of the upper dentition of an adult silvery mole-rat.





anterior molars are not totally resorbed (**Figure 131c**), but rather they are shed when they reach the front of the jaw. Even if the mechanism is convergent with the rodent's dental system, it still reminds one of a "treadmill" (**Figure 131d**), and is clearly optimised for gnawing abrasive plants. Apart from these differences, we found that the three mammals and some of their extinct and extant relatives shared some biological traits essential

for continuous dental replacement. They comprise a forward movement of new teeth from the rear to the front of the jaw (mesial drift), the continued eruption of teeth after the age of sexual maturity (delayed eruption), and the growth of extra teeth (supernumerary teeth).

What is the main biological interest of this rodent? Manatees and the pygmy rock wallaby are not suitable for an accurate study of continuous dental replacement, because of their size and their endangered status.

Mice, the usual biological model, do not have any of the dental characteristics previously detailed. Consequently, this mole-rat could be the better biological model for an extensive study of the continuous dental replacement's underlying mechanism, which could represent a basis to understand the developmental and molecular processes leading to additional molars. Further research on this topic will be of high interest, notably regarding the knowledge of dental stem cells in relation to the origin of extra teeth in mammals, and thus leading to the eventual goal of the regeneration of dental tissue in humans.

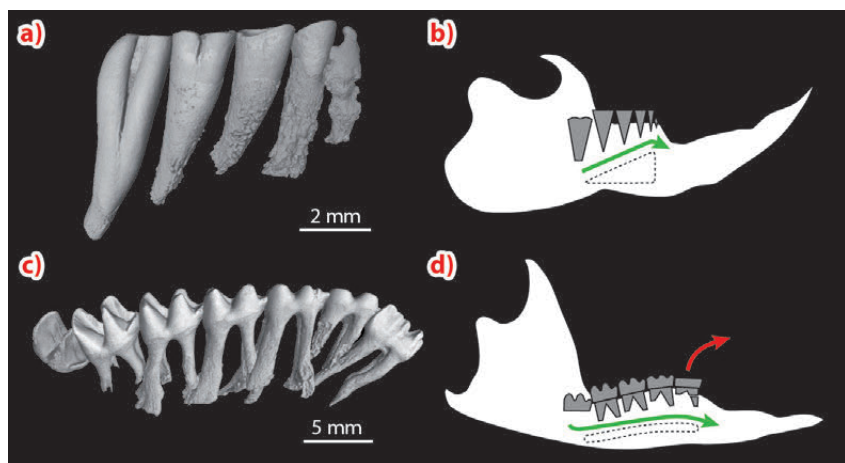


**Fig. 131:** a) 3D reconstruction in lateral view of a lower tooth row and b) model of dental replacement of the silvery mole-rat. c) 3D reconstruction in lateral view of a lower tooth row and d) model of dental replacement of the pygmy rock-wallaby (green arrows: molar progression; red arrow: tooth loss).

## ■ Imaging of materials

### Principal publication and authors

Z. Asghar (a), G. Requena (a) and E. Boller (b), *Acta Materialia* **59**, 6420-6432 (2011).

(a) Vienna University of Technology, Institute of Materials Science and Technology, Vienna (Austria)  
(b) ESRF

### References

- [1] Requena *et al.* *AdvEngMat* (2011).
- [2] Z. Asghar, G. Requena and E. Boller, *Pract. Metallogr* **9**, 471 (2010).
- [3] Z. Asghar, G. Requena and F. Kubel, *Mater. Sci. Eng A* **527**, 4691 (2010).

## 3D multiphase networks providing high temperature strength to aluminium-silicon piston alloys

Cast aluminium-silicon alloys are widely used in automotive components such as cylinder heads and pistons. The temperature rise in the combustion chamber of a diesel engine can reach up to ~ 300-400°C and, therefore, high temperature strength is an important requirement for piston alloys. The high temperature strength of cast Al-Si alloys is provided by a transfer of load from the ductile  $\alpha$ -aluminium matrix to rigid and usually highly interconnected 3D networks of eutectic silicon. However, if cast Al-Si alloys are solution treated above 500°C, the eutectic silicon rapidly disintegrates and spheroidises, reducing the strength of the alloy [1]. The loss in strength can be avoided to some degree by the addition of transition elements such

as nickel and copper that form thermally stable rigid aluminides [2,3]. The reasons for the improvement of mechanical properties of Al-Si alloys by additions of nickel and copper are still a matter of scientific investigations with important technological implications. Here, we report on the effect of different additions of nickel, copper and iron on the high temperature strength of cast Al-Si piston alloys. This was investigated with respect to the microstructural architecture formed by the aluminides and the eutectic silicon. Absorption and phase contrast synchrotron microtomography was used to study samples of the alloys AlSi12, AlSi12Ni, AlSi12Cu5Ni1 and AlSi12Cu5Ni2 in as-cast condition and after solution treatment using the ID19 beamline.

**Figure 132** shows the largest particles of the eutectic silicon and of the aluminides within the considered volumes for the studied alloys after 4 h solution treatment at 490°C. The tomographic results show that the interconnectivity of the eutectic silicon is highly conserved after the solution treatment for the aluminide-containing alloys (**Figure 132b, e and f**).

**Figure 133** shows the evolution of the proof stress,  $\sigma_{0.2}$ , at 300°C as a function of the solution treatment time at 490°C. The solution treatment caused a decrease in the high temperature strength of the alloys within the first 4 h.

The aluminide-containing alloys exhibit higher strengths than the AlSi12 alloy due to the larger volume fraction of rigid phases, amounting to 18–24%, the high interconnectivity of the aluminides and their high contiguity with the eutectic silicon. The alloys AlSi12Ni1 and AlSi10Cu5Ni1 contain ~ 8 vol.% of aluminides. However, the aluminides in the AlSi10Cu5Ni1 alloy present a higher degree of interconnectivity (~ 94% in as-cast condition and ~ 75% after stabilisation) than the AlSi12Ni1 alloy (~ 60% in as-cast condition and ~ 50% after stabilisation). X-ray diffraction analysis revealed that the addition of copper produces various aluminides increasing the contiguity:  $\text{Al}_7\text{Cu}_4\text{Ni}$ ,  $\text{Al}_2\text{Cu}$ ,  $\text{Al}_4\text{Cu}_2\text{Mg}_8\text{Si}_7$  and  $\text{AlSiFeNiCu}$ . ~ 90% of all the aluminides and all the eutectic silicon are forming a highly interconnected rigid 3D structure in AlSi10Cu5Ni1 which increases the high temperature strength by ~ 100% with respect to the Cu-free alloy AlSi12Ni (**Figure 133**).

The piston alloys AlSi10Cu5Ni1 and AlSi10Cu5Ni2 show similar strength in the as-cast condition. AlSi10Cu5Ni2 contains more aluminides (~ 13 vol.%) and it retains a ~ 15% higher strength level than AlSi10Cu5Ni1 after the solution treatment. Furthermore, the 3D network of the rigid phases is practically fully preserved (~ 97%) during solution treatment of the AlSi10Cu5Ni2 (**Figure 132d, f**), owing to the larger degree of contiguity between the aluminides and eutectic silicon. This results in an extra increase of load transfer from the Al matrix to the reinforcing 3D network of aluminides and silicon which is more important at high temperatures where the matrix becomes relatively softer.

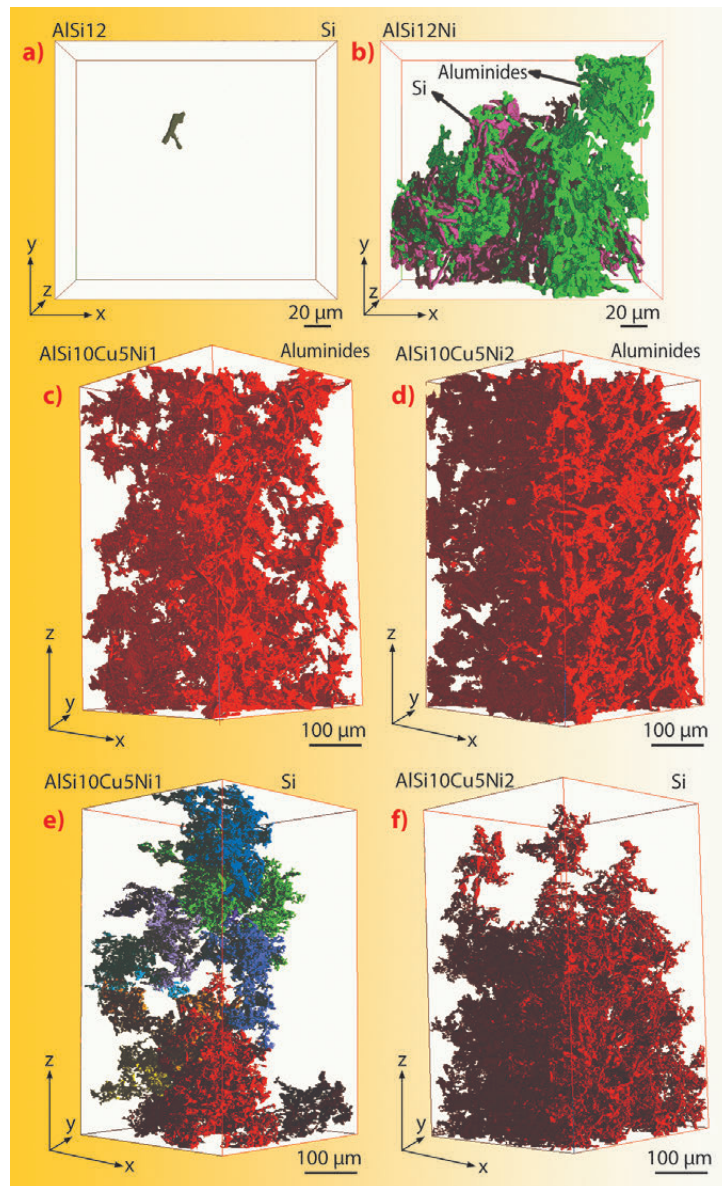


**Fig. 132:** 3D structures of aluminides and Si after 4 h of solution treatment: a) Si in AlSi12, b) Si and aluminides in AlSi12Ni, c) aluminides in AlSi10Cu5Ni1, d) aluminides in AlSi10Cu5Ni2, e) Si in AlSi10Cu5Ni1 and f) Si in AlSi10Cu5Ni2.

The results indicate that the design of cast Al-Si alloys for high temperature applications requires a deep understanding of their 3D architecture and the mechanisms governing its evolution with temperature and time. Synchrotron microtomography is a powerful tool to achieve these tasks mainly due its non-destructive nature, suitable sample-size-to-resolution ratio and the possibility to use phase contrast to reveal the eutectic Si embedded in the Al matrix.

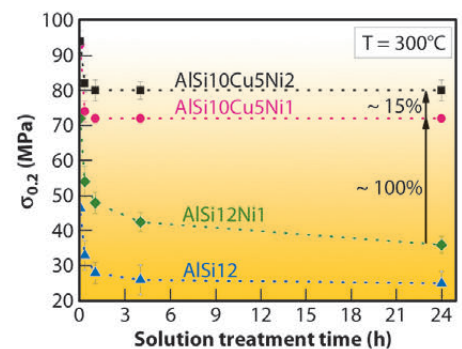


**Fig. 133:** Proof stress  $\sigma_{0.2}$  at 300°C for the investigated alloys as a function of the solution treatment time.



### Principal publication and authors

P. Benito (a), W. de Nolf (b),  
S. Bugani (a), F. Basile (a),  
G. Fornasari (a), K. Janssens (b),  
E. Scavetta (c), D. Tonelli (c) and  
A. Vaccari (a), *Adv. Funct. Mater.*  
20, 4117–4126 (2010).  
(a) *Dip. Chimica Industriale e dei  
Materiali, University of Bologna  
(Italy)*  
(b) *Department of Chemistry,  
University of Antwerp (Belgium)*  
(c) *Dip. Chimica Fisica e  
Inorganica, University of Bologna  
(Italy)*

## Insights into structured catalysts for hydrogen production by microscopic synchrotron techniques

The steam reforming of methane ( $\text{CH}_4 + \text{H}_2\text{O} \leftrightarrow \text{CO} + 3\text{H}_2$ ) is the most widespread process to large scale  $\text{H}_2$  production. The reactor consists of multitubes filled with heterogeneous catalysts, mainly nickel supported on a ceramic material such as  $\text{MgAl}_2\text{O}_4$  or  $\text{Al}_2\text{O}_3$ , which increases the velocity of the reaction. Steam reforming is highly endothermic, it operates at high temperatures (around  $900^\circ\text{C}$ ) and therefore a large amount of heat must be supplied. However, thermal gradients take place within the catalytic bed, causing a decrease in catalytic performance and in the reactor tubes lifetime.

Metallic structured catalysts, made of a metallic foam coated by a catalyst, enhance the heat transfer and therefore the efficiency of the process. In particular we have used FeCrAlY foams coated with a nickel catalyst. The coating was performed by a novel electrochemical method [1]. It consists of the generation of a catalyst precursor by applying a cathodic potential at the FeCrAlY foam, which is immersed in a solution containing  $\text{Ni}(\text{NO}_3)_2$  and  $\text{Al}(\text{NO}_3)_3$ , with  $\text{KNO}_3$  as supporting electrolyte. The cations precipitate on the surface of the electrode as layered hydrotalcite-type compounds. Catalysts are obtained by calcination of this precursor at  $900^\circ\text{C}$ . The nature of the coating depends on the potential applied and the synthesis time. The structural characterisation of the catalytic film, which is of key importance for the development of the catalysts, cannot be done by conventional XRD techniques because of the complex nature of the support and the thin layer.

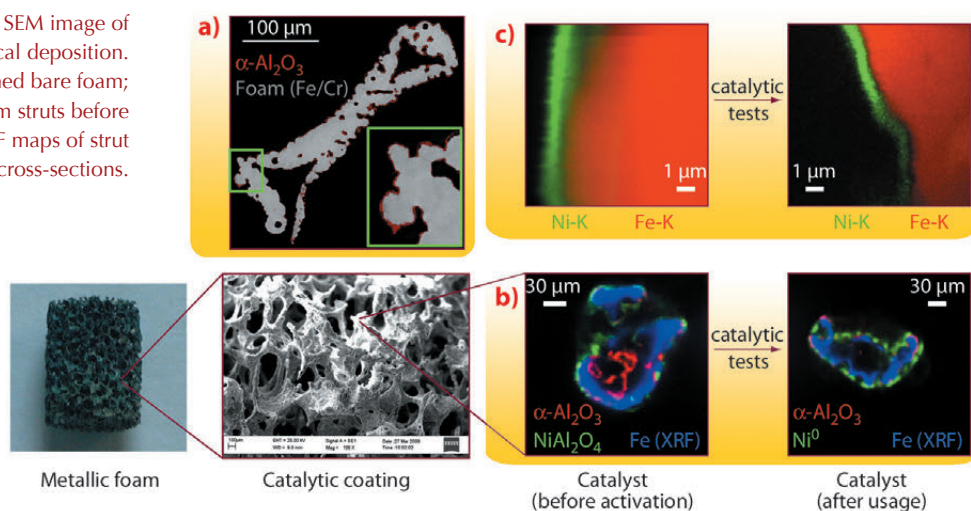
We characterised bare and coated FeCrAlY foams at different length scales by absorption tomography at beamline ID19,  $\mu$ -XRF/XRD tomography at beamline ID22 with a  $3.4 \times 1.8 \mu\text{m}$  beam and by submicroscopic XRF measurements (nano-XRF tomography) using a  $100 \times 130 \text{ nm}$  focal spot size at the ID22n endstation to complete the information obtained by SEM/EDS. The different stages in the life of a catalyst, after electrochemical synthesis, calcination and catalytic tests, were studied.

Absorption tomography of a calcined bare foam revealed the presence of a thin layer coating both the inner and outer surface of the hollow FeCrAlY foam (Figure 134a); however, after coating it was not possible to distinguish between the catalyst and this layer. Complementarily,  $\mu$ -XRF/XRD tomography of foam struts (Figure 134b) gave information about the nature and the spatial distribution of the crystalline phases in the catalytic coating ( $\text{NiO}$  and  $\text{NiAl}_2\text{O}_4$ ), both of them located on top of an  $\alpha\text{-Al}_2\text{O}_3$  layer as observed by XRD. The distribution of  $\text{NiO}$  appeared not to be homogeneous as it was present in the zones where a large amount of Ni was deposited as confirmed by XRF. After catalytic tests, the coating remained on the support and an intermixed layer containing  $\text{Ni}^0$ ,  $\gamma/\eta\text{-Al}_2\text{O}_3$  and  $\alpha\text{-Al}_2\text{O}_3$  phases was identified, confirming that a stable active layer was formed.

However, the layer thicknesses could not be estimated since they were of the same order as the size of the primary X-ray

**Fig. 134:** Bare foam (bottom-left) with a SEM image of a coated foam prepared by electrochemical deposition.

- a) Absorption tomography of a calcined bare foam;  
b)  $\mu$ -XRD/XRF tomograms of coated foam struts before and after catalytic tests; c) nano-XRF maps of strut cross-sections.







beam. The actual thickness of the catalytic layer was obtained by nano-XRF mapping and tomography of strut cross-sections (Figure 134c). The hydrotalcite precursor was formed by a 1  $\mu\text{m}$  film in which we also observed some potassium, originating from the supporting electrolyte. After calcination the layer thickness decreased by a half, whereas after catalytic tests no further decrease was observed. The gap in between the foam and the nickel arose

from the intermediate  $\text{Al}_2\text{O}_3$  layer, which was not visible by XRF in air.

In summary, tomographic measurements (X-ray absorption,  $\mu\text{-XRF/XRD}$  and nano-XRF) allowed the characterisation of “as made” catalysts at different length scales, obtaining information about the distribution of the phases and the elements, important parameters for further development of these structured catalysts.

#### References

- [1] F. Basile, P. Benito, G. Fornasari, V. Rosetti, E. Scavetta, D. Tonelli and A. Vaccari, *Appl. Catal. B: Env.* **91**, 563–572 (2009).

## Local structure of single Co-implanted ZnO nanowires investigated by nano-X-ray absorption spectroscopy

Cobalt-doped zinc oxide nanowires offer unique advantages for spintronics applications owing to their large geometrical aspect ratio and predicted room-temperature ferromagnetism [1]. However, controlled doping of semiconductor nanowires with transition metals during growth remains a challenge. Ion implantation is an alternative that allows a better control of both concentration and distribution of transition metals ions. Determining the doping homogeneity and local order of individual nanostructures is crucial to understand their behaviour in nanodevices. The average local atomic structure and secondary phases in ensembles of nanowires have already been studied by X-ray absorption near edge structure (XANES) and extended X-ray absorption fine structure (EXAFS) [2]. However, the examination of single nanowires remains an experimental challenge mainly due to the beam instability during the energy scan, and chromaticity of the nanofocusing lens. In this work, we have used a  $100 \times 100 \text{ nm}^2$  monochromatic X-ray beam at station ID22NI to explore the short-range order in single Co implanted ZnO nanowires. In addition, the linear polarisation of the synchrotron nanobeam made our study capable of detecting preferentially oriented defects induced by the ion implantation process.

Figure 135a shows the scanning electron microscopy (SEM) image of a single nanowire. The positions indicated by 1, 2, and 3 correspond to the areas where XANES and EXAFS spectra were recorded. The elemental map of Co with the respective concentration estimated from the XRF quantification

is displayed in Figure 135b, showing homogeneous distributions of Co along the nanowire without any signature of clusters or nanoaggregates. XANES data from the nanowire with its c-axis oriented perpendicular and parallel to the polarisation vector of the X-ray beam are shown in Figures 135c and 135d, respectively. The spectra exhibit the peaks associated to the hexagonal structure, without any evidence of lattice damage in the nanowire.

The chemical state of the implanted Co ions was investigated by nano-XANES. Figure 136a shows the XANES spectra around the Zn K edge (solid circles) and Co K edge (open circles) taken at points 1 and 2. Despite the low Co content, the quality of the XANES data around the Co K edge is good and reproduces

#### Principal publication and authors

- J. Segura-Ruiz (a), G. Martinez-Criado (a), M.H. Chu (a), S. Geburt (b) and C. Ronning (b), *Nano Lett.* **11**, 5322–5326 (2011).  
(a) ESRF  
(b) Institute of Solid State Physics, University of Jena (Germany)

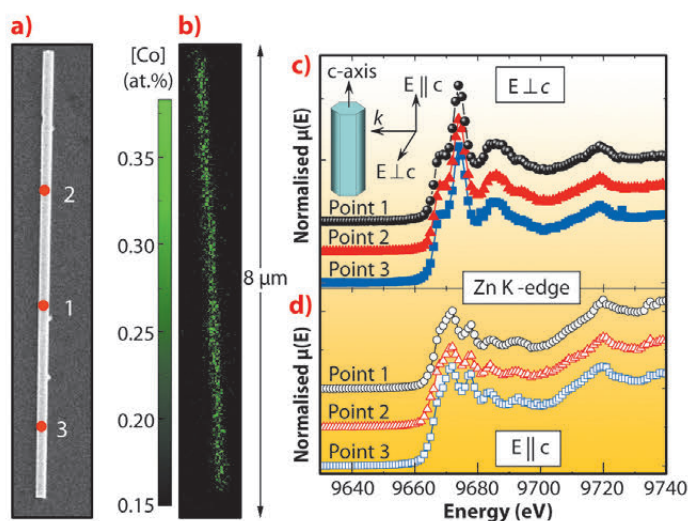
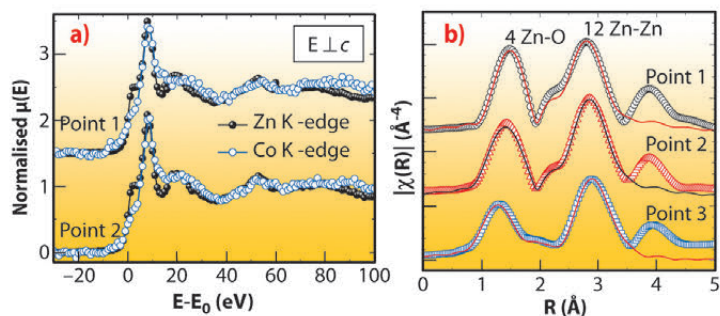


Fig. 135: a) SEM image of a single Co implanted nanowire. b) Elemental map collected at 12 keV for Co with the respective atomic fraction estimated from the XRF quantification. Zn K edge XANES spectra recorded along the nanowire: c) with the c-axis oriented perpendicular, and d) parallel to the electric field vector of the X-ray nanobeam.



**Fig. 136:** a) XANES spectra around the Zn K edge (solid circles) and Co K edge (open circles) taken at points 1 and 2. For comparison between Zn and Co XANES spectra, the energy has been rescaled to the respective absorption K edges calculated from the first derivative of the XANES signal. b) Magnitude of the Fourier transforms of the EXAFS functions (open symbols) and their best fits (solid lines).



well the oscillations of the Zn K edge spectra at both points, suggesting Co ions incorporated into the wurtzite host lattice on the Zn sites. Furthermore, the good match between the XANES spectra of the nanowire and that of a high quality wurtzite  $\text{Zn}_{0.9}\text{Co}_{0.1}\text{O}$  epitaxial film [3] (not shown), suggests oxidation state  $2^+$  for implanted Co ions. Finally, nano-EXAFS measurements around the Zn K-edge allow us to study the local order of the host lattice. **Figure 136b** shows the magnitude of the Fourier transforms of the EXAFS functions. The spectra show two dominant peaks related to the first O- and second Zn-shells. In general, there is no

evidence of amorphisation, and the Zn-O and Zn-Zn spacings remain equal to those of pure ZnO (1.98 and 3.25 Å) along the nanowire. This confirms the good recovery of the radiation damaged ZnO lattice through the thermal annealing.

In summary, we have carried out X-ray absorption spectroscopy in different regions along single nanowires. Our findings revealed implanted ions incorporated homogeneously along the nanowire as  $\text{Co}^{2+}$  and occupied Zn sites into the host lattice. The radiation damage in the ZnO host lattice was completely recovered through thermal annealing.

#### References

- [1] Y.W. Heo, D. Norton, L. Tien, Y. Kwon, B. Kang, F. Ren, S. Pearton and J. LaRoche, *Mater. Sci. Eng. R* **47**, 1–47 (2004).
- [2] B.D. Yuhas, S. Fakra, M.A. Marcus and P. Yang, *Nano Lett.* **7**, 905–909 (2007).
- [3] A. Ney, K. Ollefs, S. Ye, T. Kammermeier, V. Ney, T.C. Kaspar, S.A. Chambers, F. Wilhelm and A. Rogalev, *Phys. Rev. Lett.* **100**, 157201 (2008).

## Cultural Heritage

### Visualising and interpreting the brain of *Australopithecus sediba*

#### Principal publication and authors

K.J. Carlson (a,b), D. Stout (c), T. Jashashvili (a,d,e), D.J. de Ruiter (f,a), P. Tafforeau (g), K. Carlson (f) and L.R. Berger (a,h), *Science* **333**, 1402–1407 (2011).

a) Institute for Human Evolution, University of the Witwatersrand, Johannesburg (South Africa)  
 b) Department of Anthropology, Indiana University, Bloomington (USA)  
 c) Department of Anthropology, Emory University, Atlanta (USA)  
 d) Georgian National Museum, Tbilisi (Georgia)  
 e) Anthropological Institute and Museum, University of Zürich (Switzerland)  
 f) Department of Anthropology, Texas A&M University (USA)  
 g) ESRF  
 h) School of Geosciences, University of the Witwatersrand, Johannesburg (South Africa)

Evolution of the modern human brain from that of our last common ancestor with chimpanzees has seen a radical volume increase in the human lineage. Humans have evolved an average brain volume about four times that of chimpanzees, and have among the largest brains relative to body size of any living animal. In addition to these size differences, crucial organisational differences distinguish human and chimpanzee brains. Relative priority and timing of these critical processes in the evolution of the human brain – size increase and cortical reorganisation – have been debated since the discovery of the genus *Australopithecus* early in the 20<sup>th</sup> century [1].

The consensus opinion is that an australopithecine species gave rise to our own genus, *Homo*, between 2.3 and 1.8 million years ago. *Au. sediba* has been dated to slightly less than 2.0 million years, thus fitting firmly within this period. The reconstructed endocranial cast of

*Au. sediba* (endocasts are proxies of brains estimated from the inner surface of crania) is surprisingly small (420 cm<sup>3</sup>), being only approximately 40 cm<sup>3</sup> larger than average chimpanzee endocasts. Even compared to chronologically older australopithecines from South Africa (e.g., *Au. africanus*), the *Au. sediba* endocast is smaller. Such a small brain volume from a relatively late example is inconsistent with the notion of gradual brain enlargement amongst australopithecines and across the transition to *Homo*. The small volume also is surprising given derived *Homo*-like morphologies exhibited by *Au. sediba* postcranial bones (e.g., hand and pelvis).

Comparing organisational details of endocasts requires high resolution surface details. In order to acquire images of appropriate resolution, we employed phase contrast X-ray synchrotron microtomography. Since the fragile fossil was embedded in matrix and far exceeded the maximum imaging size for a rock



sample at the ESRF, we used a complex acquisition protocol on beamline ID17 that was developed for high quality imaging of large fossils. The protocol permits acquisition of high quality scans despite very low transmission of X-rays through the sample (less than 0.02%) even when the theoretical optimum is approximately 11%. Based on these exceptional data, we produced an endocast rendering from the *Au. sediba* cranium with visualisation of surface details exceeding most other hominin endocasts (Figure 137). Incorporation of computer-based techniques for *in silico* fossil preparation aided production of the rendering without necessitating destructive preparation [2].



**Fig. 137:** Rendering of *Australopithecus sediba* cranium produced from images obtained on ID17 (left), with the cranium and surrounding matrix transparent to permit visualisation of the endocast inside (right).

Comparing convolution patterns on the surface of the *Au. sediba* endocast to those of humans, other australopiths, and chimpanzees highlights similarities with the latter two groups (Figure 138). When examining features beyond overall size and convolution patterns, however, we observed proportional changes in the frontal lobe of *Au. sediba* that may foreshadow proportional changes modern humans exhibit relative to chimpanzees (Figure 138). For example, prefrontal cortex, particularly anteriorly, is relatively expanded in humans compared to other apes and is thought to support uniquely human capacities for multi-tasking, reasoning, planning, and innovation. The few South African australopithecine endocasts available for comparison with the *Au. sediba* endocast, all of which are attributed to taxa chronologically older than *Au. sediba* (e.g., *Au. africanus*), exhibit similar proportional changes, but to a lesser extent than the *Au. sediba* endocast. Based on these observations, and if *Au. sediba* is a human ancestor, we find support for gradual neural reorganisation of the orbitofrontal region in the transition from *Australopithecus* to *Homo*, but little support for gradual brain enlargement before the transition to *Homo*.

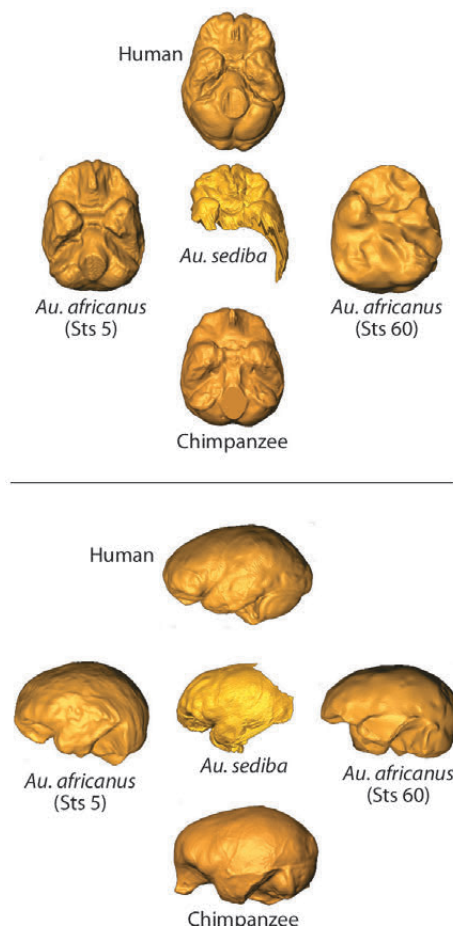


**Fig. 138:** Top panel illustrates similarly-scaled human, chimpanzee, *Australopithecus sediba* and *Au. africanus* endocasts in inferior view. Note orbitofrontal organisation in the *Au. sediba* endocast resembles the human condition more closely than do the *Au. africanus* endocasts. Bottom panel illustrates same endocasts in left lateral view. Note similarities in surface configuration of australopithecines and chimpanzees.

#### References

- [1] D. Falk, *Yearb. Phys. Anthropol.* **52**, 49-65 (2009).
- [2] A. Val, K.J. Carlson, C. Steininger, J.M. Kibii, C. Churms, B.F. Kuhn and L.R. Berger, *S Afr. J. Sci.* **107**:11/12, (2011).

## The almost unattainable radula of ammonites

Ammonites, extinct relatives of squids, octopuses, and cuttlefishes, are considered to be fossils “par excellence.” Their abundance in the fossil record and their long stratigraphic range, which covers

more than 300 million years (from the Devonian up to the end of Cretaceous), make them one of the most studied fossils. Yet, very few remains of the animal living inside the shell are known and





### Principal publication and authors

I. Kruta (a,b), N. Landman (c),  
I. Rouget (d), F. Cecca (d) and  
P. Tafforeau (e), *Science* **331**, 70-72  
(2011).

(a) UMR-CNRS 7207,  
Département Histoire de la Terre,  
Muséum National d'Histoire  
Naturelle, Paris (France)

(b) Present address: Yale  
Department of Geology and  
Geophysics, New Haven (USA)

(c) Division of Paleontology  
(Invertebrates), American Museum  
of Natural History, New York (USA)

(d) UMR-CNRS 7207, Université  
Pierre et Marie Curie - Paris 6  
(France)

(e) ESRF

### References

[1] G.E.G. Westermann, in *Topics  
in Geobiology*, 607–707 (1996).

[2] T. Engeser and H. Keupp,  
*Lethaia* **24**, 79–96 (2002).

their paleobiology and paleoecology is still enigmatic. This lack of knowledge is a limiting factor in our understanding of their evolution and ecology. Many hypotheses have been proposed on ammonite feeding habits, but very few were based on detailed analyses of the available data. One of the very few elements that can be preserved of the animal inside the shell is the buccal mass, and it shows very distinctive features that could be related to trophic specialisation [1]. In order to promote new insights in this field, extremely well preserved ammonites belonging to the genus *Baculites* from the Upper Cretaceous of South Dakota (US) were scanned at beamline ID19 using propagation phase contrast microtomography (PPC-SR $\mu$ CT) with a multiscale approach.

The ammonites under examination already presented some evidence of mandible preservation (Figure 139), but ESRF phase contrast microtomography revealed the yet unknown upper jaw and in all the specimens an extremely rare structure still embedded in the matrix: the radula. The jaw consists of an upper and lower beak, and is typical of this group

of ammonites (the aptychophorans [2]) in that the lower jaw is larger than the upper jaw and consists of two calcified halves separated along a midline. The radula (Figure 140) is found between the jaws in all the specimens. It is a toothed ribbon used by mollusks to feed and transport the food toward the oesophagus. The structure was preserved three dimensionally revealing the organisation of the teeth on the ribbon. Several teeth were still connected as they were in life and high resolution scans allowed us to see previously unknown details. The size of the radula was approximately 6 mm wide and 7 mm long and the tallest tooth cusp is 2 mm high. Teeth are very slender and show multiple cusps. The shape varies from saber to comb-like and differs from the tooth morphologies found in modern cephalopods.

The detailed anatomical study of the buccal mass, as well as comparative studies with recent cephalopods, led to the hypothesis that ammonites with this kind of feeding apparatus (*i.e.*, very large lower jaw, small and blunt upper jaw and delicate radula) fed on small organisms belonging to plankton. This hypothesis was reinforced by the discovery of a tiny snail and three small tiny crustaceans in one specimen, with one of the crustaceans having been cut into two parts (Figure 140c). Because these planktonic fossils are not found anywhere else on the specimen, the hypothesis was advanced that the specimen died while eating its last meal. Among Mesozoic ammonites, a large number of species share the same buccal mass morphology, therefore implying that all of these animals shared a similar position in the food web. One of the implications of this discovery is that the radiation of aptychophoran ammonites might be associated with the radiation of plankton during the Early Jurassic. In addition, plankton were severely hit at the Cretaceous-Tertiary boundary, and the loss of their food source probably contributed to the extinction of ammonites.

After this research, it is now clear that PPC-SR $\mu$ CT is a powerful tool for the analysis of ammonite remains. This is a starting point for new developments on ammonite paleontological studies. In this research, we came close to realising the old dream of many paleontologists: knowing what an ammonite really looked like.



**Fig. 139:** a) Part of the shell of the straight-shelled ammonite *Baculites*. The green laser indicates the part where the radula was found. Below the green spot, one of the two ribbed halves of the lower jaws that was already exposed. b) Reconstruction of *Baculites* (A. Lethiers, UPMC).

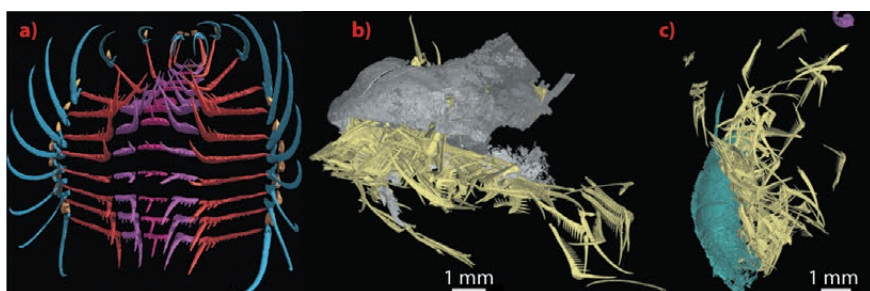


**Fig. 140:** a) Reconstruction of the radula of *Baculites*, front view, b) Lateral view of the upper jaw, in grey, apex on the left, with the radular teeth preserved inside, c) One of the three pieces of crustacean (blue) found flanking the radular teeth (yellow) with a small gastropod larval shell (pink).

## The darkening of chrome yellow pigments in paintings by Vincent van Gogh

Lead chromate based compounds, commonly known as chrome yellow, belong to a class of pigments based on either lead chromate ( $\text{PbCrO}_4$ , yellow and found in nature as the rare mineral *crocoite*), lead chromate–oxide  $[(1-x)\text{PbCrO}_4 \cdot x\text{PbO}]$ , yellow–orange and found in nature as the mineral *phoenicochroite* with structure  $\text{Pb}_2\text{O}(\text{CrO}_4)$ , in which the lead oxide conveys a reddish shade, or lead chromate sulfate  $[(1-x)\text{PbCrO}_4 \cdot x\text{PbSO}_4]$ , in which the sulfate compounds are employed to obtain paler shades of yellow. Chrome yellow was intensively used both by artists of the end of 19<sup>th</sup> century (such as V. van Gogh, G. Seurat, J.M.W. Turner, J. Constable, P. Cézanne, C. Pissarro and J. Ensor) and for industrial purposes (painting of vehicles and air planes, road paint and signs). The darkening of this pigment under sunlight was known since its invention in the first half of the nineteenth century. This phenomenon is currently observable on many oil paintings by the Masters mentioned above and among them, the most famous are the different versions of *Sunflowers* by V. van Gogh (1853–1890). Although the scientific community suspected that this degradation involves a reduction reaction of the original Cr(VI) to Cr(III), the exact alteration mechanism and the resulting Cr(III)-alteration products have never been elucidated before.

Investigations at beamline ID21 by means of microscopic X-ray absorption near-edge (SR  $\mu$ -XANES) and X-ray fluorescence spectrometry (SR  $\mu$ -XRF) around the Cr K-edge on artificially aged model samples of commercial lead chromate and two darkened paint cross-sections taken from paintings by V. van Gogh (*Bank of the Seine*, F293, 1887 and *View of Arles with Irises*, F409, 1888 - Van Gogh Museum, Amsterdam, NL) allowed it to be demonstrated for the first time that the alteration of chrome yellow is caused by the reduction of  $\text{PbCrO}_4$  to  $\text{Cr}_2\text{O}_3 \cdot 2\text{H}_2\text{O}$  (viridian green).

Among the UVA-visible aged model samples, only the one from an oil paint tube belonging to the Flemish Fauvist Rik Wouters (1882–1913) and containing

a high amount of  $\text{PbSO}_4$  proved to be particularly prone to discoloration (Figure 141a–b). A strong spatial correlation between the presence of Cr(III) compounds at the surface of the chrome yellow paint layers and the darkening was found; this was also clearly demonstrated on the Cr K-edge XANES spectra by a decrease of the intensity of the pre-edge peak at 5.993 keV and a shift of the absorption edge toward lower energies (Figure 141c).

Analogous with this historic aged model sample, Figure 142 illustrates that X-ray analysis performed on the two Van Gogh painting micro-samples revealed at the altered exposed surface the presence of Cr(III) species in areas rich in Ba and S and/or aluminum-silicate compounds, while the surrounding yellow paint contained exclusively Cr(VI).

Based on these results, we could arrive at the tentative assumption that  $\text{SO}_4^{2-}$  anions are involved in some manner in the alteration mechanism of  $\text{PbCrO}_4$ , without however being clear about the exact role they play. In this respect, a hypothesis was

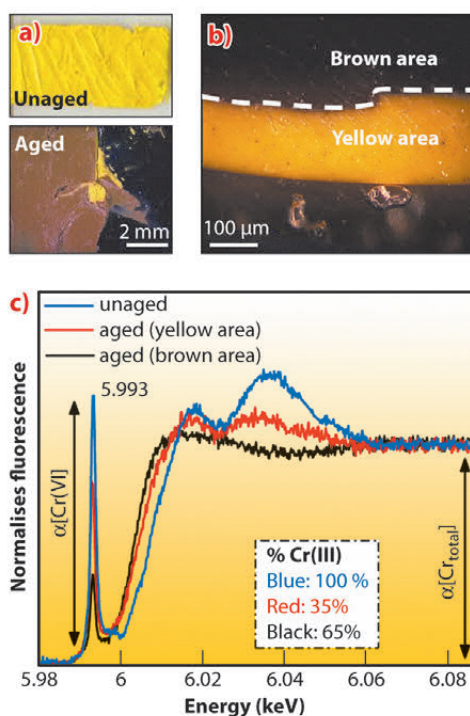


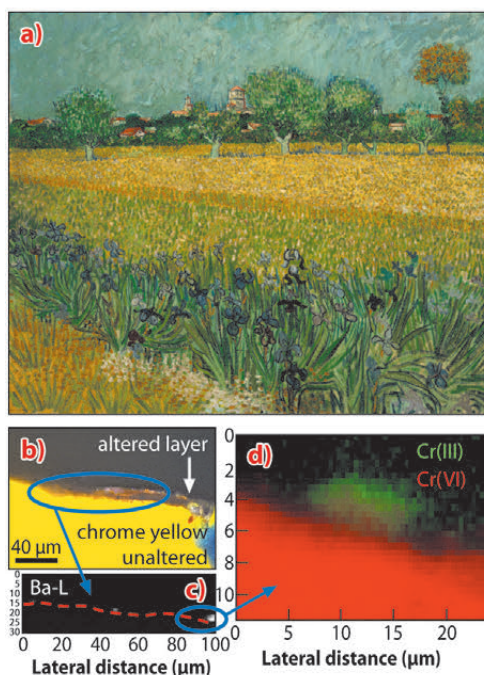
**Fig. 141:** a) Image of paint model sample taken from a historic 19<sup>th</sup> century paint tube before and after the ageing process. b) Sample of the same aged material shown in panel (a), embedded in cross-section. c) Cr K-edge XANES spectra acquired at ID21 on the model sample before and after ageing process and estimation of relative Cr(III) percentage abundances.

### Principal publications and authors

L. Monico (a, b), G. Van der Snickt (b), K. Janssens (b), W. De Nolf (b), C. Miliani (c), J. Verbeeck (b), H. Tian (b), H. Tan (b), J. Dik (d), M. Radepont (b,e) and M. Cotte (e,f), *Anal. Chem.* **83**, 1214–1223 (2011); L. Monico (a,b), G. Van der Snickt (b), K. Janssens (b), W. De Nolf (b), C. Miliani (c), J. Dik (d), M. Radepont (b,e), E. Hendriks (g), M. Geldof (h) and M. Cotte (e, f), *Anal. Chem.* **83**, 1224–1231 (2011).  
 (a) University of Perugia (Italy)  
 (b) University of Antwerp (Belgium)  
 (c) Istituto CNR di Scienze e Tecnologie Molecolari (CNR-ISTM) (Italy)  
 (d) Delft University of Technology (The Netherlands)  
 (e) C2RMF (France)  
 (f) ESRF  
 (g) Van Gogh Museum (The Netherlands)  
 (h) The Netherlands Cultural Heritage Agency (RCE) (The Netherlands)



**Fig. 142:** a) Photograph of *View of Arles with Irises* by Vincent van Gogh (1888, F 409, Van Gogh Museum, Amsterdam). b) Visible light microscopy image and c) grey scale image of Ba distribution (map size:  $30 \times 100 \mu\text{m}^2$ ; pixel size:  $0.4 \times 1 \mu\text{m}^2$ ; dwell time: 0.3 s). d) RG Cr-chemical state maps (size:  $11.6 \times 24 \mu\text{m}^2$ ; pixel size:  $0.4 \times 0.4 \mu\text{m}^2$ ; dwell time: 0.3 s). The mapped area is shown in (c) by a blue oval.



formulated: in the presence of abundant sulfate ions, a minor amount of sulfide ions can originate locally (chemical or microbial) that might act as reducing agent for the chromate ions via the regeneration of sulfates in an acidic medium. To prove this aspect of the degradation mechanism, a systematic additional study is underway.

## Development of imaging techniques

### Principal publication and authors

I. Zanette (a), T. Weitkamp (a,b), T. Donath (c), S. Rutishauser (c) and C. David (c), *Phys. Rev. Lett.* **105**, 24102 (2010).

(a) ESRF

(b) Synchrotron Soleil, Gif-sur-Yvette (France)

(c) Laboratory for Micro- and Nanotechnology, Paul Scherrer Institute, Villigen (Switzerland)

### Two-dimensional grating interferometer

Phase-contrast imaging with ultra high sensitivity is among the unique applications of modern X-ray sources. With X-ray grating interferometry, a particularly powerful phase-contrast method, details with tiny mass density differences have been successfully imaged with hard X-rays and at spatial resolutions of a few micrometres [1]. X-ray grating interferometry also provides 'dark-field' images that reveal the presence of features

such as cracks and nanopores smaller than the spatial resolution of the imaging system. Phase and dark-field signals complement, and significantly improve, the conventional absorption information. Grating-based imaging has therefore been attracting interest from many fields, including biology, medicine and materials science.

The standard one-dimensional X-ray grating interferometer (GIFM) consists of two line gratings: the phase grating G1 and the absorption grating G2, both placed between the sample and the detector. The interference pattern generated by G1, which contains information on the optical properties of the sample, is analysed with G2 in order to retrieve the differential phase and dark-field image signals in the

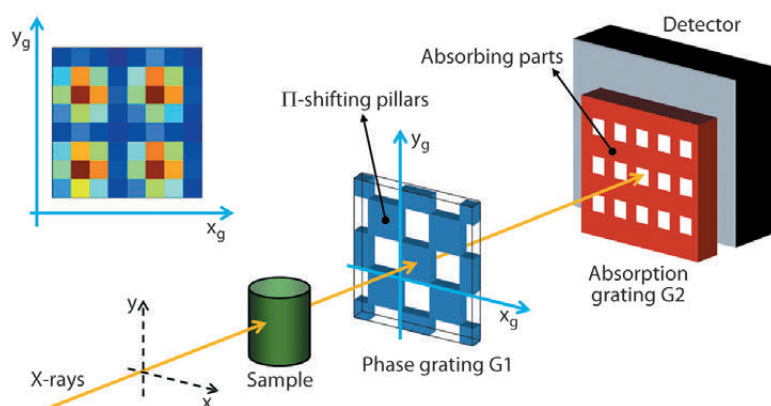


**Fig. 143:** Schematic representation of a 2D grating interferometer. The inset shows the intensity distribution measured in a detector pixel during a raster phase-stepping scan performed in  $8 \times 8$  steps over  $2 \times 2$  periods.



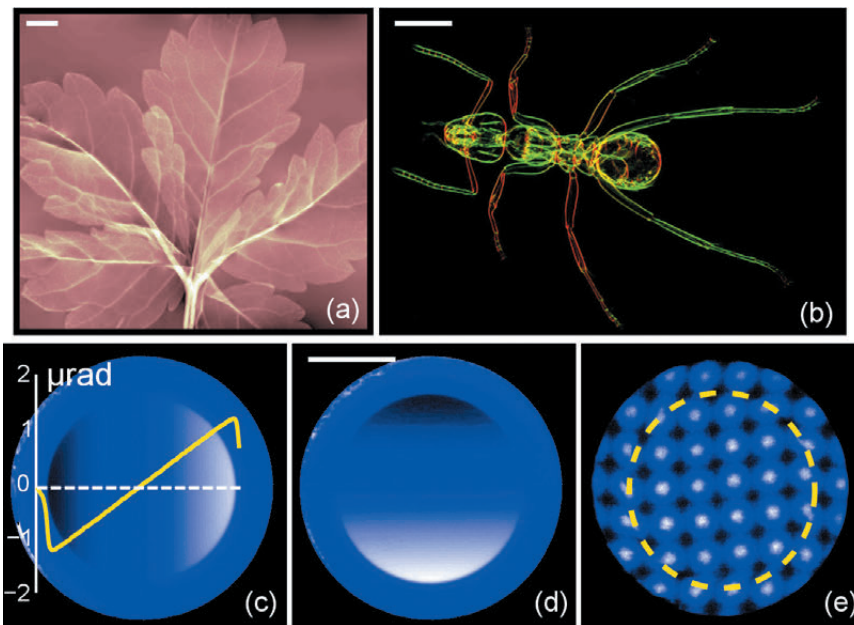


**Fig. 144:** a) Phase image of a leaf retrieved from the differential phase images along  $x$  and  $y$ . b) False-colour dark-field image of an ant which reveals the scatter direction of the features in the sample: red and green channels are given by, respectively, dark-field signals along  $x$  and  $y$ . c) and d) Refraction angle images of a single Be refractive lens with radius of curvature of 1 mm in the centre of the lens. The profile plot in figure (c) shows refraction angle values extracted at the position of the dashed horizontal line. e) 2D moiré pattern produced by the 2D GIFM and distorted by the presence of the Be refractive lens; the moiré pattern appears rotated in the lens aperture. These images were obtained at ID19 with an X-ray photon energy of 23 keV and an inter-grating distance of 480 mm. The bars in panels (a), (b) and (d) indicate a length of 1 mm.

direction perpendicular to the grating lines. In the past two years, a GIFM of this kind has been made available to external users at beamline ID19. Recent results include the visualisation of the architecture and cells of the human brain [1] and a study on the orientation and scattering strength of dentinal tubules in teeth [2].

A collaboration between the Paul Scherrer Institute (Switzerland), the Karlsruhe Institute of Technology (Germany), Synchrotron Soleil (France) and the ESRF has significantly improved this imaging technique and broadened its application areas by developing a two-dimensional (2D) GIFM. This 2D GIFM gives access to differential phase and dark-field signals in multiple directions of the image plane.

**Figure 143** shows a schematic representation of the novel device. The phase grating G1 has a checkerboard structure [3] with silicon pillars that shift the X-ray wave phase by  $180^\circ$ . The analyser grating G2 has strongly absorbing structures made of gold. The image signals are retrieved by a raster scan of G1 in the lateral directions  $x_g$  and  $y_g$  ("phase stepping"). The intensity recorded in each detector pixel during the phase-stepping scan can be approximated by a 2D sinusoid (inset in **Figure 143**). The position and amplitude of the sinusoid in  $x$  and  $y$  give, respectively, differential phase and dark-field signals along the two directions. Examples of phase and dark-field radiographs of test samples obtained with the 2D GIFM are shown in **Figure 144a** and **b**.

Due to the availability of contrast in  $x$  and  $y$ , the information content and the quality of the final images provided by the 2D GIFM are much higher than with a 1D device.

The 2D GIFM measures refraction angles with a precision down to 10 nrad, which makes it particularly interesting for the at-wavelength characterisation of X-ray optics. The potential of the 2D GIFM in metrology has recently been demonstrated on parabolic refractive lenses (**Figure 144c** and **d**) [4].

For applications which require that information is extracted from a single shot, moiré imaging based on the 2D GIFM can be used, instead of the phase-stepping technique. In this case, however, the spatial resolution is limited by the period of the moiré pattern (**Figure 144e**). Single-shot 2D moiré imaging is particularly promising for fast multimodal tomography and wave-front diagnostics at X-ray free-electron lasers.

#### References

- [1] G. Schulz, T. Weitkamp, I. Zanette, F. Pfeiffer, F. Beckmann, C. David, S. Rutishauser, E. Reznikova and B. Müller, *J. R. Soc. Interface* **7**, 1665-1676 (2010).
- [2] T.H. Jensen, M. Bech, I. Zanette, T. Weitkamp, C. David, H. Deyhle, S. Rutishauser, E. Reznikova, J. Mohr, R. Feidenhans'l and F. Pfeiffer, *Phys. Rev. B* **82**, 214103 (2010).
- [3] J. Primot and N. Guérineau, *Appl. Opt.* **39**, 5715-5720 (2000).
- [4] S. Rutishauser, I. Zanette, T. Weitkamp, T. Donath and C. David, *Appl. Phys. Lett.* **99**, 221104 (2011).



# Enabling Technologies

State-of-the-art instrumentation and associated enabling technologies are one of the pillars of the on-going Upgrade Programme. Driven by the first UPBL projects, several key technological areas have been identified and tackled, ranging from X-ray mirror engineering, diamond technologies, nano-focussing optics, pixel detectors, on-line data analysis to high-rate data collection. Overall, one of the most challenging aspects of our programme is setting a balanced human and financial investment between mid and long-term R&D projects and UPBLs implementation. 2011 has seen the maturation and consolidation of the projects initiated in 2010. In this context, ISDD and TID provide resources for the execution of the Upgrade Programme for both beamlines and the accelerator complex.

This chapter is a collection of five articles exemplifying some important and recent technical achievements, ranging from sample manipulation and production of nanobeams to the development of new frameworks for 2D detectors. Indeed, the selected articles illustrate the common ambition to provide the best response to the increasing expectations of our users' communities in terms of beamline performance. The dramatic improvements of the accelerator performances and the possibilities offered by the new experimental hall for enhanced beamlines calls for innovative scientific instrumentation. Similarly, new experimental methods require new instrumental concepts. A good example of the paradigm is given by the two first articles.

The first article deals with a method aiming at recording mega-pixel speciation maps. This so-called full-field X-ray microspectroscopy, developed at ID21, provides large field-of-view images with a sub-micrometre pixel resolution and is very well suited to the chemical characterisation of geological materials. To be successful, this new method overcame several technical challenges including new optics and the detection and processing of large 2D-hyperspectral data sets.

The second article illustrates the need for a pioneering approach when dealing with nanobeam based experiments, one branch of which is now aiming for the manipulation of a single particle in a very accurate but non-invasive way. The ID13 team explored the potential of optical tweezers based on the trapping capability of focused laser beams for the manipulation of objects with ultra-low contact forces.

The performance of most of the beamlines is determined today by the implementation and reliable operation of customised state-of-the-art detection systems. Whilst all synchrotron radiation facilities have the common goal of developing the best technologies for detectors, which is paramount to all of these facilities, their strategies and capabilities can differ significantly. A number of collaborations exist based on frameworks with varying degrees of formality, ranging from bilateral collaborations to multi-facility European networks. Among several pan-European initiatives coordinated by ESRF, HIZPAD (high-Z pixel array detectors), described in the third article, is an excellent example of multi-facility collaboration. HIZPAD, a Joint Research Activity within the FP7 project ELISA - aims to improve the detection efficiency of X-ray pixel detectors in the 20-100 keV energy range, currently limited by the poor absorption of silicon sensors. The high degree of customisation of detection systems for a given experiment, led, for instance, to a dramatic inflation in the variety of 2D detectors used on beamlines. Implementation and maintenance of this broad suite of new 2D detectors generally requires a significant amount of human resources. With the objective of optimising resources, a specific effort has been made in establishing a policy for standardising beamline components and instruments. Ideally, this standardisation has to be achieved across Europe. As described in the fourth article, LiMA (library for image acquisition), aims at meeting both objectives. Initiated by the ESRF, LiMA has been adopted by many other facilities and some detector manufacturers and today offers new, fully-standardised interfaces with enhanced capabilities for a wide range of 2D detectors for imaging, diffraction, scattering and spectroscopy experiments.

Cutting-edge instrumentation requires a very high level of optimisation and integration with a full control of all stages from modelling to fabrication, assembly and control. The in-house development of dynamically-figured multilayer mirrors for nanofocussing is a promising example of this improved synergy between the X-ray Optics, Advanced Analysis & Modelling, Mechanical Engineering and the Software groups of the ISDD and beamline teams (ID22NI, in this case). As described in the last article of this chapter, ID22NI routinely provides beam sizes of  $59 \times 43 \text{ nm}^2$  with photon flux of  $10^{12} \text{ ph/s}$  corresponding to a record flux density of  $1.5 \times 10^8 \text{ ph/s/nm}^2$ .



This is indeed the fruit of long standing R&D effort which confirms the appropriateness of our approach and which paves the way for future UPBLs.

Handling the massive flux of data coming from modern 2D detectors is another challenge which requires a coordinated approach between different groups at the ESRF. Work has started to optimise the integration

of these detectors into the ESRF IT infrastructure in order to minimise bottlenecks in the data flow from the detector to the actual data analysis. This is work in progress and we will be glad to report on this project in next year's issue of the Highlights.

R. Dimper and J. Susini

## ■ Imaging of heterogeneous rocks and materials by full-field X-ray microspectroscopy

Rocks and many other materials show complex polycrystalline arrangements with chemical and structural heterogeneity over a variety of lengthscales. The inhomogeneities may have been caused during genesis processes or later in response to environmental physicochemical changes. Microprobe techniques provide satisfactory knowledge of such materials but their use is limited by their restricted field of view. For example, X-ray absorption near-edge spectroscopy (XANES) allows elemental oxidation states to be probed with high spatial resolution. However, scanning a large area is often not feasible with realistic acquisition times. To overcome this limitation, we show the potential of coupling XANES and full-field absorption radiography with a large hard X-ray beam. We developed a new full-field experimental setup on the **ID21** beamline. It has been optimised to acquire stacks of mega-pixel XANES images with submicrometre resolution, using a CCD array detector. Acquisition times are short considering the millions of spectra obtained, and the precision of a single spectrum is sufficient for advanced XANES studies. Another originality of this approach is the association of XANES with polarisation contrast imaging (PCI). As well as providing mineralogical orientation maps, PCI was used here for the first time to correct the elemental oxidation state estimates from polarisation effects induced by polarised synchrotron radiation.

The full-field XANES setup consists of a fixed exit double crystal monochromator, a special sample holder, and a 2D-detector to detect transmitted X-rays. The detector comprises a scintillator coupled to a CCD camera through magnifying light optics. First trials showed that measurements of fine spectral features at the limit of the monochromator resolution require a quasi-perfect flat-field correction. For this purpose, the sample stage has been equipped with a linear stage able to remove and reposition the sample accurately in the beam in less than a second, thus permitting flat field acquisition with high frequency. The experimental setup is also switchable into PCI mode in a few minutes. A series of radiographs are acquired by rotating the sample in the azimuthal plane over  $\pi$ . Radiographs are then re-aligned by rotation with computing scripts to create a PCI image stack. PCI resulting from the interaction between X-ray linear dichroism and preferential absorption in relation to the minerals' refractive indices (and thus their orientation) have been successfully recorded on Fe-bearing phyllosilicates.

The potential of the full-field XANES and PCI association is demonstrated on a metasediment that underwent two distinct metamorphic events. These events led to the formation of a rock with micrometric scale heterogeneities, deformation structures associated with mineralogical

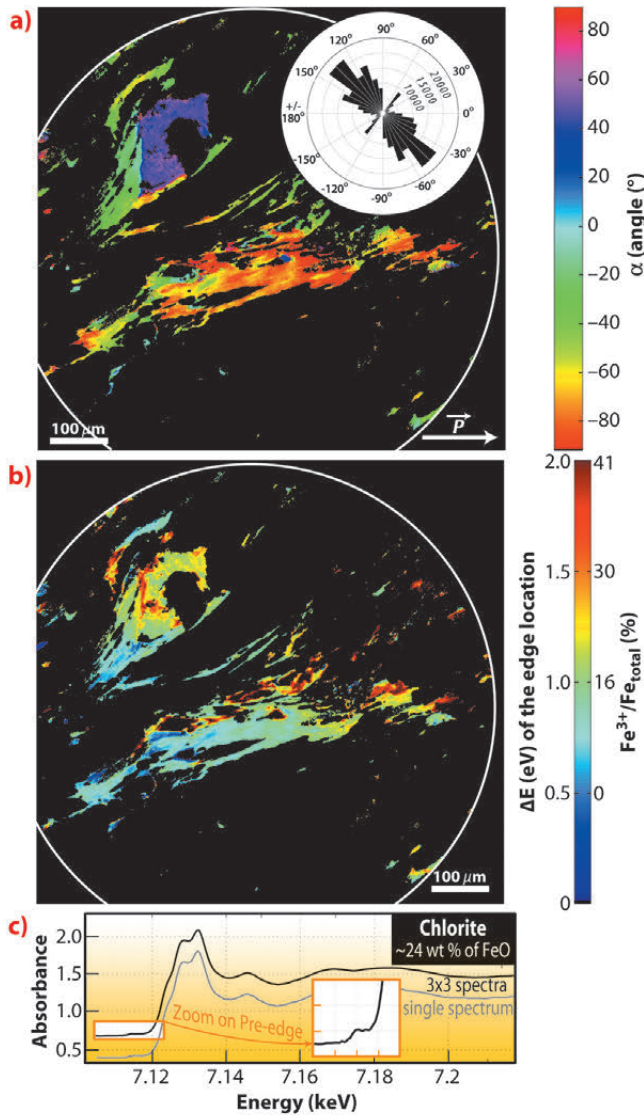
### Principal publication and authors

V. De Andrade (a,b), J. Susini (b), M. Salomé (b), O. Beraldin (b), C. Rigault (c), T. Heymes (d), E. Lewin (d) and O. Vidal (d), *Anal. Chem.* **83**, 4220-4227 (2011).  
(a) NSLS II, BNL, Upton (USA)  
(b) ESRF  
(c) HYDRASA, CNRS, Poitiers University (France)  
(d) ISTerre, Maison des Géosciences, Grenoble (France)





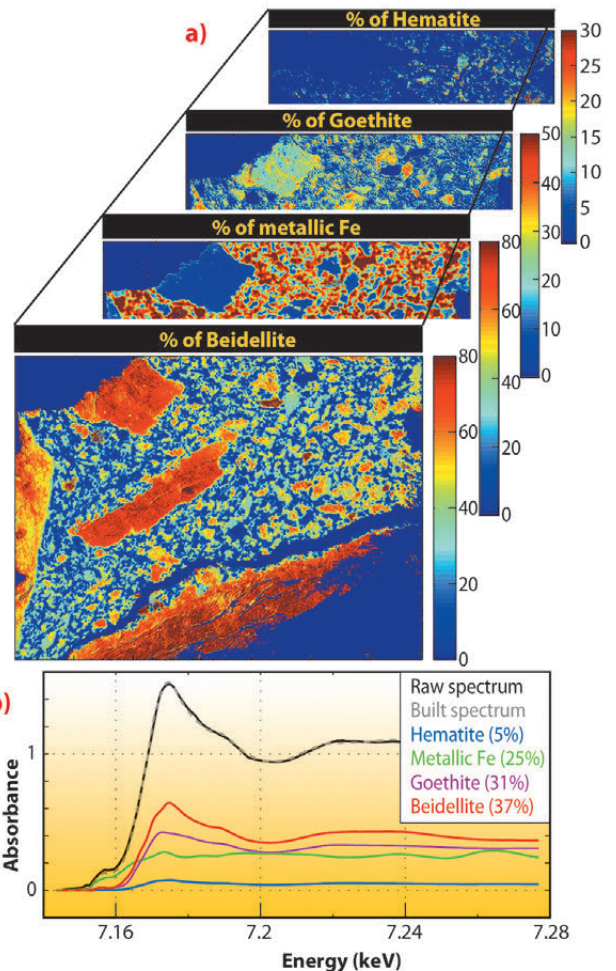
**Fig. 145:** a) C-axis orientation map of chlorite derived from PCI. b) Quantitative iron redox map of chlorite corrected for polarisation effects. c) Selection of 1 and 3x3 chlorite XANES spectra, amongst the 1M spectra constituting the image.



phases, and with expected Fe redox variations. A crystallographic orientations map derived from PCI shows two populations of phyllosilicates (**Figure 145a**).  $Fe^{3+}/Fe_{total}$  estimates change drastically after PE corrections (**Figure 145b**). The amplitude of variation stays around 0.4 but the shape of the histogram becomes comparable to a Gaussian. The  $Fe^{3+}$  map highlights subtle redox variations recorded during the rock exhumation and can be used to retrieve the pressure-temperature conditions undergone by the rock and so, to build a geodynamic model.

The second example concerns an analogous material to nuclear waste storage systems. This material is a bentonite (smectite and iron oxides) mixed with micrometric large metallic iron spherules. It was submitted to a forced fluid percolation for 4 years at 25°C. Bentonite is made of finely intercalated mineralogical phases to the micrometre or pixel scale. Mapping of these phases have been computed by fitting XANES spectra composing the hyperspectral data by linear combination of reference spectra selected from a database (**Figure 146a**).

**Fig. 146:** a) Spectra retrieved from a database of bentonite end-members mapping from a Fe K-edge XANES stack (pixel width: 645 nm) with a least square fitting method. b) Example of line fitting corresponding to a single spectrum selected in the clayey matrix.



Results show that starting material is preserved from chemical reactions in smectite and goethite rich nodules, and highlight reactive areas with apparition of reaction products like hematite and cronstedtite, while proportions of the initial bentonite compounds decrease. Sensitivity and resolution of the technique make it possible to detect small amounts of phase with low crystallinity. The spatial information reveals local chemical evolutions in clays responsible for changes in the bentonite mechanical properties.

In conclusion, this new method is unique in providing mega-pixel elemental speciation maps, with a large field of view ( $\approx 1 \text{ mm}^2$ ), while conserving a submicrometre resolution. The combined use of PCI and XANES allows a reliable redox estimate, eliminating artifacts resulting from polarisation effects that can occur when analysing monocrystals. These 2D-hyperspectral data are also very effective for the local identification of phases in finely divided materials.

## ■ Synchrotron radiation microprobing of biological matter manipulated by optical tweezers

Sample manipulation in synchrotron radiation experiments is commonly performed through mechanical contact which may induce mechanical deformations in particular for biological and soft matter materials in aqueous environments. An alternative to mechanical devices is optical tweezers which are based on the trapping capability of focused laser beams with contact forces in the femto- to nano-Newton range [1]. Optical tweezers can be used for manipulation of single particles, assembly and rotation. They also allow the generation of multiple traps, thus providing the possibility of distributing the radiation dose on several micro-objects which is of particular interest for experiments with intense synchrotron radiation micro- and nano-beams. The ability to rotate single particles allows, in principle, the development of an optical goniometer for diffraction, tomography and imaging experiments. Investigations

of single fragile objects manipulated by optical forces with high brilliance X-ray beams may enable new research fields such as serial protein crystallography at storage rings and even at XFEL sources.

We have developed a compact and portable optical tweezers setup for synchrotron radiation applications at the **ID13** beamline [2]. Objects of several micrometres up to few tenths of a micrometre in size can be trapped for extended periods of time. A laser beam of  $\lambda = 1070 \text{ nm}$  is focused by a high numerical aperture immersion objective into a glass capillary filled with the particles suspended in an aqueous environment (**Figure 147a**). The trapped objects studied were typically starch granules, and insulin crystals (**Figures 147b,c**). The selection and positioning of single objects out of a batch of many can be performed currently in

### Principal publication and authors

S.C. Santucci (a,b), D. Cojoc (b), H. Amenitsch (c), B. Marmiroli (c), B. Sartori (c), M. Burghammer (a), S. Schoeder (a,d), E. Di Cola (a), M. Reynolds (a) and C. Riekel (a), *Analytical Chemistry* **83**, 4863-4870 (2011).

(a) ESRF

(b) CNR-IOM Laboratorio TASC, Trieste (Italy)

(c) IBS, Graz (Austria)

(d) Soleil Synchrotron (France)

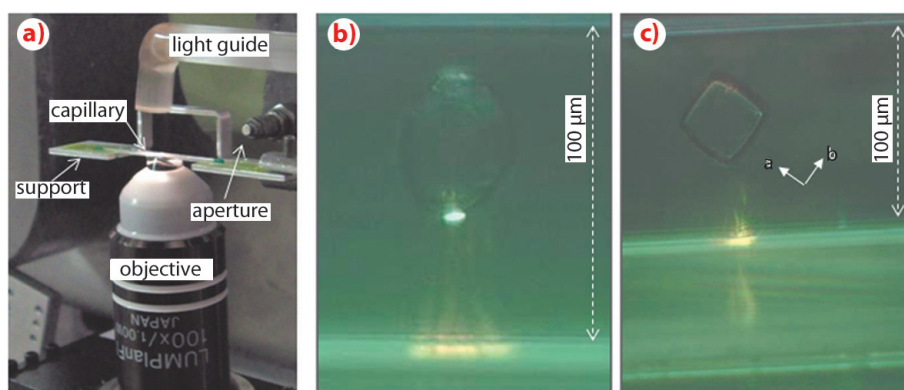


**Fig. 147:** a) Optical tweezers sample environment; the laser beam is focused by an immersion objective into the capillary. b,c) Optically trapped starch granule and insulin crystal viewed along the beam direction. The trace of the laser beam is visible through the capillary. The crystallographic orientation of the cubic insulin unit cell is indicated.



### References

[1] A. Ashkin, *Optical trapping and manipulation of neutral particles using lasers*. World Scientific Publishing Co. Pte. Ltd. (2006).

[2] S.C. Santucci *et al.*, *Analytical Chemistry* **83**, 4863–4870 (2011).

a semi-automatic manner by software routines.

We have demonstrated the feasibility of microdiffraction experiments on optically trapped starch granules and protein crystals which were repeatedly raster-scanned at 50 ms exposure/raster-point with an about 1 micrometre beam of wavelength  $\lambda \sim 0.09$  nm at around 13 keV [2]. Indeed, for the cubic insulin crystal shown in **Figure 147c**, order along the densely packed [110] direction is maintained until complete loss of long-range order. The average of all patterns collected during the first raster-scan with 50 ms/point is shown in **Figure 148a**. The inner part of the reciprocal lattice

has been indexed for the cubic  $I2_13$  space group (**Figure 148b**). The evolution of the crystal diffracting properties with increasing dose is revealed during the successive raster-scans in a composite diffraction image with the intensities of the pixels reflecting the local -1-10 reflection intensity (**Figure 148c**). We observe that the general shape of the crystal is maintained up to about 300 ms exposure when plotting successive composite diffraction images. During this period, the resolution limit of the crystal rapidly shrinks until only the inner  $hk0$  reflections remain visible (not shown). The strong intensity fluctuations visible in the 50/100 ms composite diffraction images disappear with increasing radiation damage suggesting the evolution of a more homogeneous domain size.

Our experiments demonstrate the potential of optical tweezers for manipulating objects requiring ultra-low contact forces. We think that the possibilities for room temperature protein crystallography experiments in an aqueous environment are particularly interesting in view of crystals which are difficult to cryofreeze. As the setup is compact and flexible, further customisation is possible for ad-hoc requirements of specific applications under X-rays such as particle shaping and assembly as well as particle fractionation.

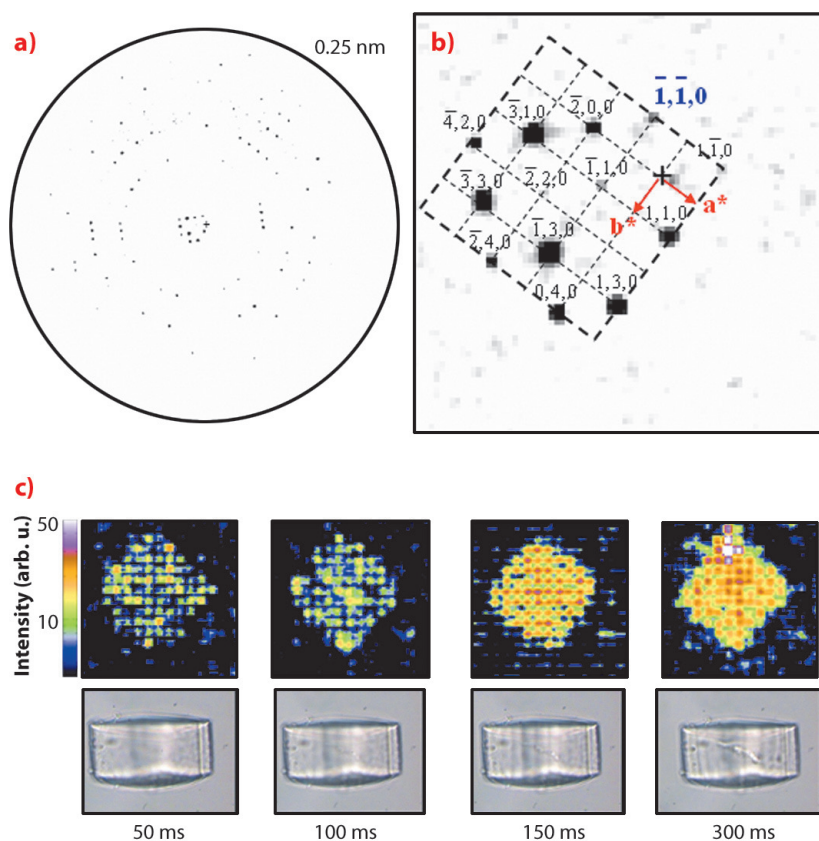


**Fig. 148:** a) Averaged diffraction pattern of the insulin crystal raster-scan at 50 ms exposure/point. b) The inner part of the  $hko$  reciprocal lattice. c) Upper row: evolution of the insulin composite diffraction images with increasing exposure time for the -1-10-reflection intensity. The times indicated correspond to the overall exposure time per point for each raster-scan. Lower row: Optical microscopy images recorded normal to the X-ray beam direction via the immersion objective. The radiation damage induced by the microbeam is revealed by stripes.

### Authors

C. Ponchut and M.Ruat  
ESRF

## ■ HIZPAD, a European collaboration for the development of pixel detectors dedicated to high X-rays energies

HIZPAD (high-Z pixel array detectors) is a Joint Research Activity of the ELISA European project that started in March 2009 and was completed in August 2011.

HIZPAD focused on the evaluation of existing high-Z pixel sensor technologies for application to X-ray pixel detectors used at synchrotron radiation and free

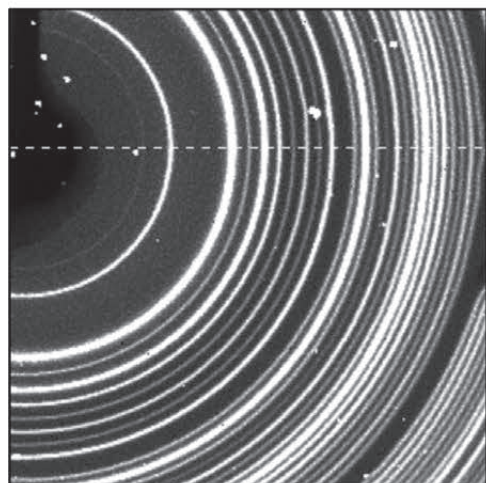


electron laser sources. This initiative emerged from the need to improve the detection efficiency of X-ray pixel detectors in the 20-100 keV energy range, limited by the poor absorption of the thin (300-500  $\mu\text{m}$ ) silicon sensors currently in use. HIZPAD was coordinated by the ESRF and gathered the major European synchrotron radiation sources as well as leading European institutes and companies in the field of pixelated semiconductor detectors.

The work programme started by a survey that included: the high-Z pixel detector needs of synchrotron radiation and free electron laser sources (carried out by SOLEIL); high-Z materials performance and sensors suppliers (Freiburger Materialforschungsinstitut (FMF), and the University of Surrey) and high-Z pixel sensor hybridisation technologies and suppliers (STFC). The survey clearly showed that CdTe and possibly CZT were the only viable options for the high-Z pixel sensor material given the time frame of our project. It also allowed us to identify the most advanced industrial providers for sensor materials and processing.

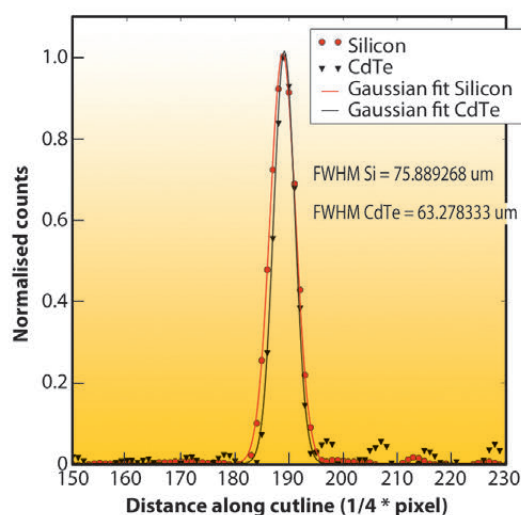
After assessment of the electrical performance of the sensor materials by the University of Surrey and by FMF, a collection of CdTe pixel sensors with pixel pitches from 55 to 172  $\mu\text{m}$  and detection areas from 2 to 14  $\text{cm}^2$  were produced and bump-bonded by X-ray Imaging Europe (XIE) to TIMEPIX [1], XPAD, and PILATUS photon-counting readout chips. CdTe linear microstrips connected to a MYTHEN readout system were also produced by PSI. A few CZT sensors were also made for later evaluation.

a)



The CdTe assemblies were then integrated into test detectors and an extensive characterisation was carried out at the ESRF [2], DESY, SOLEIL, DLS and PSI, from which we can outline the following results:

Although made of the highest grade material available, the CdTe sensors all exhibited varying amounts of insensitive regions of a few tens of pixels wide, the origin of which is still to be identified. Accepting those defects, a flatfield correction generally allowed quite a uniform image to be obtained. The sensor coupling to the readout chips remains a



#### Acknowledgement

The authors are grateful to J. Wright and G. Vaughan from ID11, V. Honkimaki, T. Buslaps and C. Chabert from ID15, E. Ziegler and T. Lafford from BM05, C. Nemoz, T. Brochart and A. Bravin from ID17, for giving access to beamtime, and also for their support and involvement during tests campaigns. The research leading to these results has received funding from the European Community's Seventh Framework Programme (FP7/2007-2013) under grant agreement n° 226716. The MEDIPIX2 and TIMEPIX readout chips are developed by CERN and the Medipix2 collaboration.

**Fig. 149:** Line-spread function of CdTe and of Si pixel sensors of same pitch (55  $\mu\text{m}$ ) at 22 keV, normalised to the same intensity.

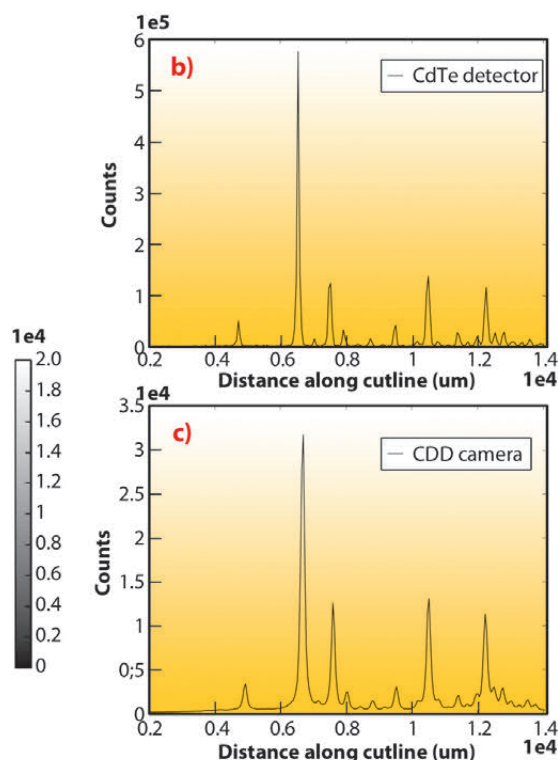


**Fig. 150:** a) Powder diffraction pattern of a  $\text{YB}_2\text{O}_3$  nanopowder acquired with a CdTe/TIMEPIX test detector. b) Cross-section along dashed cutline of diffraction pattern. c) Cross section in same portion of an image acquired with a CCD detector of same pixel size.



delicate operation and some failures were experienced.

We measured a spatial resolution of 65  $\mu\text{m}$  (PSF FWHM) on 55  $\mu\text{m}$  pixel pitch CdTe assemblies in the 22-90 keV energy domain. At 22 keV, the spatial resolution is even found slightly better than with silicon pixel devices of same pixel size (**Figure 149**).

In a powder diffraction experiment carried out at ID11, a materials science beamline, we compared a CdTe pixel test detector with a CCD-based X-ray detector of similar pixel size. At 50 keV, the CdTe pixel device produced a signal that was 10-times higher than that of the

CCD-based detector, and in addition it had better spatial resolution and efficient filtering of low energy background noise (**Figure 150**).

In conclusion, the HIZPAD collaboration demonstrated the feasibility as well as the high interest of high-Z pixel devices for synchrotron radiation and free electron laser applications, particularly those for materials science. A key result is the dramatic increase in detection efficiency without loss in spatial resolution. Developments initiated in HIZPAD will be continued with a focus on the reduction of sensor defects as well as on the increase of detection areas.

#### References

- [1] X. Llopart, R. Ballabriga, M. Campbell, L. Tlustos and W. Wong, *Nucl. Instr. and Meth. A* **581**, 485 (2007); and erratum *Nucl. Instr. Meth. A* **585**, 106 (2008).  
 [2] M. Ruat and C. Ponchut, Proceedings of the IEEE conference RTSD workshop, Valencia, Submitted to *Trans. Nucl. Sci.* (2011).

#### Principal publication and authors

A. Homs, S. Petitdemange, E. Papillon, L. Claustre, R. Homs and A. Kirov, Proc. of ICALEPS-2011 Conf. (JaCoW.org), WEMAU011, 676-679 (2011).  
*ESRF*

## ■ LIMA: Acquiring data with imaging detectors

The ESRF beamline control software coordinates many devices during execution of experiments. These include dozens of 2D detectors which are used for quantitative data analysis on different X-ray applications: imaging, diffraction, scattering, spectroscopy, and beam and sample monitoring. An effort has already been made to unify the control of these devices with a single TACO/TANGO interface. However, each detector offers specific hardware capabilities, and the software development kits (SDK) provided by different manufacturers are not compatible. In practice, common code was not always shared and new software features were rarely back-ported to existing detectors. In addition, improvements in the X-ray beam brilliance and detector efficiency constantly encourage faster experiments, either to explore new time-resolved phenomena or to increase the sample analysis rate.

To simplify the integration of new 2D detectors a library for image acquisition, LIMA, has been developed at the Beamline Control Unit of the ESRF ISDD Software Group. LIMA's design followed three goals: Firstly, to be control system-independent in order to promote collaboration with other institutes; secondly, to export a common set of features for every detector, providing alternative software solutions when not implemented by hardware. Thirdly, because it is oriented towards high-performance acquisition, it aims to

exploit every optimisation available in the detector and makes intensive use of parallel algorithms. The library clearly separates the roles of a low-level hardware layer, which interfaces to the detector SDK, and a control layer on top of it, responsible for configuring the generic part of the acquisition and managing the software image processing. A modular design of both layers allows the integration of new hardware capabilities and software extensions while keeping backward compatibility. This structure permits library evolution with minimal effort. Different kinds of imaging applications can be built on top of the LIMA library, including device servers for distributed control or standalone graphical user interfaces (GUI).

Several operations can be applied to an image before it is considered ready for data analysis. First, a frame reconstruction might be necessary if not performed at the hardware level on multi-chip or parallel readout designs. Next, basic geometric transformations can be activated, including pixel binning, region-of-interest (ROI) selection, horizontal/vertical mirror (flip) and standard 90/180/270° rotations. Detectors providing stripe-like data at a high frame rate are supported by the built-in stripe concatenation mode. A full stack of images is handled in a single read/save operation, notably reducing the single-frame overhead.

Constraints in some detector hardware limit the pixel integration process, either

by time (ESRF Frelon) or by dose (ESRF Maxipix). This is solved in LIMA by means of software accumulation. It is activated by specifying a maximum frame exposure time; the control layer calculates the actual number of hardware frames depending of the requested total exposure time. In addition to the accumulated image, a saturation pixel mask is also obtained, necessary to detect non-linear software artifacts. Finally, depending on the experimental conditions, software operations like background subtraction, flat-field correction and pixel masking can be executed. An example sequence of these operations is shown in **Figure 151**.

Data reduction algorithms are available for online analysis. Statistical calculations, performed on a per-ROI basis (ROI counters), and centroid determination, used in beam position monitoring applications, can be activated. User-defined image processing tasks in C++ or Python are also allowed. All of these software tasks are executed in parallel, allowing the system to scale to multi-CPU/cores when performance is an issue.

Metadata is handled in LIMA by means of (image) headers, sets of “key: value” lines. Three kinds of headers are identified: static, common and frame. The static header has constant data like the detector brand and model. The common header stores data associated with a sequence of frames (scan), like the start date and time, the sample name and a snapshot of all motor positions. The frame header contains real-time information: time-stamp, detector metadata, software

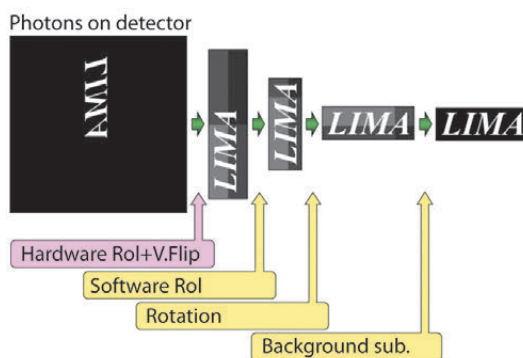


**Fig. 151:** Example sequence of image operations performed by hardware (pink) and by software (yellow).

processing details (execution time), as well as optional user-defined data. The library provides three triggers to save each image to disk: on user demand (manual); when the frame is ready (auto-frame); when both the frame and its associated user-defined header are ready (auto-header). Currently available file formats are EDF, CBF (crystallographic binary file) and Nexus/HDF5. In addition, LIMA allows parallel saving on multiple file streams to different destinations: the central storage server, an online data analysis workstation, or a NAS with user disks used to take data back to home.

Although still under development, LIMA already controls around a dozen detectors and is in production on several beamlines. A summary of the supported detectors and their measured performance at the ESRF is shown in **Table 1**. LIMA is an active collaboration between many facilities, with contributions from SOLEIL, PETRA III, and ADSC detector manufacturer, and beta-testers/observers including ALBA, ILL, MAX-lab and the commercial company Nexeya Systems.

Detector	Configuration	Max. frame rate (frame/s)	Max. data rate (MByte/s)	
			Acq.	Save
ESRF Frelon	FTM-Binning 1	30	120	120
	FTM-Binning 2	60	60	60
ESRF Maxipix	Single chip	1 400	180	180
	2×2	360	180	180
	5×1	280	180	180
Dectris Pilatus	6M	10	240	70*
	1M	30	120	120
	300K	200	230	230
Prosilica	GC655C	90	56	-
	GC1380C	20	53	-
Basler	acA1300	30	83	-
PCO.Dimax	Gig-Ethernet	1 200	9 300	90
	Camera-Link	1 200	9 300	270

**Table 1:** Detectors controlled with LIMA at the ESRF and their performances.

\* Pilatus 6M





#### Principal publication and authors

R. Barrett, R. Baker, P. Cloetens, Y. Dabin, C. Morawe, H. Suhonen, R. Tucoulou, A. Vivo, and L. Zhang, *Proc. SPIE* **8139**, 813904 (2011). *ESRF*

#### References

[1] Zhang, *et al.*, *J Synchrotron Rad* **5**, 804-807 (1998).

## ■ New focusing record with dynamically-figured multilayer mirrors

The ID22NI (nanoimaging) endstation has recently benefitted from a significant improvement in its focused beam characteristics thanks to a new focusing multilayer mirror system wholly designed and assembled at the ESRF. Users are now able to routinely access beam sizes of  $59 \times 43 \text{ nm}^2$  (H x V) with photon flux of  $10^{12}$  ph/s corresponding to a record flux density of  $1.5 \times 10^8$  ph/s/nm<sup>2</sup>.

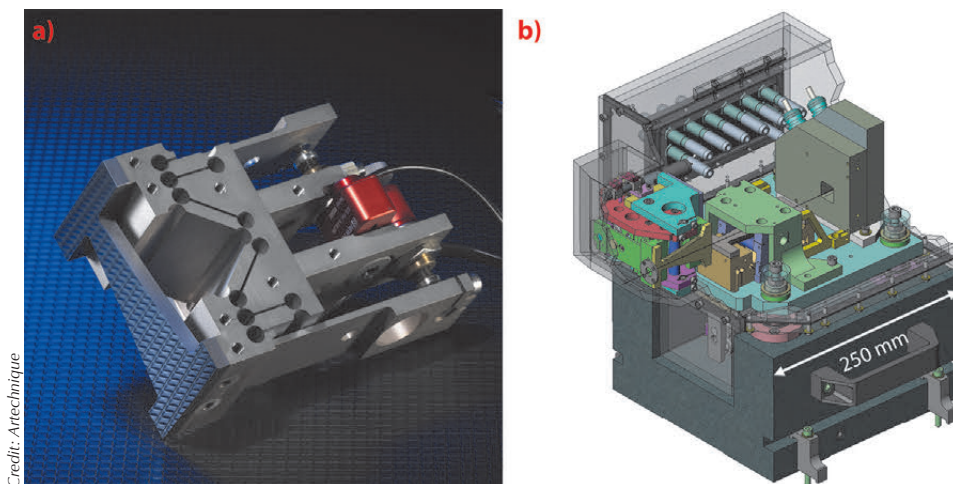
For micro or nanoprobe X-ray applications, the Kirpatrick-Baez (KB) configuration consisting of two successive mirror reflections in perpendicular planes is commonly used to produce a finely focused beam at the experimental station. In this scheme, one mirror focuses the beam vertically and a second mirror horizontally. As part of a long-running ESRF development programme, optomechanical systems have been implemented that create the required elliptical cylinder figures through precise bending of initially flat mirror substrates [1]. The bending is controlled using motorised actuators and can be readily adapted to the experimental requirements, allowing flexibility in the choice of the mirror focal length and incidence angle. Systems based on these in-house technologies are installed at around half of the ESRF beamlines. Due to high mirror reflectivities, large acceptances and achromatic focusing behaviour, this approach is capable of delivering exceptionally high fluxes into small focus probes.

Often the KB systems are used in combination with multilayer coated substrates. This allows the mirrors to be used at larger incidence angles and is particularly beneficial for use at high energies and/or to increase the acceptance for a given mirror length. Multilayers reflect a restricted energy band pass (typically ~1-10%) at an energy governed by the Bragg diffraction law. Consequently, if the beamline application demands energy tunability then the incidence angle must be adjusted according to the required energy. In this instance the dynamical figuring becomes particularly powerful since it allows the mirror figure to be optimised at different X-ray incidence angles.

For ID22NI, these mirror bending technologies have been pushed to their limits in providing a KB system which can routinely deliver high-flux hard X-ray beams focused in two dimensions to the 50 nm scale at a standard length ESRF beamline.

The system consists of two W/B<sub>4</sub>C multilayer coated mirror substrates adhesively bonded to flexure-hinge based bender systems and assembled in the KB configuration. The high demagnification ratios and short working distances needed to guarantee the small beam size require the mirrors to be bent to radii as short as 14 m. To achieve the required slope errors it was necessary to optimise the width profile of the mirror substrates using an

**Fig. 152:** a) The horizontally focusing mirror bender design. b) a schematic of the ID22NI KB system.



Credit: Artechnique

iterative finite element analysis procedure. The mirrors were manufactured from silicon with control of the substrate width with a precision better than  $2\ \mu\text{m}$  then polished using classical techniques. Due to the curvature of the bent substrates, the incidence angle of the X-rays varies strongly along the mirror and necessitates a variation in the multilayer d-spacing to ensure that the required photon energies are efficiently diffracted along the full mirror length. The deposition of high quality multilayers with such steep d-spacing gradients is challenging but these were successfully manufactured at the ESRF Multilayer Laboratory.

The coated mirrors were bonded to their respective bender mechanisms (**Figure 152a**) and the quality of the bent figure verified at the ESRF Optical Metrology Laboratory. The measured slope errors were as low as  $0.06$  ( $0.11$ )  $\mu\text{rad}$  RMS for the vertically (horizontally) focusing mirrors. Following integration in a highly compact KB assembly designed to minimise thermal drifts and vibrational instabilities (**Figure 152b**), the system was installed at the ID22NI end-station.

At ID22NI the system operates at photon energies in the range  $17\text{--}30\ \text{keV}$  with 'pink' beam illumination with the multilayer energy band pass ( $\sim 8\%$ ) relaying the emission of the single line undulator source (energy band width  $\sim 1.7\%$ ) with a transmission in excess of  $50\%$ . **Figure 153a** shows measurements of the beam profile performed at  $17\ \text{keV}$  demonstrating a focal spot size of  $59 \times 43\ \text{nm}^2$  FWHM (HxV). **Figure 153b** shows an X-ray fluorescence map of a test sample acquired using the focused beam - other examples of measurements made using the system appear elsewhere in these highlights.

These new developments are the fruit of a close collaboration between the X-ray Optics, Advanced Analysis & Modelling and Mechanical Engineering Groups of the ISDD and the ID22 beamline team. In addition, software developments by the ISDD Beamline Control Unit have made focusing optimisation within the beamline environment rapid and reliable.

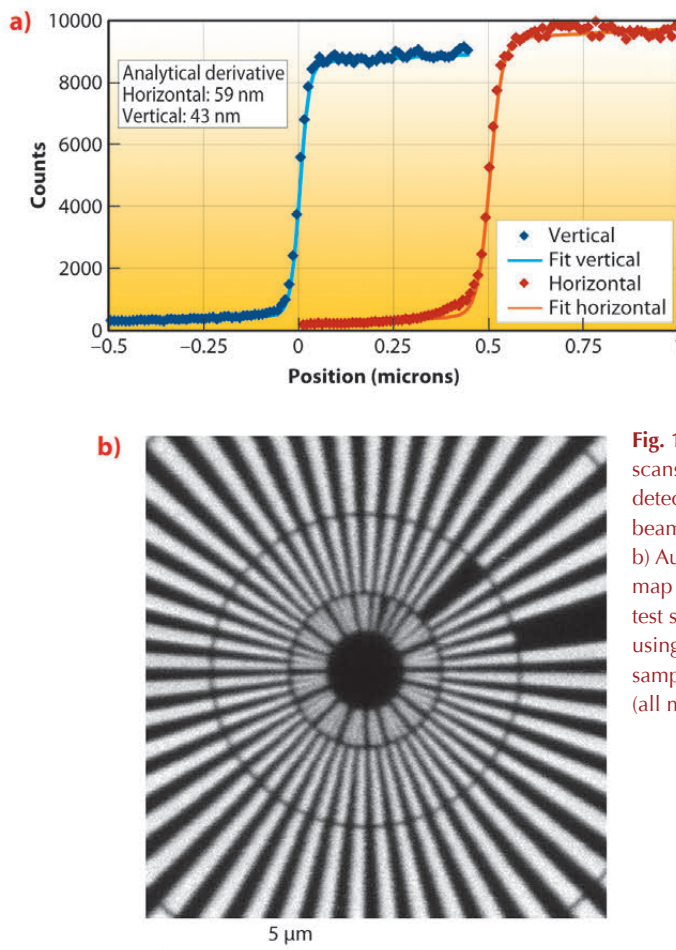


**Fig. 153:** a) Knife-edge scans (Au L fluorescence detection) across the beam focus. b) Au L X-ray fluorescence map of a gold resolution test structure acquired using raster scanning of sample in the focal plane (all measured at  $17\ \text{keV}$ ).



# Accelerator and X-ray Source

Throughout 2011, the Accelerator and Source Division has continued its efforts to ensure reliable operation as well as upgrading a number of systems. Some new developments have been carried out and many of these are described hereafter.

## ■ Beam parameters of the storage ring

**Table 2** presents a summary of the characteristics of the storage ring electron beam.

**Table 3** gives the main optic functions, electron beam sizes and divergences at various source points. For insertion device source points, the beta functions, dispersion, sizes and divergences are calculated in the middle of the straight section. For bending magnets two representative source points have been selected for each type (even or odd cell number) of magnet, corresponding to magnetic fields of 0.4 T and 0.85 T. These points differ by the observation angles, of respectively 3 and 9 mrad from the entrance of the magnet.

Electron beam profiles are Gaussian and the size and divergence are presented

in terms of rms values. The associated full width at half maximum sizes and divergences are 2.35 times higher. Horizontal electron beam sizes and divergences are given for the multibunch filling modes and apply to almost all filling patterns except when the current per bunch is larger than 4.5 mA, for which a slightly larger size and divergence are attained because of the increased energy spread of the electron beam.

Vertical electron beam sizes and divergences are given for a vertical emittance of 4 pm, which is now the standard for 2 x 1/3 and 7/8+1 filling modes. The vertical sizes and divergences are about 1.4 times larger in uniform filling mode (due to ion effects, which are partially corrected by the use of a vertical bunch-by-bunch feedback). To increase the lifetime of the stored beam, the vertical beam sizes and divergences are deliberately increased by about a factor 4 in the 16-bunch, 4-bunch and hybrid filling patterns.

**Table 2:** Principal characteristics of the electron beam.

Energy	[GeV]	6.04
Maximum current	[mA]	200
Horizontal emittance	[nm]	4
Vertical emittance	[pm]	4
Revolution frequency	[kHz]	355
Number of bunches		1 to 992
Time between bunches	[ns]	2.82 to 2816

		Even ID (ID2, ID6...)	Odd ID (ID1, ID3...)	Even BM (ID2, ID6...) 3 mrad	Even BM (ID2, ID6...) 9 mrad	Odd BM (ID1, ID3...) 3 mrad	Odd BM (ID1, ID3...) 9 mrad
Magnetic field	[T]	Variable	Variable	0.4	0.85	0.4	0.85
Horiz. Beta function	[m]	37.6	0.35	1.33	1.06	2.12	1.61
Horiz. Dispersion	[m]	0.134	0.031	0.062	0.051	0.089	0.075
Horiz. rms e- beam size	[µm]	413	50	99	85	132	113
Horiz. rms e- divergence	[µrad]	10	107	116	114	104	99
Vert. Beta function	[m]	2.95	2.97	41.7	42.0	32.1	32.2
Vert. rms e- beam size	[µm]	3.4	3.4	12.9	13.0	11.3	11.4
Vert. rms e- divergence	[µrad]	1.17	1.16	0.50	0.50	0.36	0.36

**Table 3:** Beta functions, dispersion, rms beam size and divergence at the various source points.





The lifetime, bunch length and energy spread mainly depend on the filling pattern. These are given in **Table 4** for a few representative patterns. Note that in both 16-bunch and 4-bunch filling patterns, the energy spread and bunch length decay with the current (the value indicated in the table corresponds to the

maximum current). The bunch lengths are given for the usual radio-frequency accelerating voltage of 9 MV (8 MV for 16-bunch and 4-bunch).

Filling pattern		Uniform	7/8 + 1	Hybrid	16-bunch	4-bunch
Number of bunches		992	870+1	24x8+1	16	4
Maximum current	[mA]	200	200	200	90	40
Lifetime	[h]	50	45	30	16	9
Rms energy spread	[%]	0.11	0.11	0.11	0.12	0.16
Rms bunch length	[ps]	20	20	25	48	55

**Table 4:** Current, lifetime, bunch length and energy spread for a selection of filling modes.

## Summary of accelerator operation

In 2011, 647 shifts (5173 hours) of beam were initially scheduled. Out of these, 5077 were effectively delivered (including 39.2 hours of refill). This represents a beam availability of 98.91%, which is an excellent figure, barely lower than the all-time record of 99.04% for 2009 and slightly greater than the 98.78% for 2010. Dead time due to failures accounts for the remaining 1.1%. The number of failures has been reduced compared to 2010 thanks to the absence of noticeable repetitive failures. Undoubtedly the efforts in preventive maintenance (e.g. replacement of water flow-meters with more reliable ones) have been particularly beneficial this year. Consequently, the previous record for mean time between failure (76 hours in 2009) has been significantly bettered in 2011, reaching the excellent figure of 107.8 hours.

But that was not the only record for the year since, during the first run of 2011, the beam was delivered for 795 hours (33 days!) without a single failure and interrupted only by the scheduled machine dedicated days or radiation tests (See **Figure 154**). Besides this record, which was the first sign of a good year, others runs proceeded particularly well as there were 23 long delivery periods (each more than 100 hours) without a single interruption.

Despite these excellent results, operation was particularly delicate due to the lack of redundancy on the radio frequency (RF) system caused by the installation of a new solid-state amplifier on the booster. Fortunately, this upgrade did not have a significant impact on the operation.

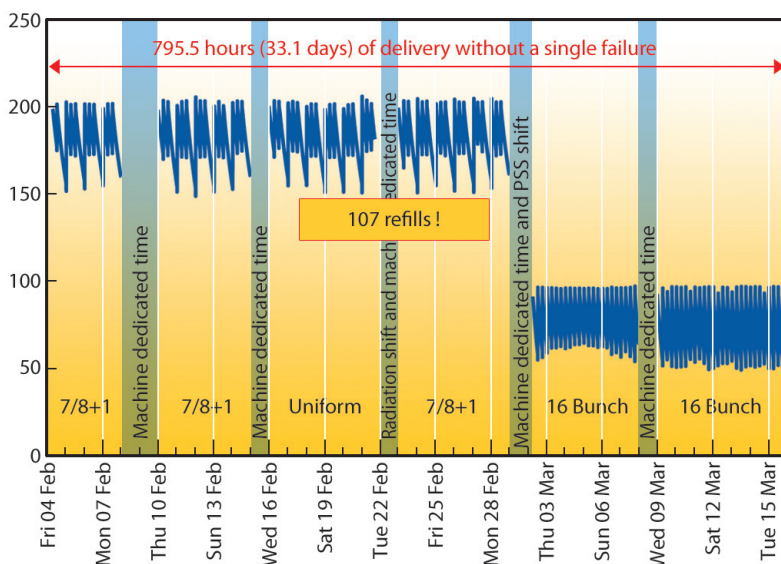


**Fig. 154:** The ESRF record delivery without a single failure, interrupted only by scheduled machine dedicated days.



Throughout the whole year, the beam was regularly delivered with a very low vertical

emittance in multibunch modes. **Table 5** presents an overview of operation in 2011.

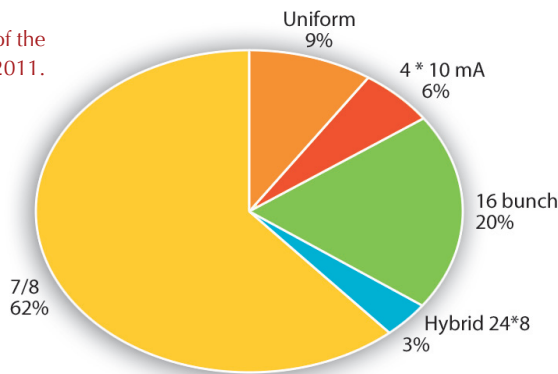
RUN NUMBER	TOTAL 2010	2011-01	2011-02	2011-03	2011-04	2011-05	TOTAL 2011
Start		21/01/2011	25/03/2011	27/05/2011	19/08/2011	14/10/2011	
End		16/03/2011	18/05/2011	27/07/2011	05/10/2011	05/12/2011	
Total number of shifts	<b>867</b>	162	162	183	141	156	<b>804</b>
Number of USM shifts	<b>700.813</b>	127.4	132	149.1	112.1	126	<b>646.625</b>
Beam available for users (h)	<b>5489.8</b>	995.8	1038.1	1175.7	871.7	996	<b>5077.2</b>
<b>Availability</b>	<b>98.78%</b>	<b>98.60%</b>	<b>99.35%</b>	<b>99.12%</b>	<b>97.94%</b>	<b>99.35%</b>	<b>98.91%</b>
Dead time for failures	<b>1.2%</b>	1.4%	0.7%	0.9%	2.1%	0.6%	<b>1.1%</b>
Dead time for refills	<b>0.9%</b>	0.9%	1%	0.6%	0.8%	0.5%	<b>0.8%</b>
Average intensity (mA)	<b>146.6</b>	149	132	180	102	178	<b>150.3</b>
Number of failures	<b>83</b>	7	6	9	19	7	<b>48</b>
<b>Mean time between failures (h)</b>	<b>67.5</b>	145.6	176	132.6	47.2	144	<b>107.8</b>
Mean duration of a failure (h)	<b>0.82</b>	2	1.1	1.2	1	0.9	<b>1.18</b>

**Table 5:** Overview of storage ring operation in 2011.

## Filling patterns

**Figure 155** presents the distribution of filling modes delivered in 2011. The only major change compared to 2010 is

**Fig. 155:** Distribution of the longitudinal filling modes in 2011.



that the uniform mode is now limited to specific user requirements. The preferred standard mode is now the “7/8 +1” filling mode which has become the best compromise satisfying the majority of the different user communities.

With the exception of the specific timing modes (16 bunch, 4 bunch and hybrid) for which the lifetime has to be increased by deliberately increasing the vertical emittance, all others modes were delivered with the vertical emittance as low as possible, *i.e.* 5 pm.rad or lower.

## Operation of the storage ring at low emittance

The last two years saw major efforts to reduce the vertical emittance. Benefits are manifold: higher brilliance, lower radiation dose during injections and, possibly, higher photon flux towards high energies by further reducing the vertical aperture of in-vacuum undulators.

In an ideal machine like the ESRF storage ring, the vertical emittance should be below the pico-meter (pm) level. However,

in reality, if no correction is carried out it may reach a few hundreds of pm. There are two main sources of vertical emittance: vertical dispersion and betatron coupling. The dispersion represents the dependency of the electron off-axis orbit upon its energy. Turn by turn, electrons lose energy as synchrotron radiation and gain some energy back thanks to the RF cavities. Non-zero vertical dispersion results then in electrons subjected to vertical



displacements, as in the horizontal plane. When integrating such displacements over all electrons inside bunches, the result is a nonzero vertical beam size and emittance. Tilts of quadrupole magnets and vertical misalignment of sextupoles are instead responsible for betatron coupling: The natural horizontal oscillations of the electrons within a bunch, induced by the emission of synchrotron radiation, are partially transferred to the vertical plane. As for dispersion, when integrating the vertical oscillations of all electrons, a thick vertical beam size and nonzero divergence are generated. An important difference between the two sources is that the contribution to the vertical emittance from vertical dispersion is constant along the storage ring, whereas the fraction of emittance generated by coupling varies along the machine. Values ranging from 100 pm to 450 pm have been measured at twelve emittance monitors when no correction is applied, see **Figure 156**.

The minimisation of the vertical emittance is carried out in two steps. The vertical dispersion and betatron coupling need to be precisely measured and then they have to be efficiently corrected by means of the skew quadrupole correctors installed around the storage ring. Two main factors in the two year period 2009/2010 made an unprecedented coupling measurement and correction possible. Installation of the most advanced beam position monitoring system, LIBERA, greatly increased the resolution in the measurement of the beam orbit response matrix, from which coupling is inferred. A new correction algorithm developed at the ESRF resulted in a faster and more effective simultaneous reduction of betatron coupling and vertical dispersion. Already in June 2010 a record-low vertical emittance of 5 pm was achieved during machine dedicated time.

However, at that time, it was difficult to preserve such a low value during beam delivery, because of the continuous changes in the apertures of insertions devices (IDs) carried out by users: despite the high magnetic quality of the great majority of IDs, a few of the earliest ones are known to be a gap-dependent source of coupling. To cope with this issue, two countermeasures were undertaken. The coupling induced by two of these IDs was measured and corrected locally by dedicated correctors placed at the ends of

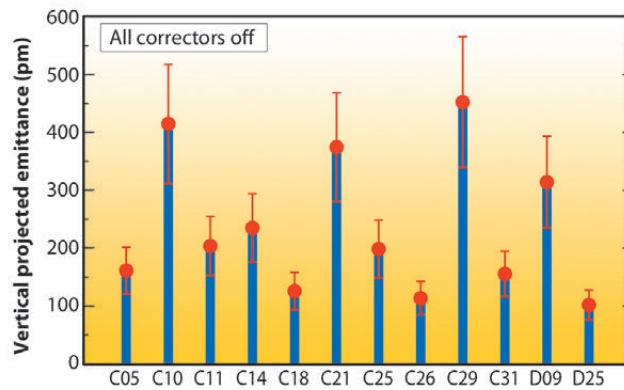


**Fig. 156:** Vertical emittance measured at twelve monitors along the ring with all correctors turned off (January 16, 2010).

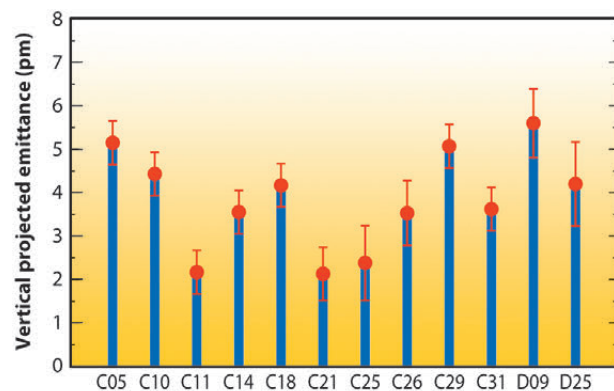


**Fig. 157:** Vertical emittance measured at twelve monitors along the ring after coupling correction (June 1, 2011)

their straight sections. A feed-forward loop powers these magnets and it depends on the ID gap aperture, according to a look-up table created during the measurement. On top of this, a unique coupling feedback was also implemented to periodically trim the currents of the 32 skew quadrupole correctors distributed around the storage ring so to retrieve the lowest emittance possible. At the end of 2010, the ESRF storage ring running in the 7/8+1 mode was routinely operating with a vertical emittance at the level of 7 pm, down from the typical 20-30 pm of 2009.

After the successful 2010 campaign, the late Pascal Elleaume wondered whether an ultra-low vertical emittance of 2 pm could be achieved by increasing the number of skew quadrupole correctors. Besides the dedicated IDs correctors, at that time 32 skew quadrupoles were used. Even though 52 trim coils installed in the storage ring were still available, studies demonstrated that 2 pm could be achieved by adding just 32 new skew correctors, the benefit of going beyond this number being minimal. During the winter shutdown of 2010 those coils were powered up and connected to the control system. After a few months of fine-tuning the correction with the new magnets, a vertical emittance between





### References

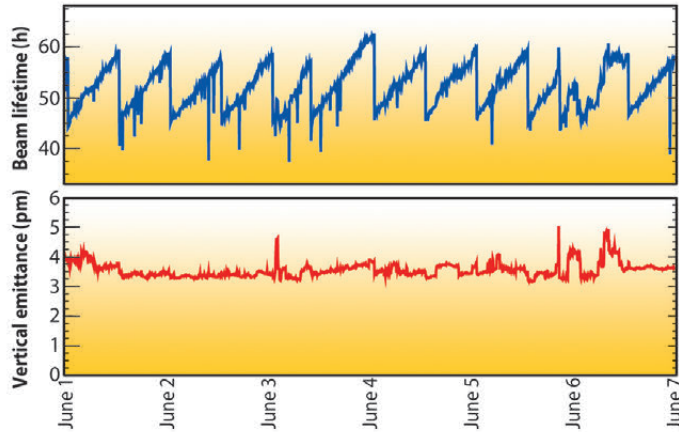
J. Chavanne *et al.* *Vertical emittance reduction and preservation at the ESRF electron storage ring*, in *Proceedings of the IPAC2011 Conference, San Sebastián, Spain (2011)*.

3 and 4 pm could be routinely achieved, see **Figure 157**. While the larger number of correctors further reduced betatron coupling efficiently, the vertical dispersion remained almost unchanged and is now believed to be the main source of vertical

emittance and the missing stage on the way towards the target of 2 pm. Studies are on-going to better understand and to overcome this issue.

During the initial period of low vertical emittance, the beam lifetime after refill deteriorated from 45 hours to 30 (in the 7/8 +1 mode), hence casting some concerns on the continuous use of this special mode. Further corrections of the sextupolar resonances, however, allowed the traditional lifetime of 45 hours at 200 mA to be recovered. Since spring 2011, therefore, the 7/8+1 mode has been delivered routinely at the lowest achievable emittance. Vertical emittance and beam lifetime during a typical week of delivery are reported in **Figure 158**.

**Fig. 158:** Beam lifetime (top) and average vertical emittance (bottom) measured during a week of beam delivery (7/8+1 filling mode) in June 2011. Data acquired during refills are not displayed.



## ■ Six metre long insertion device straight sections

The programme of extension of the insertion device straight sections from 5 to 6 m is progressing according to schedule. As of December 2011, ID18, ID30, ID24 and ID20 have been extended and equipped with 6 m long narrow aperture (8 mm) NEG coated ID chambers. The modifications were performed during the long shutdowns and at each occasion the machine was returned to user operation without any difficulty. Another set of five sections has been prepared and will be

installed during 2012. The design of the first 7 m section, which will be installed at the end 2012 on ID23, has been finalised. The preparation of the installation and the procurement of equipment have started.

## ■ New HOM-damped cavities in the storage ring

The ESRF upgrade included an option for an increase of the storage ring current from 200 to 300 mA, which has already been tested successfully with the existing RF system. At this current level the higher-order mode tuning of the existing five-cell copper cavities becomes extremely delicate and in view of a future stable and reliable operation in user mode, strongly HOM-damped normal conducting cavities were developed at the ESRF. The design, manufacture and test of operational prototypes received funding

from the European Union via the FP7/ESFRI/ESRFUP programme. The first of these cavities is already under test in the storage ring. Although the 300 mA option was not retained for the first phase of the ESRF upgrade, the aim is now to validate the new cavity design for a possible later increase in current.

**Figure 159** shows the first HOM damped cavity built by Research Instruments and installed for test in cell 25 at the location of the former five-cell cavity



#5. The design is based on the 500 MHz cavity that was developed at BESSY and which is used at ALBA and the MLS ring in Berlin. However, the cavity has been fully redesigned in house for the ESRF frequency of 352.2 MHz, with several substantial improvements. The geometry was optimised numerically and checked with an aluminium model, yielding excellent accelerating mode characteristics and very efficient HOM damping by means of comparatively compact HOM dampers. In the BESSY/ALBA design, inevitable gaps remain between the ridges of the HOM dampers that protrude into the cavity and the sleeves of the cavity ports, which lead to unexpected thermal problems and a persistent HOM. The suppression of these gaps constitutes a major improvement of the ESRF design. It was achieved by electron beam welding the coupling sections of the HOM dampers to the cavity body and connecting the other elements of the HOM dampers face-to-face with RF spring contacts, at a sufficient distance from the body where the RF fields and surface currents are sufficiently decayed not to burn the RF springs [1].

**Figure 160** shows the resulting extremely low residual HOM impedances measured on the first delivered cavity: with 18 such cavities installed in the ESRF storage ring, the threshold current for HOM driven beam instabilities would be about 2 A, well above the nominal beam current of the machine. The first beam tests with this cavity during the last run of 2011 were extremely promising. Vacuum conditioning for high RF power and high beam intensity was much easier than expected, even in 16 bunch filling mode, which is the most demanding in terms of power deposited by the beam into the HOM dampers: this cavity was transparent to normal user operation. Also the first tests with

active operation of the cavity for beam acceleration were very successful.

A second cavity was delivered by SDMS and a third one is being manufactured by CINEL. They will also be tested one by one on cell 25 before all three will be installed on the first 7 m straight section in cell 23 during the summer in 2013, as shown in **Figure 161**. The cavities will then be powered by three 150 kW RF solid state amplifiers, which are currently being manufactured. The replacement of all existing five-cell cavities with 18 new cavities in total is envisaged for later upgrade phases.

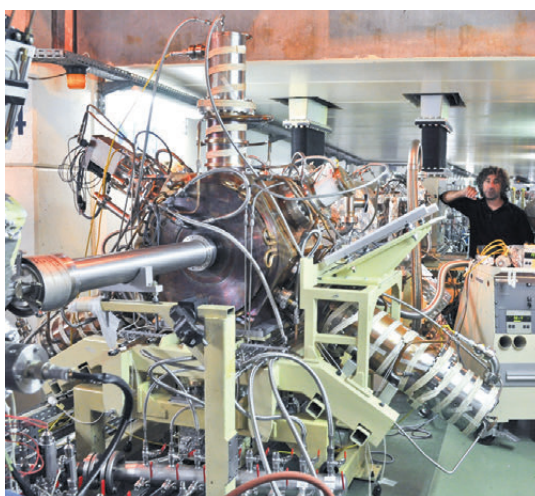


**Fig. 159:** The first new HOM-damped cavity installed in the storage ring.

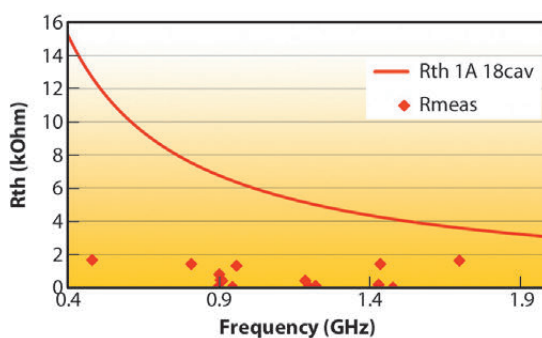


**Fig. 160:** Residual HOM impedances are a factor two below the design threshold of 1 A for coupled bunch instabilities with 18 cavities on the storage ring.

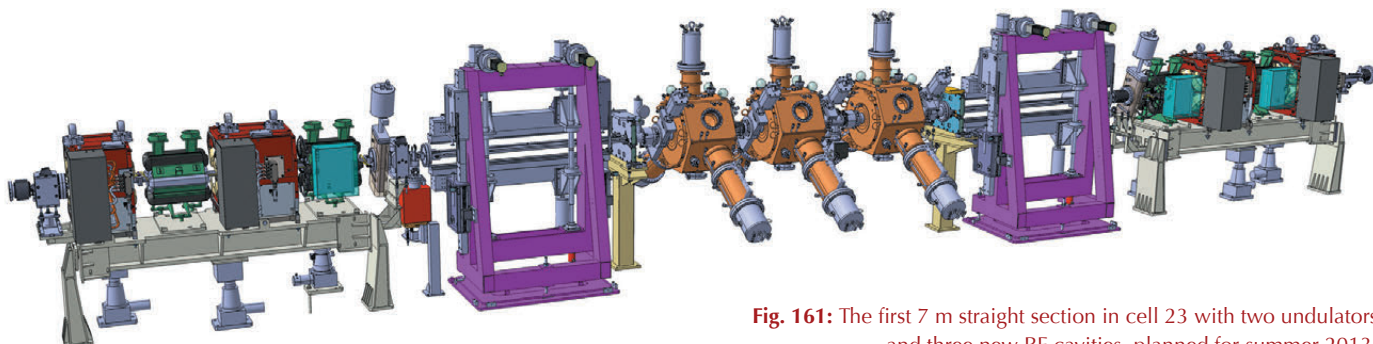


**Fig. 161:** The first 7 m straight section in cell 23 with two undulators and three new RF cavities, planned for summer 2013.

#### References

- [1] V. Serrière, J. Jacob, B. Ogier, L. Goirand, A. Triantafyllou, A.K. Bandyopadhyay and D. Boilot, *352.2 MHz HOM Damped Normal Conducting ESRF Cavity: Design and Fabrication*, IPAC'2011, San Sebastian, Conference proceedings pp. 68-70 (2011).





### References

[1] J. Jacob, J.-M. Mercier, M. Langlois and G. Gautier, *352.2 MHz - 150 kW Solid State Amplifiers at the ESRF, IPAC'2011, San Sebastian, Conference proceedings pp. 71-73 (2011).*

## ■ High power radiofrequency solid state amplifiers

In autumn 2011, ELTA/AREVA delivered the first batch of four 352.2 MHz - 150 kW solid state amplifiers shown in **Figure 162**. These amplifiers were thoroughly tested with a dummy load and are now being connected to the booster cavities. They will be put into operation for the booster ring at the intermediate accelerator restart in March 2012. A second batch of three

150 kW amplifiers will be delivered later in 2012 to power the three new HOM-damped cavities on cell 23 of the storage ring [1].

The main objectives for the implementation of these solid state amplifiers in phase 1 of the ESRF upgrade are:

- Qualifying solid state amplifiers as alternative to high power klystrons to guarantee the long term operation of the ESRF, thereby preparing a possible replacement of other klystron transmitters in further upgrade phases.
- Saving electrical power on the booster: thanks to the anti flicker system needed for the cycling at 10 Hz (huge capacitor banks with a total of 3.2 F in the 280 V DC power supply) up to only 400 kW will be drawn from the mains as compared to 1200 kW with the former klystron transmitter.
- Qualifying with beam a new storage ring RF unit comprising three HOM-damped cavities powered by three solid state amplifiers, which replaces one five-cell copper cavity powered by a klystron.

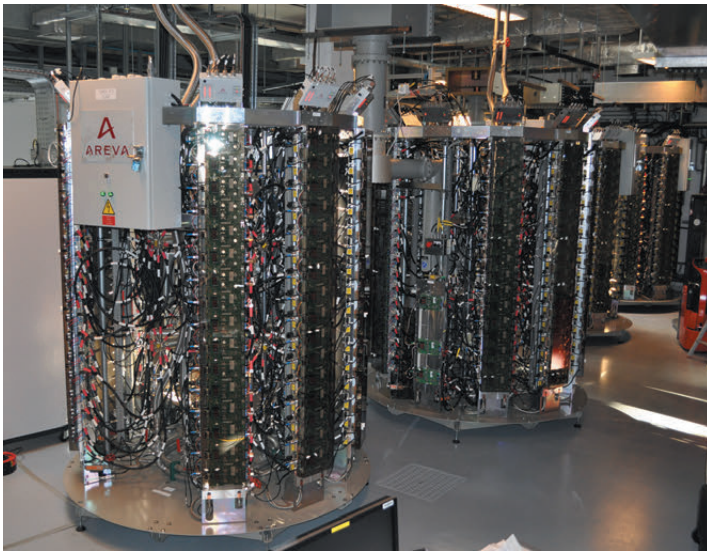


**Fig. 162:** First four 150 kW solid state amplifiers installed in the booster RF room.

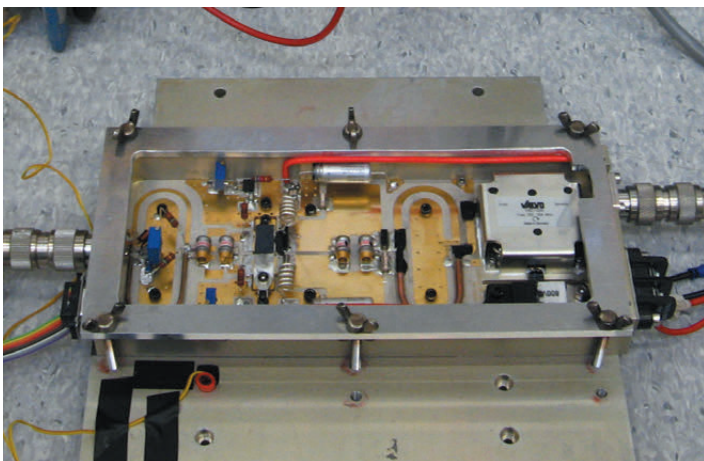


**Fig. 163:** 650 W RF module under test.

ELTA has benefited from a transfer of technology from SOLEIL, where the elementary building blocks were qualified. For this project, SOLEIL developed a new RF module using the latest sixth generation LDMOS-FET (BLF578 from NXP), which allowed a doubling of the nominal power of the basic RF module from 330 W in the existing SOLEIL amplifiers to 650 W for the ESRF amplifiers (**Figure 163**). By combining the power from 128 such RF modules, a single coaxial combiner tree or "tower" delivers more than 75 kW. Only two such towers are needed to build a 150 kW amplifier.

The RF modules are mounted on water cooled plates together with individual 280 VDC to 50 VDC converter boards. The 280 V DC power supplies and the anti-flicker system for the booster were implemented in collaboration between the RF Group and the Power Supply Group.





## ■ Next generation of solid state amplifier under development

The RF group is already working on the next generation of solid state amplifier. The existing RF modules in **Figure 163** are using LDMOS transistors in class AB push-pull operation, which require balun transformers at the input and the output. These baluns are made with coaxial lines accurately cut to dimension, bent and welded onto the printed circuit board. The ESRF is now developing a new RF module using printed circuit suspended baluns, which should alleviate this tedious fabrication process. Recent results are extremely promising, as 800 W output power was obtained with reasonably low circuit temperatures.

A new type of combiner using a single cavity was developed at the ESRF in collaboration between the RF and Mechanical Engineering Groups. In its ultimate version shown in **Figure 164**, it couples 132 modules into one 352.2MHz cylindrical cavity. A prototype with only 18 inputs has been built and tested at low level with promising results. The expected advantages are the small footprint as compared to the existing coaxial combiner trees, the possibility of easily adapting the number of modules and good power transfer efficiency.

A research programme was launched to further develop high-power solid-state amplifiers using cavity combiners for particle accelerators. It receives funding from the EU as work package WP7 via the FP7/ESFRI/CRISP programme involving CERN-SLHC, ESS and GSI-FAIR as partners. The deliverables will be a 75 kW prototype amplifier at 352.2 MHz for the ESRF and feasibility studies for CERN, ESS and FAIR at other frequencies.

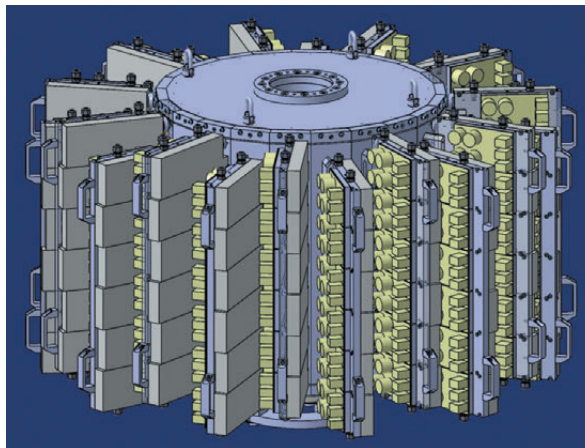


**Fig. 164:** 75 kW cavity combiner with 22 pallets, each integrating 6 RF modules and their power supplies.





SOURCE POSITION	NUMBER OF INDEPENDENT END-STATIONS	BEAMLINE NAME	STATUS
ID01	1	Anomalous scattering	Operational since 07/97
ID02	1	High brilliance	Operational since 09/94
ID03	1	Surface diffraction	Operational since 09/94
ID08	1	Dragon	Operational since 02/00
ID09	1	White beam	Operational since 09/94
ID10	2	Soft interfaces and coherent scattering	Operational from 06/12
ID11	1	Materials science	Operational since 09/94
ID12	1	Circular polarisation	Operational since 01/95
ID13	1	Microfocus	Operational since 09/94
ID14A	2	Protein crystallography EH 1	Operational since 07/99
		Protein crystallography EH 2	Operational since 12/97
ID14B	2	Protein solution small-angle scattering EH 3	Operational since 12/98
		Protein crystallography EH 4	Operational since 07/99
ID15A	1	High energy diffraction	Operational since 09/94
ID15B	1	High energy inelastic scattering	Operational since 09/94
ID16	1	Inelastic scattering I	Operational since 09/95
ID17	1	Medical	Operational since 05/97
ID18	1	Nuclear scattering	Operational since 01/96
ID19	1	Topography and tomography	Operational since 06/96
ID21	1	X-ray microscopy	Operational since 12/97
ID22	1	Microfluorescence	Operational since 12/97
ID23	2	Macromolecular crystallography MAD	Operational since 06/04
		Macromolecular crystallography microfocus	Operational since 09/05
ID24	1	Dispersive EXAFS	Operational since 02/96
ID26	1	X-ray absorption and emission	Operational since 11/97
ID27	1	High pressure	Operational since 02/05
ID28	1	Inelastic scattering II	Operational since 12/98
ID29	1	Multiwavelength anomalous diffraction	Operational since 01/00
ID31	1	Powder diffraction	Operational since 05/96
BM14	1	Macromolecular crystallography (MAD)	Operational since 01/10
BM23	1	X-ray absorption spectroscopy	Operational since 03/11

**Table 6:** List of the ESRF public beamlines.

SOURCE POSITION	NUMBER OF INDEPENDENT END-STATIONS	BEAMLINE NAME	FIELD OF RESEARCH	STATUS
BM01	2	Swiss-Norwegian BL	X-ray absorption & diffraction	Operational since 01/95
BM02	1	D2AM (French)	Materials science	Operational since 09/94
BM08	1	Gilda (Italian)	X-ray absorption & diffraction	Operational since 09/94
BM20	1	ROBL (German)	Radiochemistry & ion beam physics	Operational since 09/98
BM25	2	SPLINE (Spanish)	X-ray absorption & diffraction	Operational since 04/05
BM26	2	DUBBLE (Dutch/Belgian)	Small-angle scattering	Operational since 12/98
			EXAFS	Operational since 06/01
BM28	1	XMAS (British)	Magnetic scattering	Operational since 04/98
BM30	2	FIP (French)	Protein crystallography	Operational since 02/99
		FAME (French)	EXAFS	Operational since 08/02
BM32	1	IF (French)	Interfaces	Operational since 09/94

**Table 7:** List of the Collaborating Research Group beamlines.





## ■ User operation

After 17 years of successful operation of the facility for scientific Users, we look back on user operation over the year 2011, during which we saw further beamline upgrade works and, notably, the beginning of the first ever “long shutdown” since the ESRF began user operation back in 1994. The shutdown of the ESRF accelerator and beamlines from Monday 5th December is for a 5-month period during which the construction works for the new EX2 experimental hall extension will commence. As a consequence of this, the total beamtime available for 2011 was reduced by 20% compared with previous years. The early part of 2011 also saw the closure of one and a half beamlines (ID20 and BM05) to the public, while at the end of the year ID32 was also closed and BM16 ceased operation as a Spanish CRG beamline. Within the Upgrade Programme, the EXAFS beamline ID24 was closed for upgrade whilst BM23 re-opened to full operation for 2011. As soon as the beam was stopped in December, work began on several more Upgrade Beamline projects including the rebuilding of ID10A/B/C as one beamline complex ID10, the move of ID16 to ID20 and the move of ID14-3 to BM29. In total, 29.5 ESRF publicly funded beamlines and 9.5 CRG beamlines were available for users in 2011. **Figure 166** shows the number of applications for beamtime received since 2005. Since the beginning of the Upgrade Programme work in 2010, the number of applications received has evened off due to the unavailability of some beamlines undergoing upgrade and the closure of others. Despite this, there has been no decrease in the number of proposals received and it is therefore evident that

the number of proposals received per operating beamline continues to increase.

Proposals for experiments are selected and beamtime allocations are made through peer review. Review Committees of specialists, for the most part from European countries and Israel, have been set up in the following scientific areas:

- chemistry
- hard condensed matter: electronic and magnetic properties
- hard condensed matter: crystals and ordered systems
- hard condensed matter: disordered systems and liquids
- applied materials and engineering
- environmental and cultural heritage matters
- macromolecular crystallography
- medicine
- methods and instrumentation
- soft condensed matter
- surfaces and interfaces.

The Review Committees met twice during the year, around six weeks after the deadlines for submission of proposals (1 March and 1 September). They reviewed 2035 applications for beamtime, and selected 778 (38.2%), which were then scheduled for experiments.

The principle feature of this period was the difficulty faced by reviewers in deciding which proposals should be recommended for beamtime during the second half-year scheduling period; in this period only 60% of the usual beamtime was available and a similar number of proposals were received as in the previous year. Consequently only 32% of submitted proposals could be accepted for this scheduling period (compared to ~46% in previous years), and competition for the available beamtime was fierce.

Requests for beamtime, which is scheduled in shifts of 8 hours, totalled 30 557 shifts or 244 456 hours in 2011, of which 10 995 shifts or 87 960 hours (36.0%) were allocated. The distribution of shifts requested and allocated, by scientific area, is shown in **Table 8**.

**Table 8:** Number of shifts of beamtime requested and allocated for user experiments, year 2011.

Scientific field	Total shifts requested	Total shifts allocated
Chemistry	3 453	1 029
Hard Condensed Matter: Electronic & Magnetic Properties	3 661	1 232
Hard Condensed Matter: Crystals & Ordered Structures	3 942	1 245
Hard Condensed Matter: Disordered Systems	1 059	432
Applied Materials & Engineering	3 302	1 052
Environmental & Cultural Heritage Matters	2 492	777
Macromolecular Crystallography	3 579	2 162
Medicine	1 252	447
Methods & Instrumentation	842	252
Soft Condensed Matter	3 113	1 149
Surfaces & Interfaces	3 862	1 218
<b>Totals</b>	<b>30 557</b>	<b>10 995</b>



The breakdown of shifts scheduled for experiments by scientific area in the first half of 2011 is shown in **Figure 167**. The full year 2011 saw 5475 visits by scientists to the ESRF under the user programme, to carry out 1345 experiments; the number of users in each experimental team averaged just over 4 persons while the average duration of an experimental session was 9 shifts. This can be further broken down to show an average duration of 3 shifts for MX experiments and 14.5 shifts for non-MX experiments. The annual number of experimental sessions and user visits since 2005 is shown in **Figure 166**. The particularly high figures in 2009 are mainly due to the fact that an extra week of beam time was made available to users during that year to compensate partly for the anticipated reduction in beam time available in later years following the start of the reconstruction work of the Upgrade Programme. The effect of the reduction in beamtime available in 2011 due to the long shutdown is clearly visible in the lower-than-normal numbers of experimental sessions carried out and user visits.

One of the principle measurable output parameters of the ESRF is the number and quality of publications accepted in peer-reviewed journals. **Figure 168** shows how this number has been rising continuously over the past years, with a publication output systematically on a level of one publication per experimental session and reaching record numbers of more than 1800 for the years 2009 and 2010. The year 2011 promises to be equally fruitful, with 1692 publications already registered in the ILL/ESRF Library database. Since the ESRF began user operation back in 1994, a total of 19396 publications have been accepted in peer-reviewed journals. Of these, more than 200 every year are published in high impact factor journals.

User responses to questionnaires show once again that the ESRF continues to maintain its excellent reputation concerning the assistance and service given by scientists and support staff on beamlines, and travel and administrative arrangements, in addition to the quality both of the beam and of the experimental stations. Facilities on site, such as preparation laboratories, the Guesthouse and a canteen open 7 days a week, also make an important contribution to the quality of user support.

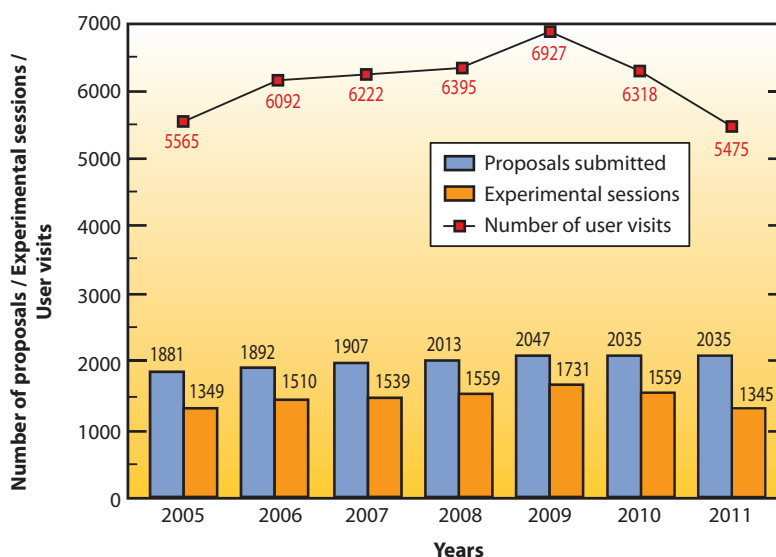


**Fig. 166:** Numbers of applications for beamtime, experimental sessions and user visits, 2005 to 2011.

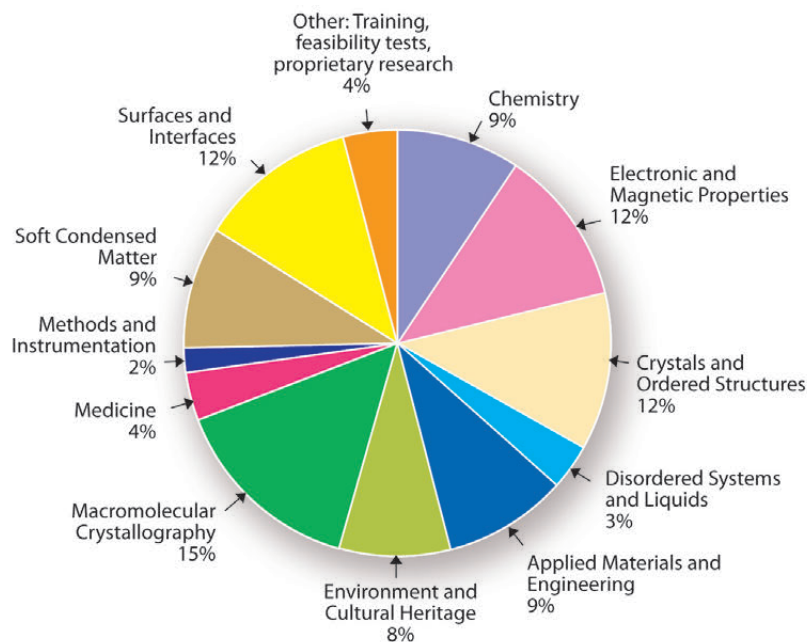


**Fig. 167:** Shifts scheduled for experiments, March to July 2011, by scientific area.

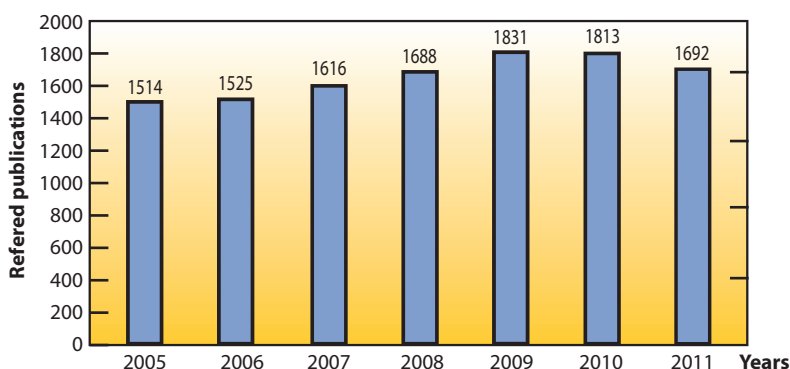


**Fig. 168:** Numbers of publications appearing in refereed journals, 2005 to 2011.



## Administration and finance

### Expenditure and income 2010

Expenditure	kEuro	Income	kEuro
Accelerator and Source		2010 Members' contributions	87 270.3
Personnel	5 617.2	Funds carried forward from 2009	915.5
Recurrent	1 467.5	Other income	
Operating costs	1 225.6	Scientific Associates	4 963.1
Other recurrent costs	241.9	Sale of beamtime	1 723.2
Capital	4 647.5	Compensatory funds	0.0
Accelerator and Source developments	4 647.5	Scientific collaboration and Special projects	3 775.6
Beamlines, experiments and in-house research			
Personnel	18 461.0		
Recurrent	6 125.7		
Operating costs	3 136.7		
Other Recurrent costs	2 989.0		
Capital	6 193.5		
Beamline developments	5 091.5		
Beamline refurbishment	1 102.0		
Technical and administrative supports			
Personnel	27 224.8		
Recurrent	12 352.7		
Capital	7 801.8		
Unexpended committed funds			
Funds carried forward to 2011	8756.0		
<b>Total</b>	<b>98 647.7</b>	<b>Total</b>	<b>98 647.7</b>

### Revised expenditure and income budget for 2011

Expenditure	kEuro	Income	kEuro
Accelerator and Source		2011 Members' contributions	82 152
Personnel	5 535	Funds carried forward from 2010	8 756
Recurrent	1 395	Other income	
Operating costs	1 325	Scientific Associates	4 960
Other recurrent costs	70	Sale of beamtime	1 600
Capital	6 827	Compensatory funds	0.0
Accelerator and Source developments	6 827	Scientific collaboration and Special projects	3 060
Beamlines, experiments and in-house research			
Personnel	18 099		
Recurrent	5 725		
Operating costs	1 905		
Other Recurrent costs	3 820		
Capital	9 637		
Beamline developments	9 418		
Beamline refurbishment	219		
Technical and administrative supports			
Personnel	26 191		
Recurrent	11 320		
Capital	15 329		
Unexpended committed funds			
Personnel	430		
Recurrent	40		
<b>Total</b>	<b>100 528</b>	<b>Total</b>	<b>100 528</b>

The budget for 2011 includes additional contributions from Members and Scientific Associates of 15 385 kEuro dedicated to the Upgrade Programme. The Upgrade expenditure budget amounts to a total of 29 400 kEuro including 14 755 kEuro of ESRF operating budget.

#### Expenditure 2010 by nature of expenditure

	kEuro
<b>PERSONNEL</b>	
ESRF staff	49 193.7
External temporary staff	67.9
Other personnel costs	2 041.4
<b>RECURRENT</b>	
Consumables	8 159.4
Services	9 349.7
Other recurrent costs	2 436.9
<b>CAPITAL</b>	
Buildings, infrastructure	2 933.4
Lab. and Workshops	231.5
Accelerator and Source incl. ID's and FEs	4 647.4
Beamlines, Experiments	7 995.4
Computing Infrastructure	2 745.3
Other Capital costs	89.9
Unexpended committed funds	
Funds carried forward to 2011	8 756.0
<b>Total</b>	<b>98 647.7</b>

#### Revised budget for 2011 by nature of expenditure

	kEuro
<b>PERSONNEL</b>	
ESRF staff	48 292
External temporary staff	85
Other personnel costs	1 878
<b>RECURRENT</b>	
Consumables	7 295
Services	8 765
Other recurrent costs	2 420
<b>CAPITAL</b>	
Buildings, infrastructure	10 546
Lab. and Workshops	1 528
Accelerator and Source incl. ID's and FEs	6 827
Beamlines, Experiments	9 637
Computing Infrastructure	3 227
Other Capital costs	28
<b>Total</b>	<b>100 528</b>





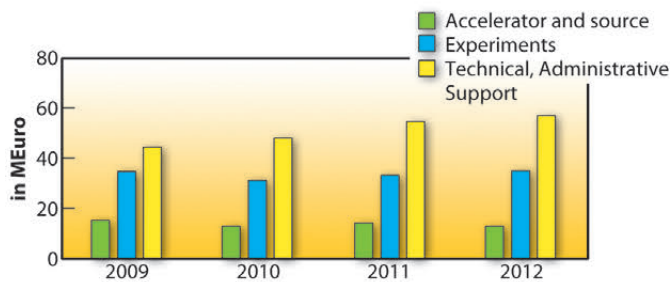
**2011 manpower (posts filled on 31/12/2011)**

	Scientists, Engineers, Senior Administrators	Technicians and Administrative Staff	PhD students	Total
<b>Staff on regular positions</b>				
Accelerator and Source	27	37.5		64.5
Beamlines, instruments and experiments*	228	86.8	24.5	339.3
General technical services	29.6	50		79.6
Directorate, administration and central services	33.6	51.7		85.3
<i>Sub-total</i>	<i>318.2</i>	<i>226</i>	<i>24.5</i>	<i>568.7</i>
<b>Other positions</b>				
Short term contracts	6.9	13.9		20.8
Staff under "contrats de professionnalisation" (apprentices)		20		20
European Union grants	1			1
Temporary workers		1		1
<b>Total</b>	<b>326.1</b>	<b>260.9</b>	<b>24.5</b>	<b>611.5</b>
Absences of staff (equivalent full time posts)				24.6
<i>Total with absences</i>				<i>586.9</i>
Scientific collaborators and consultants	9			9
External funded research fellows	5		19	24

\* Including scientific staff on time limited contract.

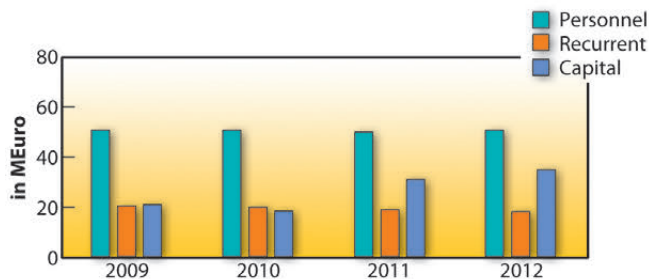
**Financial resources in 2009, 2010, 2011 and 2012, by major programme**

(current prices in MEuro for the respective years)



**Financial resources in 2009, 2010, 2011 and 2012, by nature of expenditure**

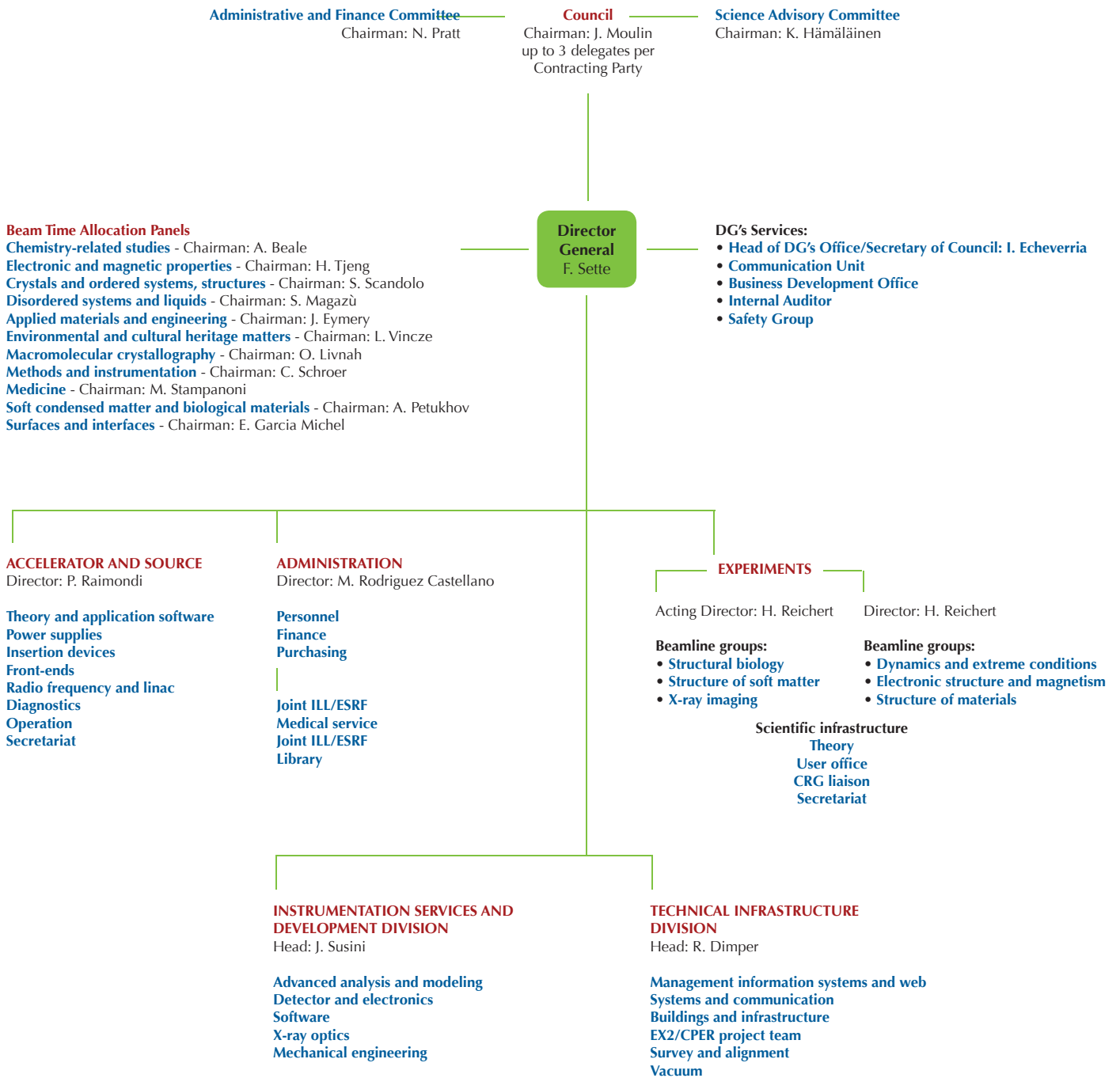
(current prices in MEuro for the respective years)





# Organisation chart of the ESRF

(as of January 2012)





**We gratefully acknowledge the help of:**

C. Argoud, J. Baruchel, M. Bowler, B. Boulanger, N.B. Brookes, K. Clugnet,  
M. Collignon, E. Dancer, R. Dimper, I. Echeverría, L. Farvacque, A. Fitch, P. Gaget,  
S. Gerlier, E. Gregoryanz, C. Habfast, E.S. Jean-Baptiste, A. Kaprolat, M. Krisch,  
G. Leonard, S. Markaryan, J. McCarthy, T. Narayanan, K. Nolan, S. Perez,  
H. Reichert, F. Sette, J. Susini, S. McSweeney, K. Wong  
and all the users and staff who have contributed  
to this edition of the Highlights.





Editor

G. Admans

Layout

Pixel Project

Printing

Imprimerie du Pont de Claix

© ESRF • February 2012

Communication Group

ESRF

BP220 • 38043 Grenoble • France

Tel. +33 (0)4 76 88 20 56 • Fax. +33 (0)4 76 88 25 42

<http://www.esrf.eu>